Advances in Civil Engineering

Advancements in Tunnel Construction 2021

Lead Guest Editor: Jianjun Ma
Guest Editors: Mingfeng Lei, Yilin Gui, and Yu Liang

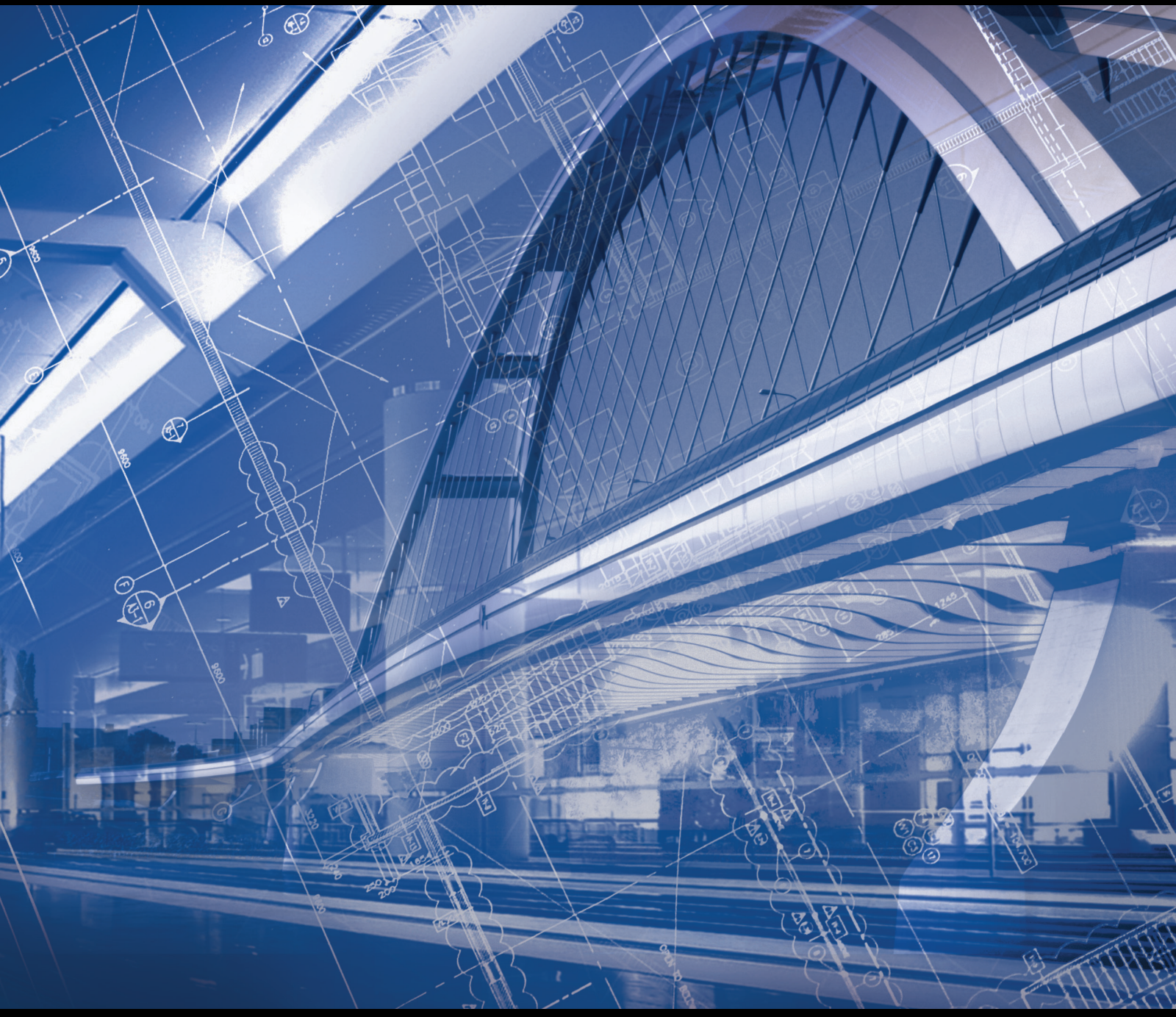

Advancements in Tunnel Construction 2021

Advances in Civil Engineering

Advancements in Tunnel Construction 2021

Lead Guest Editor: Jianjun Ma
Guest Editors: Mingfeng Lei, Yilin Gui, and Yu Liang

Contents

Hindawi
Advances in Civil Engineering
Volume 2022, Article ID 2214008, 10 pages
https://doi.org/10.1155/2022/2214008

Research Article

DLSM Simulation Analysis of the Influence of Blasting Construction on Adjacent Tunnels in Rock Mass with Discontinuities

XuHui Li,[1] **GuoLong Qiao**,[1] **and Junwei Guan**[2]

[1]*Guangdong Pearl River Delta Water Supply Co., Ltd., GuangZhou 510000, China*
[2]*School of Civil Engineering, Sun Yat-Sen University, Zhuhai 519000, China*

Correspondence should be addressed to Junwei Guan; guanjw3@mail2.sysu.edu.cn

Received 22 February 2022; Accepted 4 April 2022; Published 28 April 2022

Academic Editor: Mingfeng Lei

In order to study the influence of blasting construction of rock mass with discontinuities on adjacent tunnels, a feasible blasting scheme is formulated to ensure the safety of adjacent tunnels during construction. Based on the water resources allocation project in the Pearl River Delta, a tunnel construction model is established by using continuous-discontinuous medium mechanics calculation model, Distinct Lattice Spring Model (DLSM), to simulate the impact of blasting construction of the left tunnel on the right adjacent tunnel. According to the numerical simulation results, the stress wave transmission process of the left tunnel with blasting time $t = 18$ ms is analyzed. Furthermore, the effects of the positions of the discontinuity, the width of the discontinuity, and the angle between the discontinuity and the horizontal direction on the adjacent tunnel are studied. The modelling results show that the existence of discontinuities plays a certain role in improving the safety of adjacent tunnels in the blasting stage. The farther the distance between the discontinuity and the adjacent tunnel is, the smaller the impact of blasting on the adjacent tunnel is. In the process of blasting, the larger the width of discontinuity is, the more effective it is to block the influence of blasting stress wave on the adjacent tunnel. The smaller the angle between discontinuity and horizontal direction, the smaller the impact of blasting on adjacent tunnels.

1. Introduction

With the development of China's economy in recent years, the infrastructure construction has also developed with a fast speed. Major projects, such as the South-to-North Water Division Projects and West-to-East Gas Pipeline, have been implemented, indicating that the domestic tunneling projects are no longer limited to single-track tunnels. The double-track tunnel projects will bring higher economic benefits. With the increase of tunnel burial depth, the rock hardness and construction difficulties will increase, and the requirements of tunnel construction methods also are tending to be higher gradually. Among these construction methods, Drilling and Blasting method (D&B) is one of the most efficient and economic options [1].

During the D&B process, whether it is a double-track tunnel project or a single-track tunnel project, the surrounding rock mass of the tunnel will inevitably be affected during construction. Apart from that, when the site of D&B process is located near the buildings or existing tunnels, the impacts bringing to the building surroundings induced by blast stress wave also cannot be neglected [2], and it can even cause the instability of the surrounding buildings and structures. Although the technology is developing, new blasting technology [3] also has been continuously applied to tunnel excavation in rock stratum, and these technologies can effectively control the stress wave and disturbance zone. In most cases, it is limited by the efficiency and rock strength; the traditional blasting techniques are still widely used. Therefore, analyzing the impacts of tunnel brought by blasting has both practical significance and engineering values. The current general research method is to simulate the physical process of blasting by numerical simulation [4], so as to analyze the influence of blasting on

tunnel surrounding rock, due to the limitation of monitoring means. Jia et al. [5] established the numerical model of the influence of blasting on lining vibration by using finite element method and provided the simulation methods of loading time and peak load and analyzed the impact of tunnel lining by blasting. Bi and Zhong [6] analyzed the impacts of existing tunnels by ANSYS according to different tunnel spacing and types of surrounding rock. Yu et al. [2] applied ANSYS/LS-DYNA to simulate the vibration response mechanism of the framework of adjacent buildings frame structure under tunneling blasting effects. And current analysis software types used in blasting simulations are FLAC3D, MIDAS/GTS, LY-dynamics and so on. These software types are mostly analyzed based on the finite element, ignoring the features like discontinuity and non-uniformity [7]. Apart from that, related numerical methods also include the discrete element [8], the boundary element [9], and discontinuous deformation [10]. Although these methods are successfully used in many blasting related analyses, the blasting belongs to a large deformation and the grasp of spread rules of stress waves is strictly controlled during the simulation processes. These analyzing methods still pose limitations on this aspect and continuous surface. Distinct Lattice Spring Model (DLSM) [11] is a continuous-discontinuous numerical calculation method, which can show the reality of continuity of layered rock mass and discontinuity between joints, with good optimization according to the spread law of stress waves, and can show the process of stress wave spreading again. As pointed out and investigated by Zhao [12], DLSM is very efficient in wave propagation problems. It could simulate the wave propagation problems with good accuracy and good agreements with experimental results. It is known that wave propagation is one of the key features of explosion problems; thus DLSM might have special potential on modelling of blasting wave propagation problems. Similar work based on DLSM can be found in [13, 14] for the cases of zonal disintegration and cavity on tunnel stability. Field work analysis for tunnel stability also can be referred to soil-water inrush case study by Huang et al. [15] and tunnel lining study by Lei et al. [16].

In this paper, in order to analyze the effect of blasting process of one side to another side of tunnel during the construction process of double-line tunnel, the numerical analysis model DLSM is used to analyze the actual tunnel engineering case in the Pearl River Delta water resources allocation project. Firstly, the general situation of specific projects is briefly introduced. Then the related principles of DLSM software are introduced, and the models and related methods constructed in this paper are introduced. Finally, through numerical simulation, the influence of the position of discontinuity, the width of discontinuity, and the angle between discontinuity and horizontal direction on adjacent tunnels are studied.

2. Project Overview

Located in the south central of Guangdong province, Pearl River Delta water resources allocation project is a crucial water resources allocation project put forward in "Comprehensive planning for the Pearl River Basin (2012–2030)" and it is also one of the 172 major water conservancy projects to save and supply water in China. The total length of the main water delivery line is about 90.3 km, starting from Liyuzhou, the mainstream of Xijiang River. After being pressurized by the pumping station, the water will be delivered to the newly built Gaoxinsha Reservoir at the intersection of Nansha New District by a double-line shield tunnel, with a line length of about 41.0 km. After being pressurized by Gaoxinsha Pumping Station, the water is delivered to Shaxi high-level pool on the south side of Shaxi Reservoir in Dongguan by single-line shield tunnel and then delivered to Luotian Reservoir in Shenzhen by single-line mountain tunnel, with the line length of about 49.3 km, of which the single-line shield tunnel is about 30.7 km long and the mountain tunnel is 18.1 km long.

The proposed water pipeline of the project is located in the plain area of the Pearl River Delta, among which the Liyuzhou-Gaoxinsha pipeline is located in Foshan area and Guangzhou area, respectively. In this area, the surface water system is developed, the river network is dense, and the groundwater level is shallow. The underground structure is mainly composed of Quaternary strata silt, silty sand layer, medium-coarse sand layer, cohesive soil layer, muddy siltstone layer, etc., among which the sand gravel layer has strong water permeability. Therefore, most of the water resources allocation projects along the Pearl River Delta pass through the areas along the route in the form of tunnels, in which TBM or drilling and blasting method is used for construction in some areas with rock strata underground. The main stratum introduction is shown in Table 1 and Figure 1.

Apart from that, the local soil layers are mingled with strongly weathered siltstone, totally weathered argillaceous siltstone, wear weathered granite, conglomerate, and siltstone containing conglomerate, among which the strongly weathered and fully weathered argillaceous siltstone are relatively soft, and weakly weathered granite, conglomerate, and siltstone containing conglomerate are hard.

3. DLSM Introduction and Model Overview

DLSM is a rock dynamics calculation model developed by Professor Zhao Gaofeng in Tianjin University based on continuum-discontinuous medium mechanics. Through DLSM, the material is dispersed into particles of different sizes, which are similar to the particles in PFC calculation software. These particles are the basic units of the material model-spherical units. At the same time, the ball units are connected with each other, and finally a material body with certain strength [8] is formed.

In DLSM calculation, when the gap between two particles is less than a given threshold, two particles will be connected together by a bond through the center point, which is composed of a normal spring and a shear spring, and the normal spring and the shear spring have certain strength. If the gap between two particles is greater than a given threshold distance, the spring will be broken, and local damage will occur. Therefore, the threshold will affect the

Table 1: Stratum conditions.

Main strata	Features
Silty soil	Light grey, dark grey, saturated, plastic flow to soft plastic condition, contains minor organic matter and humus layer, multisandwich thin layer of fine. The luster reaction is smooth with no shaking reactions. High dry strength and high toughness.
Silt	Grey, slightly dense to medium dense, the main composition id Quartz sand silt, with minor clay.
Medium to coarse sand	Grey, grey colour, saturated, slight to medium dense. Main composition are Quartz sand and it contains minor clay.
Cohesive soils	graphite, grey, light grey, grayish yellow, plastic to hard plastic, minor amount of slightly shiny shake reaction, medium dry strength, medium toughness.
Argillaceous siltstone	Dark grey, powder grain, layer structure, argillaceous cement fractures are developed and cores are in short columns.

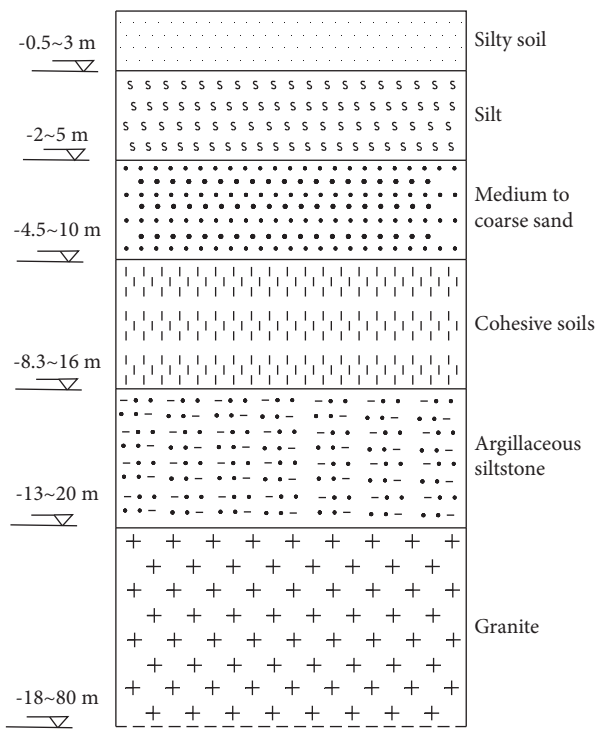

Figure 1: Stratum layout.

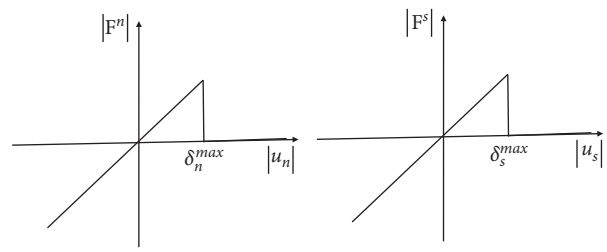

Figure 2: Constitutive model in DLSM.

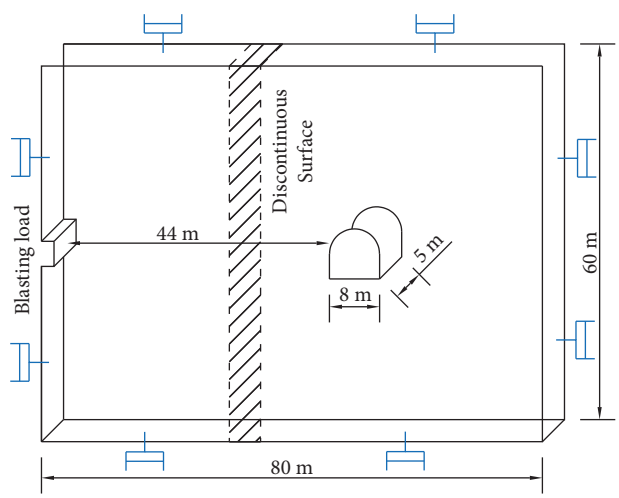

Figure 3: Calculation model diagram.

lattice structure of the model, and different thresholds will produce different lattice structures, which will have certain influence on the strength of the material system. Figure 2 is a schematic diagram of DLSM constitutive model. Because of the existence of normal spring and shear spring at the same time, when DLSM calculation software is used to analyze rock dynamic characteristics, only the elastic modulus and Poisson's ratio of rock mass can be input to calculate the strength of the spring, so that the continuity and local damage of rock mass can be fully considered. For the blasting simulation with discontinuities studied in this paper, DLSM software has unique advantages, which can well simulate the propagation of blasting stress wave in surrounding rock with discontinuities.

In this paper, the geotechnical calculation model DLSM is used to establish a 3D model. Because the newly built Gaoxinsha Reservoir from Liyuzhou to the intersection point of Nansha New District in the mainstream of Xijiang River uses a double-line shield tunnel to deliver water, the influence of the left tunnel blasting construction on the right adjacent tunnel is simulated here, and the calculation model is shown in Figure 3. The size of the model is 80 m × 60 m × 5 m, the explosion drilling is simplified to a rectangular box of 2 m × 4 m × 5 m, and the minimum distance of tunnel blasting is 44 m. In this study, only the responses of surrounding rock near the tunnel are studied. We separated the calculation region from the whole stratum. To eliminate the effects of those separated surfaces on dynamic response, nonreflection boundaries are applied on separated surfaces. The axial displacement of the front and rear faces of the tunnel is taken as the fixed boundary to simulate the plane strain problem, and the left, right, and bottom surfaces are set as no reflection boundaries.

In order to analyze the blasting impacts on each surface of the tunnel, the monitoring points are arranged at the arch

foot, arch wall, and vault, respectively. In order to simplify the calculation, the loading stress diagram is simplified to triangular impulse load, which is the same as stated by literature [17], and relative curve is shown in Figure 4. The time of maximum stress is $t_e = 0.0005$ s, the blasting end time is $t_m = 0.0025$ s, and the total time is $t = 0.018$ s. At the same time, in order to simplify the model, let the blasting stress spread even to the defiled line of blast holes, which means that the delay time of explosion on different surfaces is ignored.

Only the adjacent tunnel is studied. Only one stratum is included inside the calculation region. Thus, only one set of material parameters is used. According to the actual situation of Liyuzhou-Gaoxinsha pipeline project, relevant parameters of tunnel surrounding rock are selected, as shown in Table 2.

4. Results and Analysis

4.1. Stress Wave Transmission Process Analysis. Figure 4 shows the spread process of stress wave at $t = 6$ ms and $t = 8$ ms; Figure 5 shows the spread process of stress wave at $t = 9$ ms and $t = 11$ ms.

According to the stress wave transmission nephogram of $t = 6$ ms in Figure 5, it can be seen that, within 6 ms of blasting, the stress waves generated by blasting gradually spread around, including horizontal diffusion and vertical diffusion, mainly horizontal diffusion, and gradually spread to the vicinity of adjacent tunnels. According to the stress wave transmission nephogram of $t = 8$ ms in Figure 5, it can be seen that, after 8 ms of blasting, when the stress wave is transmitted to a position near the tunnel, the stress will be reflected and attenuated, which is the discontinuous surface near the tunnel. It can be seen that when the stress wave is transmitted to the discontinuous surface, some energy is absorbed by the discontinuous surface, and the discontinuous surface has a certain isolation effect on the stress wave. It can be seen that the existence of the discontinuous surface can weaken the blasting energy transferred to the adjacent tunnel.

At the same time, according to the cloud image of spread of stress wave at $t = 9$ ms in Figure 6, the stress wave spreads to the left side surface of tunnel within 9 ms, and the reflection and incident superposition of vibration waves occur at the vertical wall, resulting in a certain tensile stress. According to the stress wave transmission nephogram at $t = 11$ ms in Figure 6, it can be seen that, under the influence of incidence, reflection, refraction, and other effects, the stress wave is repeatedly superimposed and its intensity is constantly decreasing, and the wave surface and shape are gradually becoming complex.

Figure 7 shows the vibration process curves of 6 monitoring locations which are left foot, right waist, vault, left waist, left foot, and bottom. It can be seen that the vibration speed is maximum at left waist location, which is close to 0.9 m/s, and then its left foot, which is slightly smaller than left waist with 0.78 m/s. And then its vault and bottom speed is 0.2 m/s. The measuring point with the smallest vibration velocity is the right waist, only 0.065 m/s. In Chinese standard GB-6722 (2014), the allowable maximum velocity for the hydraulic tunnel safety is 0.15 m/s. In our simulations, we could note that the maximum velocity in most part of the tunnel is far beyond this limit. Thus, the tunnel subjected to adjacent blasting is not safe. To control its response, supports should be implemented as quickly as possible to bring effective constrains on surrounding rocks and suppress the responses of surrounding rock mass. The vibration velocity on the left side of the tunnel reached the maximum value at about 11 ms and then gradually decreased due to the dissipation and superposition of blasting stress waves. It can be seen that the blasting vibration of the left waist and left foot of the tunnel is the most sensitive area of the surrounding rock of the whole tunnel, so it is necessary to strengthen monitoring and pay special attention for protection.

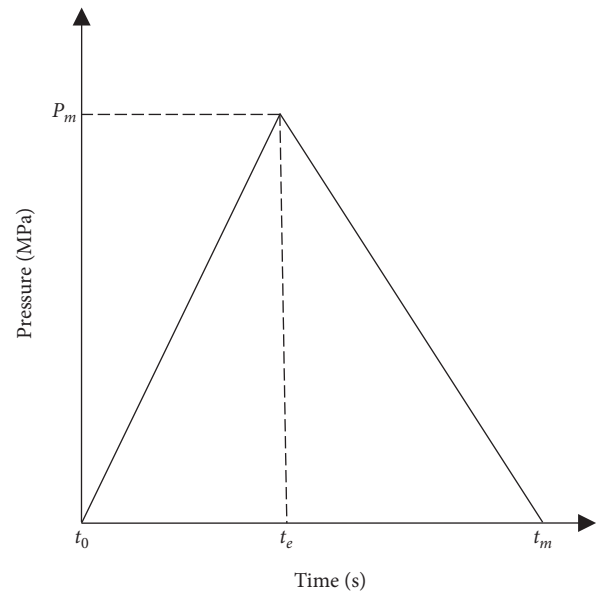

Figure 4: Loading curve.

Table 2: Geotechnical parameters used in calculation.

Density (kg/m^3)	Normal elastic modulus (GPa)	Elastic modulus of joint (GPa)	Poisson's ratio	Inner friction angle (°)	Cohesion (kPa)
2650	74	7.4	0.18	20	30

4.2. The Influence of the Distance between Discontinuities and Adjacent Tunnels. When analyzing the effects of discontinuous surface on the nearby tunnel, the width of discontinuities is uniformly set at 0.5 m, as shown in Figure 8. Figures 9 and 10, respectively, show the influence of blasting construction on adjacent tunnels when there is no discontinuity in the tunnel, with the discontinuity being 4 m and 12 m on the left side of the tunnel. The influence on the tunnel is mainly reflected by the horizontal wave velocity generated by the left arch foot, arch waist, and vault. These three positions are also the three positions where the

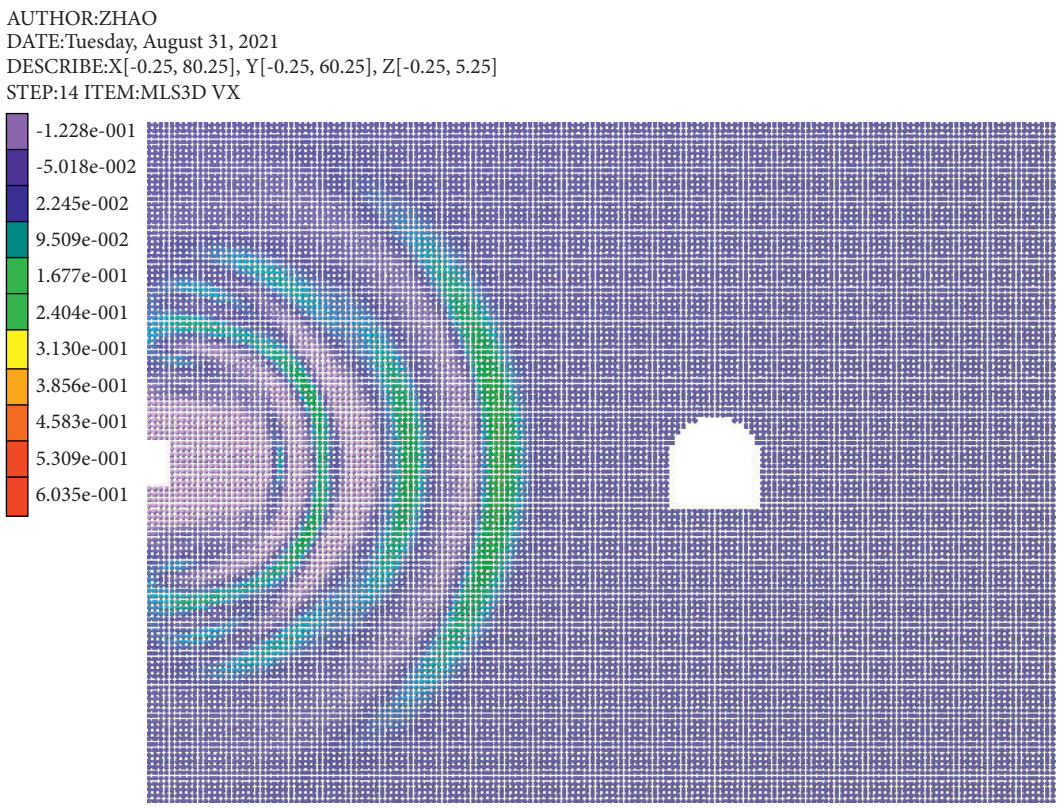

(a)

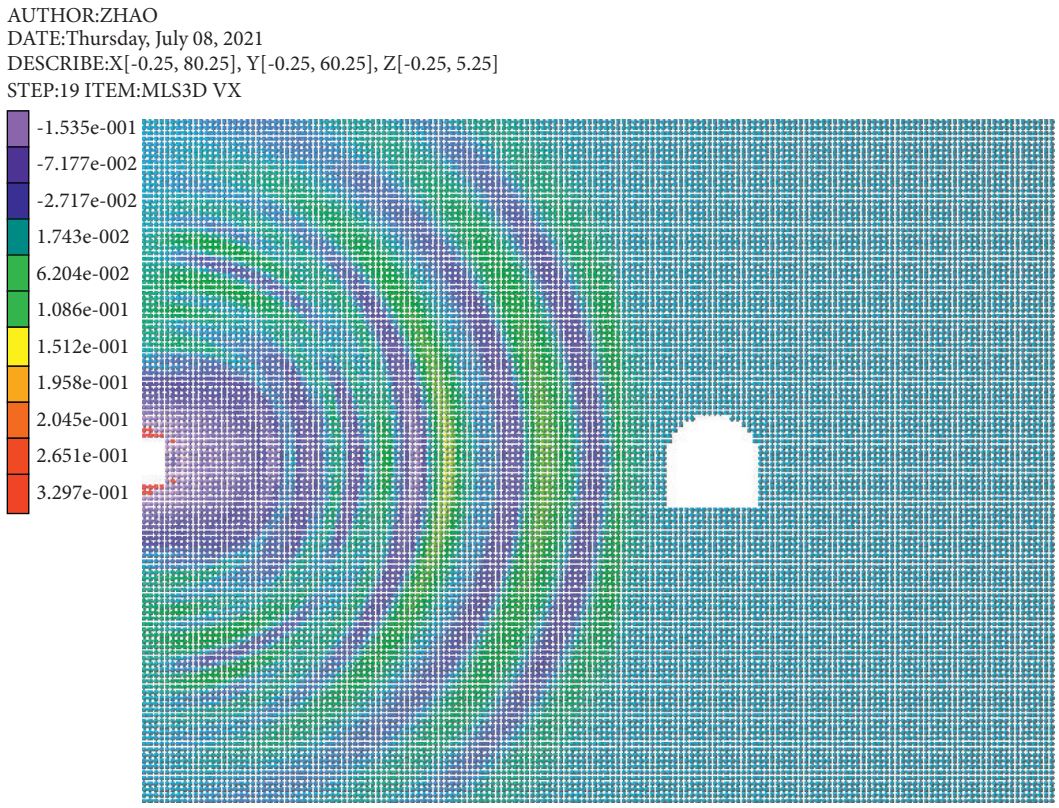

(b)

Figure 5: Cloud chart of stress wave transmission when (a) $t = 6$ ms and (b) $t = 8$ ms.

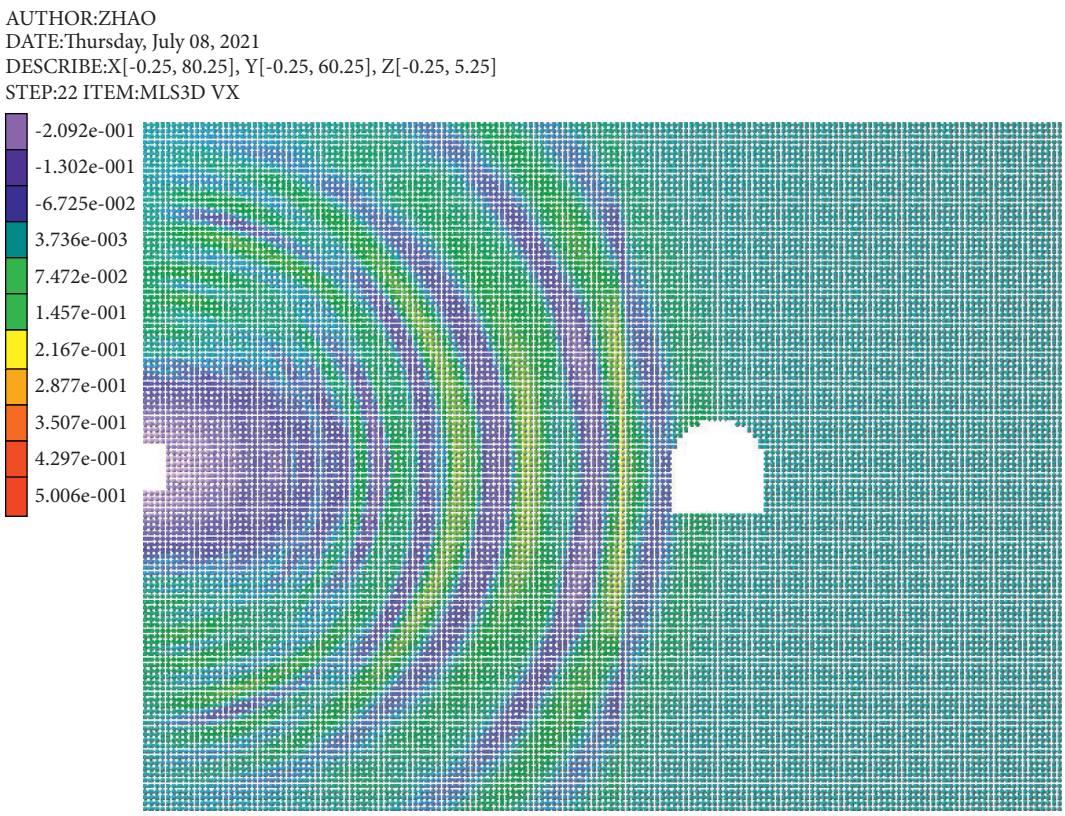

(a)

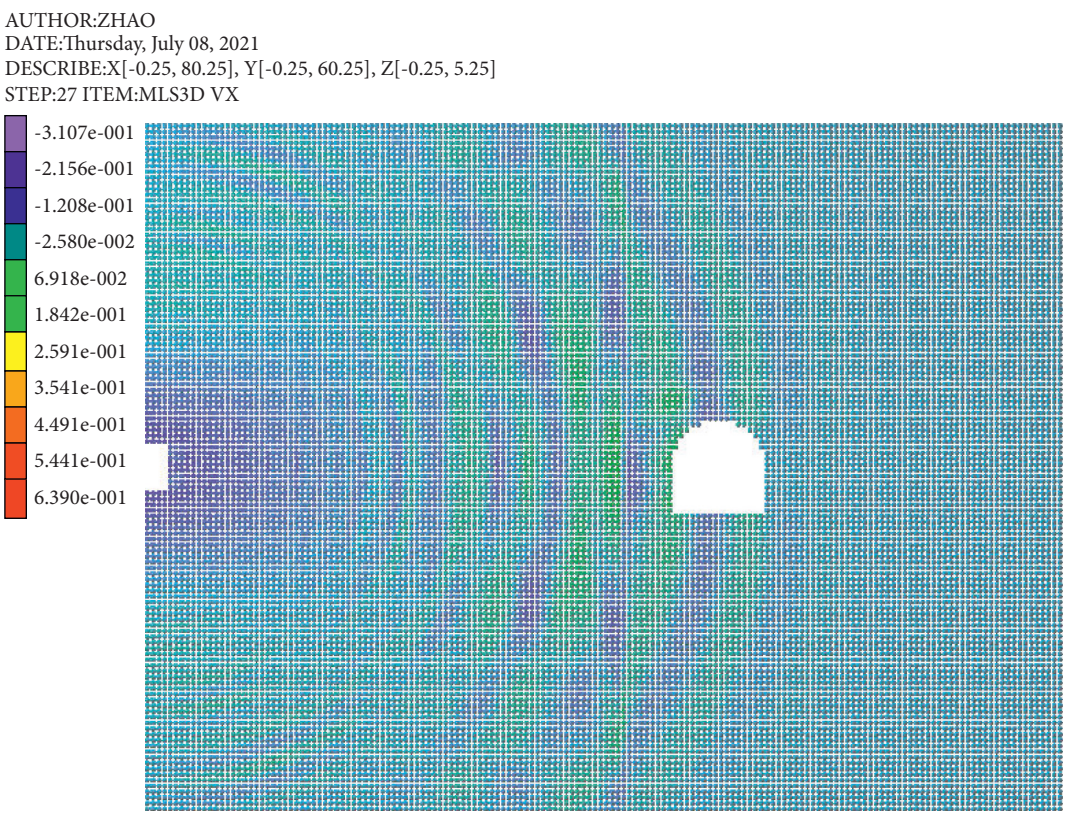

(b)

Figure 6: Cloud chart of stress wave transmission when (a) $t = 9$ ms and (b) $t = 11$ ms.

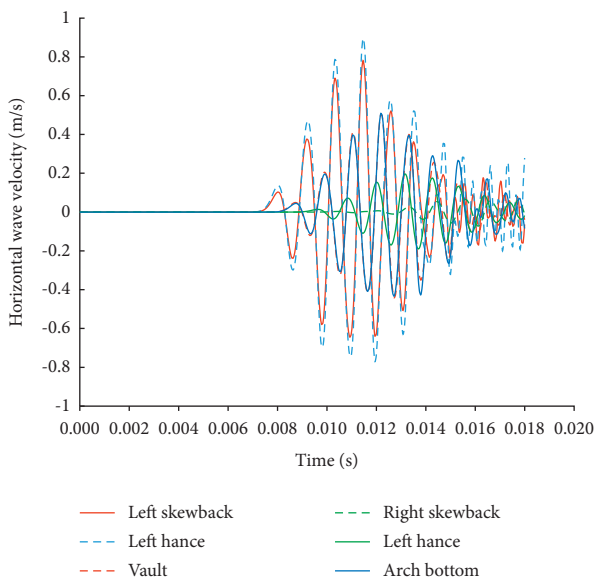

Figure 7: Time historic curve of wave velocity in different parts of tunnel.

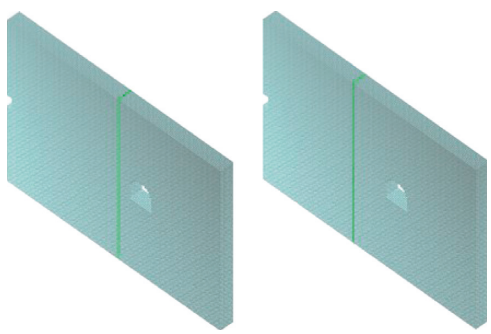

Figure 8: Schematic diagram of the model when the distance between the discontinuity and the adjacent tunnel is 4 m and 12 m, respectively.

surrounding rock of the tunnel is most likely to be damaged during blasting construction. Figure 9 is a schematic diagram of the model when the distance between discontinuity and adjacent tunnel is 4 m and 12 m.

It can be seen from Figure 9 that when there is no discontinuity in the rock mass, the maximum horizontal wave velocity of the left arch foot, arch waist, and vault of the tunnel is 0.7808 m/s, 0.8948 m/s, and 0.5035 m/s, respectively. According to Figure 9, when the discontinuity is 4 m on the left side of the tunnel, the maximum horizontal wave velocities of the arch foot, arch waist, and vault on the left side of the tunnel are 0.4296 m/s, 0.7202 m/s, and 0.3836 m/s, respectively. When the discontinuity is 12 m on the left side of the tunnel, the maximum horizontal wave velocities of the arch foot, arch waist, and vault on the left side of the tunnel are 0.4181 m/s, 0.7002 m/s, and 0.3837 m/s, respectively. It can be seen that the discontinuous surface can effectively block the impact of blasting stress wave on adjacent tunnels, and with the increase of the distance between the discontinuous surface and adjacent tunnels, the horizontal wave velocity of the left arch foot, arch waist, and

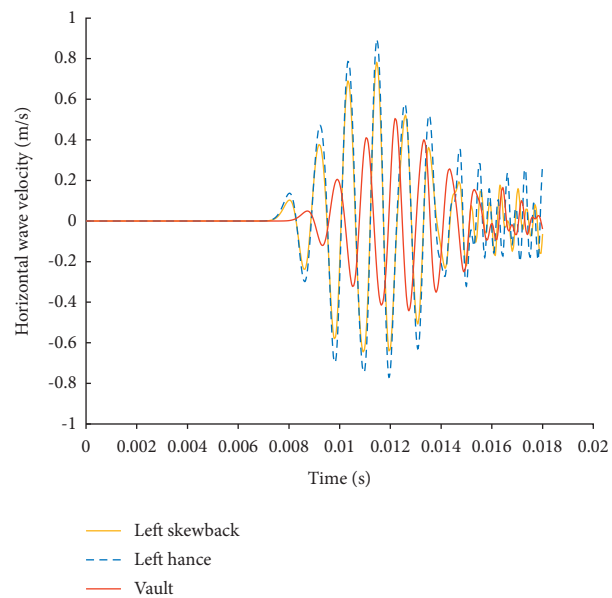

Figure 9: Horizontal wave velocity of each measuring point in tunnel without discontinuity.

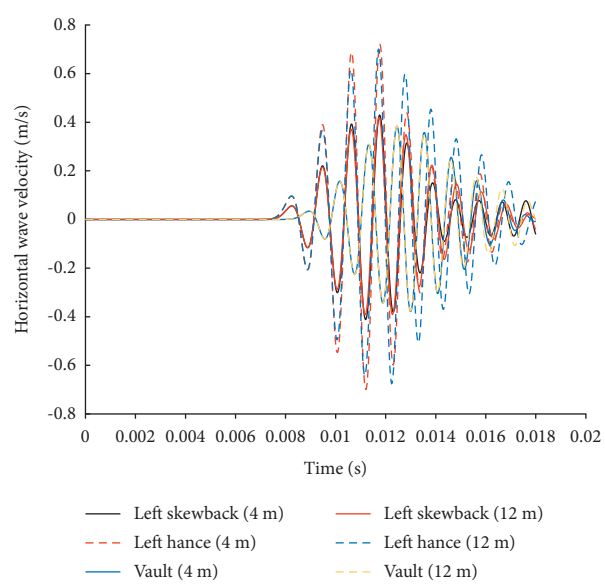

Figure 10: Horizontal wave velocity of each measuring point in tunnel when discontinuity is 4 m and 12 m on the left side of tunnel, respectively.

vault gradually decreases, and the impact of blasting construction on adjacent tunnels is smaller, and the adjacent tunnels are much stable. Note that the response velocity of the tunnel, however, is greater than the safety control limit according to GB-6722 (2014) [18]. To ensure the safety during constructions, implementation of support should be applied to control the dynamic response.

4.3. Analyses of Effects of Discontinuity Width on Tunnel. When studying the influence of discontinuity width, the distance between discontinuity and adjacent tunnel is set to

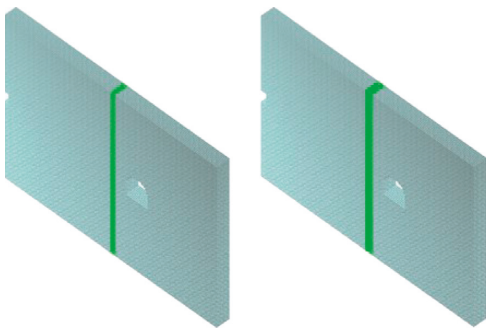

Figure 11: Schematic diagram of the model when the width of discontinuity is 2 m or 3 m, respectively.

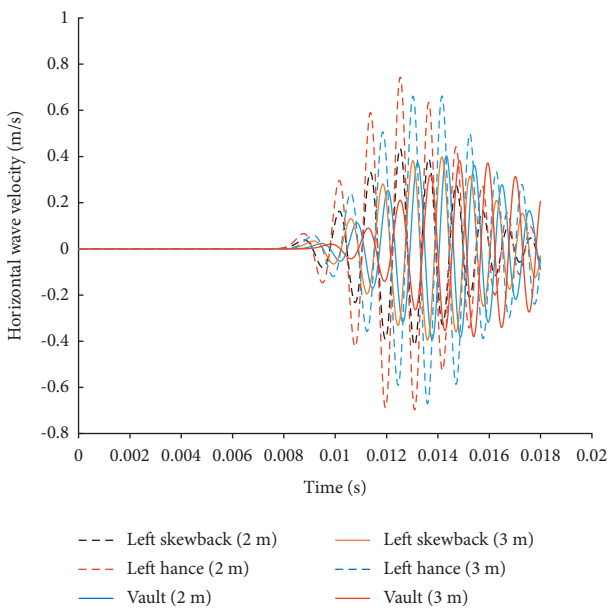

Figure 12: Horizontal wave velocity of each measuring point in tunnel when the width of discontinuity is 2 m and 3 m, respectively.

4 m. Figure 11 shows the impact of blasting construction on adjacent tunnels when the discontinuity width is 2 m and 3 m, respectively. The impact on the tunnel is mainly reflected by the maximum horizontal wave velocity generated by the left arch foot, arch waist, and vault. Figure 11 is the schematic diagram of the model when the width of discontinuities is 2 m and 3 m, respectively.

According to Figure 12, when the width of discontinuity is 2 m, the maximum wave speed from foot, waist, and vault is 0.4335 m/s, 0.7436 m/s, and 0.4026 m/s, respectively. When the width of discontinuity surface is 3 m, the maximum horizontal wave speed of the left arch foot, waist, and vault is 0.3983 m/s, 0.6612 m/s, and 0.3811 m/s, respectively. It demonstrates that, with the increase of the width of discontinuity, the maximum horizontal wave velocity of the left arch foot, arch waist, and vault of the tunnel gradually decreases, and the impact of blasting construction on adjacent tunnels becomes smaller. Based on cases mentioned above, the maximum responses of tunnel under various conditions still exceed the safety limit suggested by GB-6722 (2014) [18]. Thus, effective

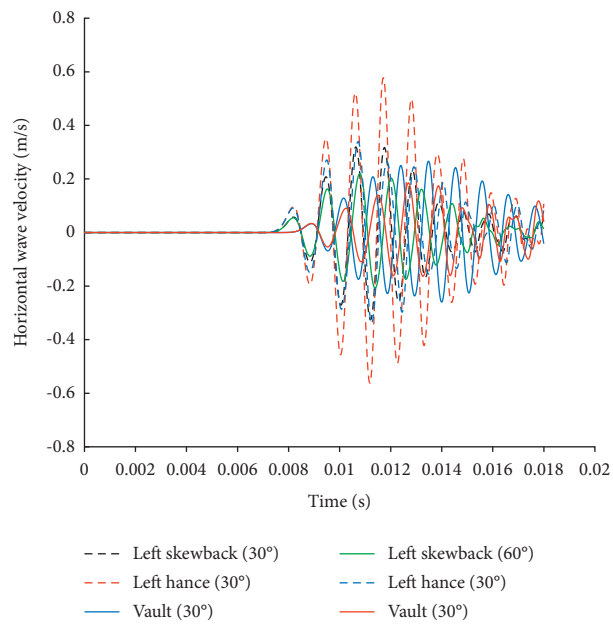

Figure 13: Horizontal wave velocity of each measuring point in tunnel when the angle of discontinuity is 30° and 60°, respectively.

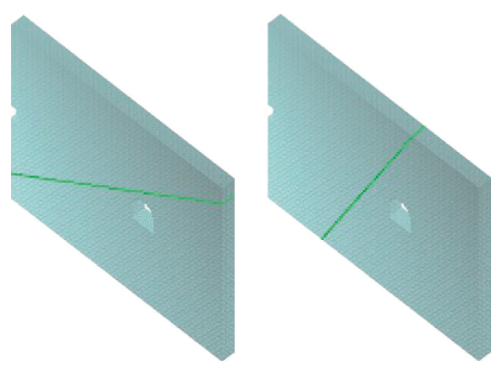

Figure 14: Schematic diagram of the model with 30° and 60° discontinuity angles.

treatments should be used to prevent the tunnel from further destructions.

4.4. Analysis of Impacts of Angle of Discontinuous Surface to the Tunnel. Figure 13 shows the influence of blasting construction on adjacent tunnels when the included angle between discontinuity and horizontal direction is 30° and 60°, respectively. The influence on the tunnel is mainly reflected by the maximum horizontal wave velocity generated by the left arch foot, arch waist, and vault for the tunnel subjected to stress wave. Figure 14 is a schematic diagram of the model when the angle of discontinuity is 30° and 60°, respectively.

It can be seen from Figure 14 that when the angle between the discontinuity and the horizontal direction is 30°, the maximum horizontal wave velocity of the arch foot, arch waist, and vault on the left side of the tunnel is 0.3185 m/s, 0.5769 m/s, and 0.2657 m/s, respectively; when the angle between the discontinuity and the horizontal direction is 60°, the maximum horizontal wave velocity of the left arch foot,

arch waist, and vault of the tunnel is 0.2199 m/s, 0.3389 m/s, and 0.1851 m/s, respectively. Compared with the case where the included angle is 90°, when the included angle is 30 and the included angle is 60°, the maximum horizontal wave velocity of the left arch foot, arch waist, and vault of the tunnel significantly decreases, and the smaller the included angle is, the more the horizontal wave velocity decreases, and the smaller the impact of blasting construction on adjacent tunnels is. In Figure 13, all the maximum measured velocities exceed the limitation in GB-6722 (2014) [18], indicating tunnel under those conditions is not safe. For the stability analysis of tunnel lining subjected to dynamic loading, some dynamic model can be applied according to [13, 19].

5. Conclusion

In this paper, based on a practical engineering project, a well-developed geotechnical calculation model DLSM is applied to establish a three-dimensional model of the tunnel. The influence of blasting construction on one side of the tunnel on the other side of the tunnel during the double-track tunnel construction is simulated, and the influence of blasting construction and the stability of the tunnel are analyzed. According to the numerical simulation results, this paper analyzes the stress wave transmission process in the left tunnel blasting time $t = 18$ ms and studies the influence of the position of discontinuity, the width of discontinuity, and the angle between discontinuity and horizontal direction on the other tunnel. The conclusions are as follows:

(1) Different positions of discontinuities (different distances from the left side of the tunnel) have certain influence on the final horizontal wave velocity of the left arch foot, arch waist, and vault. With the distance between discontinuities and the left side of the tunnel gradually increasing, the horizontal wave velocity of adjacent tunnels affected by blasting gradually decreases.

(2) With the increase of the width of discontinuity, the horizontal wave velocity of the left arch foot, arch waist, and vault of the tunnel gradually decreases, and the impact of blasting construction on adjacent tunnels becomes smaller.

(3) The influence of the angle between the discontinuity and the horizontal direction on the final horizontal wave velocity of the left arch foot, arch waist, and vault is more significant than that of the position and width of the discontinuity. With the increase of the angle between the discontinuity and the horizontal direction, the horizontal wave velocity generated by the stress wave gradually increases.

(4) The numerical model DLSM can fully consider the discontinuous and uneven characteristics of rock and soil, and thus it can accurately analyze the impact of blasting construction and tunnel stability.

Data Availability

All data presented in this paper can be available by contacting the corresponding author (Junwei Guan).

Conflicts of Interest

The authors declare that they have no known competing financial interests or personal relationships that could have appeared to influence the work reported in this paper.

References

[1] X. Feng, "Prediction of vibration response of adjacent buildings by subway drilling and explosion method," *Journal of underground space and engineering*, vol. 17, no. 2, pp. 580–589, 2021.

[2] J. Yu, H. Liu, W. Haixia, and C. Chen, "On mutual dynamic effect of tunnel blasting construction adjacent to existing tunnel," *Modern Tunnelling Technology*, vol. 56, no. 6, pp. 85–92, 2019.

[3] Y. Wang, W. pan, W. Yao, Y. Zhang, and Y. D. Jia, "Experimental study on new water seal blasting dust removal technology," *Tunnel construction (Chinese and English)*, vol. 40, no. 9, pp. 1360–1367, 2020.

[4] H. Gu, "Numerical simulation of foundation blasting effect on underlying tunnel," *Subgrade engineering*, vol. 36, no. 4, pp. 128–132, 2020.

[5] L. Jia, Y. Xie, and S. K. Li, "Numerical simulation for impact of blasting vibration on nearby tunnel lining safety," *Vibration and impact*, vol. 34, no. 11, pp. 173–177, 2015.

[6] J. Bi and J. Zhong, "Study on influence of blasting vibration from excavation of a new tunnel on existed tunnel," *Engineering blasting*, vol. 10, no. 4, pp. 69–73, 2004.

[7] Y. Liu, "Numerical simulation and analysis of the influence of blasting vibration in the tunnel crossing under a temple," *Journal of Xi'an University of Architecture and Technology (NATURAL SCIENCE EDITION)*, vol. 53, no. 2, pp. 160–166, 2021.

[8] K. Rong, S. Chen, and Y. Guo, "Application of hybrid Dem/Border complex model in simulation of tunnel excavation," *Railway survey*, vol. 33, no. 6, pp. 84–87, 2007.

[9] K. Xu and Z. sun, "New developments of the boundary element method for underground constructions," *Journal of Shijiazhuang Railway Vocational and technical college*, vol. 12, no. 3, pp. 27–31, 2013.

[10] S. Guo, X. Wu, and Y. Ning, "DDA simulation of rock fracture by blasting loads under geostress conditions," *Engineering blasting*, vol. 24, no. 5, pp. 8–14, 2018.

[11] G. Zhao, J. Fang, and Z. Jian, "A 3D distinct lattice spring model for elasticity and dynamic failure," *International Journal for Numerical and Analytical Methods in Geomechanics*, vol. 35, no. 8, 2011.

[12] G. Zhao, "Development of micro-macro continuum-discontinuum coupled numerical method," *Doctoral dissertation*, 2010.

[13] J. Ma, P. Yin, L. Huang, and Y. Liang, "The application of distinct lattice spring model to zonal disintegration within deep rock masses," *Tunnelling and Underground Space Technology*, vol. 90, pp. 144–161, 2019.

[14] J. Ma, J. Guan, J. Duan, L. Huang, and Y. Liang, "Stability analysis on tunnels with karst caves using the distinct lattice spring model," *Underground Space*, vol. 6, 2020.

[15] L. Huang, J. Ma, M. Lei, L. Liu, Y. Lin, and Z. Zhang, "Soil-water inrush induced shield tunnel lining damage and its

stabilization: a case study," *Tunnelling and Underground Space Technology*, vol. 97, Article ID 103290, 2020.

[16] M. Lei, D. Lin, Q. Huang, C. Shi, and L. Huang, "Research on the construction risk control technology of shield tunnel underneath an operational railway in sand pebble formation: a case study," *European Journal of Environmental and Civil Engineering*, vol. 24, no. 10, pp. 1558–1572, 2020.

[17] Y. Li and S. Ma, *Explosion Mechanics*, Science Press, Beijing, China, 1992, in Chinese.

[18] Chinese Society of Engineering Blasting, *GB6722–2014 Safety Regulations for Blasting*, Chinese Standarad.Press, Beijing, China, 2014, in Chinese.

[19] J. Ma, J. Chen, W. Chen, and L. Huang, "A coupled thermal-elastic-plastic-damage model for concrete subjected to dynamic loading," *International Journal of Plasticity*, vol. 153, Article ID 103279, 2022.

Hindawi
Advances in Civil Engineering
Volume 2022, Article ID 9698675, 8 pages
https://doi.org/10.1155/2022/9698675

Research Article

The Creep Test Study and Macro-Detail Analysis of Argillaceous Red Sandstone in Different Water-Containing States

Shuntao Guo,[1] Shujie Wen,[1] Hongyu Guo,[2] and Helin Fu[3]

[1]*School of Civil Engineering and Eurveying and Mapping Engineering, Jiangxi University of Science and Technology, Ganzhou, China*
[2]*China Construction Fifth Engineering Division Corp. Ltd, Changsha, China*
[3]*School of Civil Engineering, Central South University, Changsha, China*

Correspondence should be addressed to Shujie Wen; wenshujie@jxust.edu.cn and Helin Fu; fu.h.l@mail.csu.edu.cn

Received 17 December 2021; Revised 9 March 2022; Accepted 12 March 2022; Published 30 March 2022

Academic Editor: Qian Chen

In order to study the creep characteristics and failure mechanism of argillous red sandstone in a water-bearing state, uniaxial creep tests of argillous red sandstone under dry and saturated states are carried out under fractional loading. Burgers model is used to fit the test results and identify the parameters, and scanning electron microscopy is carried out on the cross section of the damaged sample. The mechanism of creep difference of argillaceous red sandstone with different water content is studied from the microscopic point of view. The results show that the uniaxial compressive strength of the saturated clay red sandstone is 46% of that of the dry clay red sandstone. The deformation level of the saturated clay red sandstone is lower than that of the dry clay red sandstone. The limit deformation of the creep failure of the water-bearing clay red sandstone is much smaller than that of the dry clay red sandstone. The long-term strength of the muddy red sandstone is 46.4 MPa in the dry state and only 14.1 MPa in the saturated state, as calculated at the steady-state creep rate. It is found that the Burgers model can describe the attenuation and stable creep of muddy red sandstone well. Through macro- and microanalysis, it is found that the compression failure form of argillaceous red sandstone belongs to x-shaped conjugate inclined plane shear failure. After saturation, the internal pores of argillaceous red sandstone become larger, and the cementation ability decreases, resulting in the decrease of rock sample strength.

1. Introduction

The stability of the geotechnical body is an important prerequisite for the safety of geotechnical engineering [1]. Most of the rock engineering instability is due to the rheological damage caused by the gradual accumulation of damage inside the rock over time. Water as the main cause of various geological hazards is an important factor affecting the creep characteristics of rocks. This is more obvious for soft rocks, which are with high mud content and are easy to disintegrate and soften with water. If the influence of water on the creep properties of muddy red sandstone is ignored, it will cause huge engineering accidents. Many scholars have studied the creep properties of soft rocks [2–6] and the effect of water on the mechanical properties of soft rocks [7–10]. Baud et al. [11] performed triaxial compression tests on the Berea, Boise, Darley Dale, and Gosford sandstones and found that the brittle strength of the rocks was reduced by 5–17% in the presence of water. Wu et al. [12] conducted graded loading creep experiments on salt rocks and established a viscoelastic-plastic damage creep model for salt rocks based on creep results, and the reasonableness of the model was further verified based on sensitivity analysis of the parameters. Zhang et al. [13] investigated the effect of saturation on the strength, elastic modulus, crack initiation stress, and damage stress threshold of siltstone. Yao et al. [14] found that the peak stress and elastic modulus in coal rocks decreased with increasing water content, but the closure stress, crack initiation stress, and damage stress thresholds did not change with increasing water content. Wang et al. [15] studied the triaxial creep behavior of the Brazilian Formation mudstone and obtained a model that

could accurately simulate the creep of the Brazilian Formation mudstone by improving the burgers model. Based on graded incremental addition and removal test, Ping et al. [16] found that the strength at destruction accounted for 57.6% of the uniaxial compressive strength for dry specimens and 86.5% for specimens in a water environment, with a low percentage of destruction strength at drying to compressive strength. Yu et al. [17] conducted uniaxial compression and multistage loading tests on red sandstone at different water contents and found that water can significantly reduce the elastic modulus of red sandstone, and the steady-state creep strain rate of dry, saturated, and soaked specimens increased with the stress level in a power law. Miyazaki [18] conducted creep tests on olivine and proposed a model based on Orowan's law to predict the creep strain rate under high temperature and low-stress states. Nadimi et al. [19] conducted a triaxial creep test on the surrounding rock in the cave of the hydropower station to estimate the deformation law of the surrounding rock of the cave and calculated the parameters of the surrounding rock creep model through the results of the creep test and the in-situ test. The validity of the parameters was verified. All the above results have advanced the study of creep properties of soft rocks, but there are few reports on the in-depth study of creep properties of muddy red sandstones in different water-bearing states and the macroscopic mechanism analysis of their variability.

This paper takes the muddy red sandstone at the construction site of the river crossing tunnel in Rongjiang New Area as the research object. The creep test with graded loading is performed under uniaxial compression of the muddy red sandstone in dry and full water state, and the creep characteristics of the muddy red sandstone in different water states are studied. Furthermore, electron microscope scanning on the damaged specimen section is performed to study the fine mechanism of the difference of creep characteristics of the muddy red sandstone in different water states. Through the creep curve, a suitable creep model is selected to fit the curve, and the rheological and mechanical parameters of the muddy red sandstone are obtained by nonlinear fitting. The parameters can be used for numerical simulation, which will provide data reference for engineering research and long-term operation.

2. Specimen Preparation and Test Equipment and Programs

2.1. Specimen Preparation. The muddy red sandstone tested was taken from the construction site of the river crossing tunnel in Rongjiang New Area, Ganzhou, Jiangxi. The specimens were drilled, cut, and polished into cylindrical specimens of Φ50 mm × 100 mm, and the size of the specimens met the requirements of the "Engineering Rock Test Methods Standard". There were a large number of microfractures in the muddy red sandstone. In order to reduce the dispersion of the experimental results, the RSM-SY5 (*T*) nonmetallic acoustic detector was used to screen the polished specimens before the test [20]. Specimens with similar wave speeds were selected, and the specimen for storage was sealed immediately after the test.

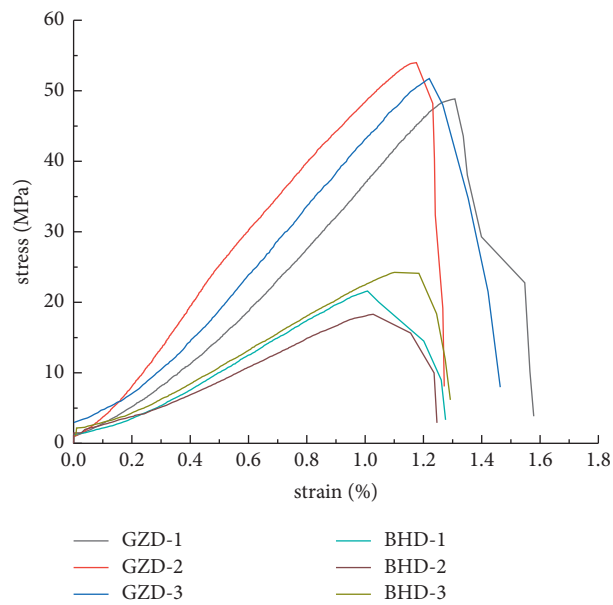

Figure 1: Uniaxial compressive stress-strain relationship curve.

2.2. Test Equipment. The test was conducted using the RMT-150C rock mechanics testing machine developed by the Wuhan Institute of Geotechnics, Chinese Academy of Sciences. The strain was measured by applying strain gauges, the strain collector was ZI-120P, and a data collector was developed by Zhubang Measurement and Control. The collector was connected to a computer system and could store a large amount of data and view real-time curves with a minimum acquisition interval of 1 s. The acquisition interval was set as 1 s for the uniaxial compression test and 30 s for the creep test in order to prevent too much data.

2.3. Test Protocols. Since the rocks at the entrance of the river tunnel were close to the air-dry state, and the rocks at the bottom of the river were in the water-saturated state, and 12 specimens were selected and divided into 4 groups, including 2 groups of specimens in the dry state and 2 groups of specimens in the water-saturated state, for uniaxial compression tests and uniaxial compression creep tests, in order to obtain reasonable parameters as far as possible. The compressive strength of the specimens was tested by a uniaxial compression test, and the stress-strain curves were obtained (Figure 1). The basic physical and mechanical parameters of the specimens in dry and water-filled states are shown in Table 1. Due to the physical and chemical softening effect of water on muddy red sandstone, the strength of muddy red sandstone in the water-saturated state was only about half of that in the dry state. The uniaxial compression test yielded a peak stress of 51.4 MPa for muddy red sandstone in the dry state and 23.9 MPa in the water-saturated state. The first stage was taken as 40% of the peak

Table 1: Physical and mechanical parameters of argillaceous red sandstone samples.

Water content status	Density (g/cm3)	Compression strength (MPa)	Elastic modulus (GPa)	Poisson's ratio	Wave velocity	Porosity	Softening factor
Drying	2.49	51.4	6.03	0.33	2633	9.01%	—
Saturated	2.55	23.9	2.29	0.40	2532	—	0.46

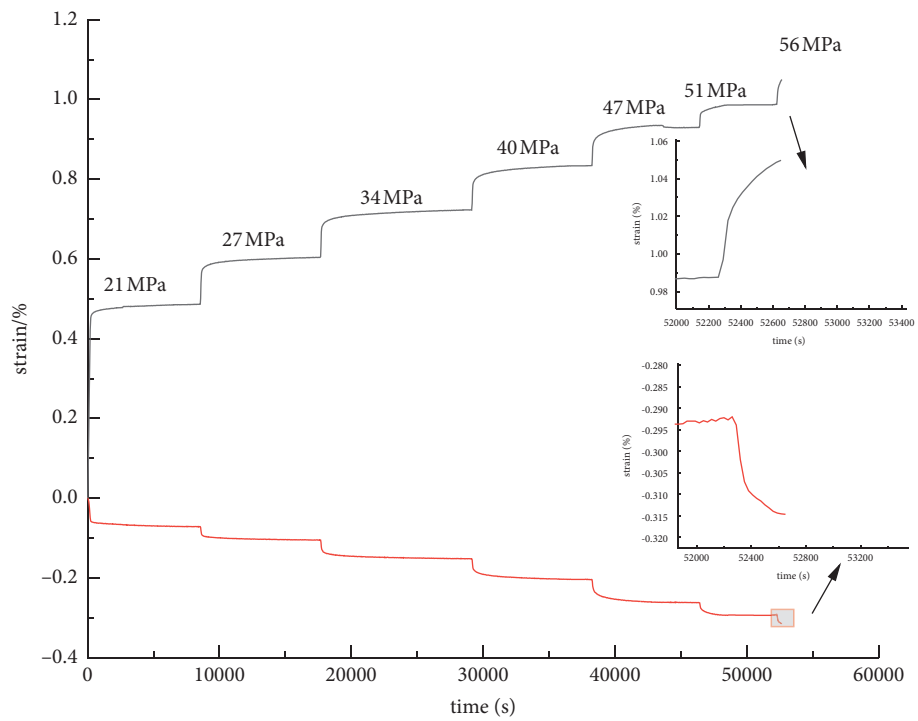

Figure 2: Creep curves of specimens in a dry state.

stress, and each stage was increased by 10% until the specimen was damaged. The creep duration was 2.5 hours.

3. Analysis of Test Results

The full ephemeral creep curves of muddy red sandstone in dry and water-filled states were obtained by graded loading creep tests, as shown in Figures 2 and 3.

As can be seen from Figure 2, the creep characteristics of the specimen and the loaded stress were closely related. Taking the specimen in the dry state as an example, when the axial differential stress increased from 21 MPa to 51 MPa, the axial strain increased by 0.5%, and the lateral strain increased by 0.222%. Meanwhile, the stress of the first stage loading is 40% of the peak stress; that is, the axial compression strain has reached 49% of the strain at destruction after the stress gradient increases from 0 MPa to 21 MPa. This indicates that most of the microfractures in the rock have closed during the first stage stress increase, which results in a sharp increase in strain, while the increase in lateral strain is not as pronounced.

As shown in Figure 3, the axial stress of the water-filled specimen was applied from 0 MPa to 12 MPa and stabilized at 12 MPa when the axial strain was stabilized at 0.487%, about 69% of the damage strain, and the lateral strain was stabilized at 0.214%, about 77% of the strain at the damage, and the damage started at the third level of stress.

Compared with the specimens in the dry state, the stresses generated by the first stage of loading and the deformation at the time of damage were accounted for a larger proportion of the deformation of the specimens in the water-saturated state. Both two specimens produced a deformation of about 0.49% under the first stage of stress, but the stresses on the water-saturated specimens were only half of those in the dry state. This is because the fissures in the specimen become larger and gradually penetrate after filling with water, increasing the damage to the specimen, so the rock is more likely to be deformed when squeezed by external forces [21, 22].

The long-term strength of rocks is a stress limit to distinguish stable creep and unstable creep of rocks [23], beyond which the creep of rocks proceeds toward unstable creep. It can be seen from Figures 4 and 5 that under the action of low stress, the steady-state rate of rock sample increases slowly with the increase of stress. When the stress value exceeds the long-term strength, the creep rate increases rapidly. Steady-state creep rate increases exponentially with increasing stress In this paper, the long-term strength of the rock is derived from the steady-state rate (Figures 4 and 5), and it can be seen from the figure that the

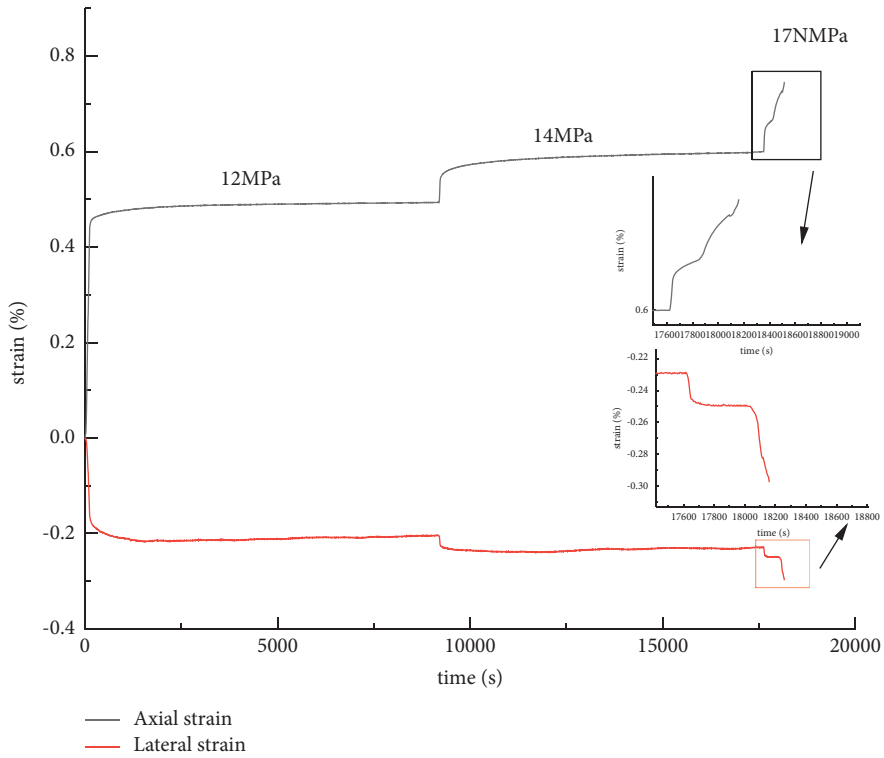

Figure 3: Creep curves of specimens in a saturated state.

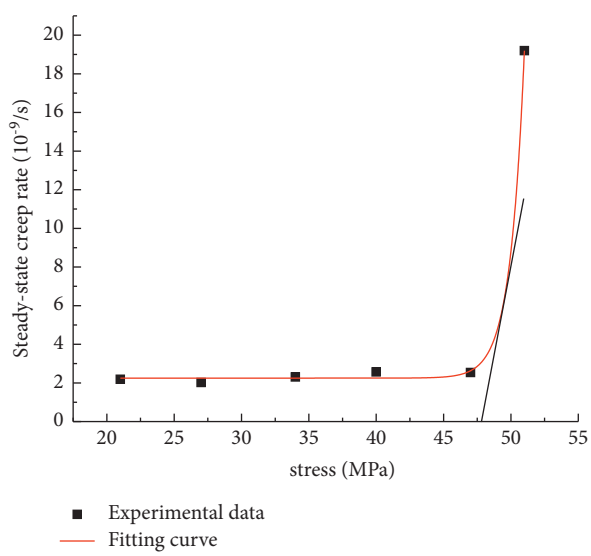

Figure 4: Creep rate-stress curve of specimens in a dry state.

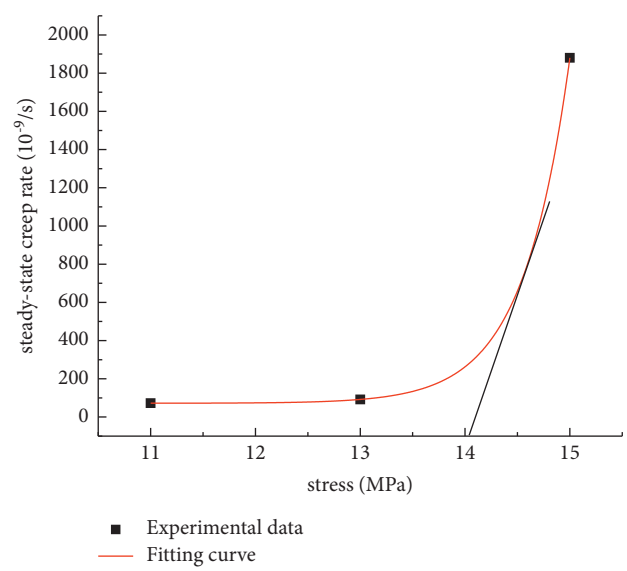

Figure 5: Creep rate-stress curve of specimens in a saturated state.

uniaxial long-term strength of the muddy red sandstone in the dry state is about 46.4 MPa, and the long-term strength in the saturated state is about 14.1 MPa. It can be seen that water has a great influence on the strength of the muddy red sandstone, and the long-term strength in the saturated state is only about 30% of that in the dry state.

4. Creep Model and Parameter Identification

4.1. The Burgers Model. From the creep experimental curves, it can be seen that the muddy red sandstone exhibits obvious viscoelasticity and transient elasticity under all levels of stress. Burgers model, which consists of Maxwell body and

Kelvin body in series, can describe these properties well, as shown in Figure 6.

For Maxwell bodies, the instanton equation is $\sigma + \beta/E\dot{\sigma} = \beta\dot{\varepsilon}$, and the creep equation is $\varepsilon(t) = \sigma_0/E + \sigma_0/\beta t$. For Kelvin bodies, the instanton equation is $\sigma = E\varepsilon + \beta\dot{\varepsilon}$, and the creep equation is $\varepsilon(t) = \sigma_0/E[1 - e^{(-E/\beta)t}]$.

By connecting K and M bodies in series, the creep equation of the burgers model can be obtained after a series of computational transformations of the equation [24].

$$\varepsilon(t) = \frac{\sigma_0}{E_1} + \frac{\sigma_0}{\beta_1}t + \frac{\sigma_0}{E_2}\left(1 - e^{\left(-E_2 t/\beta_2\right)}\right), \quad (1)$$

where E_1 and E_2 are elastic coefficients; β_1 and β_2 are Newtonian viscosity coefficients; and σ_0 is the stress at all levels of graded loading.

From (1), it can be seen that at the instant of σ_0 when the stress arrives, this is when $t = 0$, $\varepsilon(0) = \sigma_0/E_1$, only the Hooke body E_1 plays a role.

4.2. Parameter Identification. Boltzmann superposition principle was used to shift the coordinate of the creep test curve. With the help of Origin's custom function, the burgers model was added into Origin's function library, the creep curve under all levels of stress was fitted nonlinearly, and the parameters were identified by the Levenberg-Marquardt optimization algorithm. The resulting curves are shown in Figures 7 and 8, and each creep parameter is shown in Table 2.

From the fitting results of creep parameters in Table 2, it can be seen that the viscosity coefficients β_1, β_2 of the specimens in the dry state increase with the increase of stress level, indicating that the viscosity is increasing, while the viscosity coefficient in the saturated state decreases with the increase of stress instead. This is because the action of water reduces the cohesion between the rock particles, and the particles are easily separated as the stress increases.

The correlation coefficients of the creep curves fitted by the burgers model for all levels of stress are above 0.91, and the results show that the burgers creep model can well describe the creep properties of muddy red sandstone. The parameters obtained from the fitting can be used for numerical simulation at the same time, which has some application value for analyzing and studying the long-term stability of the project.

5. Macro- and Microanalysis of Failure Specimen

5.1. Macroanalysis. At the end of each test, the failure specimen fragments were collected and pieced back to the original shape as far as possible, and the fragments were fixed with adhesive tape. Figure 9 shows the specimens after uniaxial failure in the dry state and the water-filled state.

Regardless of the dry or waterlogged state of the failure specimen, there is a conical fragment at the top. The axial main fracture arises in the middle of the rock but does not extend to the ends of the sample. The fracture splits into two fractures from the middle and propagates to both sides, forming a "herringbone" shear fracture surface. This failure mode is X-shaped conjugate oblique shear failure, and the shear stress at the failure surface exceeds the strength limit. At the same time, the maximum shear stress sustained by the failure surface before the failure is also related to the positive stress, and it was known as a compression-shear failure. The

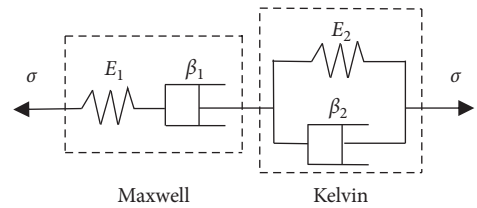

Figure 6: Burgers model.

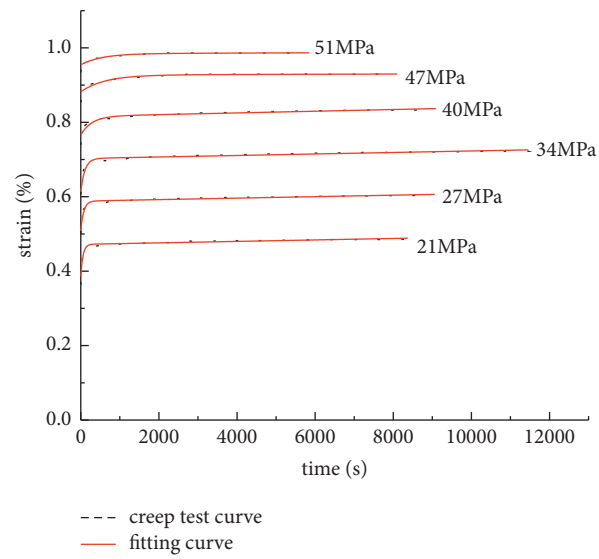

Figure 7: Creep curves of various stresses in a dry state.

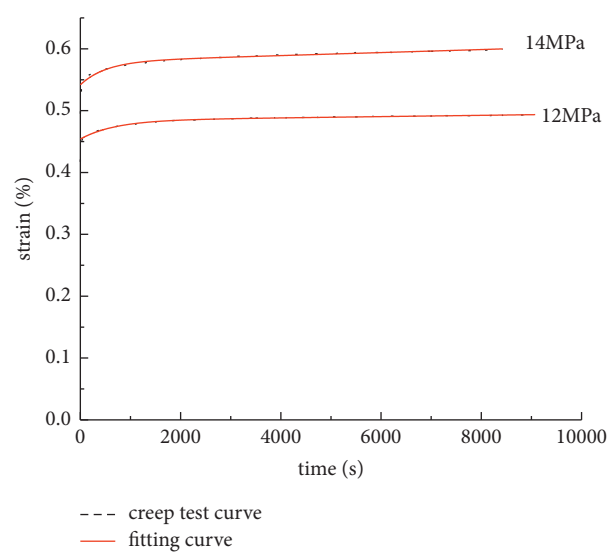

Figure 8: Creep curves of various stresses in a saturated state.

Table 2: Nonlinear fitting creep parameters of argillaceous red sandstone.

Water content status	Stress/MPa	E_1/GPa	E_2/GPa	$\beta_1/GPa \cdot s$	$\beta_2/GPa \cdot s$	R^2
Drying	21	5.44	24.38	1.07×10^6	1401.96	0.935
	27	5.31	33.83	1.36×10^6	2555.14	0.939
	34	5.54	38.40	1.68×10^6	4089.46	0.944
	40	5.22	80.41	1.75×10^6	22650.70	0.939
	47	5.33	103.73	1.50×10^7	64030.86	0.940
	51	5.34	177.32	1.26×10^7	104305.88	0.918
Saturated	12	2.64	39.77	1.17×10^7	27427.59	0.975
	14	2.58	37.37	5.74×10^5	19164.10	0.960

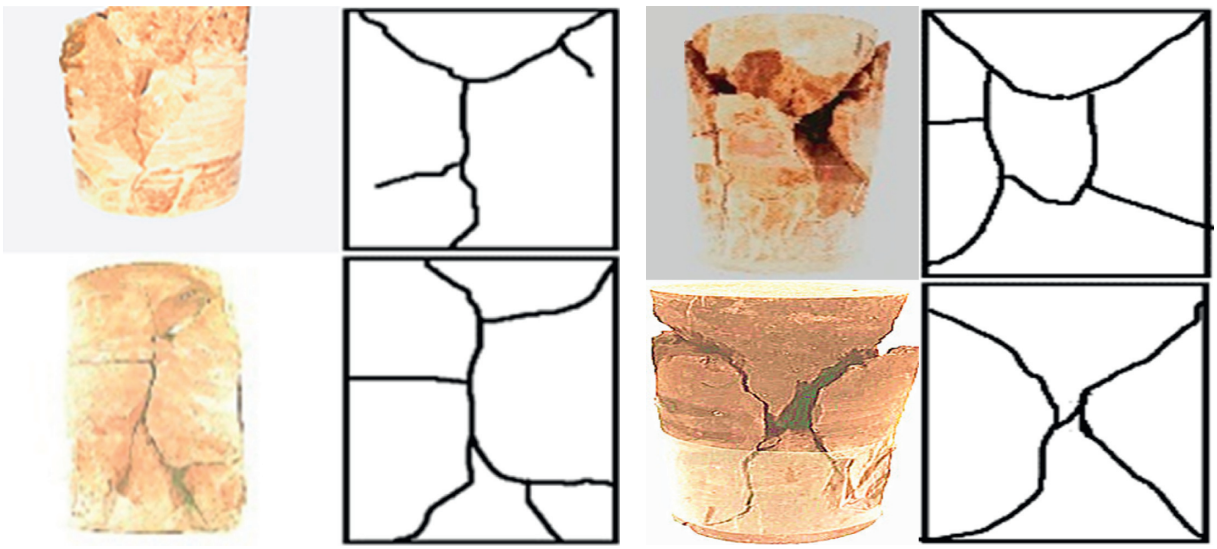

(a) (b)

Figure 9: Creep failure specimens. (a) Creep failure specimens in dry states. (b) Creep failure specimens in saturated states.

fragments after the destruction of the specimen in the dry state are larger in size and smaller in number. When the specimen is destroyed, only a small amount of powder is generated, while a large crush sound is heard. However, when a saturated specimen was broken, there was no loud sound, and a large amount of debris and powder was produced. This is because the specimen is saturated with water, which dissolves the clay minerals in the rock. As a result, the cementing material is destroyed, and the cementing ability between the internal particles is reduced. And the particles fall off and are failed by external extrusion. At this time, the small particles act as "ball" between the fragments (Figure 10), reducing the friction between the fracture surface and resulting in faster destruction and lager deformation of the specimen.

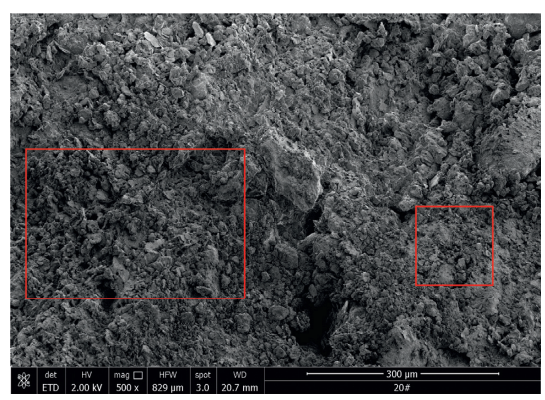

Figure 10: SEM of fracture in a saturated state.

5.2. Detailed View Analysis. There are many rock microscopic analysis methods, most is to scan the rock samples, such as X-ray CT image technology [25, 26], which could be a very good description of the structure characteristics of rock. This paper used MLA650 F type of field emission scanning electron microscopy to scan the sample and got the argillaceous sandstone under different conditions of electron microscopy. Thus, a comparative analysis could be carried out.

Four sectional specimens were selected from two different states and different types of test failure specimens. Specimens are carefully cut, and the back of the fracture is polished to make a thickness of about 0.5 cm. Gold was sprayed and placed on the sample stage for electron microscopy scanning. The fine morphology of the specimens with different water content is shown in Figures 11 and 12.

From Figure 12, it can be seen that the number of pores of the specimens after full water are obviously more than the

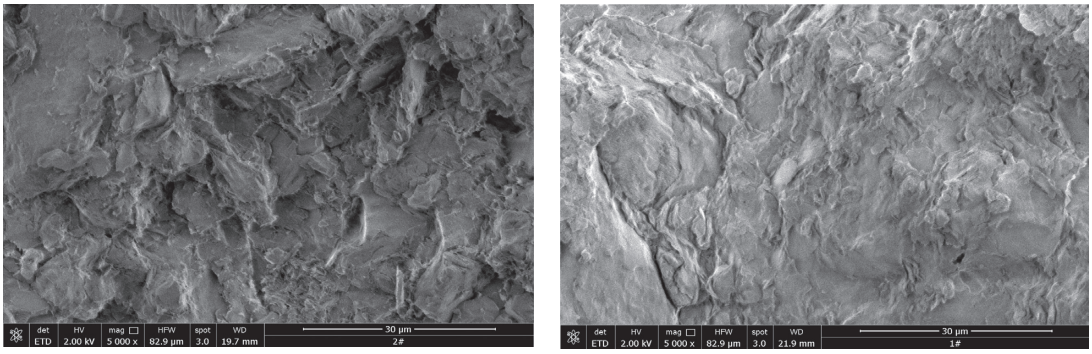

(a) (b)

Figure 11: SEM of fracture in a dry state. (a) Electron micrograph of Sample 1. (b) Electron micrograph of Sample 2.

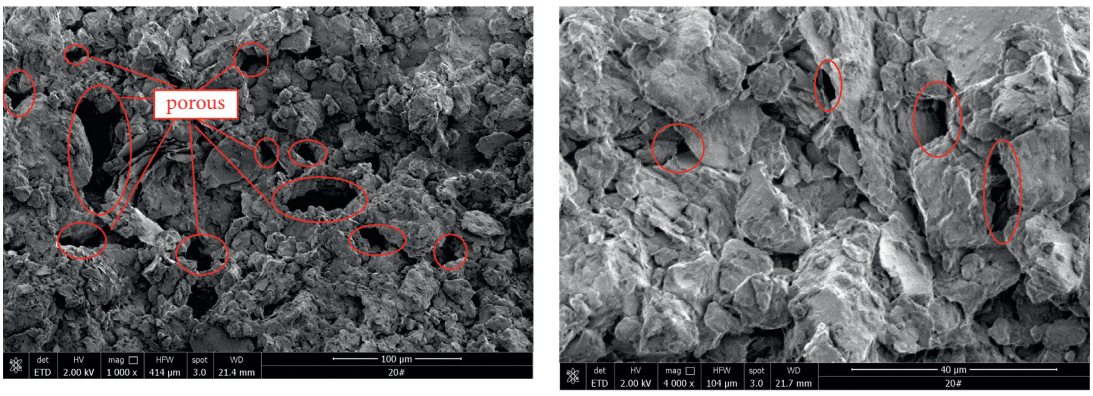

(a) (b)

Figure 12: SEM of fracture in a saturated state. (a) Electron micrograph of Sample 3. (b) Electron micrograph of Sample 4.

dry state, because of the water pressure, and water enters the fissures so that the fissures are expanding, and the fissures are gradually penetrating each other.

Comparing Figures 11 and 12, it can be seen that the cementation between the particles in the water-saturated state is more loose, and the crystal particles are larger because the clay minerals in the rock are dissolved in water, which weakens the cementation ability between the crystals. At the same time, this makes the particles in the rock swell, so that the strength of the rock sample in the water-saturated state is reduced, and the deformation will be larger than that of the specimen in the dry state under the same stress.

6. Conclusion

(1) The creep deformation of the rock samples under the first level of axial pressure in the dry and water-saturated states is larger than the deformation produced by the increase in stress at any of the later levels, which can reach more than 49% of the ultimate creep at both states. The long-term strengths of muddy red sandstone in the dry and saturated states were calculated to be 46.4 MPa and 14.1 MPa, respectively.

(2) The rheological mechanical parameters of the burgers model were determined by nonlinear fitting of creep curves using the burgers model, indicating that the burgers model is applicable to muddy red sandstone.

(3) The action of water causes rock particles to fall off and acts as a "ball" on the fracture surface, which reduces the friction of the fracture surface and weakens the rock strength. At the same time, the water-filled muddy red sandstone has larger internal pores and lower cementation capacity due to the action of water, which makes it easier for the rock to deform.

Data Availability

The data presented in this study are available on request from the corresponding author.

Conflicts of Interest

The authors declare no conflicts of interest.

Authors' Contributions

S.G. contributed to formulation, writing, and analysis of the paper; S.W. contributed to conceptualization and project

administration; H.F. reviewed and edited the manuscript; H.G. contributed to supervision. All authors have read and agreed to the published version of the manuscript.

Acknowledgments

This research was funded by the National Natural Science Foundation Project (no. 51978668) (in China).

References

[1] Y. Yu, G. L. Feng, C. J. Xu, B. R. Chen, D. X. Geng, and B. T. Zhu, "Quantitative threshold of energy fractal dimension for immediate rock-burst warning in deep tunnel: a case study," *Lithosphere*, vol. 2021, Article ID 1699273, 2022.

[2] H.-S. Deng, H.-L. Fu, Y. Shi, Y.-Y. Zhao, and W.-Z. Hou, "Countermeasures against large deformation of deep-buried soft rock tunnels in areas with high geostress: a case study," *Tunnelling and Underground Space Technology*, vol. 119, Article ID 104238, 2022.

[3] P. A. L. P. Firme, D. Roehl, and C. Romanel, "An assessment of the creep behaviour of Brazilian salt rocks using the multi-mechanism deformation model," *Acta Geotechnica*, vol. 11, no. 6, pp. 1445–1463, 2016.

[4] P. A. L. P. Firme, N. B. Brandao, D. Roehl, and C. Romanel, "Enhanced double-mechanism creep laws for salt rocks," *Acta Geotechnica*, vol. 13, no. 6, pp. 1329–1340, 2018.

[5] Z. Liu, C. Zhou, B. Li, L. Zhang, and Y. Liang, "Effects of grain dissolution-diffusion sliding and hydro-mechanical interaction on the creep deformation of soft rocks," *Acta Geotechnica*, vol. 15, no. 5, pp. 1219–1229, 2020.

[6] C. Xia, Z. Liu, and C. Zhou, "Burger's bonded model for distinct element simulation of the multi-factor full creep process of soft rock," *Journal of Marine Science and Engineering*, vol. 9, no. 9, p. 945, 2021.

[7] A. Lu, X. Chang, S. Hu, X. Yu, and L. Ming, "Impact of moisture content on the brittle-ductile transition and microstructure of sandstone under dynamic loading conditions," *Advances in Civil Engineering*, vol. 2021, Article ID 6690171, 2021.

[8] S. Okubo, K. Fukui, and K. Hashiba, "Development of a transparent triaxial cell and observation of rock deformation in compression and creep tests," *International Journal of Rock Mechanics and Mining Sciences*, vol. 45, no. 3, pp. 351–361, 2008.

[9] J. Q. Guo, X. L. Liu, and C. S. Qiao, "Experimental study of mechanical properties and energy mechanism of karst limestone under natural and saturated states," *Chinese Journal of Rock Mechanics and Engineering*, vol. 33, no. 2, pp. 296–308, 2014.

[10] S. Huang, Y. He, G. Liu, Z. Lu, and Z. Xin, "Effect of water content on the mechanical properties and deformation characteristics of the clay-bearing red sandstone," *Bulletin of Engineering Geology and the Environment*, vol. 80, no. 2, pp. 1767–1790, 2021.

[11] P. Baud, W. Zhu, and T.-F. Wong, "Failure mode and weakening effect of water on sandstone," *Journal of Geophysical Research: Solid Earth*, vol. 105, no. B7, pp. 16371–16389, 2000.

[12] F. Wu, H. Zhang, Q. Zou, C. Li, J. Chen, and R. Gao, "Viscoelastic-plastic damage creep model for salt rock based on fractional derivative theory," *Mechanics of Materials*, vol. 150, Article ID 103600, 2020.

[13] D. Zhang, R. Pathegama Gamage, M. Perera, C. Zhang, and W. Wanniarachchi, "Influence of water saturation on the mechanical behaviour of low-permeability reservoir rocks," *Energies*, vol. 10, no. 2, p. 236, 2017.

[14] Q. Yao, T. Chen, M. Ju, S. Liang, Y. Liu, and X. Li, "Effects of water intrusion on mechanical properties of and crack propagation in coal," *Rock Mechanics and Rock Engineering*, vol. 49, no. 12, pp. 4699–4709, 2016.

[15] Y. Wang, L. Cong, X. Yin, X. Yang, B. Zhang, and W. Xiong, "Creep behaviour of saturated purple mudstone under triaxial compression," *Engineering Geology*, vol. 288, Article ID 106159, 2021.

[16] C. Ping, L. Wan, and Y. Wang, "Viscoelasto-plastic properties of deep hard rocks under water environment," *Transactions of Nonferrous Metals Society of China*, vol. 21, no. 12, pp. 2711–2718, 2011.

[17] C. Yu, S. Tang, C. A. Tang et al., "The effect of water on the creep behavior of red sandstone," *Engineering Geology*, vol. 253, pp. 64–74, 2019.

[18] T. Miyazaki, K. Sueyoshi, and T. Hiraga, "Olivine crystals align during diffusion creep of Earth's upper mantle," *Nature*, vol. 502, no. 7471, pp. 321–326, 2013.

[19] S. Nadimi, K. Shahriar, M. Sharifzadeh, and P. Moarefvand, "Triaxial creep tests and back analysis of time-dependent behavior of Siah Bisheh cavern by 3-Dimensional Distinct Element Method," *Tunnelling and Underground Space Technology*, vol. 26, no. 1, pp. 155–162, 2011.

[20] H. F. Deng, J. L. Li, and C. J. Deng, "Analysis of sampling in rock mechanics test and compressive strength prediction methods," *Rock and Soil Mechanics*, vol. 32, no. 11, pp. 3399–3403, 2011.

[21] H Liu, Z. Li, Y. Zhang, and D. Wang, "The weakening mechanisms of the rock mechanics of marlite bank slopes under water–rock interaction conditions," *Carbonates and Evaporites*, vol. 35, pp. 1–11, 2020.

[22] N. Zhang, "Interaction between water and soft rocks," *Soft Rock Mechanics and Engineering*, Springer, Cham, Switzerland, pp. 235–249, 2020.

[23] L. Q. Li, W. Y. Xu, W. Wang, and Y. Q. Guo, "Estimation of long-term strength for Xiangjiaba sandstone based on creep tests," *Engineering Mechanics*, vol. 27, no. 11, pp. 127–136, 2010.

[24] Y. Zhang, W. Y. Xu, J. F. Shao, H. B. Zhao, and W. Wang, "Experimental investigation of creep behavior of clastic rock in Xiangjiaba Hydropower Project," *Water Science and Engineering*, vol. 8, no. 1, pp. 55–62, 2015.

[25] W. Lin, X. Li, Z. Yang et al., "A new improved threshold segmentation method for scanning images of reservoir rocks considering pore fractal characteristics," *Fractals*, vol. 26, no. 02, Article ID 1840003, 2018.

[26] W. Lin, S. Xiong, Y. Liu, Y. He, S. Chu, and S. Liu, "Spontaneous imbibition in tight porous media with different wettability: pore-scale simulation," *Physics of Fluids*, vol. 33, no. 3, Article ID 032013, 2021.

Hindawi
Advances in Civil Engineering
Volume 2022, Article ID 5469345, 7 pages
https://doi.org/10.1155/2022/5469345

Research Article

Influence of Underground Tunnel Excavation on Upper-level Existing Pipelines

Xingfa Feng,[1] Xian Yang,[2] Yongsuo Li,[3] and Xingyu Ding[2]

[1]*CCTEG, Chongqing Eenineering (GROUP) Co., Ltd, Chongqing 40000, China*
[2]*College of Civil Engineering, Hunan City University, Yiyang, Huhan 4130003, China*
[3]*School of Municipal and Geomatics Engineering, Hunan City University, Yiyang, Huhan 4130003, China*

Correspondence should be addressed to Xian Yang; yangxjj@163.com

Received 10 December 2021; Accepted 19 January 2022; Published 28 February 2022

Academic Editor: Yu Liang

Winkler elastic foundation beam theory is often used to observe the influence of underground engineering construction on pipelines. Excavation under existing pipelines disturbs the lower strata to varying extent, which creates significant differences in the subgrade coefficients. Ignoring these differences can severely impact the accuracy of calculation results. A theoretical model of the effects of underground excavation on upper-level existing pipelines was developed in this study based on Winkler elastic foundation beam theory and considering the difference of subgrade coefficients under the existing pipeline. Methods for determining the subgrade coefficient under the influence of construction disturbance and other relevant parameters are proposed. The theoretical model can be used to calculate the settlement of an existing pipeline under the influence of underground excavation. The calculated settlement was compared with settlement measurements to find that the subgrade coefficient of the excavation section is the most important parameter in the calculation process. The suitable value range of the excavation subgrade coefficient is relatively large, as it has a relatively minor influence on the calculation result. When the value of subgrade coefficient of each section is appropriate, the calculated settlement curve is in close accordance with the measured settlement curve.

1. Introduction

The gradual development and utilization of urban underground spaces have produced a number of underground excavation projects affecting existing pipelines [1–3]. In the process of an underground engineering project, disturbance to the stratum inevitably deforms the adjacent underground pipeline. When the deformation exceeds the allowable deformation of the existing pipeline and its joints, destruction of the existing pipeline may result in even serious secondary disasters. It is difficult to directly monitor the deformation of existing pipelines due to the distribution of points above ground throughout a ground excavation project. The points instead can only be monitored indirectly [4], which does not readily allow for effective accident prediction or prevention. There is an urgent demand for a straightforward and easily applied method to evaluate the safety of existing pipelines and classify construction risks. Such evaluations would facilitate the proper selection of preconstruction reinforcement or relocation treatment for existing pipelines to minimize the failure risk of existing pipelines, save costs, and shorten the construction period.

Previous studies regarding the impact of tunnel construction on existing pipelines have mainly centered on numerical simulations and theoretical analyses. Theoretical analysis methods are mainly based on the Winkler elastic foundation beam theory [5, 6], two-parameter Pasternak elastic foundation beam theory [7, 8], or energy method [9] to solve parameters such as the deformation, bending moment, and shear force of an existing pipeline as affected by tunnel construction and to select corresponding standards to judge its safety. Unlike the two-parameter elastic foundation beam theory, the Winkler elastic foundation beam theory does not reflect the continuity of foundation deformation. However, a method based on the Winkler elastic foundation beam is simpler, includes more

accumulated experiences in parameter values, and is most widely used in engineering. The two-parameter elastic foundation beam is more comprehensive in theory but includes less experience in the parameter value selection process; whether the parameter value is appropriate is directly related to the accuracy of calculation results. The Winkler elastic foundation beam theory was utilized in the present study to develop a calculation model of the influence of excavation on the upper-level pipeline.

The stratum under an existing upper-level pipeline is disturbed as an excavation project passes under it. The disturbance is most intense above the excavation section though there is also disturbance in a certain area near the excavation area. The mechanical properties of the soils in these two areas change significantly at this point compared with the original stratum, so there is also a substantial difference in the subgrade coefficient. Previous theoretical calculations have rarely considered the differences in subgrade coefficient in various areas under the existing pipeline, though ignoring such differences drives down the accuracy of calculation results and subsequent pipeline safety assessments.

Based on Winkler elastic foundation beam theory and considering the different subgrade coefficients in each area under the existing pipeline, a theoretical calculation model of the influence of concealed excavation construction on upper existing pipelines was established in this study. Important parameters in the model were acquired, and the influence of different subgrade coefficient values on the predicted deformation of the existing pipeline was observed. A case analysis was conducted to test the proposed method. This work may provide an important reference for the safety assessment of existing pipelines in similar projects.

2. Theoretical Calculation Model

Generally, underground pipelines are laid along a roadway. Most underground tunnels cross the road vertically and also intersect with the existing pipelines vertically. The impact of the underground excavation project intersecting with the existing pipeline vertically is under investigation here (Figure 1). Flexible pipes are allowed to rotate after loading, while rigid pipes are not allowed to rotate after loading. The pipe considered in this paper allows rotation angle, so it is suitable for the calculation of flexible pipe.

It is also assumed here that the excavation channel is rectangular and that the foundation is homogeneous. The existing pipeline is regarded as an elastic foundation beam on a Winkle foundation. It is assumed that the settlement of any point in the foundation is only proportional to the pressure on the unit area of the point, regardless of the pressure at other points. There is a relatively long longitudinal extension of the buried pipeline, which is assumed to be an infinite beam. During the underground excavation project, the stress area of the existing pipeline at the upper level is divided into five sections. As shown in Figure 2, the CD section is the excavation area, BC and DE sections are soil-loosening sections caused by excavation, and AB and EF sections are areas not affected by excavation. Construction disturbance creates different subgrade coefficients for each

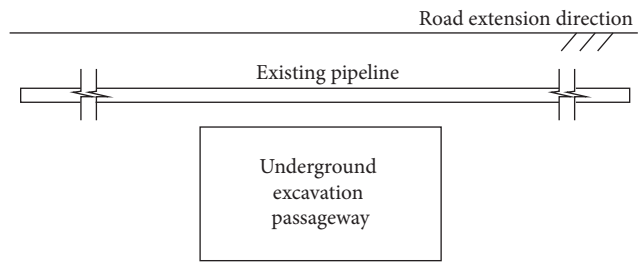

Figure 1: Locations of the underground excavation project and existing pipeline.

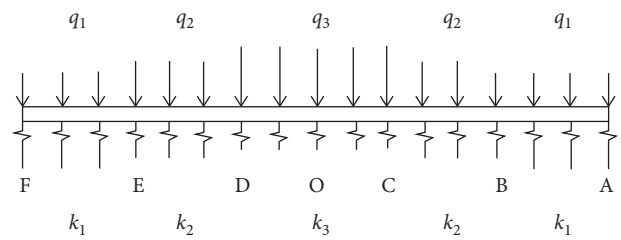

Figure 2: Stress diagram of the existing pipe under influence of excavation.

section. It is assumed that the subgrade coefficient of the AB and EF section is k_1, that of the BC and DE section is k_2, and that of the CD section is k_3.

The maximum load of the buried pipeline mainly originates in the gravity of the soil above it. The Terzaghi loose Earth pressure calculation model is generally used to determine the vertical Earth pressure on a buried pipeline [10]. In the Terzaghi model, the dislocation of soil particles produces stress transfer, which makes the surrounding soil restrict the downward moving soil so that the vertical Earth pressure borne by the underground structure is less than the gravity of the soil column. As shown in Figure 2, if other external loads on the upper part of the existing pipeline are not considered, the uniformly distributed load q_1 of sections AB and EF of the existing pipe jacking is not affected by excavation and can be calculated using the Terzaghi model. The soil above the excavation section and the excavation-affected section is impacted by construction disturbance. The mechanical properties of the soil and the holding capacity of the downward part are reduced, which increases the Earth pressure borne by the underground pipeline. It is assumed that the Earth pressure borne by the pipeline above the excavation section CD is q_3 and that of the excavation-affected sections BC and DE is q_2.

As shown in Figure 2, the deflection differential equation of each section can be obtained as follows:

$$\begin{aligned} AB&: EI\frac{d^4\omega_1}{dx^4} + k_1 b\omega_1 - q_1 = 0,\\ BC&: EI\frac{d^4\omega_2}{dx^4} + k_2 b\omega_2 - q_2 = 0,\\ CO&: EI\frac{d^4\omega_3}{dx^4} + k_3 b\omega_3 - q_3 = 0, \end{aligned} \tag{1}$$

where EI is the bending stiffness of the existing pipeline, N•m^2; ω_i is the deflection of each section of the existing pipeline, m, $i = 1, 2, 3$; x is the distance between each point in the right half of the existing pipeline and point O, m; k_i is the subgrade coefficient of each section under the existing pipeline, N/m^3, $i = 1, 2, 3$; q_i is the Earth pressure borne by each section of the existing pipeline, Pa, $i = 1, 2, 3$; and b is the calculated width of the foundation reaction, m.

The characteristic value of flexibility is determined by the calculated width of the foundation reaction.

$$\lambda_i = \sqrt[4]{\frac{k_i b}{4EI}}, \tag{2}$$

where $i = 1, 2, 3$.

The general solution for each section of the deflection differential equation and the first, second, and third derivative of each section can be obtained as follows:

$$\begin{cases} \omega_i = e^{\lambda_i x}\left(A_i \cos \lambda_i x + B_i \sin \lambda_i x\right) + e^{-\lambda_i x}\left(C_i \cos \lambda_i x + D_i \sin \lambda_i x\right) + \dfrac{q_i}{k_i}, \\ \omega_i' = \lambda_i e^{\lambda_i x}\left[\left(B_i - A_i\right)\sin \lambda_i x + \left(B_i + A_i\right)\cos \lambda_i x\right] + \lambda_i e^{-\lambda_i x}\left[\left(D_i - C_i\right)\cos \lambda_i x - \left(D_i + C_i\right)\sin \lambda_i x\right], \\ \omega_i'' = 2\lambda_i^2 e^{\lambda_i x}\left(B_i \cos \lambda_i x - A_i \sin \lambda_i x\right) + 2\lambda_i^2 e^{-\lambda_i x}\left(C_i \sin \lambda_i x - D_i \cos \lambda_i x\right), \\ \omega_i'' = 2\lambda_i^3 e^{\lambda_i x}\left[\left(B_i - A_i\right)\cos \lambda_i x - \left(B_i + A_i\right)\sin \lambda_i x\right] + 2\lambda_i^3 e^{-\lambda_i x}\left[\left(D_i - C_i\right)\sin \lambda_i x + \left(D_i + C_i\right)\cos \lambda_i x\right], \end{cases} \tag{3}$$

where A_i, B_i, C_i, D_i ($i = 1, 2, 3$) are undetermined coefficients.

If the deflection of the beam is known, the rotation angle, bending moment, and shear force of any section of the beam can be obtained according to the knowledge of Material Mechanics.

$$\begin{cases} \theta = \omega' \\ M = -EI\omega'' \\ Q = -EI\omega''' \end{cases}, \tag{4}$$

where θ denotes the corners of existing pipelines; M is the bending moment of the existing pipeline, N•m; and Q is the shear force of the existing pipeline, N.

In an actual construction project, the pipeline is quite long. Due to the constraints of the soil around the pipeline on the existing pipeline, the excavation under the pipeline has a limited range of influence. At the end far away from the excavation range (x, ∞), the boundary condition can be assumed to be fixed support. Therefore, the following boundary conditions and deformation coordination conditions hold.

Point A (x, ∞) is the fixed end:

$$\begin{cases} \omega_1 = 0, \\ \omega_1' = 0. \end{cases} \tag{5}$$

Point O is the symmetrical point:

$$\begin{cases} \omega_3' = 0, \\ \omega_3'' = 0. \end{cases} \tag{6}$$

According to the coordination among deflection, rotation angle, bending moment, and shear force at the left and right ends of points B and C, the following supplementary conditions hold.

Point B:

$$\begin{cases} \omega_1 = \omega_2, \\ \omega_1' = \omega_2', \\ \omega_1'' = \omega_2'', \\ \omega_1'' = \omega_2''. \end{cases} \tag{7}$$

Point C:

$$\begin{cases} \omega_2 = \omega_3, \\ \omega_2' = \omega_3', \\ \omega_2'' = \omega_3'', \\ \omega_2'' = \omega_3''. \end{cases} \tag{8}$$

A system of 12 equations and 12 unknowns can be established by substituting formulas (5)–(8) into formula (3). The analytical solutions of the undetermined coefficients A_i, B_i, C_i, and D_i were obtained here in MATLAB and then substituted into formulas (5)–(8) to obtain the deflection, rotation angle, bending moment, and shear force generated at each point in the existing pipeline AE during excavation of the BC section. The safety of the existing pipeline can be evaluated based on the results by selecting appropriate judgment standards.

3. Determination of Relevant Parameters in Theoretical Calculation

3.1. Calculation of Vertical Earth Pressure on the Existing Pipeline. In this study, the Terzaghi loose Earth pressure calculation model was selected to calculate the vertical Earth

pressure q_1 on the existing pipeline not affected by excavation. The soil above the excavation section and the excavation-affected section is impacted by the construction disturbance. The mechanical properties of the soil and holding capacity of the downward moving part are reduced, thus increasing the Earth pressure on the pipeline. Based on the simplified calculation and partial safety considerations, the holding capacity of the surrounding soil to the downward moving part can be ignored. The Earth column theory can be directly used to calculate the Earth pressure q_2 and q_3 on the existing pipe jacking above the excavation section and the excavation-affected section.

3.2. Determination of the Excavation-Affected Section Length. The angle between the fracture surface and the tunnel excavation surface can be assumed as $(45^\circ - \varphi/2)$ in the soil-loosening area caused by tunnel excavation [11] (Figure 3). The length of the loose section can be calculated as follows:

$$a = (H + h)\tan\left(\frac{\pi}{4} - \frac{\varphi}{2}\right), \tag{9}$$

where a is the length of the excavation-affected section, m; H is the distance between the top of the excavation area and the existing pipeline, m; h is the height of the excavation area, m; and φ is the internal friction angle of soil, $^\circ$.

3.3. Determination of Foundation Reaction Width. Assuming that the diameter of the existing pipeline is D, the calculated width of soil reaction b is as follows [12]:

When $B \leq 1$ m,

$$b = 0.9(1.5\mathrm{d} + 0.5). \tag{10}$$

When $b > 1$ m,

$$b = 0.9(\mathrm{d} + 1), \tag{11}$$

where d is the outer diameter of the existing pipeline, m.

3.4. Determination of the Subgrade Coefficient under Construction Disturbance. The subgrade coefficient is the most important parameter in this theoretical model. There have been few previous studies on the influence of construction disturbance on subgrade coefficients, but there are many research results regarding other soil mechanical properties under construction disturbance. Xu Yongfu [13] pointed out that the soil disturbance caused by shield tunneling decreases the deformation modulus by 30–70%, and that the cohesion and internal friction angle are related to the soil strain rate: when the soil strain rate increases from 0 to 6%, the cohesion is completely lost, and the internal friction angle decreases linearly to 50% of the original value. Liu Zhe [14] divided tunnel excavation disturbance into three areas according to volumetric strain rate (Figure 4): area A, where the volumetric strain exceeds 3%; area B, where the volumetric strain is 1–3%; and area C, where volumetric strain is less than 1%. The change range of deformation modulus in each region was found to be greater than that of cohesion and internal friction angle, while the overall change in

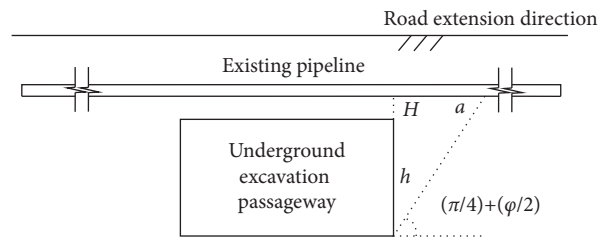

Figure 3: Loose soil area length calculation.

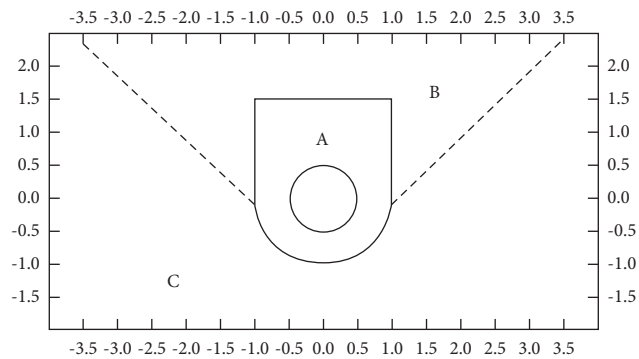

Figure 4: Area disturbed by tunnel excavation.

internal friction angle was minimal. At different points in area A, the deformation modulus decreased by 37–91.7%, the cohesion decreased by 31.4–63.7%, and the internal friction angle decreased by 3.6–12.3%. At different points in area B, the deformation modulus decreased by 8.1–24.1%, the cohesion decreased by 2.5–23.1%, and the internal friction angle decreased by 1.1–2.3%.

For specific projects, the subgrade coefficients of undisturbed soil and disturbed soil should be determined by an in-situ plate load test or indoor consolidation test. If no test data are available, the method proposed by Vesic [15] can be used to determine the subgrade coefficient (formula (8)), where it is not only related to the mechanical properties of the foundation soil itself but also to the action width and stiffness of the beam [16, 17]. The subgrade coefficient can be also determined by the known deformation modulus and Poisson's ratio. According to the spatial relationship between the existing pipeline and the underground excavation space, and based on the existing literature, the underground excavation disturbance zoning can be defined as shown in Figure 4. The average deformation modulus and average internal friction angle of the soil in each area can then be estimated. The Poisson's ratio can be obtained by formulas (11)–(12) according to the average internal friction angle, and then, it can be substituted into formula (8) together with the estimated deformation modulus to calculate the subgrade coefficient under the influence of construction disturbance.

$$k = \frac{0.65E_s{}'}{1 - v'^2}\sqrt[12]{\frac{E_s{}'b^4}{\left(1 - v'^2\right)EI}}, \tag{12}$$

Table 1: Subgrade coefficient values.

Condition	Subgrade coefficient	k_1 (kN/m^3)	k_2 (kN/m^3)	k_3 (kN/m^3)
Subgrade coefficient value in excavation section	Calculated parameter 1	1.4×10^4	$0.3k_1$	$0.1k_1$
	Calculated parameter 2	1.4×10^4	$0.3k_1$	$0.05k_1$
	Calculated parameter 3	1.4×10^4	$0.3k_1$	$0.075k_1$
	Calculated parameter 4	1.4×10^4	$0.3k_1$	$0.125k_1$
	Calculated parameter 5	1.4×10^4	$0.3k_1$	$0.15k_1$
Subgrade coefficient value in excavation-affected section	Calculated parameter 1	1.4×10^4	$0.3k_1$	$0.1k_1$
	Calculated parameter 6	1.4×10^4	$0.6k_1$	$0.1k_1$
	Calculated parameter 7	1.4×10^4	$0.5k_1$	$0.1k_1$
	Calculated parameter 8	1.4×10^4	$0.4k_1$	$0.1k_1$
	Calculated parameter 9	1.4×10^4	$0.2k_1$	$0.1k_1$

where E_{si} is the deformation modulus of the soil in each section under the existing pipeline, Pa; v_i is the Poisson's ratio of the soil in each section under the existing pipeline.

According to the relevant theories of soil mechanics, Poisson's ratio can be calculated according to the lateral pressure coefficient k_{0i} of each section of soil.

$$v_i = \frac{k_{0i}}{1 + k_{0i}}. \tag{13}$$

The lateral pressure coefficient can be measured with a tri-axial shear meter or lateral pressure meter. When test data are lacking, it can also be determined empirically based on the internal friction angle of each section of soil φ_i.

$$k_{0i} = 1 - \sin\varphi_i. \tag{14}$$

4. Case Calculation and Analysis

The case analysis data used in this study were taken from the literature [18]. The Wuhan Zhuodaoquan interchange underground pedestrian passage project is located on the east side of the intersection of Luoyu Road, Zhuodaoquan South Road, and Zhuodaoquan North Road. Zhuodaoquan Park is on the south side of the passage, and Zhuodaoquan Middle School is on the north side. It crosses the Zhuodaoquan interchange and Luoyu Road, connecting the sidewalks on the north and south sides.

The buried depth of the underground pedestrian passage is 3 m, the width is 8 m, and the height is 3.55 m. The overburdened soil of the underpass is mainly silty clay with cohesion of 15 kPa, internal friction angle of 12°, gravity of 19.3 kN/m^3, and subgrade coefficient of 1.4×10^4 kN/m^3. (This subgrade coefficient was calculated by the method in Section 3.3 according to the deformation modulus given in the literature.) There is a DN100 cast iron pipe above the underpass with an outer diameter of 114 mm and a buried depth of 1.5 m. The existing pipeline settlement calculated by the proposed method was compared against the field-measured settlement under different subgrade coefficients (Table 1) in the excavation section and excavation-affected section (Figures 5-6).

As shown in the figures above, when the subgrade coefficient of the excavation section is 10% of the original subgrade coefficient and the subgrade coefficient of the excavation-affected section is 30% of the original subgrade coefficient, the calculated settlement curve is consistent with the measured settlement curve (calculated value 1 and measured value). The maximum settlement occurs at the midpoint of the concealed excavation section, and the calculated value is slightly greater than the measured value. The widths of both the left and right sides of the settlement curve calculated and measured are about 12 m. There is only a slight difference between the measured and calculated values of each measuring point. The calculated value slightly exceeds the measurement for the area with a large settlement (0–3 m from the midpoint of the excavation section) but still satisfies the engineering requirements for a safe prediction. With an increase in the distance from the center, the measured curve shows a continuous decreasing trend while the calculated curve shows a sudden change. The reason for this difference is the inherent deficiency of the Winkle elastic foundation beam theory, which does not reflect the continuity of foundation deformation.

The results of calculations show that the subgrade coefficient of the excavation section is the most critical parameter in the calculation, which directly affects the settlement calculation results of the maximum settlement and the area with maximum settlement (the interval 0-3m from the midpoint of the excavation section). In this case, when the subgrade coefficient of the excavation section is 25% less than the applicable value ($0.1k_1$), the calculated maximum settlement value increases by 35%. When the subgrade coefficient of the excavation section is 25% greater than the applicable value ($0.1k_1$), the calculated maximum settlement value increases by 20%. It can be seen that the value of this parameter has a great impact on the calculation results and is directly related to the accuracy of prediction and evaluation. Therefore, if possible, indoor and in-site tests shall be used to determine the subgrade coefficient of the excavation section.

The subgrade coefficient of the excavation-affected section appears to have negligible impact on the maximum settlement, little impact on the settlement calculation results of the maximum settlement area (0–3 m from the midpoint of the concealed excavation section), and a relatively large impact on the second-largest settlement area (3–9 m from the midpoint of the concealed excavation section). If the subgrade coefficient value in the excavation section is accurate and its value in the excavation-affected section (relative to $0.3k_1$) increases or decreases by 30%, the difference in the calculated maximum settlement and maximum settlement area values is relatively small, and all values are conservative. The difference among calculated values in

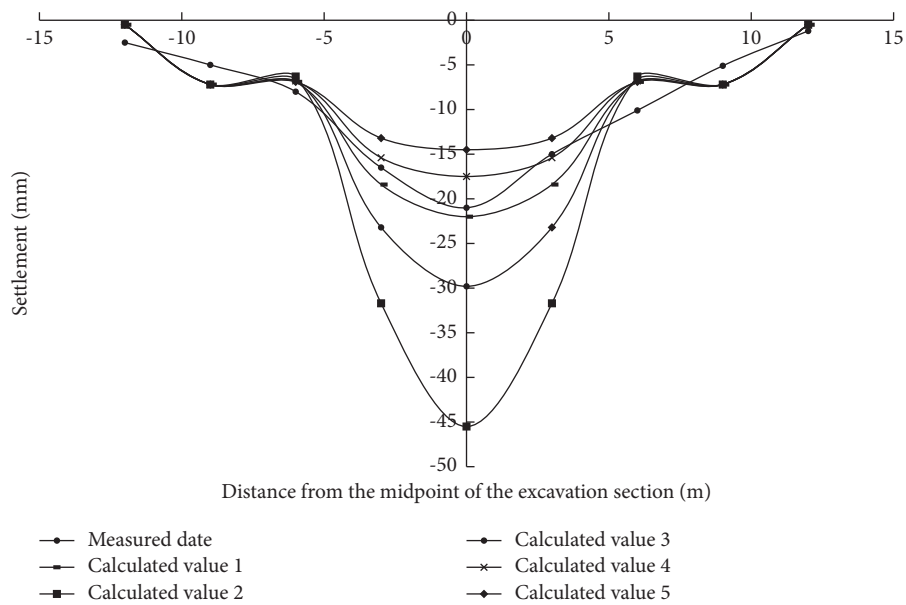

Figure 5: Comparison of measured and calculated settlement different subgrade coefficient values in excavation section.

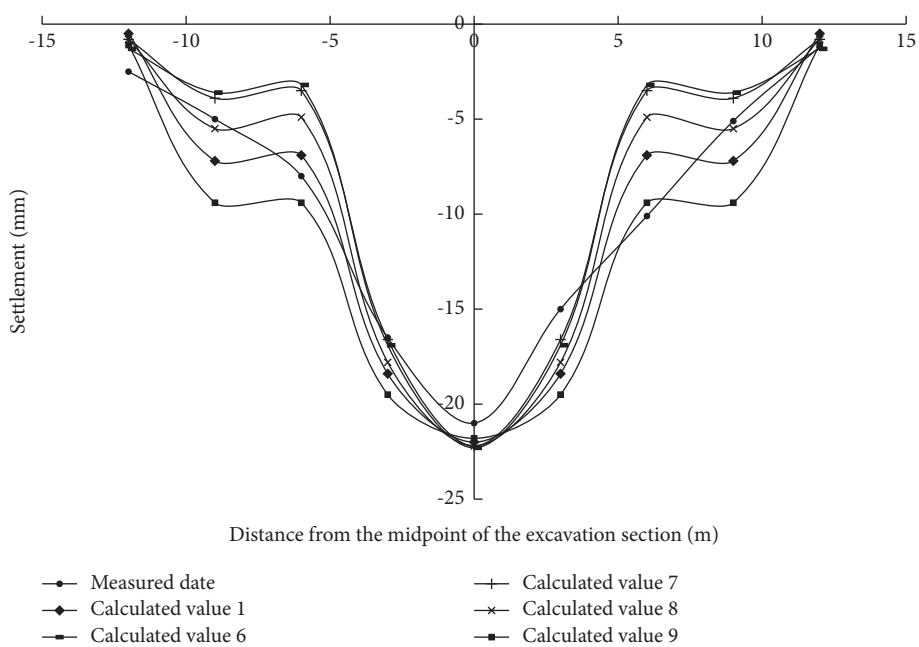

Figure 6: Comparison of measured and calculated settlement different subgrade coefficient values in excavation-affected section.

the second-largest settlement area is relatively large, but the absolute difference in calculated values is below 2.5 mm. Overall, the appropriate value range of this parameter is relatively large, and the deviation is within 30%, which indicates the relatively little impact on the pipeline settlement value calculation results.

5. Conclusion

Based on the Winkler elastic foundation beam theory and considering the difference of the subgrade coefficient in each area under the existing pipeline, a theoretical calculation model for the effects of underground excavation on an upper-level upper existing pipeline was established in this study. The deflection, rotation angle, bending moment, and shear force of each point of the existing pipeline can be calculated using this model, and then, the safety of the existing pipeline can be evaluated by selecting appropriate judgment criteria. Further, model parameters such as the vertical Earth pressure of each section on the existing pipeline, the length of the excavation-affected section, the calculated width of the foundation reaction, and the subgrade coefficient under the influence of construction disturbance were empirically determined. When there is no test

data for reference, the estimated deformation modulus and Poisson's ratio values can be determined based on the disturbance zoning. The subgrade coefficient under construction disturbance can be calculated according to the method proposed by Vesic.

The proposed method was used to calculate the settlement of an existing pipeline under the influence of excavation, and the results were compared against measured settlement values. When the subgrade coefficient is appropriate, the calculated settlement curve is in close agreement with the measured settlement curve. With an increase in the distance from the center, the measured curve shows a continuous decreasing trend while the calculated curve shows a sudden change. The reason for this difference is the inherent deficiency of the Winkle elastic foundation beam theory, which does not reflect the continuity of foundation deformation.

The foundation bed coefficient of the excavation section is the most important parameter in the calculation process. Its value significantly affects the final calculation results and is directly related to the accuracy of predictions and evaluations. If possible, both indoor and on-site tests should be conducted to determine the subgrade coefficient of the excavation section. The appropriate value range of the subgrade coefficient of the excavation-affected section is relatively large, and the value deviation is within 30%, which indicates a relatively slight impact on the pipeline settlement calculation results.

Data Availability

All data included in this study are available upon request to the corresponding author.

Conflicts of Interest

The authors declare that they have no conflicts of interest.

Acknowledgments

This study was supported by the Natural Science Foundation of Hunan Province (2021JJ30078).

References

[1] D. Zhang, "Case study on pipeline relocation of Lanzhou Zhongchuan International Airport comprehensive transportation hub project," *Water & Wastewater Engineering*, vol. 046, no. 002, pp. 85–89, 2020.

[2] Z. Zhang, M. Zhang, and Q. Zhao, "A simplified analysis for deformation behavior of buried pipelines considering disturbance effects of underground excavation in soft clays," *Arabian Journal of Geosciences*, vol. 8, no. 10, pp. 7771–7785, 2015.

[3] Y. Xia, N. Jiang, C. Zhou, and X. Luo, "Safety assessment of upper water pipeline under the blasting vibration induced by Subway tunnel excavation," *Engineering Failure Analysis*, vol. 104, no. 06, pp. 626–642, 2019.

[4] S. Hu and Y. Li, "Study of settlement control and monitoring plan for shallow excavation tunneling under-crossing existing pipeline," *Municipal Engineering Technology*, vol. 30, no. 05, pp. 81–85, 2012.

[5] P. B. Attewall, J. Yeates, and A. R. Selby, *Soil Movements Induced by Tunneling and Their Effects on Pipelines and structures*, Blackie and Son Ltd, London, 1986.

[6] B. Gao, "Theory analysis of rigid connection pipeline deformation affected by tunneling construction of metro tunnel," *Journal of Disaster Prevention and Mitigation Engineering*, vol. 37, no. 02, pp. 116–121, 2017.

[7] Y. Shang, *Study on the Influence Mechanism of Environment and Monitoring & Early-Warning of the shield*, Shanghai Jiao Tong University, Shanghai, 2018.

[8] W. Gang, B. Wang, and X. Xu, "Vertical displacement of underground pipeline caused by shield tunnel crossing in Pasternak foundation," *Science Technology and Engineering*, vol. 17, no. 33, pp. 158–165, 2017.

[9] W. Gang, C. C. Hong, and X. Xu, "Calculation of pipeline settlement induced by double-O-tube shield tunneling based on energy method," *Chinese Journal of Underground Space and Engineering*, vol. 115, no. 04, pp. 155–160, 2019.

[10] K. T. Terzaghi, *Theoretical Soil Mechanics*, INC, 1943.

[11] H. Wang, *Research on Mechanism of Pipe Roof Reinforcement and Tunnel Face Stability*, Dalian University of Technology, Dalian, 2009.

[12] Ministry of Construction of the People's Republic of China, *Code for Design of Building Foundation (GB50007-2011)*, China Architecture & Building Press, Beijing, 2011.

[13] Y. Xu and J. Sun, "The influence of shield tunneling on surrounding soil," *Tunnel and Rail Transit*, vol. 12, no. 2, pp. 9–13, 1999.

[14] Z. Liu, *Study on Disturbance of Subway Tunnel Construction and its Effect on the Bridge Pier and Line of the Adjacent High-Speed railway*, Beijing Jiaotong University, Beijing, 2018.

[15] A. B. Vesic, "Beams on Elastic Sub-grade and the Winkler's hypothesis," in *Proceedings of the 5th international conference of soil mechanics*, pp. 845–850, Paris, France, 1961.

[16] K. Terzaghi, "Evalution of conefficients of subgrade reaction," *Géotechnique*, vol. 5, no. 4, pp. 297–326, 1955.

[17] M. A. Biot, "Bending of an infinite beam on an elastic foundation," *Journal of Applied Physics*, vol. 12, no. 2, pp. 155–164, 1937.

[18] Y. Zhang, *Study on the Influence of Shallow Excavation on Municipal Underground pipeline*, Wuhan University of Technology, Wuhan, 2015.

Hindawi
Advances in Civil Engineering
Volume 2022, Article ID 3075834, 10 pages
https://doi.org/10.1155/2022/3075834

Research Article

Research on the Deformation Characteristics of Pressure Culvert Linings Based on Monitoring

Liang Jingwei,[1] Wang Xiang,[1] Cao Lei ,[2] and Jiang Chu[1]

[1]*Hunan Institute of Water Resources and Hydropower Research, Changsha 410007, China*
[2]*School of Water Resources and Hydropower, Hunan Polytechnic of Water Resources and Electric Power, Changsha 410131, China*

Correspondence should be addressed to Cao Lei; 815172232@qq.com

Received 24 December 2021; Accepted 15 January 2022; Published 18 February 2022

Academic Editor: Yu Liang

It is of great significance to study the deformation characteristics of the lining of a long-distance pressure culvert. The lining of a pressure culvert has the characteristics of strong concealment and remarkable influence on the whole performance. The existing research on deformation characteristics mostly adopts nondestructive detection, and the accuracy is restricted by many factors. In this paper, the lining of a pressure culvert is taken as the research object, and in situ tests of the structure are carried out and numerical simulations are conducted. Based on field monitoring data, the mechanical and deformation responses of the lining structure under external water and earth pressure are analyzed. On this basis, the finite element method is used to establish a three-dimensional finite element model, which further analyzes the deformation and mechanical characteristics of the lining structure under different conditions of internal water pressure, geological conditions, and internal water pressure alongside geological conditions. Therefore, theoretical guidance and technical support for the lining structure design of long-distance pressurized water delivery culverts are provided.

1. Introduction

With the rapid development of the urban economy, the problem of urban water use is becoming increasingly serious. To solve this problem effectively, the transregional water transfer project is a flexible and reliable solution, and the pressure culvert is a common hydraulic structure in water diversion projects [1–3]. The safety performance of water delivery culverts depends on the quality of the lining to a great extent [4–6]. Therefore, it is necessary to evaluate the lining quality of long-distance pressure culverts.

In engineering practice, there are many methods to evaluate the lining quality of long-distance pressure culverts. One such treatment method is nondestructive testing which is an effective and widely used method to ensure the safety of tunnel, such as the ground penetrating radar (GPR) [7–9], the multichannel analysis of surface waves (MASW) [10, 11], the infrared thermography (IRT) [12–15], and the Rayleigh waves [16]. However, the results of nondestructive testing were different from the reality results in some special stratum conditions, and this illustrated that the method of nondestructive testing also presents some limitations. Although some engineers have found that some advanced equipment can help mitigate these problems, the higher cost of equipment and complex operation process make it difficult to popularize and apply. It is therefore of great engineering interest and necessity to find a new method which not only has superior performance to ensure the accuracy of the test results but also is less expensive and easy to operate.

This paper takes the lining of a pressure water conveyance culvert as the research object. As a typical case, a pressure culvert of a water supply project is selected to carry out structural in situ tests and numerical simulations. Based on the field monitoring data, the mechanical and deformation responses of the lining structure under external water and earth pressure are analyzed. On this basis, the finite element method is used to establish a three-dimensional finite element model, by which further analysis of the

deformation and mechanical characteristics of the lining structure under the conditions of different internal water pressure and geological conditions plus internal water pressure is carried out.

2. General Situation of a Water Supply Project

The diameter of the pressure culvert of a main trunk line for a water supply project is 5.1 m, the landform is the undulating platform and hill, the topography is high and low, the peak and valley are distributed alternately perpendicular to the line, there are two shallow river valleys and two gullies on the water delivery line, the buried depth ranges from 7 m to 18 m, and the geological conditions of the overburden are mainly clay, mucky clay, and sandy gravel clay. To avoid the alternation of a double pipe and a single hole, a pipe with a 5.1 m inner diameter should be chosen, and the internal water pressure of these four pipes is 0.5 to 0.55 MPa. At present, the maximum internal diameter of PCCP pipe used in China is 4.0 m, which is the culvert pipe project of South-North Water Transfer Project. There is no engineering example in our country for PCCP pipe with 5.1 m inner diameter, and the equipment used to transport such large size whole precast culvert pipe depends on importing it, with the whole technology lacking and the uncertainty being too high. Therefore, the use of cast-in-place prestressed culverts in a project site with the corresponding implementation of all aspects and conditions is a practical method.

The maximum difficulty coefficient of cast-in-place prestressed culverts is 280.5, and the maximum depth of soil cover is 18 m. The total length of the prestressed culvert is 2265 m, the inner diameter is 5.1 m, and the round arch vertical wall is adopted outside. Top and sidewall thickness is 0.45 m, the bottom thickness is 0.8 m, and a high-strength nonbonding low-relaxation steel strand to provide culvert prestressed is used. The practical application of 5.1 m large-scale cast-in-place concrete prestressed culverts is rare in China and is one of the major technical problems in the entire water supply project.

3. Deformation Response of the Lining Structure under Stress Based on Monitoring

To understand the deformation characteristics of the anchor steel strand, an anchor cable dynamometer, a fully distributed optical fiber, and a magnetic flux sensor were installed at different section positions of the culvert, and real-time monitoring of the tension effect on the prestressed steel strand was performed under three working conditions: pressure water (culvert water pressure gradually increased to 0.602 MPa), filling soil, and pressure water after soil filling (culvert water pressure gradually increased to 0.56 MPa).

3.1. Tension Effect of Prestressed Steel Strand under Water Pressure

3.1.1. Monitoring Situation of Anchor Cable Dynamometer. In the process of the water pressure test, the whole curve of 3 pairs (6 pieces) of anchor cable dynamometer with different sections of culvert pipe (sections 1 and 2) is shown in Figure 1. The test result of the anchor cable dynamometer shows that the water pressure of the culvert pipe increases gradually to 60.2 m head, and there is no obvious change in the prestress value of the anchorage end of the steel strand.

3.1.2. Monitoring of Fiber Bragg Grating Intelligent Steel Strands. During the water pressure test, valid data were detected on the ZGD1 and ZGD2 fiber smart steel strands at sections 1and 2 (Figure 2). The variation of prestressed steel strand increases with the increase of water head; the variation of tension prestress of steel strand from the upper part to the top of culvert pipe is larger than that of other parts, and the maximum value of section 1 is approximately 3.54 kN, and that of section 2 is approximately 10.2 kN. Generally, the tension of prestressed steel strands changes slightly.

3.1.3. Magnetic Flux Sensor Test Results. One cycle of (16) magnetic flux sensors was arranged, and the variation law of the effective tensioning prestress along the circumference of the steel strand under different water pressures was monitored. As shown in Figure 3, with increasing internal water pressure, the effective tension on the steel strand changes slightly. The effective tension curves of the 16.3 m and 60.2 m heads are basically matching. Compared with the curve when 100% tension was just reached, the effective prestress value of the steel strand at the bottom of the culvert pipe decreased greatly, while the effective prestress value of the steel strand above the middle of the culvert pipe decreased relatively slightly after approximately 4 months. As shown in Figure 4, under the condition of a 60.2 m water head, the effective prestress value of the steel strand along the circumferential path of the culvert pipe is small, and the tension increases to a maximum gradually along the path to the middle and upper parts of the culvert pipe. Then, along the path to the top of the culvert pipe, the tension gradually decreases to the minimum, and the variation law of the effective tension prestress basically shows the M-shaped law of left and right axis symmetry. The maximum effective tension at the lower part of the culvert is 112.0 kN, and the minimum effective tension at the top of the culvert is 84.6 kN.

3.2. Tension Effect of Prestressed Steel Strands under Soil Filling Conditions

3.2.1. Test Results of Anchor Cable Dynamometer. During the filling test, there are 3 pairs (6 pieces) of anchor cable dynamometers, among which the no. 1 anchor cable dynamometer can monitor the corresponding data, and its entire curve is shown in Figure 5. The test results of the anchor cable dynamometer show that the tensile prestress value of the anchor end of the steel strand basically does not change during the filling process of the prestressed culvert pipe.

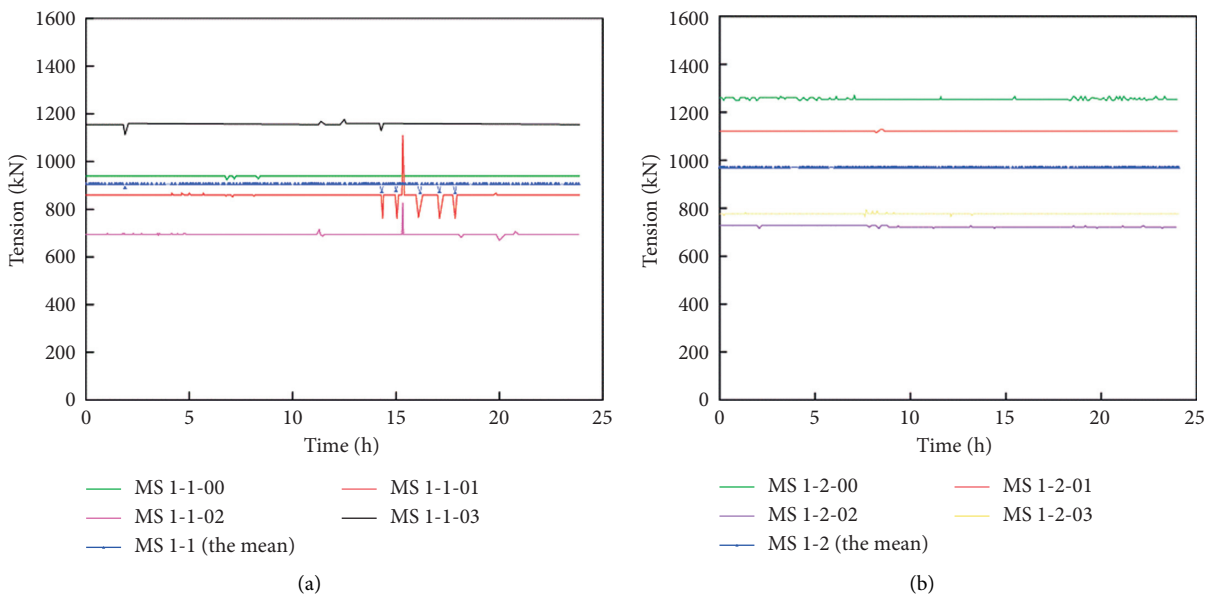

Figure 1: Test result curve of the anchor cable dynamometer in the water pressure test: (a) section 1; (b) section 2.

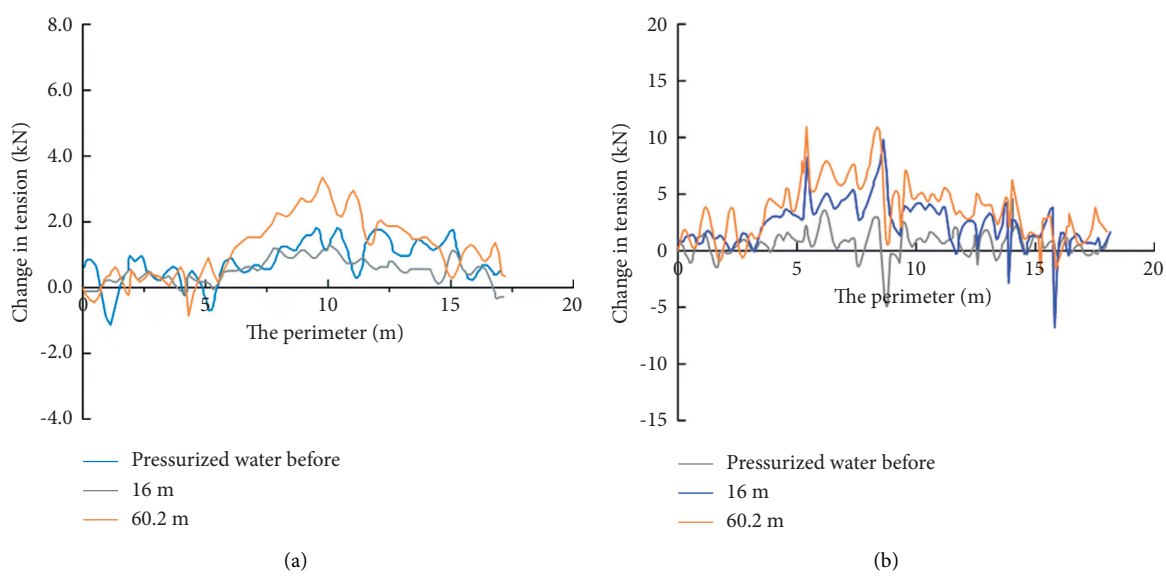

Figure 2: Test result curve of the distributed fiber intelligent steel strands during the section water pressure test: (a) section 1; (b) section 2.

3.2.2. Magnetic Flux Sensor Test Results. One ring (16 sensors) of magnetic flux was arranged to monitor the variation law of the effective prestressing force of the steel strand at different locations along the circumference under earth pressure after the filling is completed. As shown in Figure 6, the effective tension on the steel strand under the upper 13 m overburden pressure has no obvious change and basically matches the effective tension curve under the conditions of 16.3 m and 60.2 m head. Compared to the curve that just reached maximum tension, the effective prestressed value of the steel strand at the bottom of the culvert pipe decreases greatly, while the effective prestress value of the steel strand above the middle of the culvert pipe decreases relatively slightly. As shown in Figure 7, after the filling is completed, the effective prestress value of the steel strand along the circumferential path of the culvert pipe is small, and the tension increases to a maximum (115.0 kN) gradually along the path to the middle and upper parts of the culvert pipe. Then, along the path to the top of the culvert pipe, the tension gradually decreases to the minimum (94.3 kN), and the variation law of the effective tension prestress basically shows the M-shaped law of left and right axis symmetry.

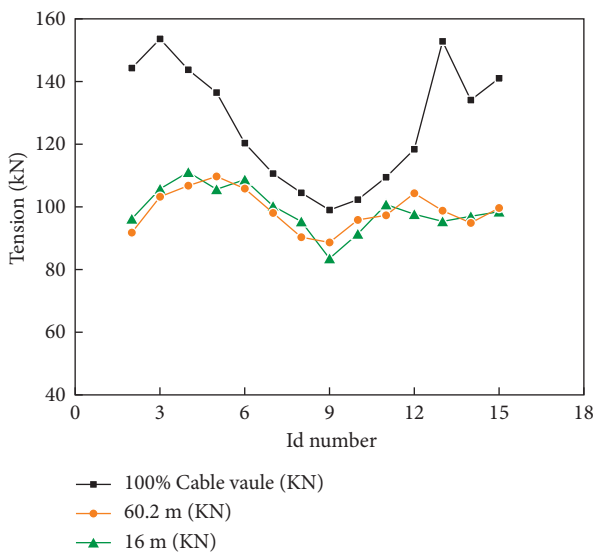

Figure 3: Test curve of the water pressure test of the magnetic flux sensor.

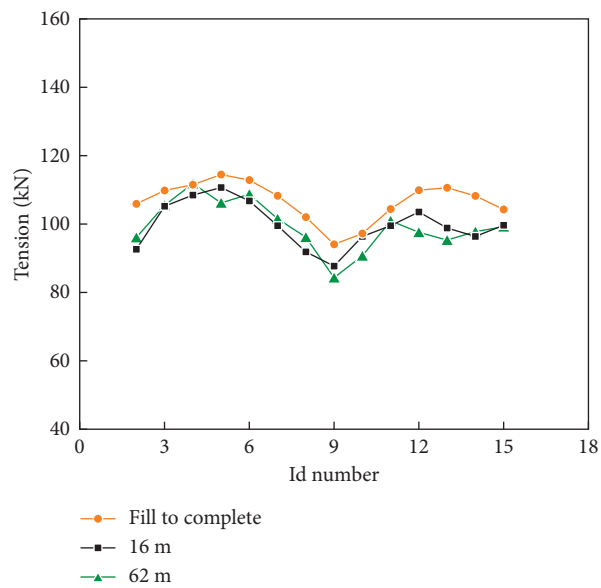

Figure 6: Test curve of the magnetic flux sensor filling test.

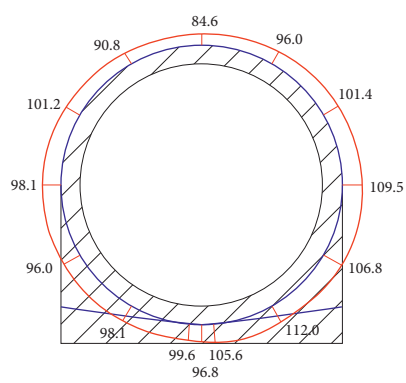

Figure 4: Water head test curve at 60.2 m in the water pressure test of the magnetic flux sensor (kN).

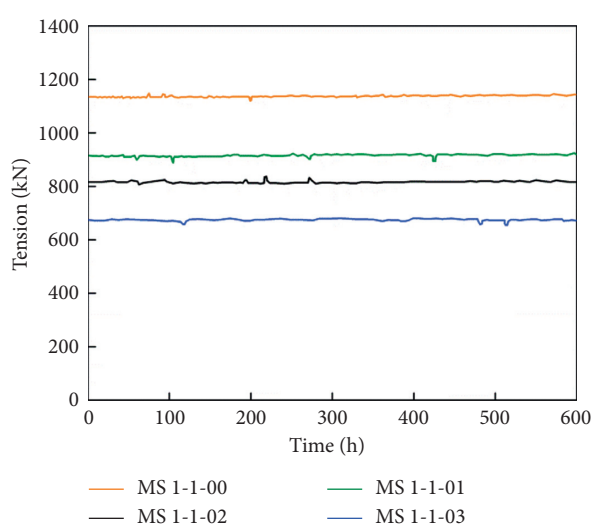

Figure 5: Test result curve of the anchor cable dynamometer in the soil filling test.

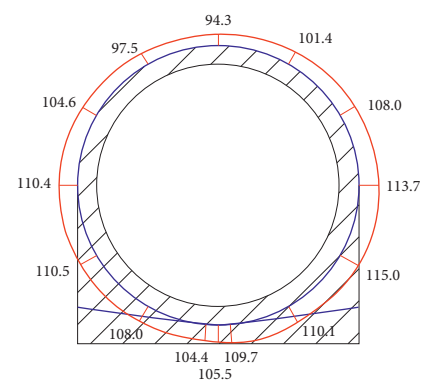

Figure 7: Test curve of the magnetic fluxsensor after soil filling (kN).

3.3. Tension Effect of Prestressed Steel Strand under Water Pressure after Filling

3.3.1. Test Results of Anchor Cable Dynamometer. In the process of the water pressure test after filling, the whole curve of 3 pairs (6 pieces) of anchor cable dynamometers of different sections is shown in Figure 8. The test results of the anchor cable dynamometer show that during the process of water pressure of the culvert pipe, it gradually increased to a 56 m head after filling, and the tensile prestress value of the anchor end of the steel strand basically has no obvious change.

3.3.2. Magnetic Flux Sensor Test Results. One ring (16 magnetic flux sensors) was arranged to monitor the variation law of the effective prestressing force of the steel strand at different positions along the circumference under the condition of water injection and pressure again after the completion of soil filling. As shown in Figure 9, the effective tension on the steel strand changes slightly under the action

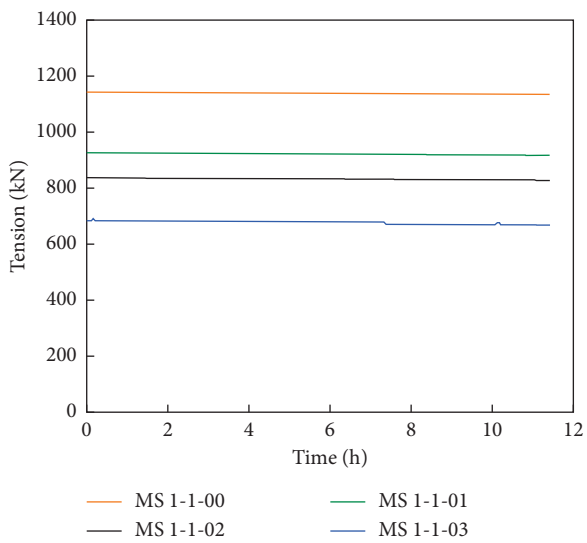

Figure 8: Test curve of the water pressure test process after soil filling by the magnetic flux sensor.

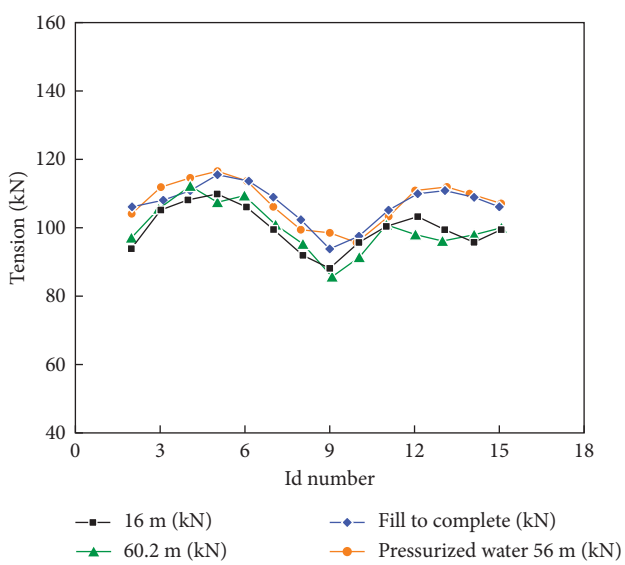

Figure 9: Test curve of the water pressure test process of the magnetic flux sensor after soil filling.

of water pressure after soil covering and basically matches the effective tension curve under the previous working conditions. As shown in Figure 10, at 56 m head of water condition after soil filling, the effective prestress value of the steel strand along the circumferential path of the culvert pipe is small, and in the middle and upper parts along the path to the culvert, the tension gradually increased to a maximum. Then, the effective prestress value tension gradually decreasing to a minimum, and the variation law of the effective tension prestress basically shows the *M*-shaped law of left-axis and right-axis symmetry. The maximum effective tension in the middle and lower parts of the culvert pipe is 117.0 kN, and the minimum effective tension in the middle and upper parts of the culvert pipe is 96.5 kN.

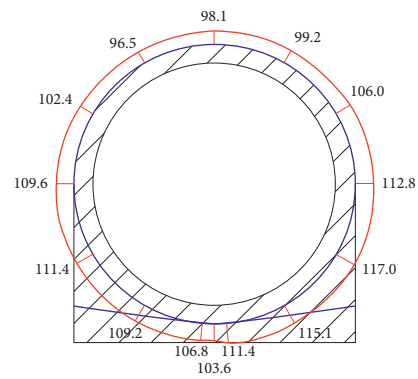

Figure 10: Water head test curve at 56 m in the water pressure test of the magnetic fluxsensor after soil filling (kN).

3.4. Evaluation of the Tensile Effect on the Prestressed Steel Strand. The tensile force measured by the force meter is 953.8 N to1065.3 N, indicating that the tensile force of the six prestressed steel strands basically reaches the design value of 1171.8 kN. When the steel strand is locked, the tension at some measuring points is lost greatly, and the maximum loss is 273.1 kN. After the completion of strand tension, the effective prestress of the strand located at the bottom of the culvert pipe reaches the maximum and gradually decreases along the circumferential path of symmetry on both sides until the tension reaches the minimum at the top of the culvert pipe.

In the process of the water pressure test, with increasing water pressure, the size and distribution law of the effective tension prestress of the steel strand have no significant change, as shown in the results of the numerical simulation. Compared to the effective prestress distribution curve of the steel strand at the completion of tension, the effective prestress value of the steel strand at the bottom of the culvert pipe decreases greatly, but the effective prestress value of the steel strand above the middle of the culvert pipe decreases relatively slightly. Along the circumferential path of the culvert pipe, the effective prestress value at the bottom of the steel strand is small. Along the path to the middle and upper parts of the culvert pipe, the tension gradually increases to the maximum, and then along the path to the top of the culvert pipe, the tension gradually decreases to the minimum, and the effective prestress basically shows an M-shaped change law.

4. Analysis of the Lining Structure Based on the 3D Nonlinear Numerical Simulation

The lining structure is analyzed based on a 3D nonlinear numerical simulation. When establishing the model, the axis direction is divided according to the spacing of the prestressed steel strand. When the spacing is 300 mm, the axis direction is divided into 40 sections, that is, the length of a culvert pipe is 12 m. In the finite element model, the *Z* axis is the vertical direction, the *X* direction pointing to the flow direction is positive, and the *Y* direction is the horizontal axis, and the *X* direction is the vertical *X* axis, satisfying the

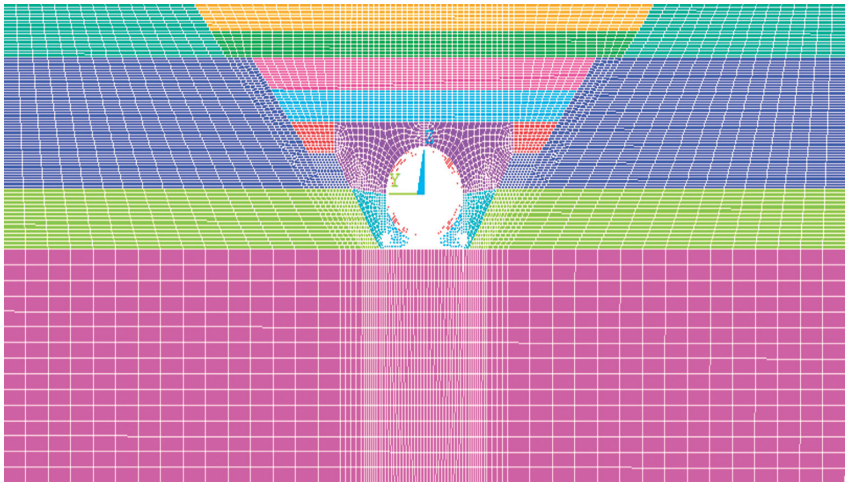

Figure 11: Overall model of the soil layer and prestressed culvert pipe.

right-hand rule. In the finite element model, prestressed steel strands, steel bars, and concrete are modeled separately by solids, and the contact mechanical action of steel strands on concrete is considered. During the finite element analysis, the prestress of the steel strand is applied by the cooling method, and the overall model is shown in Figure 11.

4.1. Working Condition of Calculation. According to the construction, tension, and actual operation of the cast-in-place prestressed culvert, the calculation conditions are set as follows: water filling pressure condition (0.55 MPa water pressure); filling condition; and water filling pressure condition (0.55 MPa water pressure).

4.2. Calculating Parameters. The physical and mechanical parameters of the rock and soil mass are listed in Table 1. The elastic modulus of the steel strand is $1.95e^5$ MPa, Poisson's ratio is 0.3, and linear expansion coefficient $\alpha = 2e^{-5}$. The elastic modulus of concrete is $3.25e^4$ MPa, and Poisson's ratio is 0.167.

4.3. Analysis of Calculation Results

4.3.1. Water Filling Conditions. Figures 12 and 13 show the calculation results of applying internal water pressure by filling water without overlying soil.

When an internal water pressure of 0.55 MPa is applied, the prestressed culvert expands outward as a whole. Due to the stiffness difference between the vertical and horizontal directions of the structure itself, the deformation of the structure is mainly in the horizontal direction, and the maximum incremental deformation value is 0.595 mm, which appears at the waist of the arch. The maximum vertical deformation occurs from the shoulder to the waist of the arch, with a magnitude of 0.169 mm. The incremental deformation of the structure presents a symmetry which corresponds to the structure itself. Under the influence of structural expansion and deformation, the concentration of compressive stress at the bottom of the circular culvert decreases, and the level of circumferential compressive stress decreases to a certain extent. The maximum compressive stress occurs at the anchor groove. At the same time, the maximum tensile stress value decreased to 2.211 MPa, which still appeared at the overlapping part of the steel strand at the bottom of the circular culvert. Compared to the field-measured monitoring data, the variation law is consistent with the actual situation.

4.3.2. Working Condition of the Filled Soil. After the completion of 18 m filling, the newly filled soil will settle itself and cause further settlement due to additional stress caused by its dead weight on the soil of the lower test foundation pit. Figure 14 shows the total deformation of the prestressed culvert structure due to soil settlement. To further determine the deformation and structural stress variation characteristics of concrete culvert structures caused by bearing earth pressure, the "follow-up" deformation caused by soil subsidence is deducted. Here, the center of the bottom of the concrete culvert is taken as the fixed point to obtain the relative deformation of the concrete culvert structure with respect to the fixed point, as shown in Figure 15.

Figure 16 shows that because the upper filled soil formed the asymmetric structure of the culvert soil pressure, the vertical earth pressure was large, and the horizontal earth pressure was small. Combined with the concrete culvert structure stiffness asymmetry, the vertical stiffness and horizontal stiffness were small, thus causing shrinkage in concrete culvert structure and presenting vertical direction and horizontal expansion deformation characteristics. The value of vertical convergent deformation was significantly greater than that of horizontal convergent deformation. The horizontal expansion deformation is 1.0 mm. The maximum vertical relative deformation is 2.4 mm, which appears in the vault and is vertically downward. Compared to the field-measured monitoring data, the variation law is consistent with the actual situation.

Table 1: Physical and mechanical parameters of rock mass.

Calculated parameters	Clay	Mud clay	Clay containing sand and gravel
Deformation modulus (MPa)	14	16	20
Cohesive force (kPa)	10	10	3
Angle of internal friction (°)	14	14	20
Saturated unit weight (kN/m^3)	19.1	19.1	19

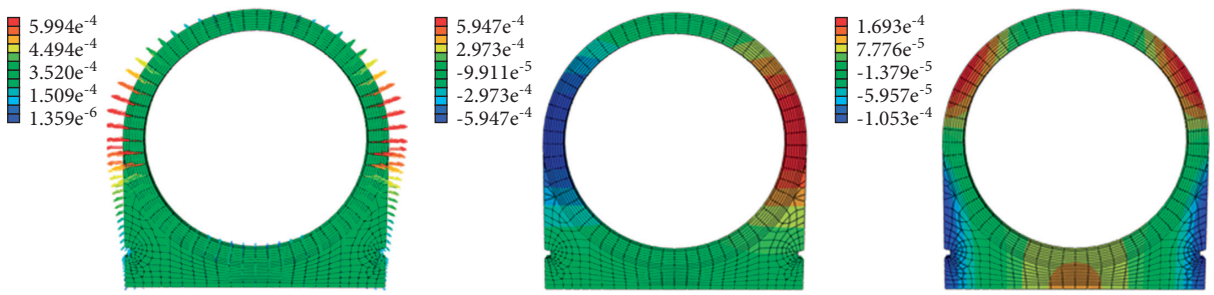

(a) (b) (c)

Figure 12: Incremental deformation of the prestressed culvert structure: (a) deformation vector diagram; (b) horizontal deformation; (c) vertical deformation.

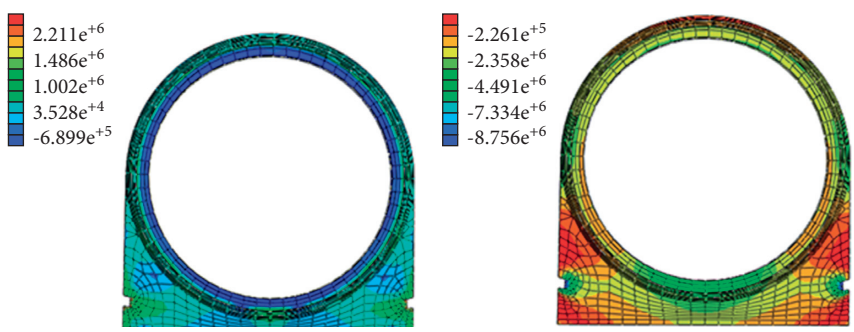

(a) (b)

Figure 13: Stress cloud diagram of the prestressed culvert structure: (a) maximum principal stress; (b) minimum principal stress.

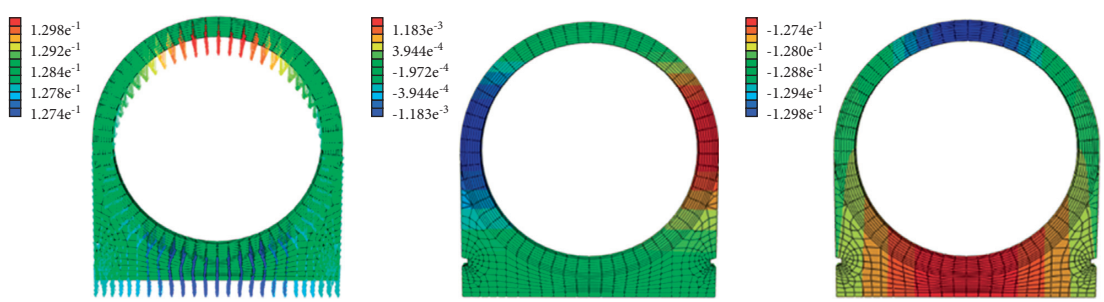

(a) (b) (c)

Figure 14: Incremental deformation of prestressed culvert structure: (a) deformation vector diagram; (b) horizontal deformation; (c) vertical deformation.

4.3.3. Water Filling Condition after Soil Filling. The internal water pressure is simulated on the basis of the filling condition. Figure 17 shows the incremental deformation cloud diagram of the prestressed culvert under internal water pressure. The horizontal expansion deformation of the prestressed culvert is larger than the vertical expansion deformation due to the asymmetry of the stiffness of the culvert and the soil pressure. The deformation morphology

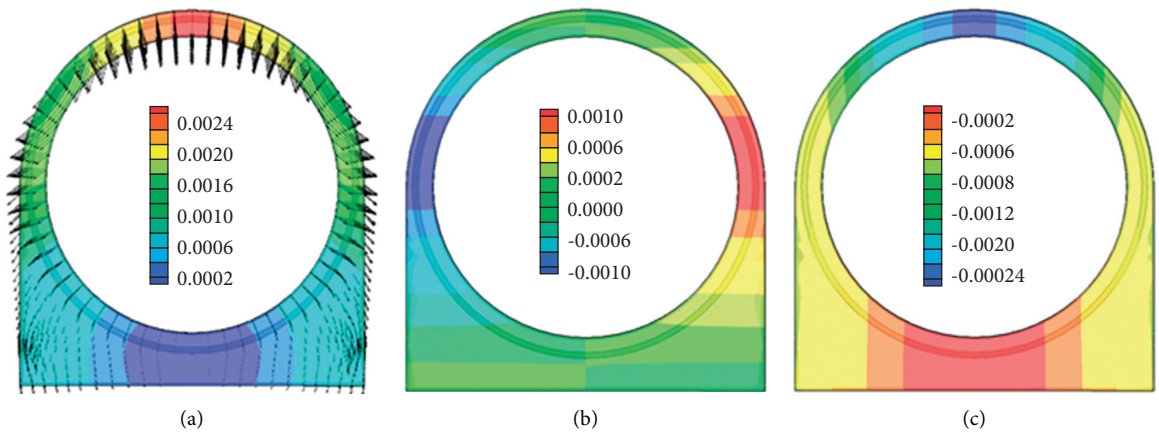

Figure 15: Relative deformation cloud diagram of prestressed culvert structure: (a) resultant displacement; (b) horizontal displacement; (c) vertical displacement.

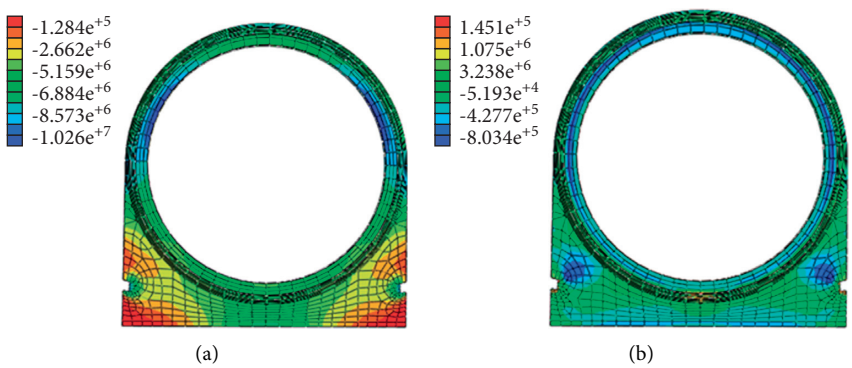

Figure 16: Stress cloud diagram of the prestressed culvert structure: (a) maximum principal stress; (b) minimum principal stress.

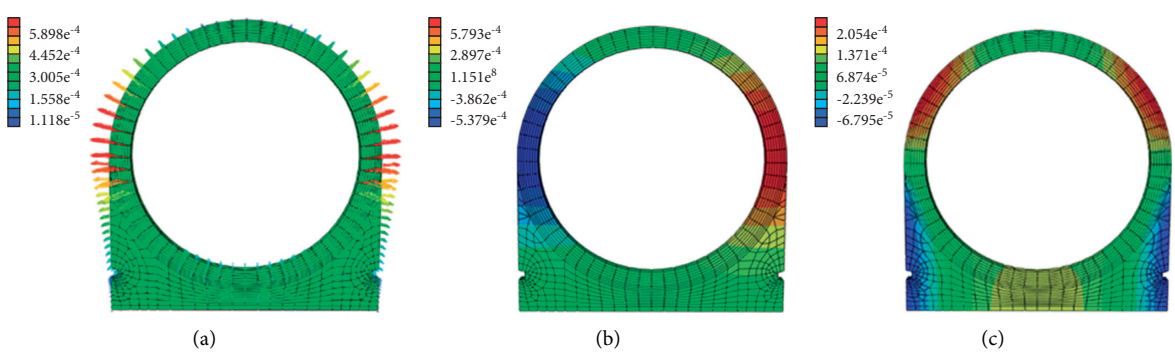

Figure 17: Incremental deformation of the prestressed culvert structure: (a) deformation vector diagram; (b) horizontal deformation; (c) vertical deformation.

shows symmetry consistent with the structure. The deformation near the arch waist of the prestressed culvert is the largest and is mainly in the horizontal direction, and the maximum horizontal deformation value is 0.579 mm. The deformation diminishes from the arch waist to the vault. The maximum vertical displacement occurred on the left and right arch shoulders with a magnitude of 0.205 mm. Compared to the field-measured monitoring data, the variation law is consistent with the actual situation. Affected by the expansion deformation of the culvert pipe caused by internal water pressure, the circumferential compressive stress of the prestressed culvert decreases, and the maximum compressive stress is 8.775 MPa. At the same time, the tensile stress at the bottom and outside of the prestressed culvert increases, and the maximum value for it is 1.529 MPa (Figure 18).

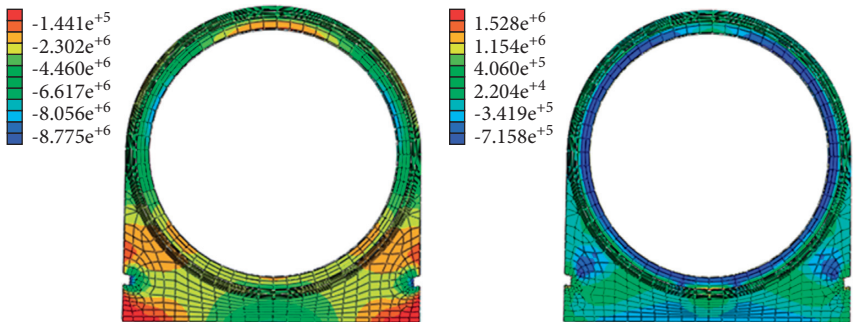

(a) (b)

Figure 18: Stress cloud diagram of the prestressed culvert structure: (a) maximum principal stress; (b) minimum principal stress.

5. Conclusion

(1) During the in situ test of the culvert lining, a magnetic flux sensor, a fully distributed fiber optic strain gauge, a fiber grating strain gauge, and a vibrating string anchor cable dynamometer were used to measure the tension of the steel strand. The test conditions included tension, water pressure, soil filling, and water pressure after soil filling, all of which required −30°C cold weather and +35°C hot weather. The test results show that the testing effect of the magnetic flux sensor is obviously better than the distributed optical fiber strain gauge and fiber Bragg grating strain gauge. The test data of vibrating string anchor cable are relatively stable under different conditions, but they can only test the tension at the locking end of steel strand.

(2) Three-dimensional finite element analysis results show that the upper filled soil formed the asymmetric structure of the culvert soil pressure, with the vertical earth pressure being big and the horizontal earth pressure being small. Moreover, the stiffness asymmetry is causing shrinkages in the concrete culvert structure and presents a vertical direction and a horizontal expansion deformation characteristic. The value of the vertical convergent deformation is significantly greater than that of horizontal convergent deformation. The horizontal expansion deformation is 1.0 mm. The maximum vertical relative deformation is 2.4 mm, which appears in the vault and is vertically downward. Compared with the field-measured monitoring data, the variation law is consistent with the actual situation.

(3) The deformation near the arch waist of the prestressed culvert is the largest and is mainly in the horizontal direction, and the maximum horizontal deformation value is 0.579 mm. The deformation diminishes from the arch waist to the vault. The maximum vertical displacement occurred on the left and right arch shoulders with a magnitude of 0.205 mm. Compared to the field-measured monitoring data, the variation law is consistent with the actual situation.

Data Availability

The datasets generated and/or analyzed during the current study are available from the corresponding author upon reasonable request.

Conflicts of Interest

The authors declare that they have no conflicts of interest.

Acknowledgments

This study was supported by the Natural Science Foundation of Hunan Province (2019-JJ-50336 and 2021JJ60063) and the Major Water Conservancy Science and Technology Project of Hunan Province (XSKJ2018179-01).

References

[1] A. Moawad, J. A. Mccorquodale, and G. Abdel-Sayed, "Hydraulic loading in culvert inlets," *Canadian Journal of Civil Engineering*, vol. 22, no. 6, pp. 1104–1112, 1995.

[2] B. L. McGuigan and A. J. Valsangkar, "Earth pressures on twin positive projecting and induced trench box culverts under high embankments," *Canadian Geotechnical Journal*, vol. 48, no. 2, pp. 173–185, 2011.

[3] O. S. Oshati, A. J. Valsangkar, and A. B. Schriver, "Performance of two cast-in-place box culverts under high embankments," *Canadian Geotechnical Journal*, vol. 49, no. 12, pp. 1331–1346, 2012.

[4] J. Vaslestad, A. Madaj, and L. Janusz, "Field measurements of old brick culvert slip lined with corrugated steel culvert," *Transportation Research Record: Journal of the Transportation Research Board*, vol. 1892, no. 1, pp. 227–234, 2004.

[5] B. P. Tullis and D. S. Anderson, "Slip-lined culvert inlet end treatment hydraulics," *Journal of Irrigation and Drainage Engineering*, vol. 136, no. 1, pp. 31–36, 2010.

[6] S. J. Korky, M. Najafi, J. E. Syar, and V. K. Nandyala, "Evaluation of literature on design and performance of spray applied pipe linings for renewal of culverts and drainage structures," *Pipelines 2019: Multidisciplinary Topics, Utility Engineering, and Surveying*, pp. 75–83, American Society of Civil Engineers, Reston, VA, 2019.

[7] A. Atef, T. Zayed, and A. Hawari, "Multi-tier method using infrared photography and GPR to detect and locate water leaks," *Automation in Construction*, vol. 61, pp. 162–170, 2016.

[8] T. Thitimakorn, N. Kampananon, N. Jongjaiwanichkit, and S. Kupongsak, "Subsurface void detection under the road surface using ground penetrating radar (GPR), a case study in the Bangkok metropolitan area, Thailand," *International Journal of Geo-Engineering*, vol. 7, no. 1, pp. 1–9, 2016.

[9] D. H. Chen and A. Wimsatt, "Inspection and condition assessment using ground penetrating radar," *Journal of Geotechnical and Geoenvironmental Engineering*, vol. 136, no. 1, pp. 207–214, 2010, 207–214.

[10] M. Karray and G. Lefebvre, "Détection des cavités sous les pavages par l'analyse modal des ondes de Rayleigh (MASW)," *Canadian Geotechnical Journal*, vol. 46, no. 4, pp. 424–437, 2009.

[11] M. Le Feuvre, A. Joubert, D. Leparoux, and P. Côte, "Passive multi-channel analysis of surface waves with cross-correlations and beamforming. Application to a sea dike," *Journal of Applied Geophysics*, vol. 114, pp. 36–51, 2015.

[12] C. Meola, G. M. Carlomagno, and L. Giorleo, "The use of infrared thermography for materials characterization," *Journal of Materials Processing Technology*, vol. 155-156, pp. 1132–1137, 2004.

[13] C. Ibarra-Castanedo and X. Maldague, "Pulsed phase thermography reviewed," *Quantitative Infrared Thermography Journal*, vol. 1, no. 1, pp. 47–70, 2004.

[14] C. Ibarra-Castanedo, J. R. Tarpani, and X. P. V. Maldague, "Nondestructive testing with thermography [J]," *European Journal of Physics*, vol. 34, no. 6, pp. 91–109, 2013.

[15] D. Kalhor, S. Ebrahimi, R. B. Tokime et al., "Cavity detection in steel-pipe culverts using infrared thermography," *Applied Sciences*, vol. 11, no. 9, p. 4051, 2021.

[16] J. Sun, X. Chen, and X. Tian, "Engineering infrastructure nondestructive testing with Rayleigh waves: case studies in transportation and archaeology," *Journal of Geophysics and Engineering*, vol. 4, no. 3, pp. 268–275, 2007.

Hindawi
Advances in Civil Engineering
Volume 2022, Article ID 3709415, 12 pages
https://doi.org/10.1155/2022/3709415

Research Article

Calculation Model and Numerical Validation of Horizontal Capacity of Micropiles with Different Section Forms

Wan-li Chao,[1] Jin Yang,[1] Wen-jie Liu,[1] Shi-qiang Pan,[1] Zong-wei Deng,[2] Yu-xuan Jin,[1] and Gui-hai Fu[2]

[1]*Hunan Communications Research Institute Co., Ltd., Changsha 410007, China*
[2]*College of Civil Engineering, Hunan City University, Yiyang 413049, China*

Correspondence should be addressed to Jin Yang; fay99e@163.com and Wen-jie Liu; liuwje@163.com

Received 6 December 2021; Accepted 21 December 2021; Published 10 February 2022

Academic Editor: Mingfeng Lei

With the popularized application of micropile for slope reinforcement, there are many kinds of pile section form, such as single steel bar, multisteel bar, and tube. In order to obtain the theoretical calculation model of horizontal capacity of micropiles with different types, numerical simulations for two common conditions, namely, soil-soil and soil-rock, were carried out to study micropile reinforced slope's deformation and failure regulation. The dominated indicator for micropile horizontal capacity was acquired. By using the equivalence principle, four kinds of micropiles' capacity calculation model were deduced. Then, FEM numerical analysis was used for validation. The results show that the flexural capacity of micropile is a critical and dominated indicator which should be considered seriously in slope reinforcement design. When the ultimate flexural capacity is reached, the displacement of micropile reinforced slope will increase rapidly. The primary factor affecting the flexural capacity of micropiles is pile diameter, followed by section reinforcement ratio. The calculation results of the calculation model of flexural capacity proposed in this paper are close to those of numerical ones and are safer. The calculation model can provide reference for micropile selecting and slope reinforcement design, especially for quick design of emergency engineering.

1. Introduction

A variety of slope reinforcement measures have been used in construction, including anchor rod frame, retaining wall, antislip pile, and micropile. Among all kinds of reinforcement structures, micropile is promising in the engineering field with its unique performance characteristics considering the lightening, miniaturization, and economic and environmental protection of landslide support structure projects [1, 2]. The micropile is usually a tiny diameter bored pile with a hole diameter less than 300 mm and a length diameter ratio greater than 30. High-capacity body reinforcements are used as the principal load bearing element in micropiles [3]. These bodies usually contain steel bar, steel tube, waste rail, and so forth. Because of the benefit of strong adaptability and fast construction, it is widely applied in reinforcement engineering, especially emergency engineering [4].

Traditionally, researchers believed that micropiles could only carry vertical loads in the form of tree root piles, due to the relatively large length and slenderness of micropile. In the last 30 years, with the development of micropile technology and its application in engineering, researchers have gradually recognized that micropile can carry lateral loads (see Figure 1) and its horizontal capacity is essential to its operational performance [5–7].

At present, the horizontal capacity calculation method of micropile can be roughly divided into three categories: the method based on the calculation theory of ordinary antislip piles, the equivalence method, and the numerical calculation method. The first method originates from the pile-soil interaction theory of general passive piles, which can be applied to the case where the micropiles are arranged more sparsely and cannot form a monolithic structure with the soil. Multiple theories have been developed for analyzing the mechanical behavior. In early development, the mechanical

Figure 1: Construction process of micropiles' reinforced slope (Hunan Lou-Di, China).

response of a single pile subjected to lateral loads was investigated [8]. With further research, the nonlinear behavior of laterally loaded pile groups was analyzed based on the semianalytical or Winkler elastic method [9, 10]. Some works were carried out on uplift load capacity recently, including single and group calculation method [11].

The equivalence method considered traditional retaining structure as a whole composite structure for the micropile group with small pile spacing that the micropile and the surrounding soil form a whole structure to bear the load together. The calculation method can be developed based on the calculation method of this retaining structure [12–14]. It can be further divided into the following methods according to the different equivalence methods:

(1) Reinforced concrete beam method: this method is a semiempirical and semitheoretical method. The composite structure of the micropile and the rock-soil body around the pile is treated as a reinforced concrete beam and analyzed according to the calculation method of the reinforced concrete beam. The equations are given without the pile-soil adhesion. Meanwhile, the empirical calculation formula is proposed considering the partial adhesion between pile and soil.

(2) Equivalent section method: this method considers the micropile combined structure as a flexible retaining wall. It carries out the design verification based on the calculation theory of retaining walls and the principle of equal deformation.

(3) Equivalent stiffness method: this method equates the small combination pile to a certain thickness of underground continuous wall according to equal flexural stiffness.

Numerical analysis can simulate the actual working conditions, which is the most rigorous solution and the most potential calculation method. Chen el al. [15] carried out numerical simulation of the flexible micropile (l/d more than 50 in general) with finite element software ABAQUS. It is shown that the larger the diameter and the larger the friction angle of soil, the larger the lateral bearing capacity of micropiles. Lee et al. [16] investigated the behaviour of piled raft installed in soft clay using a 3D finite element analysis. They demonstrated that using a limited number of strategically located piles increases the raft bearing capacity and reduces its settlement. Cho et al. [17] utilized 3D FEM to study the settlement behaviour of pile raft foundation in clay soils. The soil was modeled using an elastic-perfectly plastic material with the Mohr-Coulomb failure criterion, and the piles were modeled as linear elastic material. The results indicated that the average settlement of the piled raft can be effectively reduced by widely spaced piles, while the differential settlement was reduced by placing the piles within the central area of the raft. Alnuaima et al. [18] carried out FEM calculation on micropiles and verified it with centrifuge tests. Some cases were analyzed taking into account a number of factors, such as the number of micropiles, the spacing to micropile diameter, and the raft thickness. It was found that a micropile system can increase the tolerable bearing pressure by 100% compared to an isolated raft system, and an adjustment factor was introduced to account for the raft flexibility.

All these studies above have provided guidance for analyzing the horizontal capacity of micropile. However, horizontal capacity indicators for micropiles include flexural capacity, shear capacity, and uplift capacity. It is necessary to acquire the dominated indicator in preventing slope deformation and failure process. Moreover, many current calculation methods simplify micropile as steel pipe pile. In fact, nowadays different section forms are developed for micropile in order to meet different engineering demands. Reports concerning theoretical calculation model for different micropile section forms are few. In this study, the deformation and failure behaviour of slopes reinforced by micropile was firstly investigated. The dominated horizontal capacity indicator for micropile was acquired. Then, the corresponding capacity calculation models for four typical micropile section forms were deduced. Then, a numerical simulation validation work was carried out. Finally, the ultimate capacity of commonly used pile type was listed and compared, which facilitates quick determination of micropile selecting in engineering design.

2. Dominated Capacity Indicator of Micropile in Reinforced Slope

2.1. FEM Introduction. In order to find out which indicator is more critical and dominated for horizontal resistance of deformation and failure, FEM numerical simulations are carried out. Figure 2 shows the analytical model of the three-dimensional system of micropile reinforced slope. The model consists of two stacked narrow blocks to, respectively, simulate the soil layers which are above and below the potential sliding surface of the slope. A contact surface is set between the two blocks to simulate the potential sliding surface. The model's thickness, heights of the upper and lower blocks, and the length of the upper block are represented as s, h_a, h_b, and l, respectively. The micropile is laid in

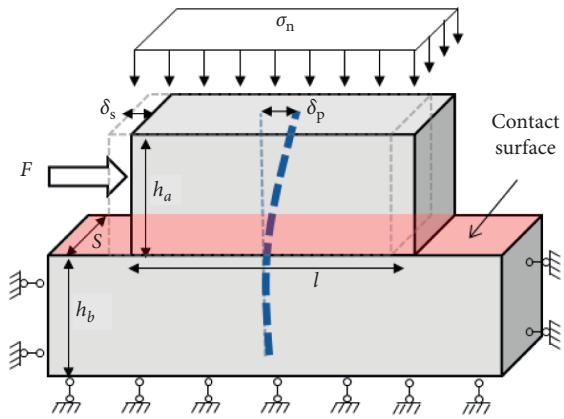

Figure 2: Analysis model of ultimate capacity of micropile.

the middle of the model through the length. The simple support constraints are set at the left, right, and lower boundaries of the lower block of the model. The model is equilibrated under the uniform load σ applied at the upper boundary of the upper block, simulating the formation of relatively uniform Earth pressure in the model. This process aims to simplify the calculation and facilitate the analysis. Then, the horizontal uniform load, which is represented as the combined force F, is applied at the left boundary of the upper block to simulate the landslide thrust. Under the action of the thrust force, the horizontal displacement generated at the left boundary of the upper block is δ_s. The horizontal displacement generated at the top of the multipile is δ_p. According to the principle of the in situ direct shear test, the horizontal thrust force F is the total resistance of the micropile reinforced slope system.

Two patterns are simplified for the geological layers. The first pattern is homogeneous soil layers both above and below the sliding surface (referred to as "soil-soil pattern" hereafter). The second one is set as a homogeneous soil layer above the sliding surface and a homogeneous rock layer below the sliding surface (referred to as "soil-rock pattern" hereafter). These two soil patterns represent soil slope and soil-rock combination slope, respectively. The shear strength of the potential sliding surface is dependent on the residual strength of the soil. The cohesion and internal friction angle are discounted according to the nature of the different geological layers. The micropiles are designed using the pile unit model built into FLAC3D. The average and tangential cohesion and internal friction angles of the micropile are the same as those of the contact soil layer. The average and tangential stiffness of the contact surfaces are taken as kn = ks = 100 GPa for the pile unit parameters of the different soil layer patterns, respectively [19]. The parameters for the FEM are shown in Tables 1 and 2, which are mainly estimated by several material tests according to "Standard for Geological Testing Method" [20] and "Standard for Test Method of Concrete Structures" [21].

Figure 3 shows the grid model of the resisting force analysis (only one element thickness of the model is shown). Micropile is arranged in the middle of the model with a diameter of 0.2 m and a pile length of 20 m. The thickness of the model is $s = 3$ m and $h_a = h_b = 10$ m. A uniform and horizontal load is applied to the upper and left boundaries of the upper block. The load is gradually increased.

2.2. Analysis of Slope Resistance Results of Soil-Soil Mode with Multipile Antislip Reinforcement. Figure 4 shows the variation curves of the total resistance (under support condition) and the sliding surface resistance (under unsupported condition) with the boundary displacement. It can be seen that the failure process of micropile supporting slope can be divided into three steps, namely, small deformation step, deflection step, and uplift step.

Take "soil-soil pattern," for example, when the horizontal thrust pressure is less than 32 kPa, and the horizontal resistance of the system is mainly provided by the shear strength of the block surface. The horizontal resistance generated by the micropile is negligible due to the small horizontal displacement. When the horizontal thrust pressure is between 32 kPa and 40 kPa, the deflection of micropile enhances. The horizontal resistance provided by the sliding surface is constant, and the extra horizontal resistance is mainly provided by the flexural capacity of micropile. It can be seen that the micropile has obvious displacement control on the slope in the deflection step. In this step, the horizontal displacement is about 1/2 of that without support.

As the pressure increases continually, the bending moment is close to the limitation, namely, ultimate flexural capacity. When the horizontal thrust pressure surpasses 40 kPa, an apparent horizontal displacement increase with nearly 40 cm can be observed. Therefore, the horizontal thrust pressure of 40 kPa is the maximum when the controlled displacement of the slope is within 10 cm. However, the micropile still possesses a considerable pullout resistance due to the relatively large shear strength between the pile and the soil. The deformation and failure process of the soil-rock slope with micropile support is similar.

In general, when the ultimate flexural capacity of micropile is reached, the displacement will increase rapidly. At the same time, the antiuplift capacity has not been fully played. Therefore, flexural capacity is the primary and dominated indicator that needs to be considered in reinforcement design.

3. Derivation of Steel Tube Pile Flexural Capacity Formula

3.1. Typical Section Form of Micropile. The micropile consists of cement paste and reinforcing material, and the reinforcing material generally includes steel tube and steel bar. Four typical types of micropile cross-section forms are commonly used. "M25" means that the compressive strength of the cement mortal is nearly 25 MPa. This kind of cement mortal is widely used in micropile engineering because of advantages in cost and mechanical properties. As shown in Figure 5, the reinforcing material of the A-1 and A-3 section is one steel bar and three steel bars, respectively. The reinforcing material of the B and C section is

Table 1: Geotechnical parameters.

Materials	Modulus of elasticity E (MPa)	Poisson's ratio V	Cohesion c (kPa)	Angle of internal friction φ (°)
Soil layer	50	0.35	35	25
Rock layer	1000	0.25	100	30
Sliding surface	—	—	15	25

Table 2: Micropile parameters.

Materials	Pile diameter D (m)	Modulus of elasticity E (GPa)	Poisson's ratio v	Ultimate bending moment M_u (kN·m)	Ultimate pulling force N_u (kN)
Piles	0.2	50	0.2	70	1100

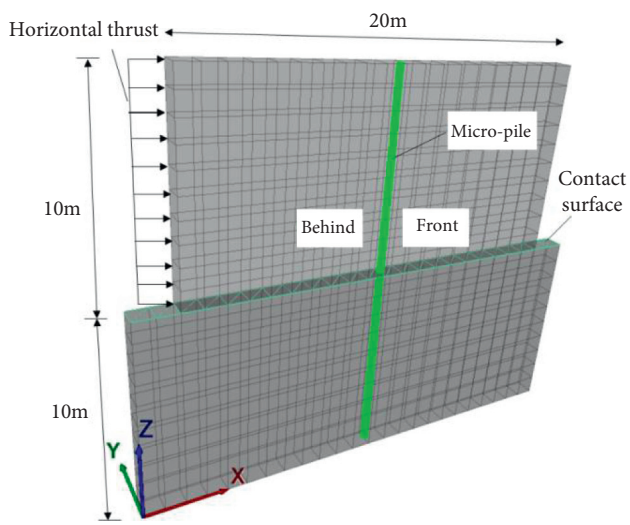

Figure 3: FEM grid model with one element thickness.

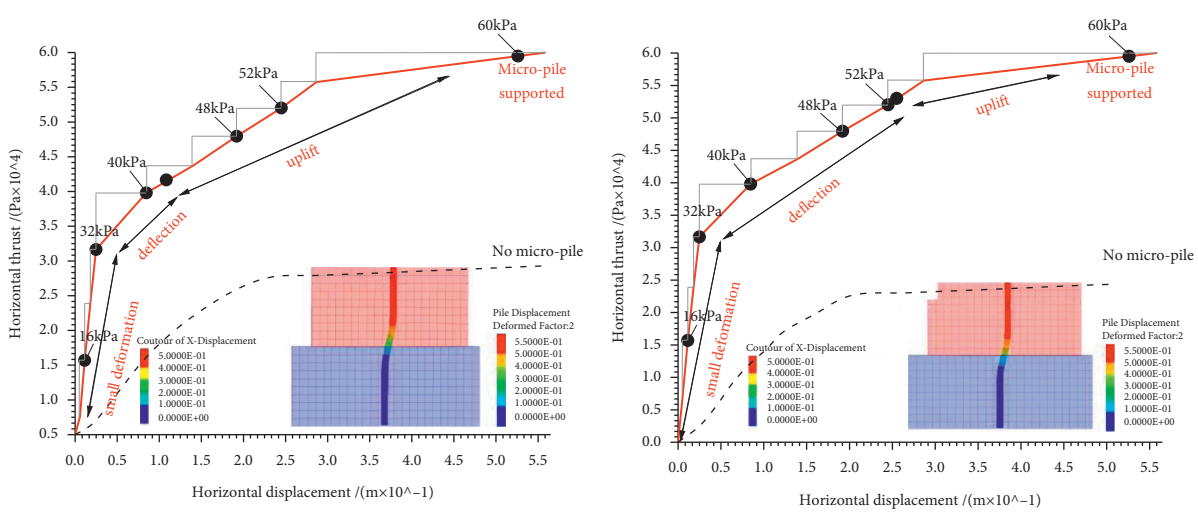

Figure 4: Direct shear load-displacement curve. (a) Soil-soil pattern. (b) Soil-rock pattern.

steel tube and the combination of a steel tube and three steel bars, respectively. The design parameter H is the outer diameter of the steel tube, and s is the distance from the shape center of the steel section to the shape center of the pile section.

3.2. Derivation of the Flexural Capacity Formula for A-1 Section. The reinforced body of the A-1 micropile section is a single reinforcement, referred to as a single reinforcement section, and the following assumptions are made to simplify the calculation: the tensile strength of the slurry in the tensile

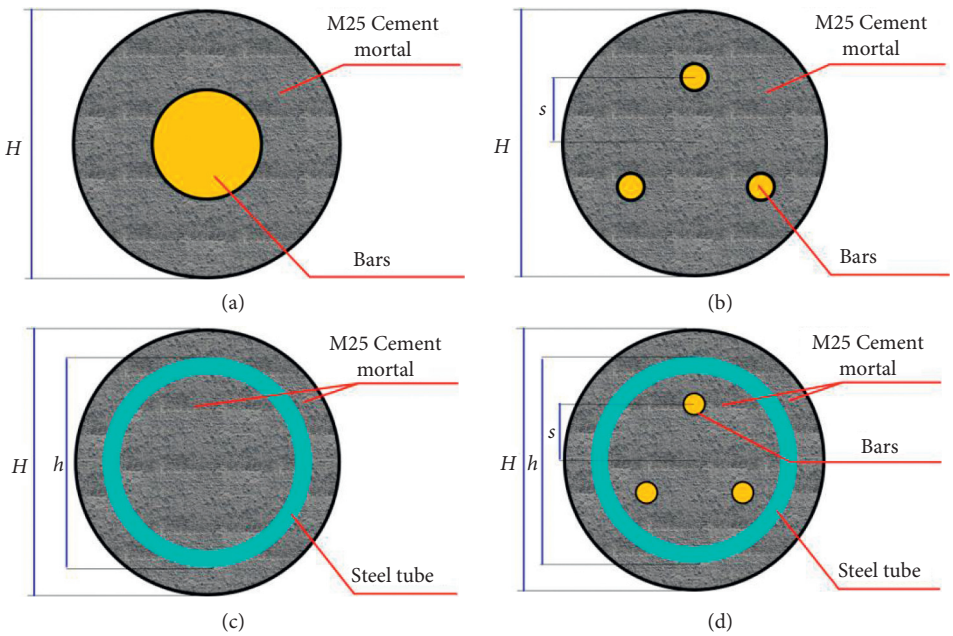

Figure 5: Section form of four typical piles. (a) Type A-1 section. (b) Type A-3 section. (c) Type B section. (d) Type C section.

zone outside the reinforcement can be disregarded since it has little effect on the ultimate bending moment. The slurry yielding occurs only in the compressive zone above the reinforcement. Therefore, the yielding area of the compressive zone can be assumed as ¼ of the total slurry area. In contrast, the stress of the slurry in other parts is relatively low and is not considered. To simplify the calculation, the circular reinforcement cross section is equivalent to the upper and lower symmetrical I-beam rectangular cross sections. The rectangular height of the web is the diameter of the reinforcement d. The area of both tension and compression flange is both ¼ of the total slurry area. Besides, all the slurry in the flange is assumed in compression yields, and the tensile and compressive yield stresses of the reinforcement are assumed equal. In addition, the yield stresses of the web reinforcement are assumed rectangularly distributed, as shown in Figure 6.

I-beam section size is as follows:

$$\begin{aligned} t &= \frac{H}{2} - \frac{d}{2}, \\ l &= \frac{A}{4t} \\ &= \frac{\pi/4H^2 - \pi/4d^2}{4t} \\ &= \frac{\pi}{16t}\left(H^2 - d^2\right), \\ b &= \frac{\pi/4 \cdot d^2}{d} \\ &= \frac{\pi\, d}{4}, \end{aligned} \tag{1}$$

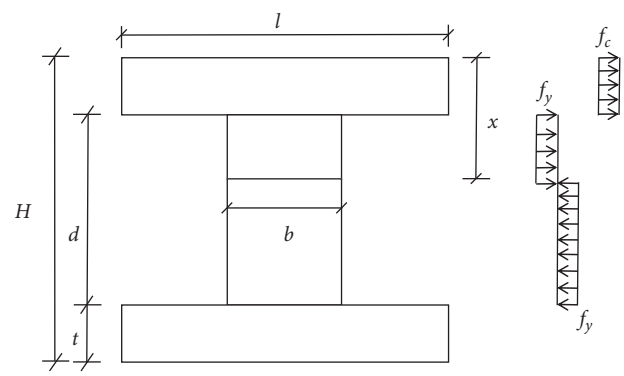

Figure 6: Sketch of single reinforcement section calculation.

where t is the flange thickness; l is the flange width; b is the web width; H is the pile diameter; d is the reinforcement diameter; and A is the total area of the slurry.

The static equilibrium conditions are presented in the following equation:

$$f_c \cdot t \cdot l + f_y \cdot b \cdot (x - t) = f_y \cdot b \cdot (H - t - x). \tag{2}$$

The height of the pressure zone can be obtained from the following equation:

$$x = \frac{H}{2} - \frac{f_c \cdot t \cdot l}{2 f_y \cdot b}. \tag{3}$$

As a result, the formula for the flexural capacity of the A-1 section can be acquired:

$$M_u = f_y \cdot b \frac{(H - t - x)^2}{2} + f_y \cdot b \frac{(x - t)^2}{2} + f_c \cdot b \cdot l\left(x - \frac{t}{2}\right), \tag{4}$$

where f_y is the yield strength of the reinforcement; f_c is the compressive yield strength of the slurry; and x is the height of the compressed zone.

3.3. Derivation of the Flexural Capacity Formula for A-3 Section and B Section. The reinforcement body of the A-3 micropile section contains three bars, and the position of the bars is symmetrical about the shape center of the section. The flexural capacity of the micropile in this section form against bending is influenced by the direction of the load action, which will affect the final flexural capacity calculation. To avoid this situation, the reinforcement section is converted into a circular section according to the principle of static equivalence. The conversion principle of the cross section is shown in the following equation.

$$\begin{aligned} t &= \frac{3\pi d^2}{8\pi s} \\ &= \frac{3d^2}{8s}, \end{aligned} \tag{5}$$

where d is the diameter of the reinforcement; t is the thickness of the equivalent steel tube; and s is the distance from the shape center of the reinforcement section to the shape center of the pile section.

The circular section can be regarded as equivalent steel tube so that the flexural capacity formula of the A-3 type section is the formula of the B type steel tube section.

The reinforced body of the B type micropile section is steel tube. And its cross-sectional form is the same as that of the steel tube pile. Therefore, the derivation of the calculation formula of flexural capacity of the B type section is based on the formula derivation of steel tube pile. Moreover, through the numerical test, the thickness of the protective layer on the outside of the steel tube of the B type micropile is relatively large so that its provision of flexural capacity is nonnegligible. Therefore, the contribution of the thickness of the protective layer to the flexural capacity needs to be considered into the capacity calculation of B type section. In order to simplify the calculation, the following assumptions are made. (1) The derivation process is based on the steel tube pile flexural equation. (2) The contribution of the steel tube outer pressure zone protective layer slurry to the flexural capacity is considered. (3) The steel tube inner pressure zone height x is unrelated to the pressure zone protective layer slurry. (4) The slurry in pressure zone protective layer is in the state of pressure yielding with the bowed shape. The angle of the bow span is the same as that in the steel tube inner pressure zone, shown in Figure 7.

(a) Calculation of bow section characteristics.

Calculation angle:

$$\alpha_1 = \frac{\pi}{2} - \alpha_0. \tag{6}$$

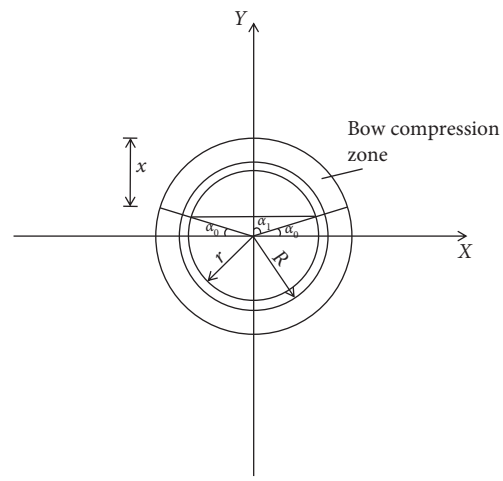

Figure 7: Distribution of pressure zones in B section.

Bow center position:

$$e = \frac{2H \sin^3 \alpha_1}{3\left(2\alpha_1 - \sin 2\alpha_1\right)}. \tag{7}$$

Bow area:

$$A_e = \frac{(H/2)^2 \cdot \left(2\alpha_1 - \sin 2\alpha_1\right)}{2}, \tag{8}$$

where $\alpha 1$ is the angle between the horizontal line and the line connecting circle center with lower edge of compression zone; H is the pile diameter; e is the distance from the center of the bow to the center of the pile; A_e is the area of the bow.

(b) Calculation of flexural capacity.

Based on the above assumptions which are biased towards insecurity, the flexural capacity is mainly based on the bearing capacity provided by the steel tube, the core slurry body considered, and the bending moment of the bowed-to-neutral axis in the compressed zone of the protective layer. Therefore, the final expression of flexural capacity is calculated as follows:

$$\begin{aligned} M_u &= M_s + M_c \\ &= f_y t (R + r)^2 \cos \alpha_0 + \frac{2}{3} f_c r^3 \cos^3 \alpha_0 \\ &\quad + f_c \cdot A_e \cdot \left(e - r \sin \alpha_0\right). \end{aligned} \tag{9}$$

3.4. Derivation of Flexural Capacity Formula for C Section. The reinforced body of the C type micropile section is the combination of a steel tube and three reinforcement bars. Compared to B type section form, the three reinforcement bars in the C type section are set inside the steel tube so that they can be designed according to the design method of the B

type section. Regarding safety design, the contribution of the three reinforcement bars to the flexural capacity can be calculated according to the most unfavorable flexural form, as shown in Figure 8. Therefore, the flexural capacity of the reinforcement bars can be assumed as follows. (1) The ultimate bending moment of the section is calculated by the most unfavorable flexural capacity form of the reinforcement. (2) The height x of the compressive zone is unrelated to the stress on the reinforcement. (3) The stress on the reinforcement is calculated per the assumption of the flat section.

(a) Calculation of the stress in the shape of the center of the steel bar

Stress in tensile reinforcement:

$$\sigma = \frac{s + r \sin \alpha_0}{R + r \sin \alpha_0} f_y. \tag{10}$$

Stress in compressed reinforcement:

$$\sigma = \frac{s/2 - r \sin \alpha_0}{R + r \sin \alpha_0} f_y, \tag{11}$$

where s is the distance from the cross-sectional center of the reinforcement to the cross-sectional center of the pile; r and R are the inner and outer diameter of the steel tube, respectively; and f_y is the yield strength of the reinforcement.

(b) Calculation of flexural capacity of C section.

Based on the above assumptions which are on the unsafe side, the flexural bearing capacity in equation (9) is based on flexural capacity provided by the steel tube and core slurry, the bow of the protective layer pressure zone, and the bending moment of the reinforcement stress on the neutral axis. Therefore, the final expression of the flexural capacity is presented in the following equation.

$$\begin{aligned} M_u &= M_s + M_c \\ &= f_{yt} t (R + r)^2 \cos \alpha_0 + \frac{2}{3} f_c r^3 \cos^3 \alpha_0 + f_c \cdot A \\ &\quad \cdot (a - r \sin \alpha_0) + f_y A_s \\ &\quad \left[\frac{(s + r \sin \alpha_0)^2}{R + r \sin \alpha_0} + 2 \cdot \frac{(s/2 - r \sin \alpha_0)^2}{R + r \sin \alpha_0} \right], \end{aligned} \tag{12}$$

where A_s is the cross-sectional area of a single bar.

4. Numerical Validation

As for the flexural capacity of micropile, in order to simplify the expression of the formula, there are certain assumptions in the derivation process, so it is necessary to use numerical method to verify the applicability and accuracy of the proposed formula.

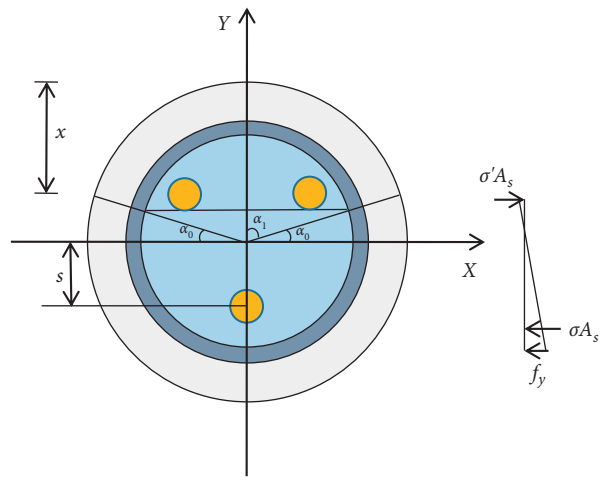

Figure 8: The most unfavourable bending section form.

4.1. Numerical Model Used for Validation. The model is a supported beam subjected to symmetrical loading which can be seen in Figure 9. The cross section in the span is in a pure bending state, and the bending moment is maximum because the mechanical model is symmetrical. After simplification, half of the mechanical model is taken for simulation. Therefore, by stepwise increasing the load F until the pile bends and breaks, the maximum bending moment is obtained, which is the flexural capacity of the pile. The numerical simulation uses four typical sections to verify the proposed formula, including 100-A, 100-B, and 200-C. The yield strength of the reinforcement material is taken as 235 MPa. The compressive and tensile yield strengths of the cement mortar body are 40 MPa and 4 MPa, respectively.

4.2. Numerical Validation of 100-A Section Flexural Resistance. The form of the 100-A section and the loading method are shown in Figure 10. The mechanical states of the pile body and the stress distributions in the left end section corresponding to the situations of $F = 8$ kN and 28 kN are shown in Figure 11. When the load is small, the cement mortar slurry is pulled apart, and then the cement mortar slurry in the tension zone starts to yield under pressure, followed by the yielding of cement mortar in the compression zone and reinforcement in the tension zone. As the load increases, the yielding range of the cement mortar slurry and the reinforcement gradually expands toward the pile core until it is damaged. Throughout the process, the displacement of the left end section gradually increases with the load increase.

The load-deflection curve of the whole process of numerical test is shown in Figure 12. The crack load is about 4.2 kN because the stress on cement mortar surpasses its tensile yield strength. The ultimate load can be roughly derived as 24 kN, and the corresponding ultimate flexural capacity (bending moment) is 9.6 kN·m. Beyond this load, the deflection increases quickly. In contrast, the ultimate bending moment calculated by equation (4) is 9 kN·m,

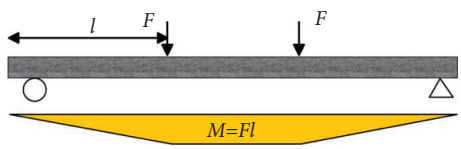

Figure 9: Mechanical models of flexural loading.

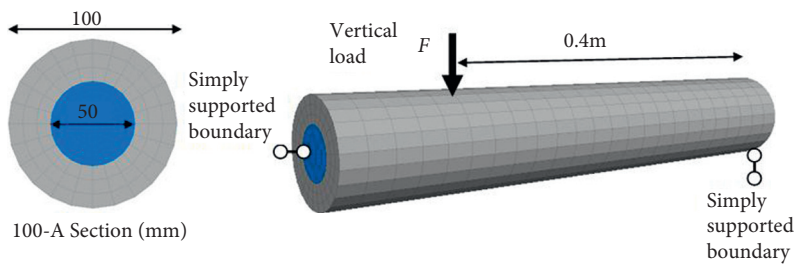

Figure 10: 100-A section form and loading method.

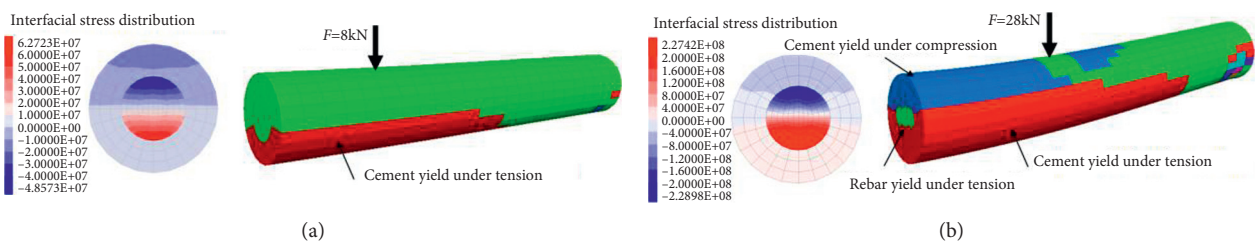

Figure 11: Mechanical states of 100-A micropile. (a) $F = 8$ kN. (b) $F = 28$ kN.

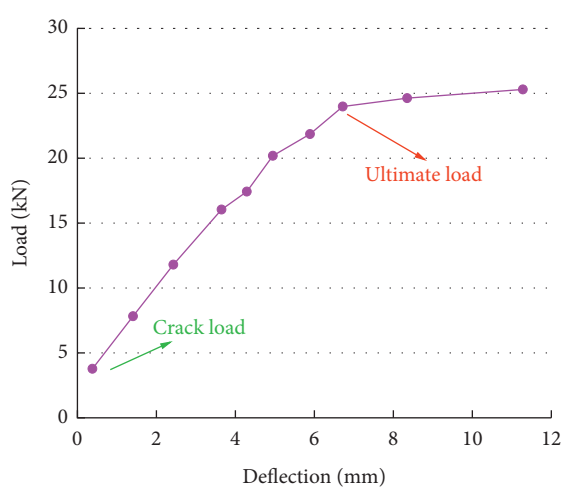

Figure 12: Relationship between load and deflection for 100-A.

indicating that the flexural capacity calculated by the calculation model formula is on the safe side and is close to the numerical validation result.

4.3. Numerical Validation of 100-B Section Flexural Resistance. The form of the 100-B section and the loading method are shown in Figure 13. The mechanical states of the pile body and the stress distributions in the left end section corresponding to the situations of the taken load $F = 4$ kN and 18 kN are shown in Figure 14, respectively. In the case of the small load, the cement mortar slurry is pulled apart, followed by the yielding of the cement mortar slurry in the compression zone under pressure. Then, the steel tube in the tension zone starts to yield. As the load increases, the yielding range of the cement mortar slurry and steel tube gradually expands toward the pile core until the structural damage.

The load-deflection curve of the whole process of numerical test is shown in Figure 15. The ultimate load can be roughly derived as 18 kN, and the corresponding ultimate bending moment is 7.2 kN·m. In contrast, the ultimate bending moment calculated by the calculation model formula (9) is 7 kN·m, which indicates that the flexural capacity calculated by the calculation model formula is on the safe side and is close to the numerical validation result.

4.4. Numerical Validation of 200-C Section Flexural Resistance. The form of the 200-C section and the loading method are shown in Figure 16. The mechanical states of the pile body and the stress distributions in the left end section corresponding to the situations of the taken load $F = 40$ kN and 115 kN are shown in Figure 17, respectively. When the load is small, the cement mortar slurry is pulled apart, and then the cement mortar slurry in the compression zone starts to yield under pressure, followed by the yielding of the steel tube in the tension zone. As the load increases, the yielding range of the cement mortar slurry and steel tube

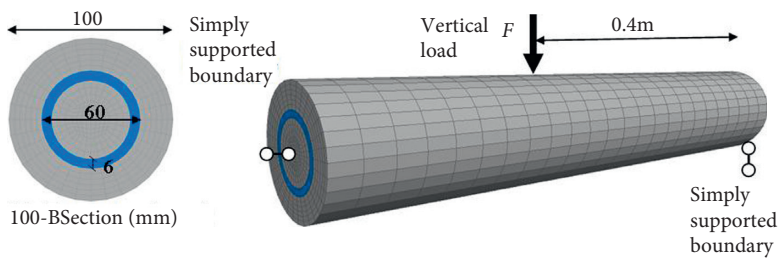

Figure 13: 100-B section form and loading method.

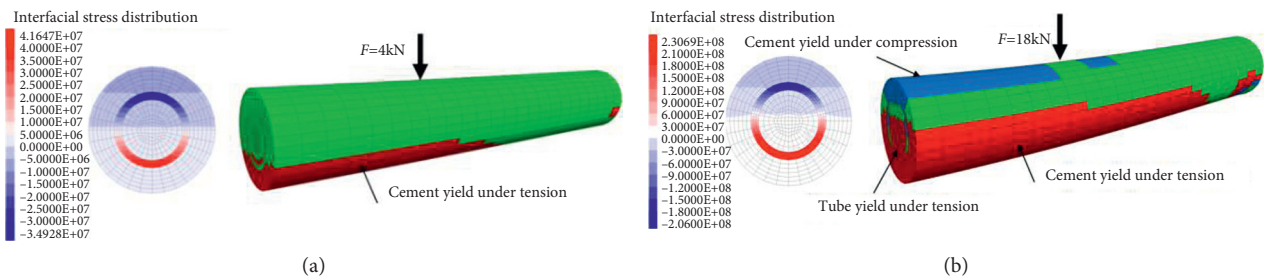

Figure 14: Mechanical states of 100-B micropile. (a) $F = 4$ kN. (b) $F = 18$ kN.

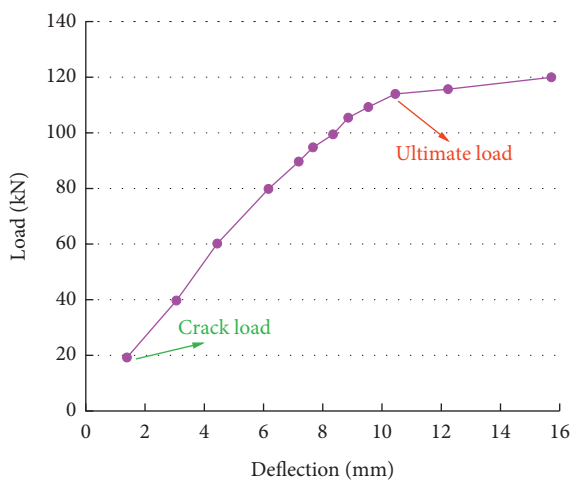

Figure 15: Relationship between load and deflection for 100-B.

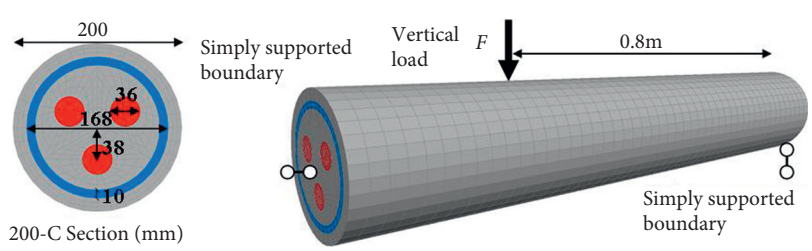

Figure 16: 200-C section form and loading method.

gradually expands toward the pile core until the damage. In the damage state, the stress of the steel in the tensile zone is close to the yield stress, and part of it has yielded. The steel in the compressive zone has not yielded, whereas the stress at its edge is close to the yield stress.

The load-deflection curve of the whole process of numerical test is shown in Figure 18. The ultimate load is 115 kN, and the corresponding ultimate bending moment is 92 kN·m. In contrast, the ultimate bending moment calculated by the calculation model formula (12) is 88.4 kN·m.

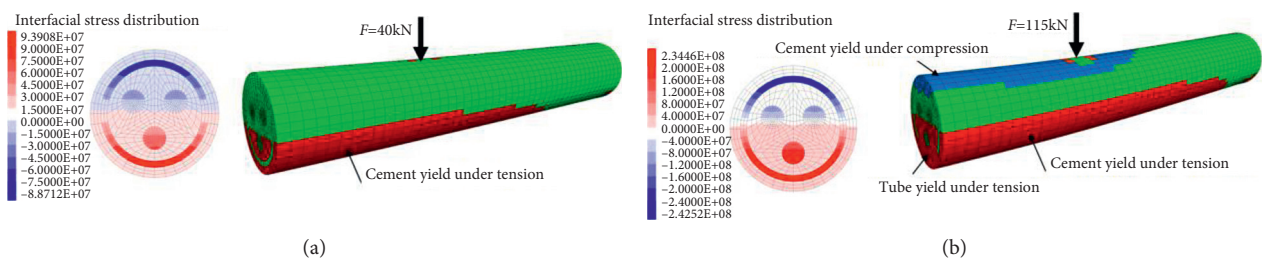

Figure 17: Mechanical states of 200-C micropile. (a) $F = 40$ kN. (b) $F = 115$ kN.

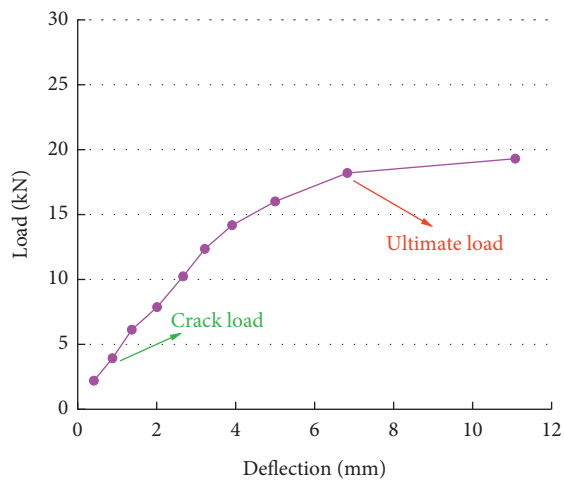

Figure 18: Relationship between load and deflection for 200-C.

Table 3: Flexural capacity for types A-1 and A-2.

The interface morphology	Type (A)	Pile diameter D (mm)	Bar number n	Bar diameter d (mm)	Ultimate flexural capacity M_u (kN·m)
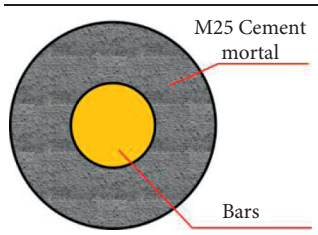	75-1	75	1	32	2.57
				36	3.44
				40	4.50
	100-1	100	1	36	4.07
				40	5.21
				50	9.04
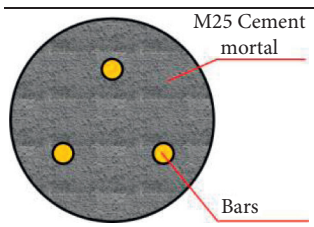	200-3	200	3	36	47.79
				40	53.79
				50	73.55
	300-3	300	3	36	88.14
				40	105.41
				50	150.57

Thereby, the theoretical flexural capacity is close to the numerical validation result and is safer.

5. Summary

According to calculation model formula, ultimate flexural capacity for different commonly used micropiles in engineering is listed in Tables 3 and 4 and Figure 19. In Figure 19, for example, "75 mmA-1φ32 mm" represents the A section form with 75 mm pile diameter and one bar with 32 mm bar diameter.

The ultimate flexural capacity calculated by calculation model formulas can be used as a reference for slope reinforcement design, especially for slope emergency engineering. It can be seen that the first important factor of ultimate flexural capacity for micropile is pile diameter,

Table 4: Capacity for types B and C.

The interface morphology	Type	Pile diameter D (mm)	Tube outer diameter h (mm)	Bar diameter d (mm)	Ultimate flexural capacity M_u (kN.m)
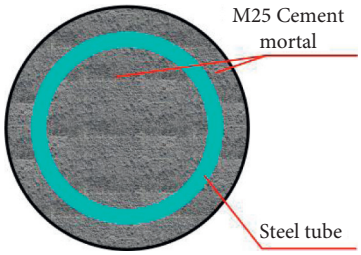	100-B	100	45	—	5.21
			57	—	6.61
			60	—	7.03
			140	—	69.22
			159	—	84.02
	200-B	200	168	—	91.90
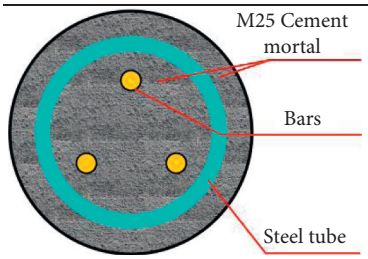	200-C	200	140	25	64.15
			159	32	79.42
			168	36	88.41
			235	40	238.63
			245	45	246.50
	300-C	300	273	50	295.88

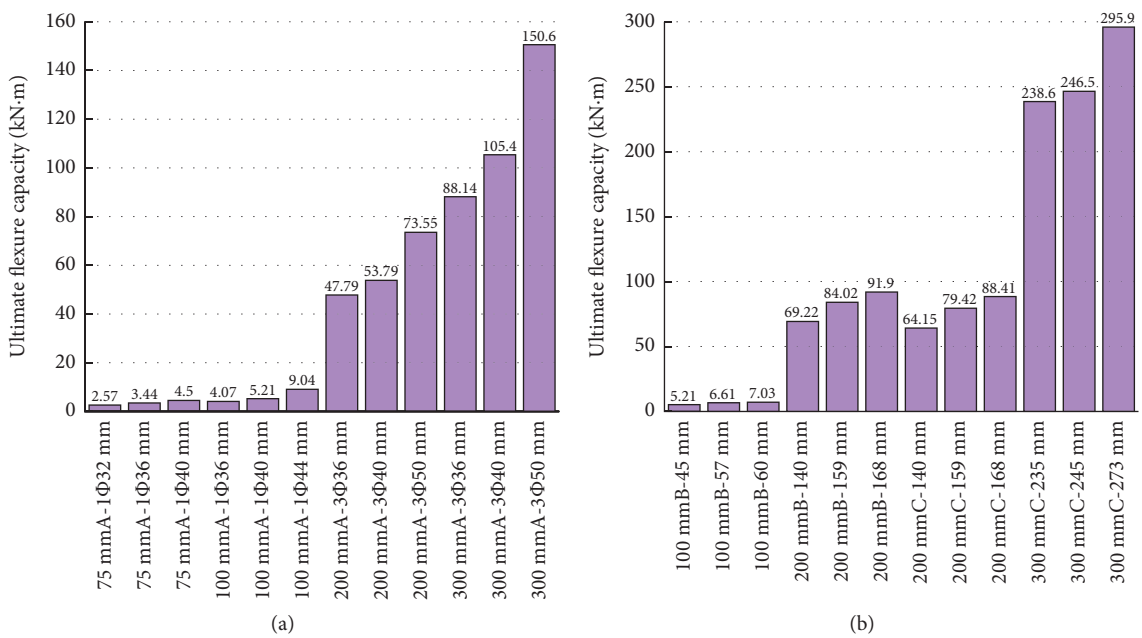

Figure 19: Ultimate flexural capacity of different micropiles calculated by calculation model formula. (a) A-1 and A-3. (b) B and C.

followed by the reinforcement ratio. For example, compared with 100 mmA-1φ36 mm, 200 mmA-3φ36 mm′'s M_u increases by nearly 1000%. Compared with 200 mmA-3φ36 mm, 200 mmA-3φ50 mm′'s M_u increases by nearly 54%. That is why type C has the highest ultimate flexural capacity.

6. Conclusion

The dominated indicator of micropile in slope reinforcement was acquired by numerical simulation in this paper. Various calculation model formulas to calculate the flexural capacity of different types of micropiles were proposed and validated by numerical simulation. The conclusions drawn in this study can be classified as follows:

(1) When the ultimate flexural capacity is reached, the displacement of slope reinforced by micropile will increase rapidly. At the same time, the antiuplift capacity has not been fully played. Flexural capacity is the primary and dominated indicator that needs to be considered in reinforcement design.

(2) The crack load for micropile is easy to be reached because of low tensile strength of cement mortar. The whole micropile tends to reach ultimate flexural capacity when rebar or tube reaches yield limit.

(3) According to the summary of ultimate flexural capacity, it can be seen that M_u for A-1 is very small and it is not suitable for using in reinforcement engineering with large horizontal force.

(4) The first important factor of ultimate flexural capacity for micropile is pile diameter, followed by reinforcement ratio. That is why type C has the highest ultimate flexural capacity.

(5) The calculation results from calculation model formula are close to numerical ones and tends to be safer, so it has application values in micropile selecting and slope reinforcement design, especially for slope emergency engineering.

Data Availability

The data used to support the findings of this study are available from the corresponding author upon request.

Conflicts of Interest

The authors declare that they have no conflicts of interest.

Acknowledgments

This work was supported by Hunan Transportation Science and Technology Project (201501 and 201907), the Natural Science Foundation of Hunan Province, China (2020JJ4156 and 2021JJ50142), and the National Natural Science Foundation of China (51674041 and 51474103).

References

[1] K. T. Chau, C. Y. Shen, and X. Guo, "Nonlinear seismic soil-pile-structure interactions:shaking table tests and FEM analyses," *Soil Dynamics and Earthquake Engineering*, vol. 29, no. 2, pp. 300–310, 2008.

[2] Y. Mascarucci, S. Miliziano, and A. Mandolini, "A numerical approach to estimate shaft friction of bored piles in sands," *Acta Geotechnica*, vol. 9, no. 3, pp. 547–560, 2014.

[3] X. J. Su, "Study on the treatment effect of micro-pile strengthening tunnel creep mountain," *Geotechnical Foundation*, vol. 32, no. 5, pp. 480–483, 2018, in Chinese.

[4] G. S. Ghataora, L. Lee, and U. K. Ling, "Changes in properties of clay surrounding cast in situ piles," *Geotechnical & Geological Engineering*, vol. 29, no. 1, pp. 57–63, 2011.

[5] Z. L. Zong, X. L. Lu, and Q. S. Li, "Comparative test study on compressive and uplift resistance of static pressure steel pipe grouting micro-piles," *Geotechnical Mechanics*, vol. 39, no. S1, pp. 362–368, 2018, in Chinese.

[6] Q. Abbas, W. Choi, G. Kim, I. Kima, and J. Leeb, "Characterizing uplift load capacity of micropiles embedded in soil and rock considering inclined installation conditions," *Computers and Geotechnics*, vol. 132, pp. 1–12, 2021.

[7] H. Seo, M. Prezzi, and R. Salgado, "Instrumented static load test on rock-socketed micropile," *Journal of Geotechnical and Geoenvironmental Engineering*, vol. 139, no. 12, pp. 2037–2047, 2013.

[8] D. A. Bruce, I. Juran, and A. F. Dimillio, "High capacity grouted micropiles:the state of practice in the United States," in *Proceedings of the 15th International Conference on Soil Mechanics and Geotechnical Engineering*, pp. 851–854, Cambridge University Press, Istanbul, Turkey, August 2001.

[9] F. M. Abdrabbo and K. E. Gaaver, "Simplified analysis of laterally loaded pile groups," *Alexandria Engineering Journal*, vol. 51, no. 2, pp. 121–127, 2012.

[10] G. Russo, "A method to compute the non-linear behaviour of piles under horizontal loading," *Soils and Foundations*, vol. 56, no. 1, pp. 33–43, 2016.

[11] D. Kyung and J. Lee, "Uplift load-carrying capacity of single and group micropiles installed with inclined conditions," *Journal of Geotechnical and Geoenvironmental Engineering*, vol. 143, no. 8, pp. 17–31, 2017.

[12] R. Salgado, F. S. Tehrani, and M. Prezzi, "Analysis of laterally loaded pile groups in multilayered elastic soil," *Computers and Geotechnics*, vol. 62, pp. 136–153, 2014.

[13] H. Tahghighi and K. Konagai, "Numerical analysis of nonlinear soil-pile group interaction under lateral loads," *Soil Dynamics and Earthquake Engineering*, vol. 27, no. 5, pp. 463–474, 2007.

[14] N. G. Salisbury and S. A. Davidow, *Current Design and Construction Practices for Micropile Supported Foundations of Electrical Transmission Structures in North America*, pp. 1–7, International Society for Micropiles, PA, USA, 2014.

[15] Z. Chen, L. Mei, and G. X. Mei, "Numerical simulation of lateral bearing capacity of flexible micropile," *Rock and Soil Mechanics*, vol. 32, no. 7, pp. 2219–2224, 2011, in Chinese.

[16] J. Lee, Y. Kim, and S. Jeong, "Three-dimensional analysis of bearing behavior of piled raft on soft clay," *Computers and Geotechnics*, vol. 37, no. 1, pp. 103–114, 2010.

[17] J. Cho, J. H. Lee, S. Jeong, and J. Lee, "The settlement behavior of piled raft in clay soils," *Ocean Engineering*, vol. 53, pp. 153–163, 2012.

[18] A. M. Alnuaim, M. H. El Naggar, and H. El Naggar, "Performance of micropiled rafts in clay: numerical investigation," *Computers and Geotechnics*, vol. 99, pp. 42–54, 2018.

[19] G. M. Álamo, A. E. Martínez-Castro, L. A. Padrón, J. J. .Aznáreza, R. Gallego, and O. Maesoa, "Efficient numerical model for the computation of impedance functions of inclined pile groups in layered soils," *Engineering Structures*, vol. 126, pp. 379–390, 2016.

[20] Standard of the People's Republic of China, "Standard for geological testing method," China Planning Press, Beijing, China, 2019, in Chinese.

[21] Standard of the people's Republic of China, "Standard for Test Method of concrete Structures," China Building Industry Press, Beijing, China, 2012, in Chinese.

Hindawi
Advances in Civil Engineering
Volume 2022, Article ID 3743472, 16 pages
https://doi.org/10.1155/2022/3743472

Research Article

Prediction Method of TBM Tunneling Parameters Based on Bi-GRU-ATT Model

Qinglong Zhang,[1] Boyu Yang,[2] Yanwen Zhu,[1] Chen Guo,[2] Chong Jiao,[2] and Anmin Cai[2]

[1]*Department of Civil Engineering, School of Civil and Resource Engineering, University of Science and Technology Beijing, Beijing 100083, China*
[2]*China Huaneng Clean Energy Research Institute, Beijing 102209, China*

Correspondence should be addressed to Anmin Cai; am_cai@qny.chng.com.cn

Received 17 December 2021; Accepted 27 December 2021; Published 10 February 2022

Academic Editor: Mingfeng Lei

With tunnel boring machines (TBMs) widely used in tunnel construction, the adaptable adjustment of TBM operating status has become a research focus. Since the prediction of tunnel geological conditions is still challenging before excavating, the prediction of important TBM operating parameters plays an important role in the research on TBM adaptable adjustment. This paper proposes an intelligent prediction method of TBM tunneling parameters based on bidirectional gate recurrent unit incorporating attention mechanism (Bi-GRU-ATT) and selects a complete tunneling cycle to predict the tunneling parameters of the TBM complete tunneling cycle. Relying on the TBM3 bid section of Jilin Water Supply Project, 21 key parameters of the complete tunneling cycle are selected as the input features of the model to realize the prediction of four tunneling parameters in the complete driving cycle section of TBM. Compared with the Bi-GRU, GRU, and Long Short-Term Memory (LSTM) models, it can be seen that the Bi-GRU-ATT model has a goodness of fit for predicting TBM tunneling parameters above 0.92, and the average absolute percentage error is less than 1.8%. The results show that the prediction method of TBM tunneling parameters based on Bi-GRU-ATT model proposed in this paper has stronger learning and prediction capabilities. This prediction method provides a more feasible auxiliary intelligent decision-making method for TBM aided intelligent construction.

1. Introduction

Tunnel boring machine (TBM) integrating the functions of excavation, support, slag discharge, and transportation is one of the most advanced types of equipment for a variety of tunnel constructions, e.g., traffic, municipal, water conservancy, water supply, and gas transmission pipelines [1]. TBM has gradually replaced the traditional blasting excavation in various tunnel projects due to its high efficiency, safety, and environmental protection [2]. However, the adaptability of TBM is often limited by complex geological conditions, the poor matching of tunneling parameters and rock mass state parameters, and the high requirements on the experience of construction personnel, making it difficult to effectively solve the prediction of TBM tunneling parameters [3, 4]. Therefore, correct evaluation and prediction of TBM tunneling parameters are important issues in efficient tunnel excavation, which is of great significance for ensuring the safety and efficient construction of TBM.

In recent years, scholars have conducted a lot of research on the prediction of TBM tunneling parameters [5–7] and have achieved certain results. At present, TBM tunneling parameter prediction methods are mainly summarized into empirical formula method (combined with experiment) [8], theoretical analysis method [9], numerical simulation method [10], and machine learning method [11]. In the early empirical method research, Krause [12–14] proposed an empirical model for TBM load prediction, which is of great significance to TBM load calculation. Avunduk and Copur [15] divided the tunnel alignment into three general sections according to geological and geotechnical conditions and proposed an empirical performance prediction model for Earth pressure

balance (EPB) TBM. Ates et al. [6] recommended empirical models for predicting torque, thrust, and other design parameters. With the continuous improvement of test equipment, multifactor prediction models represented by the Norwegian University of Science and Technology (NTNU) model [16, 17] have been widely used. In addition to the above empirical methods, many scholars have also made some research progress in theoretical analysis methods. The Colorado School of Mines (CSM) has developed a well-known theoretical model [18], which analyzes the cutting force estimated through full-scale laboratory cutting tests, so that the maximum PR can be determined by theoretical derivation. Based on this, a number of scholars [19–22] extended the theoretical prediction models. In addition, some scholars predict tunneling performance based on numerical simulation methods. Kasper and Meschke [23] conducted a numerical sensitivity study to analyze the influence of TBM operating parameters and design parameters. Afrasiabi et al. [24] used numerical simulation to study the influence of different factors on TBM tunneling performance. The above studies have proved that the three methods have a certain guiding effect on the prediction of TBM tunneling parameters, but there are still great limitations when facing the complex problems related to TBM tunnels. The empirical formula method can only provide a series of TBM parameter values and cannot sensitively capture the small changes, so its applicability is extremely limited; the theoretical analysis method cannot explain the complex and changeable geology conditions in the various rock types encountered during tunnel construction; the numerical simulation method can only provide the value range of the load parameters, and the calculation is time-consuming, so it cannot provide real-time and effective guidance for the actual construction.

With the development of artificial intelligence technology [25, 26], several scholars use machine learning algorithms to analyze complex data problems generated in actual engineering and gradually introduce machine learning algorithms into the research of TBM tunneling parameter prediction. Zhou et al. [27] proposed a support vector machine (SVM) model based on particle swarm optimization (PSO) to predict the energy consumption of shield tunnels. Zhang [28] applied the extreme gradient lifting method to predict the ground settlement caused by the excavation of the EPB shield. In addition. Sun et al. [29] used the random forest to achieve TBM load prediction. Yang et al. [30] utilized support vector regression (SVR) to predict the PR of TBM and took a tunnel in China as an example to study the parameters affecting TBM performance. Wang et al. [31] established a model based on the XGBoost algorithm to implement TBM intelligent decision-making. Although machine learning methods can effectively predict TBM tunneling parameters, they cannot consider the time variation characteristics and temporal correlations between TBM tunneling data. For example, the output of SVR or random forest is determined only by the current input without resorting to the network status at the previous moment, and they cannot fully utilize the real-time parameters of TBM tunneling. Therefore, they cannot realize the real-time analysis of TBM tunnels.

To solve this problem, deep learning methods such as recurrent neural networks (RNN) [32] have been developed to model the time series data in the TBM tunnel. Compared with traditional machine learning methods, deep learning is more suitable for learning complex models from high-dimensional data. RNN is a kind of neural network that uses the sequence propagation method to process sequence data. Gao et al. [33] compared and analyzed the effects of different deep learning methods on real-time prediction of TBM tunneling parameters, and the results showed that as an improvement of the RNN network, the recurrent neural network algorithms with gate operations (such as long-short term memory (LSTM) [34] and gate recurrent unit (GRU) [35]) can well solve the problems of gradient explosion and gradient disappearance in RNN networks, and the prediction effect is better than that of the traditional RNN algorithms. However, the GRU network and the LSTM network only consider the association between the sequences in one direction and do not consider the two-way nature of information dissemination, and there are great limitations in dealing with the problem of sequence data with strong correlation before and after. In addition, if the input information is too long, the fixed-length feature vector of the neural network cannot fully store all the context information, which will cause part of the information to be lost or early historical information to be overwritten. To this end, this paper improves its network structure and propagation method and optimizes the model based on the self-attention mechanism, so that the model learns the weight distribution of input information by itself and improves its feature extraction efficiency and learning ability for long-sequence data. Based on this, an intelligent prediction method based on Bi-GRU-ATT integrated with an attention mechanism to solve this problem is proposed.

This paper divides the data set based on the TBM3 bid section of the Jilin Water Supply Project and selects the complete tunneling cycle section data to realize the parameter prediction of the complete tunneling cycle section. Using Pearson correlation analysis, twenty-one parameters with the highest correlation with the predicted parameters are selected as the input characteristics of the model from 199-dimensional tunneling parameters of the complete tunneling cycle section. The data is processed by constructing a binary state discriminant function, eliminating nonworking state and abnormal data, the complete tunneling cycle is extracted, and then the Adam optimizer is used to train the model. The comparative analysis of the Bi-GRU model, unidirectional LSTM model, and unidirectional GRU model verifies the accuracy and effectiveness of the Bi-GRU-ATT model in this paper, which has certain guiding significance for TBM intelligent construction.

2. Recurrent Neural Network

2.1. Bidirectional Gate Recurrent Unit. Gated Recurrent Unit (GRU), as an improvement of Recurrent Neural Network (RNN), introduces a special gating mechanism to control the retention and forgetting of information, which can effectively deal with the disappearance and/or explosion of

gradients in variable-length sequences, wait for long-term dependence on the problem, and fall into the problem of local optimal solutions. However, the GRU network can only propagate along the sequence in one direction. When calculating the output of the target vector, the subsequent time information cannot be used. The two-way nature of information propagation is not considered. There is a relatively major limitation in dealing with the sequence data with strong correlation before and after processing.

To solve the above problems, some scholars have improved the propagation mode of the GRU network and proposed a bidirectional GRU network. As shown in Figure 1, the Bi-GRU neural network adds a backpropagation layer to the GRU network structure to control forward and backward output, respectively, thereby improving the accuracy of information classification and realizing two-way processing of context information. The forward propagation layer calculates the sequence information at the current moment from front to back, and the backpropagation layer calculates the same sequence information from back to forward. The two network layers are connected to an output layer. The forward sequence and the reverse sequence are calculated in parallel, and the output result of the target vector is obtained by synthesizing the output of the forward and reverse sequence.

As shown in Figure 1, the structure contains two parallel layers, namely, a forward propagation layer and a backpropagation layer. Each layer is an independent GRU structure. The two structures are symmetrical, and the direction of information transmission is opposite. The input layer information propagates from front to back along the forward sequence, and the reverse sequence is calculated from back to front at the same time. The two are calculated independently and do not interfere with each other. Finally, the output values of the output layer are obtained by synthesizing the output values of the forward and reverse sequence. The calculation equation [36] is as follows:

$$h_t' = f\left(w_1 x_t + w_3 h_t' + b_t'\right), \tag{1}$$

$$h_t = f\left(w_2 x_t + w_4 h_{t-1} + b_t\right), \tag{2}$$

$$H_t = h_t' \oplus h_t. \tag{3}$$

The forward sequence and the reverse sequence are calculated by equations (1) and (2), respectively, and finally, the output of the output layer is obtained by equation (3). Among them, h_t' represents the state of the forward propagation hidden layer at time t; h_t represents the state of the hidden layer backpropagation at time t; H_t represents the output value; x_t represents the input value; $\oplus$ represents the vector stitching operation; w_1, w_2, w_3, and w_4 represent the weights to propagate along with the time series.

2.2. Self-Attention Mechanism. In the process of TBM tunneling parameter prediction, the influence of each parameter on the prediction results is different. By analyzing and identifying the importance of each sequence data, the model complexity and prediction performance are optimized. In this paper, the self-attention mechanism layer is introduced to

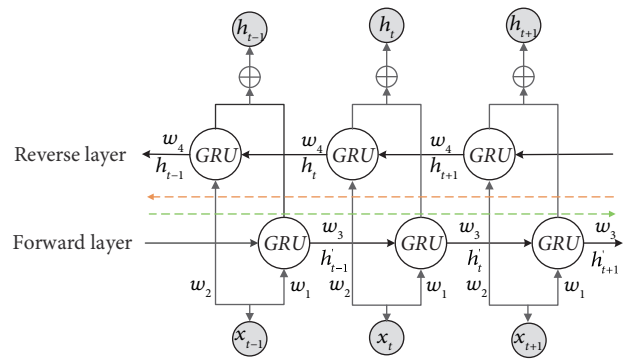

Figure 1: Bi-GRU network structure diagram.

redistribute the weight of the output vector processed by Bi-GRU. Attention mechanism originates from the research in the field of human vision. It can be understood as an encoding-encoding structure in essence. It is manifested in that this mechanism imitates the sequential information processing method of the human brain, which only focuses on key details and ignores unnecessary information when dealing with complex external information. This method can effectively avoid the waste of feature information caused by the direct transmission of the output vector of the Bi-GRU layer to the fully connected layer and indirectly improve the ability of the model to capture key information and improve the prediction efficiency of the model.

The self-attention mechanism is an improvement of the traditional attention mechanism, which reduces the dependence on external information and is better at capturing the internal correlation of data information. The core of this mechanism is the introduction of weight coefficients. By taking the hidden state set of all time steps in the Bi-GRU layer as the model input, the attention vector c is output, which is mainly divided into two calculation processes: weight calculation and weighted summation. The weight calculation equation [37] is as follows:

$$\begin{aligned} e_t &= \tanh\left(\omega x_t + b\right), \\ a_t &= \frac{\exp\left(e_t A\right)}{\sum_{k=1}^{K} \exp\left(e_t A\right)}, \end{aligned} \tag{4}$$

where a_t represents the probability of attention distribution; x_t represents the output vector of the Bi-GRU layer; $e_t A$ represents the unnormalized attention score. The higher the attention score, the higher the matching degree between the input vector and the target vector; ω, A and b represent the weight matrix and bias of the attention model, respectively.

According to the attention distribution a_t, the input vector of the attention layer is weighted and summed to obtain the output vector c of the attention model [37]:

$$c = \sum_{k=1}^{K} a_t x_t. \tag{5}$$

2.3. Bi-GRU Network with Self-Attention Mechanism. Figure 2 shows the development framework of the hybrid model. The framework module includes configuration

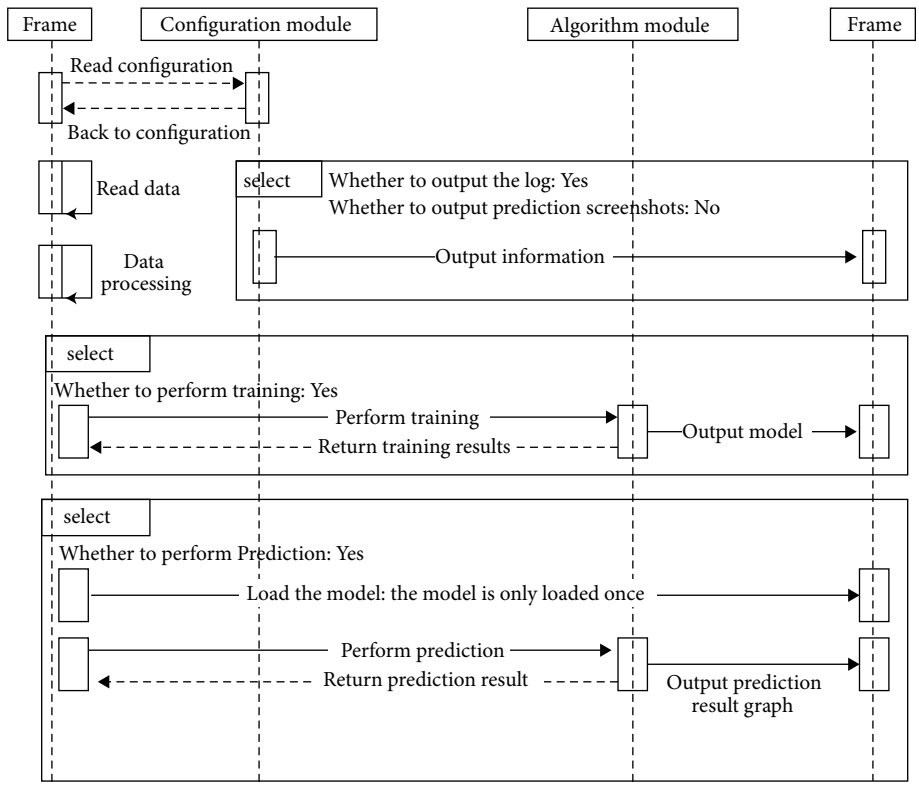

Figure 2: Bi-GRU-ATT model development framework diagram.

module, data processing module, and algorithm module, and the operation and modification of each module will not affect each other. First, read the algorithm type and algorithm parameters from the configuration module to determine the algorithm required by the model. This module does not need to modify the main frame, classify the external data, and store the training data in the specified directory according to the preprocessing method; according to the data source and different training methods and algorithms, save the training model to the automatically generated path, load the training model to execute prediction instructions, output the prediction result curve, and export the corresponding log file.

3. Model Establishment

3.1. Feature Selection. The construction conditions in the process of TBM tunneling are usually complex, often accompanied by a variety of uncertain factors that affect the prediction accuracy of TBM tunneling parameters. Therefore, it is necessary to analyze and extract the TBM tunneling parameter prediction model based on Bi-GRU. The TBM operating data contains 199-dimensional tunneling parameters, but some of them are greatly affected by human factors and have a poor linear correlation. Therefore, this paper only selects four indexes of the TBM complete excavation cycle section, namely, total thrust, penetration, cutterhead torque, and cutterhead power, as the output characteristics of the model.

The selection of input features is also of great significance to the prediction performance of the model, which can better reflect the operating status of the model under different working conditions and improve the prediction accuracy. Therefore, this paper uses Pearson correlation analysis to identify the 199-dimensional tunneling parameters of the complete tunneling cycle input by the model, eliminates irrelevant parameter variables, and selects key model parameters. The Pearson correlation coefficient is calculated as follows:

$$\eta = \frac{\sum_{i=1}^{n}\left(X_i - \overline{X}\right)\left(Y_i - \overline{Y}\right)}{\sqrt{\sum_{i=1}^{n}\left(X_i - \overline{X}\right)^2}\sqrt{\sum_{i=1}^{n}\left(Y_i - \overline{Y}\right)^2}}, \tag{6}$$

where $\overline{X}$ is the average value of the data sample X; $\overline{Y}$ is the average value of the data sample Y.

The Bi-GRU-based TBM tunneling parameter prediction model constructed in this paper uses the complete tunneling cycle data to predict the four parameters of the TBM complete excavation cycle section, namely, total thrust, penetration, cutterhead torque, and cutterhead power. According to the correlation analysis results, the 199-dimensional tunneling parameters of the complete tunneling cycle are sorted, and the 21 key parameters with the highest correlation with a certain TBM tunneling parameter to be predicted are extracted as the input features of the model, to improve the prediction accuracy of the model. The identification result of the input features of the model is shown in Figure 3.

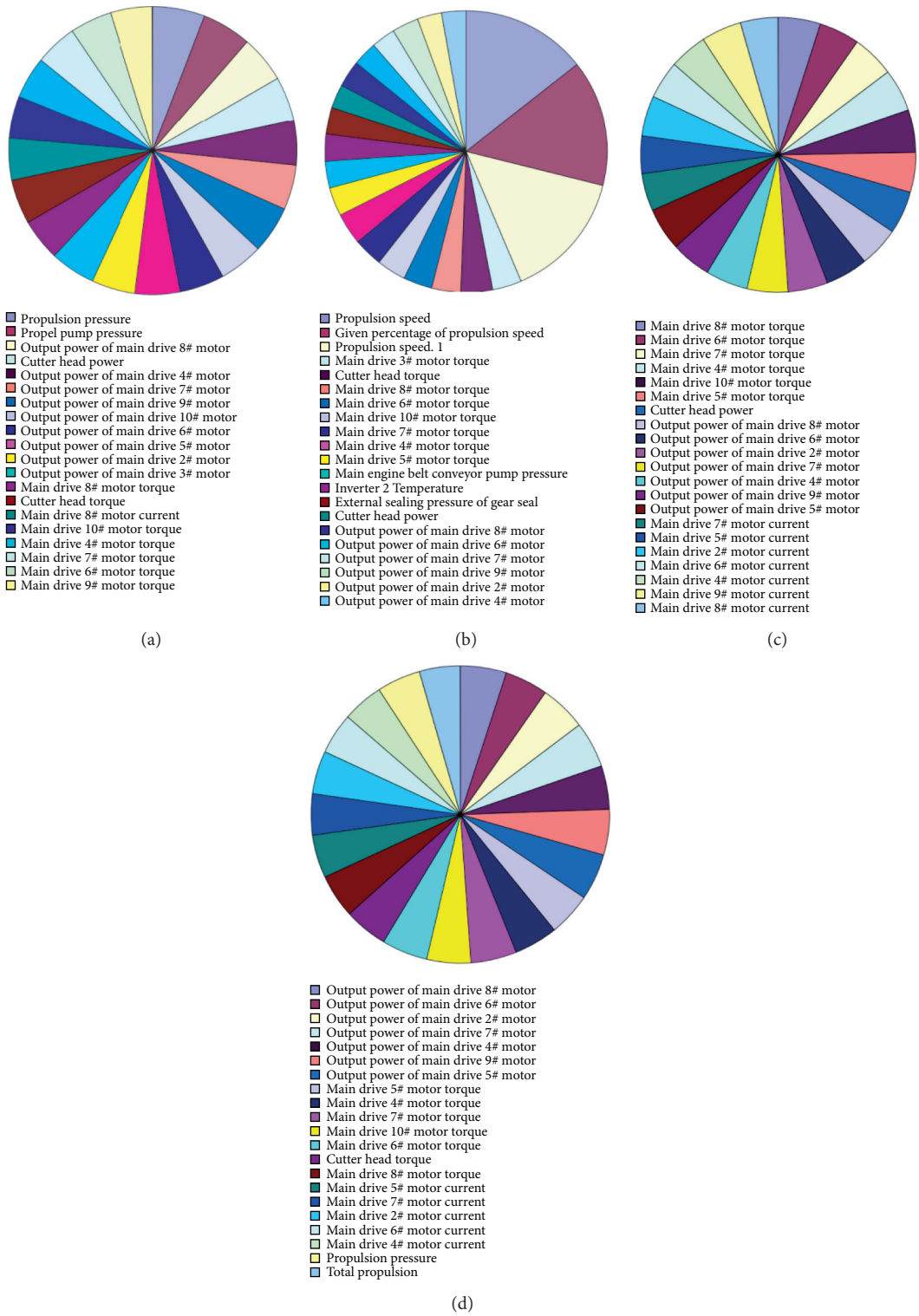

Figure 3: Identification results of input features of Bi-GRU model. (a) Model identification result of total thrust. (b) Model identification result of penetration. (c) Model identification result of cutterhead torque. (d) Model identification result of cutterhead power.

3.2. Multipart Figures. In this paper, the attention mechanism is used as a layer of the Bi-GRU model to learn the output of the model in a serial manner, giving full play to the important local feature extraction capabilities of the attention model and the sequential feature processing capabilities of the Bi-GRU model. The intelligent prediction model of TBM tunneling parameters based on Bi-GRU constructed in this paper is shown in Figure 4, which is mainly composed of five parts: input layer, Bi-GRU layer, attention mechanism, fully connected layer, and output layer.

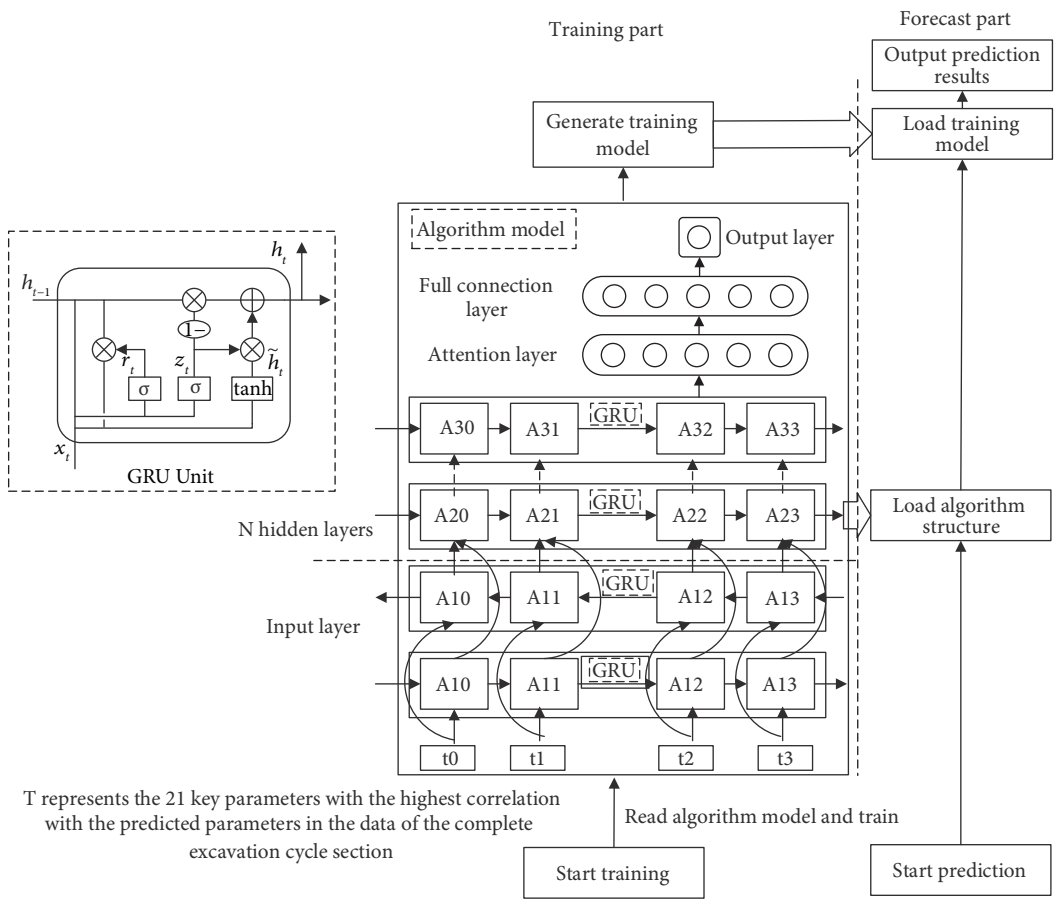

Figure 4: TBM tunneling parameter prediction model based on Bi-GRU-ATT.

(1) Input layer. After the original data is preprocessed by Pearson correlation analysis method, triple standard deviation method, and other data processing techniques, 21 key parameters with the highest correlation with the prediction parameters are selected as the input vector of the model and input to the Bi-GRU layer according to the Pearson correlation analysis results.

(2) Bi-GRU layer. Input the input vector to the forward propagation GRU layer and the backpropagation GRU layer, respectively. The two parallel layers mainly characterize the correlation between sequence data and generalize the input of each layer. By updating the gate to control the extent to which the state information at the previous moment is brought into the current state, the input features are trained along the forward sequence and the reverse sequence, respectively, and the training vectors of the forward and reverse sequences are synthesized to obtain the output vector of the Bi-GRU layer.

(3) Attention mechanism and fully connected layer. The attention layer performs weighting operations on the output vector processed by Bi-GRU, then outputs it to the fully connected layer, and maps the distributed features to the sample label space.

(4) Output layer. Output predicted values, namely, total thrust, penetration, cutterhead torque, and cutterhead power in the complete driving cycle section of TBM.

The specific algorithm flow of the Bi-GRU-ATT prediction model is as follows: first, the data set is divided into a training set and a test set at a ratio of 17 : 1. The training set is used to train the model and optimize the model parameters; the test set is used to predict the TBM tunneling parameters; the 21 key parameters with the highest correlation in the data of the complete tunneling cycle section are selected as the input of the input layer, and the basic structure and hyperparameters of the Bi-GRU-ATT model are set, including time step and iteration times. Adam optimizer is used to train the network model, and the mean square error (MSE) function is used as the loss function to automatically adjust model weights, iteratively optimize model parameters, generate and load model files, and output model prediction results. Finally, an appropriate evaluation function is selected to evaluate the prediction effect of the model and to verify the prediction performance of the model in this paper.

4. Engineering Data Set

4.1. Project Overview. The TBM3 bid section of the Jilin Water Supply Project is the control bid section with the longest single construction section, the most unexpected geological disasters, and the most difficult construction in the entire central water diversion project in Jilin Province. It is located between Chalu River and Wende River in Yongji County, Jilin City, with a total length of 22.955 km. Tunnel excavation is mainly based on full-face TBM construction, of which the TBM construction section is 20.198 km long. The stratigraphic lithology involved in this section can be roughly divided into limestone and granite, which are mainly distributed between grades II and V. According to the statistics of geological data, the proportion of the surrounding rock grade (grades II to V) of the construction section is 5.9%, 66.13%, 23.72%, and 4.25%, respectively; the distribution ratio of limestone area to granite area is 1.58 : 1. As shown in Figure 5(a), the proportions of four types of the surrounding rock grade in limestone are 5.19%, 66.70%, 22.83%, and 5.28%, respectively. Figure 5(b) shows that the proportions of the surrounding rock grade in granite are 7.03%, 65.23%, 25.14%, and 2.6%.

The data in this paper are selected from a construction section in the TBM3 bid section, with a total length of 7.5 km. TBM operating data are collected in second, and 86400 pieces of data are collected in a day, including 199-dimensional tunneling parameters such as total thrust, penetration, cutterhead torque, and cutterhead power. In this project, TBM construction usually divides the tunneling cycle according to the cylinder stroke, with about 10 ~ 20 tunneling cycles per day. Among them, the variation curve of TBM tunneling parameters on a certain day is shown in Figure 6.

4.2. Tunneling Cycle Extraction. It can be seen from Figure 6 that TBM is not always in the working state, and there is a huge amount of shutdown section data that cannot be used for machine learning between each tunneling cycle. Therefore, it is necessary to determine the working state of TBM at each time by constructing a binary state function to extract the complete tunneling cycle data. The judgment formula [38] is as follows:

$$I = f(N)f(F)f(T)f(V),$$
$$f(x) = \begin{cases} 1, x \neq 0 \\ 0, x = 0 \end{cases}, \tag{7}$$

where N is the speed of the cutter head; F is the total thrust; T is the cutterhead torque; V is the propulsion speed; I is the state discrimination function.

When $I = 1$, it is determined that the TBM is in the tunneling state, and when = 0, it is judged that TBM is in the shutdown state. According to the judgment results of the TBM working status at each time, valid data samples are extracted. Each group of continuous tunneling sequences corresponds to a complete tunneling cycle, and the data between adjacent tunneling cycles corresponds to a set of shutdown data. As shown in Figure 7, the TBM tunneling process can be divided into an ascending section and a complete tunneling cycle.

In the traditional TBM tunneling process, the operator generally predicts the parameters of the complete tunneling cycle according to the data change law of the ascending section [39]. Due to the complexity of the TBM tunneling construction environment, the driver needs to spend a lot of time identifying and extracting the ascending section data to adjust the TBM operating state, and the effective tunneling efficiency is low. To ensure safe and efficient tunneling of TBM, reduce redundant operations during the driver's operation, and optimize and adjust the current tunneling parameters, this paper selects the data of the complete tunneling cycle section to predict the four tunneling parameters, namely, the total thrust, penetration, cutterhead torque, and cutterhead power in the complete driving cycle section of TBM. Figure 8 shows the comparison between the traditional ascending segment prediction method and the full-period prediction method.

4.3. Data Processing. Due to a large amount of invalid data in the field engineering data, it is necessary to preprocess the original data in the database to extract valid data samples. First, it is necessary to identify and read the original data in the database, including the total thrust, cutterhead torque, and other tunneling parameters, and judge the data. Take the total thrust as an example; the first non-zero data of the total thrust in the input original data needs to be found and marked as P1, and then the second data with zero of the total thrust is found and marked as P2. Subsequently, it needs to be analyzed and judged whether the number of rows between data P1 and data P2 is within the range of [500 s, 5000 s]. If so, the data will be discarded; otherwise, the data will be output to the specified file, and each file can have a maximum of 300 cycles. According to this method, all the data are read successively until all the effective data are extracted, and the data processing process is completed. The specific data processing flow is shown in Figure 9.

In the process of data processing, affected by the construction environment, construction equipment, and construction experience of construction personnel during the TBM tunneling process, there are many abnormal values in the original data, which affect the prediction effect of the model. To eliminate the above-mentioned abnormal working data, the original data was processed by the triple standard deviation method. Taking the four parameters to be predicted in this paper as an example, it is necessary to calculate the mean μ and standard deviation σ of the four tunneling parameters in the entire tunneling progress. Then, it is judged whether the distance between the parameter value and the mean value is greater than $\mu + 3\sigma$; if it is greater, it is regarded as an abnormal value and replaced by the average value of 5 data points near the abnormal value.

$$X - \mu \geq = 3\sigma, \tag{8}$$

where X represents the predicted data sample; μ represents the sample mean; σ represents the sample standard deviation.

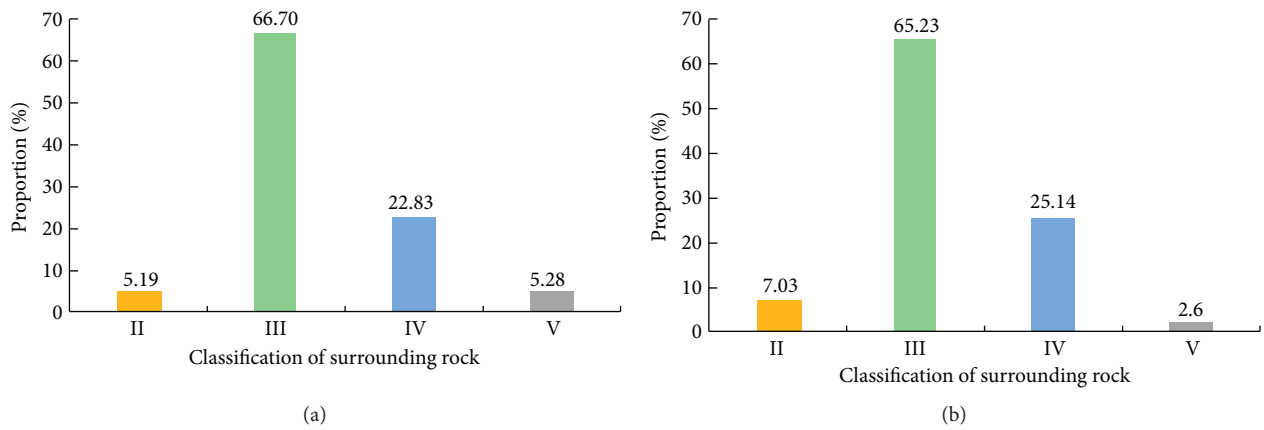

Figure 5: Engineering geological conditions. (a) Limestone classification statistics. (b) Granite classification statistics.

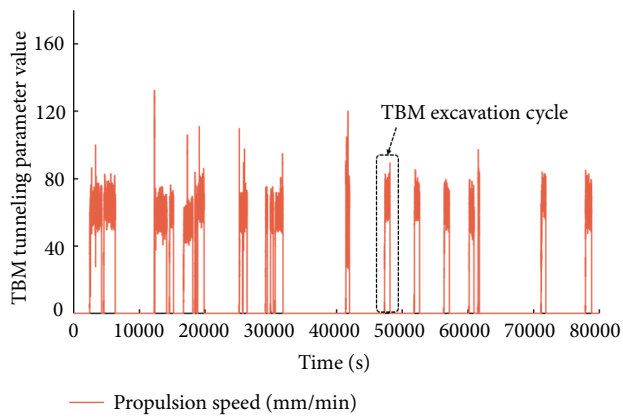

Figure 6: Variation curve of TBM tunneling parameters on a certain day.

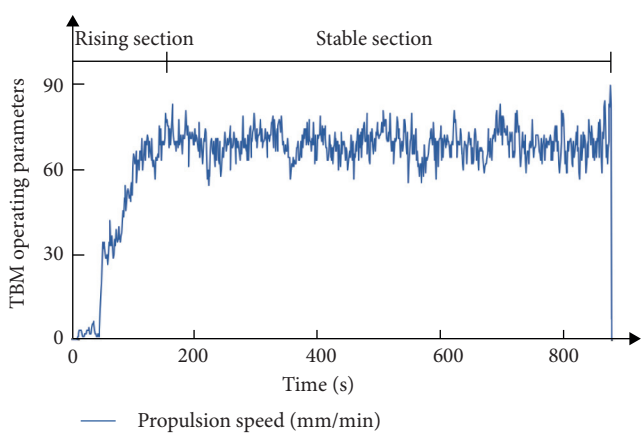

Figure 7: A complete tunneling cycle in TBM construction.

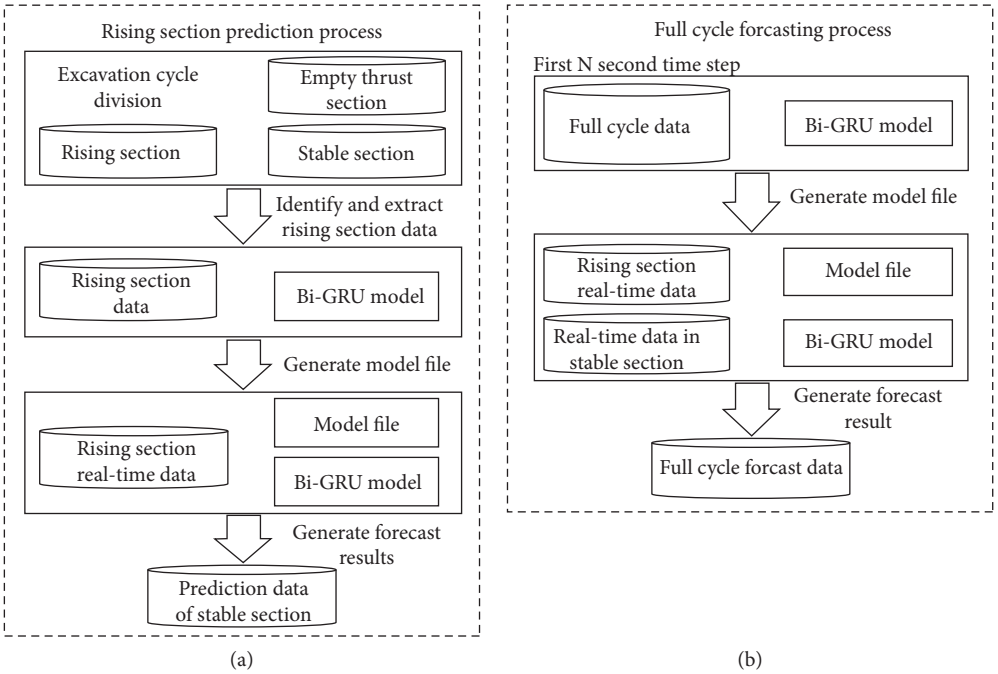

Figure 8: Comparison of complete tunneling cycle and ascending section. (a) Ascending segment prediction. (b) Full-period prediction.

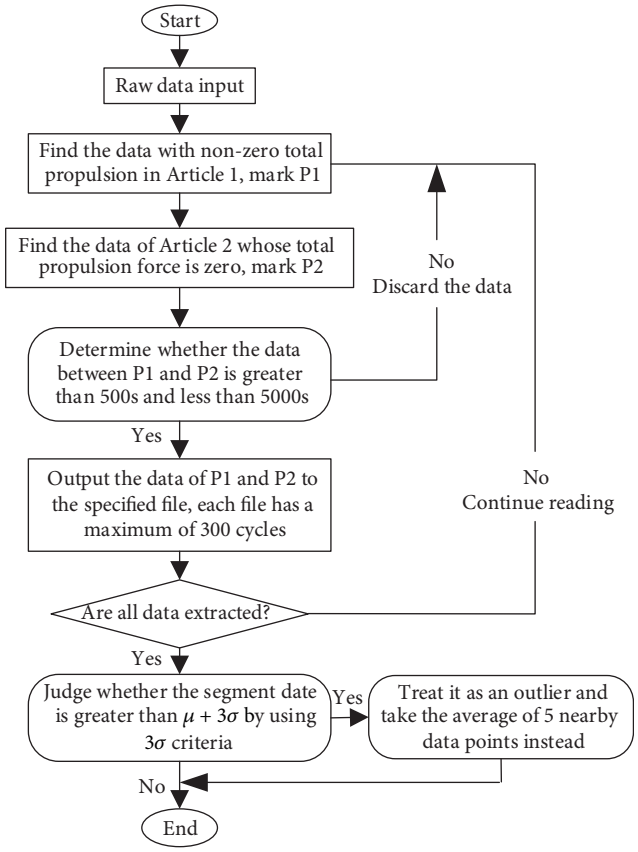

Figure 9: Data processing flowchart.

In addition, to eliminate the influence of dimensional differences in the data, the data samples need to be normalized before model training [40]:

$$x^* = \frac{x - x_{\min}}{x_{\max} - x_{\min}}, \tag{9}$$

where x^* represents the normalized data; $x_{\max}$ and $x_{\min}$ represent the maximum and minimum value of the data, respectively.

5. Model Application and Comparison

5.1. Model Evaluation Index. In order to verify the prediction effect of the model, four evaluation indexes commonly used in regression analysis are used to quantify the estimation error of the model, namely, mean absolute percentage error (MAPE), goodness of fit (R^2), mean absolute error (MAE), and root-mean-square error (RMSE), and the calculation formula is as follows:

$$\begin{aligned} \mathrm{MAPE} &= \frac{1}{n}\sum_{i=1}^{n}\frac{\left|y_i^* - y_i\right|}{y_i}, \\ R^2 &= 1 - \sqrt{\frac{\sum_{i-1}^{n}\left(y_i - y_i^*\right)^2}{\sum_{i=1}^{n} y_i^2}}, \\ \mathrm{MAE} &= \frac{1}{n}\sum_{i=1}^{n}\left|y_i^* - y_i\right| \mathrm{RMSE} = \sqrt{\frac{1}{n}\sum_{i=1}^{n}\left(y_i^* - y_i\right)^2}, \end{aligned} \tag{10}$$

where y_i is the true value; y_i^* is the predicted value of the model; i is the sample number; n is the total number of samples in the test set.

5.2. Model Application. According to the results of data processing, the nonworking status and abnormal data are eliminated, and the parameters of the complete tunneling section are averaged to obtain the data set for modeling. To improve the training model to learn the data operation law, improve the generalization ability of the model, and prevent the model from overfitting, it is necessary to increase the model training sample. Therefore, the sample set and the test sample set are divided into training according to 17 : 1. The total number of samples is 9900, and the number of training samples and the number of test samples are 9350 and 550, respectively. The training samples are used to train the model and optimize the model parameters; the test samples are used for prediction, and an appropriate evaluation function is selected to verify the prediction effect of the model. The 21 key parameters in the complete tunneling cycle that has the highest correlation with a certain tunneling parameter to be predicted are selected as the input parameters of the Bi-GRU-ATT model. The four key parameters, namely, the total thrust, penetration, cutterhead torque, and cutterhead power, are tested and verified. Figure 10 shows the prediction results of the stable section in the complete excavation cycle section of the selected Bi-GRU-ATT model with four excavation parameters.

It can be seen from the comparison curve between the predicted value and the measured value in Figure 10 that the predicted values of the four TBM tunneling parameters are in good agreement with the measured values, and the change of the predicted value curve is less than that of the measured value curve, indicating that this model can better predict the tunneling parameters of TBM complete tunneling cycle. To evaluate the prediction accuracy of the network model, it is necessary to analyze and predict the goodness of fit R^2 and MAPE of the four tunneling parameters. By calculating the prediction samples, it can be seen from Table 1 that the MAPE of each parameter is within 1.8%, and the goodness of fit R^2 is also above 0.92, which shows that the prediction model has good network generalization promotion ability and prediction accuracy and has certain guiding significance for the judgment of TBM tunneling state and the optimization and adjustment of parameters.

5.3. Model Comparison. A set of data samples are used to test the performance of Bi-GRU, GRU, and LSTM, and their errors are compared and analyzed. Figures 11–13 are the prediction result curves of the stable section in the complete excavation cycle section of the selected three models. It can be seen from the prediction results that the overall trend of the predicted value change curve and the actual measured value change curve in Bi-GRU, GRU, and LSTM models is the same, but there will be a large deviation from the actual measured value in some samples. Among them, the prediction of total thrust and penetration is in good agreement with the actual measurement results; the prediction of cutterhead torque and cutterhead power is relatively low in agreement with the actual measurement results.

For the sake of quantitatively analyzing and comparing the prediction performance of the four models, MAPE and the goodness of fit R^2 are used as the evaluation indexes to measure the prediction accuracy of the model. The comparison of prediction results of different models is shown in Table 2. The prediction accuracy of the four models for TBM tunneling parameters is Bi-GRU-ATT, Bi-GRU, GRU, and LSTM from high to low.

It can be seen from the comparison in Table 2 that the bidirectional cyclic neural network is better than the unidirectional cyclic neural network with the same structure; that is, the Bi-GRU network is better than the GRU network. As a cyclic neural network, GRU neural network has memory capabilities and can effectively process input data with time series characteristics, thereby accurately predicting the tunneling parameters of the complete tunneling cycle. The Bi-GRU neural network is equivalent to adding a backpropagation layer on the basis of the GRU neural network, which controls the forward and backward output, respectively, making full use of the time sequence information before and after the sample data, and reducing the error.

It can be seen from Table 2 that the Bi-GRU-ATT model has achieved the best prediction effect, with a

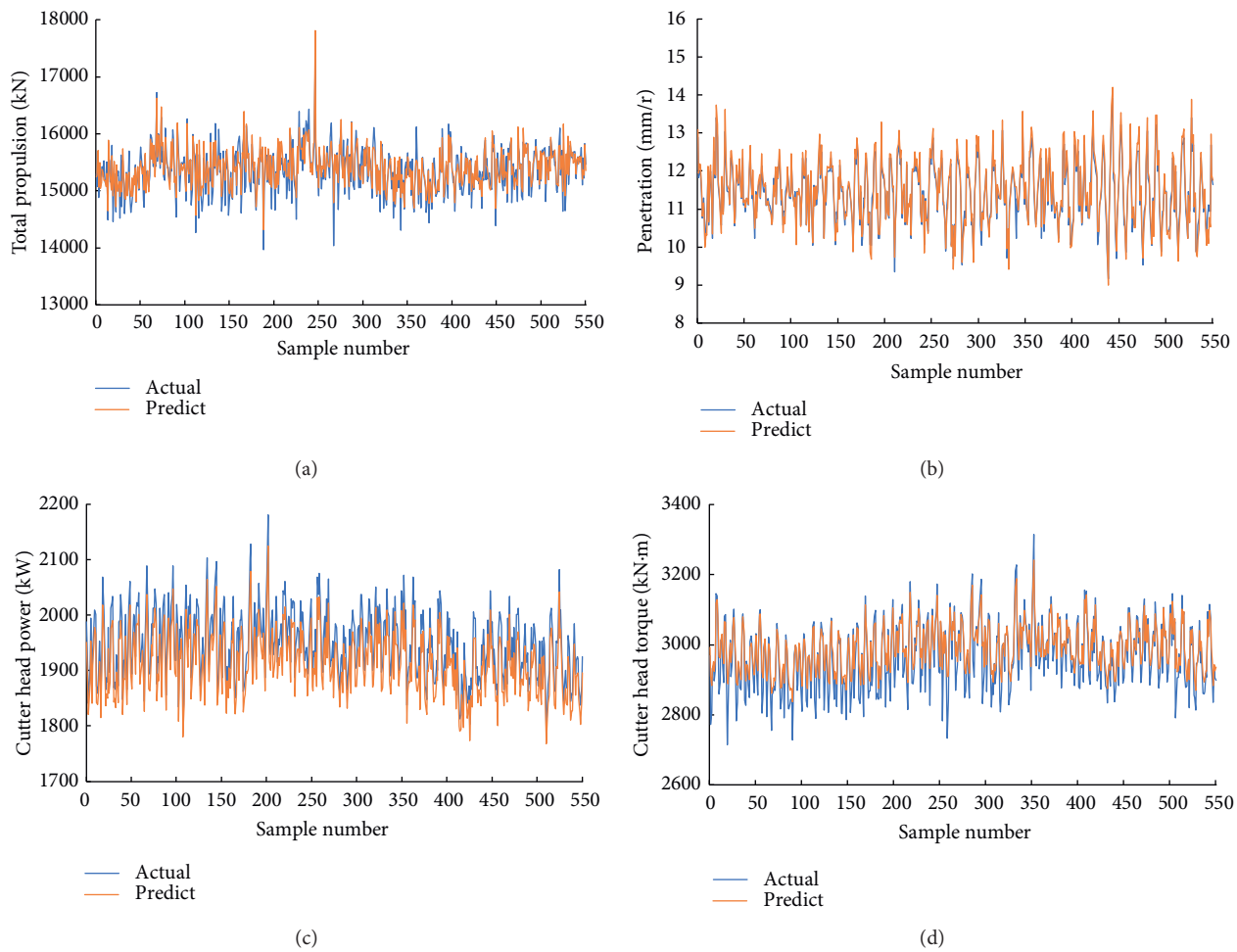

Figure 10: Prediction results of Bi-GRU-ATT model. (a) Prediction results of total thrust F. (b) Prediction results of penetration e. (c) Prediction results of cutterhead power P. (d) Prediction results of cutterhead torque T.

Table 1: Evaluation indexes of prediction results of Bi-GRU-ATT model.

Model	Parameter	MAPE (%)	R^2	MAE	RMSE
Bi-GRU-ATT	Total thrust	1.01	0.925	151.52	193.62
	Penetration	1.60	0.930	0.15	0.20
	Cutterhead torque	1.40	0.936	31.30	44.44
	Cutterhead power	1.71	0.944	34.13	34.75

goodness of fit R^2 of up to 0.944, and the minimum MAPE is 1.01%. Compared with the Bi-GRU model without attention mechanism, the highest goodness of fit R^2 is improved by up to 0.06. This shows that when the attention mechanism is added to the model, the prediction accuracy will be improved to a certain extent, which verifies the excellent performance of the attention mechanism in the TBM tunneling parameters. In addition, the prediction accuracy of unidirectional GRU is similar to that of unidirectional LSTM, but unidirectional GRU is better than unidirectional LSTM. The reason is that the unidirectional GRU only has two gate control structures, the update gate and the reset gate, which not only make its output faster than LSTM and have better performance, but also can effectively avoid the overfitting phenomenon of the model in non-high-dimensional prediction tasks.

To sum up, the Bi-GRU-ATT intelligent prediction model established in this paper has stronger learning and prediction capabilities than the other three recurrent neural network prediction models and provides a more feasible auxiliary intelligent decision-making method for TBM safe and efficient tunneling construction.

5.4. Engineering Application Effect Analysis. In the traditional TBM tunneling construction, the selection of tunneling parameters basically relies on human experience to make judgments and adjustments. The matching of tunneling parameters and rock mass state parameters is poor. Once complicated geological conditions are encountered, it is

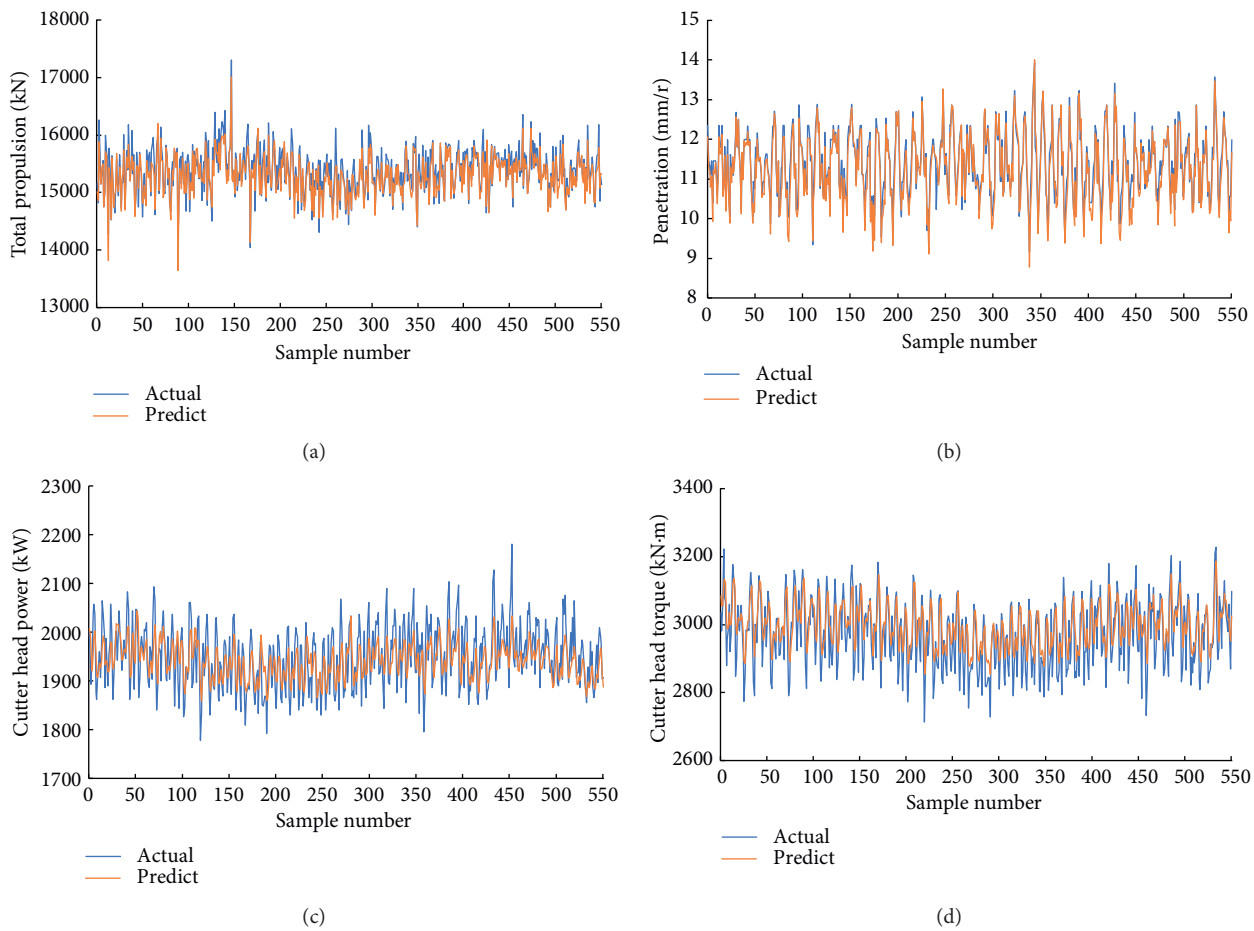

Figure 11: Prediction results of Bi-GRU model. (a) Prediction results of total thrust F. (b) Prediction results of penetration e. (c) Prediction results of cutterhead power P. (d) Prediction results of cutterhead torque T.

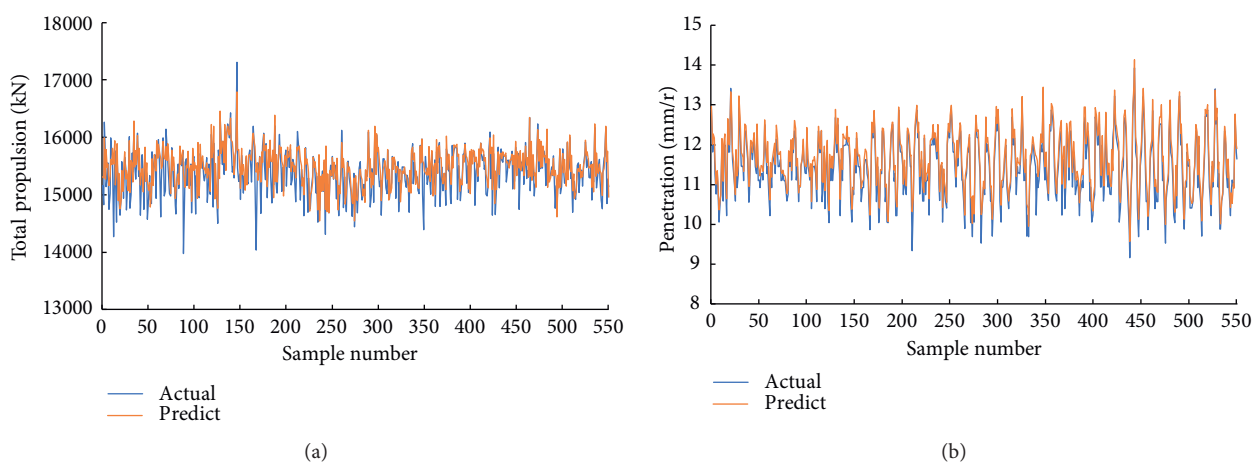

Figure 12: Continued.

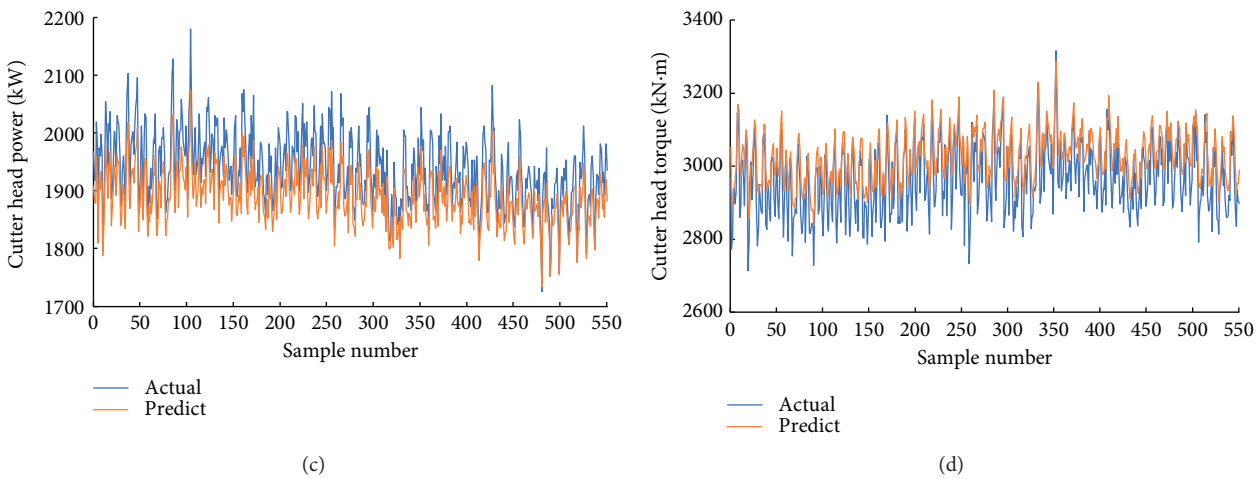

Figure 12: Prediction results of GRU model. (a) Prediction results of total thrust F. (b) Prediction results of penetration e. (c) Prediction results of cutterhead power P. (d) Prediction results of cutterhead torque T.

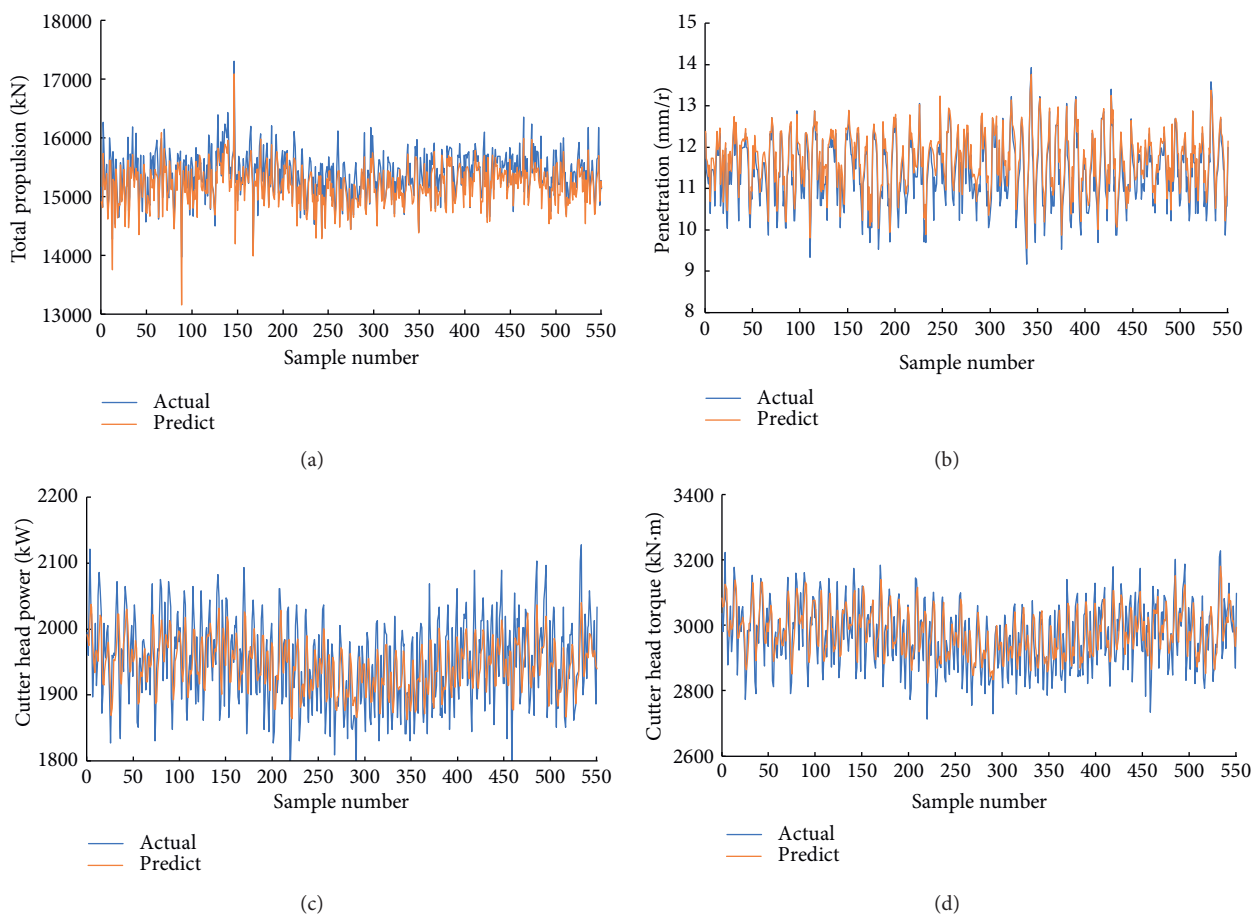

Figure 13: Prediction results of LSTM model. (a) Prediction results of total thrust F. (b) Prediction results of penetration e. (c) Prediction results of cutterhead power P. (d) Prediction results of cutterhead torque T.

difficult to adjust the tunneling state in a timely and effective manner. With the rapid development of computer technology, artificial intelligence technology is gradually applied to TBM tunnel construction. Compared with traditional methods, one of the main advantages of artificial intelligence technology is a high degree of self-programming, which means that manual supervision of this process is no longer necessary, saving a lot of labor costs. The Bi-GRU-ATT model

Table 2: Comparison of evaluation indexes of prediction results among different recurrent neural network models.

Model	Parameter	MAPE (%)	R^2	MAE	RMSE
Bi-GRU-ATT	Total thrust	1.01	0.925	151.52	193.62
	Penetration	1.60	0.930	0.15	0.20
	Cutterhead torque	1.40	0.936	31.30	44.44
	Cutterhead power	1.71	0.944	34.13	34.75
Bi-GRU	Total thrust	1.11	0.915	146.35	184.23
	Penetration	2.05	0.898	0.20	0.26
	Cutterhead torque	1.84	0.909	52.65	67.00
	Cutterhead power	2.13	0.884	38.30	46.02
GRU	Total thrust	1.21	0.859	196.68	280.99
	Penetration	2.47	0.867	0.23	0.27
	Cutterhead torque	2.26	0.879	60.87	73.37
	Cutterhead power	2.52	0.870	48.41	50.95
LSTM	Total thrust	1.44	0.870	205.60	252.02
	Penetration	2.97	0.840	0.27	0.32
	Cutterhead torque	2.04	0.889	55.88	67.97
	Cutterhead power	2.7	0.860	44.61	52.89

proposed in this study uses an adaptive algorithm to automatically adjust the processing method, processing sequence, and boundary conditions in the data processing and analysis stage according to the characteristics of the preprocessed data, so as to make it consistent with the structural characteristics and statistics of the processed data. The distribution characteristics are adapted to ensure the extraction of the rock-machine interaction relationship under real-time rock mass conditions, so as to realize the real-time prediction of the tunneling performance of the model under the given TBM control parameters, in order to promote the intelligent development of TBM tunneling; in addition, the Bi -GRU-ATT model can reflect the current rock mass state through the change law of the excavation parameter value in the complete excavation cycle and adjust and optimize the current excavation parameters in real time according to the current rock mass state information to ensure safe and efficient excavation of TBM. Although this model is based on a huge amount of construction data of TBM tunnel projects that have been built or under construction, the unknown rock mass status information still needs to be obtained through on-site drilling core sampling, in situ experiments, etc.; the artificial intelligence technology represented by this model is only used as an example. This kind of auxiliary intelligent decision-making method, the steps of planning of the excavation task, and control of the excavation state in the excavation process still inevitably require human intervention. Therefore, to further improve the intelligent prediction model of TBM tunneling parameters to adapt to the TBM tunneling construction of different engineering geological conditions is a problem that we urgently need to solve.

6. Conclusions

This paper proposes a prediction method of TBM tunneling parameter based on the Bi-GRU-ATT model and selects the normalized complete tunneling cycle section data to predict the tunneling parameters of the complete tunneling cycle. The training set and test set are divided by the operation data of the TBM3 bid section of the Jilin Water Supply Project, the nonworking state and abnormal data are eliminated, and the complete excavation cycle is extracted. Based on Pearson correlation analysis, the 199-dimensional tunneling parameters selected from the complete tunneling cycle are sorted, and the 21 key parameters with the highest correlation with a certain TBM tunneling parameter to be predicted are extracted as the input features of the model, so as to predict four TBM tunneling parameters (total thrust, penetration, cutterhead torque, and cutterhead power) in the complete driving cycle section. The advantages of this model are verified by comparing the Bi-GRU-ATT model with Bi-GRU, unidirectional LSTM, and unidirectional GRU models. The main conclusions are as follows:

(1) Bi-GRU-ATT is trained based on the complete cycle data of the TBM tunneling cycle, and the intelligent prediction method based on the Bi-GRU-ATT model is constructed, which can effectively predict four key TBM tunneling parameters. The average absolute percentage error (MAPE) of the prediction results of each parameter is less than 1.8%, and the goodness of fit R^2 is greater than 0.92, which verifies the accuracy and effectiveness of this model. The results show that this model has a good guiding significance for realizing the real-time prediction of TBM tunneling parameters and assisting the optimization and adjustment of TBM tunneling parameters.

(2) Compared with the existing methods of using ascending section data of TBM tunneling cycle to predict the tunneling parameters of the stable section, this paper selects the data of complete tunneling cycle section to predict the tunneling parameters of the complete tunneling cycle, which can significantly improve the complexity and difficulty of data processing in the TBM tunneling process and then greatly improve the preprocessing efficiency of massive TBM tunneling data.

(3) Comparing and analyzing the prediction results of recurrent neural network models, it can be seen that the Bi-GRU-ATT model proposed in this paper has better prediction performance than the other three prediction models. This model is helpful for the intelligent regulation of TBM tunneling parameters and provides a more feasible auxiliary intelligent decision-making method for TBM safe and efficient tunneling construction.

Data Availability

The data used to support the findings of this study are included within the article and can be available from the corresponding author upon request.

Conflicts of Interest

The authors declare that there are no conflicts of interest regarding the publication of this paper.

Acknowledgments

This work was supported by Fundamental Research Funds for the Central Universities (Project No. FRF-TP-20-043A1), Open Research Fund Program of State Key Laboratory of Hydroscience and Engineering (Project No. sklhse-2021-C-04), and Independent Research Project of Huaneng Renewables Corporation Limited (Project No. HNRKJ-2020-04). The costs to publish in open access have been covered by the funding.

References

[1] Z. Liu, L. Li, X. Fang et al., "Hard-rock tunnel lithology prediction with TBM construction big data using a global-attention-mechanism-based LSTM network," *Automation in Construction*, vol. 125, no. 3, Article ID 103647, 2021.

[2] J. Li, P. Li, D. Guo, X. Li, and Z. Chen, "Advanced prediction of tunnel boring machine performance based on big data," *Geoscience Frontiers*, vol. 12, no. 1, pp. 331–338, 2021.

[3] A. Afradi, A. Ebrahimabadi, and T. Hallajian, "Prediction of TBM Penetration Rate Using Fuzzy Logic, Particle Swarm Optimization and Harmony Search Algorithm," *Geotechnical and Geological Engineering*, vol. 39, 2021.

[4] A. Delisio, J. Zhao, and H. H. Einstein, "Analysis and prediction of TBM performance in blocky rock conditions at the Lötschberg Base Tunnel," *Tunnelling and Underground Space Technology*, vol. 33, pp. 131–142, 2013.

[5] Q. M. Gong and J. Zhao, "Development of a rock mass characteristics model for TBM penetration rate prediction," *International Journal of Rock Mechanics and Mining Sciences*, vol. 46, no. 1, pp. 8–18, 2009.

[6] U. Ates, N. Bilgin, and H. Copur, "Estimating torque, thrust and other design parameters of different type TBMs with some criticism to TBMs used in Turkish tunneling projects," *Tunnelling and Underground Space Technology*, vol. 40, pp. 46–63, 2014.

[7] X. Yang, G. F. Gong, H. Y. Yang, L. H. Jia, and Q. W. Ying, "A cutterhead energy-saving technique for shield tunneling machines based on load characteristic prediction," *Journal of Zhejiang University - Science*, vol. 16, no. 5, pp. 418–426, 2015.

[8] R. Gertsch, L. Gertsch, and J. Rostami, "Disc cutting tests in Colorado Red Granite: implications for TBM performance prediction," *International Journal of Rock Mechanics and Mining Sciences*, vol. 44, no. 2, pp. 238–246, 2007.

[9] S. Yagiz, "A model for the prediction of tunnel boring machine performance," *Proceedings of 10th IAEG Congress*, Article ID 383, pp. 1–10, 2006.

[10] C. Su, "Analysis of mechanical properties of two typical kinds of cutterheads of shield machine," *Advanced Science Letters*, vol. 4, no. 6-7, pp. 2049–2053, 2011.

[11] Y. Ge, J. Wang, and K. Li, "Prediction of hard rock TBM penetration rate using least square support vector machine," *IFAC Proceedings Volumes*, vol. 46, no. 13, pp. 347–352, 2013.

[12] H. Krause, *Geologische Erfahrungen beim Einsatz von Tunnelvortriebsmaschinen in Baden-Württemberg*, Springer, New York, NJ, USA, 1976.

[13] G. Meschke, J. Ninić, J. Stascheit, and A. Alsahly, "Parallelized computational modeling of pile-soil interactions in mechanized tunneling," *Engineering Structures*, vol. 47, pp. 35–44, 2013.

[14] B. Maidl, M. Herrenknecht, U. Maidl, and G. Wehrmeyer, *Mechanised Shield Tunnelling*, John Wiley & Sons, Hoboken, NJ, USA, 2nd edition, 2012.

[15] E. Avunduk and H. Copur, "Empirical modeling for predicting excavation performance of EPB TBM based on soil properties," *Tunnelling and Undergroud Space Technology*, vol. 71, pp. 340–353, 2018.

[16] Y. Seo, F. J. Macias, P. D. Jakobsen, and A. Bruland, "Influence of subjectivity in geological mapping on the net penetration rate prediction for a hard rock TBM," *Rock Mechanics and Rock Engineering*, vol. 51, pp. 1599–1613, 2018.

[17] N. R. Barton, *TBM Tunnelling in Jointed and Faulted Rock*, CRC Press, Boca Raton, FL, USA, 2000.

[18] J. Rostami, *Development of a Force Estimation Model for Rock Fragmentation with Disc Cutters through Theoretical Modeling and Physical Measurement of Crushed Zone Pressure*, Colorado School of Mines, Golden, CO, USA, 1997.

[19] X. P. Zhou and S. F. Zhai, "Estimation of the cutterhead torque for earth pressure balance TBM under mixed-face conditions," *Tunnelling and Underground Space Technology*, vol. 74, pp. 217–229, 2018.

[20] Q. Zhang, T. Huang, G. Y. Huang, Z. X. Cai, and Y. L. Kang, "Theoretical model for loads prediction on shield tunneling machine with consideration of soil-rock interbedded ground," *Science China Technological Sciences*, vol. 56, no. 9, pp. 2259–2267, 2013.

[21] I. Evans, "The force required to cut coal with blunt wedges," *International Journal of Rock Mechanics and Mining Sciences & Geomechanics Abstracts*, vol. 2, no. 1, pp. 1–12, 1965.

[22] S. Y. Zhou, Y. L. Kang, C. X. Su, and Q. Zhang, "Study on prediction model of TBM driving total thrust based on mechanical analysis," *Journal of Mechanics: Series A*, vol. 52, no. 20, pp. 76–82, 2016.

[23] T. Kasper and G. Meschke, "On the influence of face pressure, grouting pressure and TBM design in soft ground tunnelling," *Tunnelling and Underground Space Technology*, vol. 21, no. 2, pp. 160–171, 2006.

[24] N. Afrasiabi, R. Rafiee, and M. Noroozi, "Investigating the effect of discontinuity geometrical parameters on the TBM performance in hard rock," *Tunnelling and Underground Space Technology*, vol. 84, pp. 326–333, 2019.

[25] Q. L. Zhang, R. Ma, Y. Hu, Z. Z. An, T. Yin, and Q. B. Li, "Intelligent control theory of thermal stress in mass concrete structures," *Journal of Hydroelectric Engineering*, vol. 40, no. 5, pp. 11–21, 2021.

[26] A. M. Noori, R. Mikaeil, M. Mokhtarian, S. S. Haghshenas, and M. Foroughi, "Feasibility of intelligent models for prediction of utilization factor of TBM," *Geotechnical & Geological Engineering*, vol. 38, pp. 1–19, 2020.

[27] C. Zhou, L. Ding, Y. Zhou, H. Zhang, and M. J. Skibniewski, "Hybrid support vector machine optimization model for prediction of energy consumption of cutter head drives in shield tunneling," *Journal of Computing in Civil Engineering*, vol. 33, no. 3, Article ID 04019019, 2019.

[28] W. G. Zhang, H. R. Li, C. Z. Wu, Y. Q. Li, Z. Q. Liu, and H. L. Liu, "Soft computing approach for prediction of surface settlement induced by earth pressure balance shield tunneling," *Underground Space*, vol. 6, no. 4, pp. 353–363, 2021.

[29] W. Sun, M. Shi, C. Zhang, J. Zhao, and X. Song, "Dynamic load prediction of tunnel boring machine (TBM) based on heterogeneous in-situ data," *Automation in Construction*, vol. 92, no. 5, pp. 23–34, 2018.

[30] H. Q. Yang, Z. H. Wang, and K. L. Song, "A new hybrid grey wolf optimizer-feature weighted-multiple kernel-support vector regression technique to predict TBM performance," *Engineering with Computers*, vol. 36, pp. 1–17, 2020.

[31] F. Wang, G. F. Gong, L. W. Duan, and Y. F. Qin, "XGBoost based intelligent determination system design of tunnel boring ma-chine operation parameters," *Journal of Zhejiang University*, vol. 54, no. 4, pp. 633–641, 2020.

[32] P. Malhotra, L. Vig, G. Shroff, and G. Agarwal, "Long Short Term Memory Network for Anomaly Detection in Time Series," in *Proceedings of the 23rd European Symposium on Artificial Neural Networks, Computational Intelligence and Machine Learning, ESANN 2015*, Bruges, Belgium, April 2015.

[33] X. Gao, M. Shi, X. Song, C. Zhang, and H. Zhang, "Recurrent neural networks for real-time prediction of TBM operating parameters," *Automation in Construction*, vol. 15, pp. 130–140, 2019.

[34] S. Hochreiter and J. Schmidhuber, "Long short-term memory," *Neural Computation*, vol. 9, no. 8, pp. 1735–1780, 1997.

[35] R. Dey and F. M. Salemt, "Gate-variants of Gated Recurrent Unit (GRU) Neural Networks," in *Proceedings of the IEEE International Midwest Symposium on Circuits & Systems*, pp. 1597–1600, IEEE, Boston, MA, USA, August 2017.

[36] Y. F. Zhu, W. W. He, J. X. Li, Y. C. Li, and P. Q. Li, "SOC estimation of lithium battery based on Bi-LSTM/Bi-GRU cyclic neural network," *Energy storage science and technology*, vol. 10, no. 03, pp. 1163–1176, 2021.

[37] P. Xuan, Y. Ye, T. Zhang, L. F. Zhao, and C. Sun, "Convolutional neural network and bidirectional long short-term memory-based method for predicting drug-disease associations," *Cells*, vol. 8, no. 7, p. 705, 2019.

[38] C. Wang, G. F. Gong, Y. Yang, J. J. Zhou, L. W. Duan, and Y. K. Zhang, "Prediction and analysis of cutter head torque of nsvr hard rock tunnel boring machine," *Journal of Zhejiang University: Natural Science Edition*, vol. 52, no. 3, p. 479, 2018.

[39] S. K. Hou, Y. R. Liu, and K. Zhang, "Prediction of TBM tunnelling parameters based on IPSO-BP hybrid mode," *Chinese Journal of Rock Mechanics and Engineering*, vol. 39, no. 8, pp. 1648–1657, 2020.

[40] X. X. Zhou, Q. M. Gong, L. J. Yin, H. Y. Xu, and C. Ban, "Prediction of tunneling parameters in TBM stable section based on BLSTM-AM model," *Rock. Mech. Eng*, vol. 39, no. S2, pp. 3505–3515, 2020.

Hindawi
Advances in Civil Engineering
Volume 2022, Article ID 7235619, 16 pages
https://doi.org/10.1155/2022/7235619

Research Article

Effect of the Initial Support of the Tunnel on the Characteristics of Rockburst: Case Study and Mechanism Analysis

Chunchi Ma,[1,2] **Junqi Fan**,[3] **Xiang Ji**,[1,2] **Xiaoyan Shi**,[3] **and Jun Zeng**[1,2]

[1]*State Key Laboratory of Geohazard Prevention and Geoenvironment Protection, Chengdu University of Technology, Chengdu 610059, Sichuan, China*
[2]*School of Environment and Civil Engineering, Chengdu University of Technology, Chengdu 610059, Sichuan, China*
[3]*Research Instiute for National Defense Engineering of Academy of Military Science PLA China, Luoyang 471023, Henan, China*

Correspondence should be addressed to Chunchi Ma; machunchi17@cdut.edu.cn and Junqi Fan; lyfjq@163.com

Received 13 December 2021; Accepted 11 January 2022; Published 9 February 2022

Academic Editor: Ma Jianjun

Rockburst is still a stubborn disease in the field of engineering geology. The present research pays more attention to the influence of geological conditions on rockburst and less to the influence of type and stiffness of engineering support on rockburst. We explore the influence of support stiffness from weak to strong on rockburst and reveal the characteristics of fracture and microseismicity during rockburst through microseismic monitoring and numerical simulation. The main results and conclusions can be drawn: (1) Strong stiffness support makes the surrounding rock accumulates higher energy before rockburst. The evolution of microseismicity and its indexes can be used as precursors of potentially strong rockburst. (2) Strong stiffness support is easy to concentrate high stress under the action of surrounding rock pressure, and it is easy to fail under the disturbance of external load. This will produce a "sudden unloading effect" on the surrounding rock mass and may lead to a more serious rockburst. Numerical simulation verifies the existence of that effect and are consistent with the actual signs of failure. Our research is helpful to clarify the rockburst problem in the field of engineering geology, specifically to reveal the mechanism of rockburst and the early warning criteria of rockburst hazard under the action of supporting structure, which can provide practical data and theoretical support for scientific and reasonable prevention and control of rockburst risk in tunnel and underground engineering.

1. Introduction

Rockburst is a kind of geological hazard with complicated development mechanism, which is influenced by stratigraphic lithology, geological structure, ground stress and multi-field coupling factors and greatly threatens the field of geological engineering and geotechnical engineering. When the tunneling or underground opening is implemented in the hard-brittle rock under high ground stress, the stress adjustment will cause damage to the surrounding rock, so that the elastic strain energy stored in the rock mass will be released suddenly, resulting in loosening, spalling, ejection and even throwing. Rockburst is that a type of dynamic instability and geological disaster characterized by the abruptness and violent nature. Prediction and early warning of rockburst are challenging, posing significant challenges to the construction safety and, thus, necessitating continuous exploration of the development laws, early warning techniques, and support methods of deep geological disasters to serve the safety construction in deep engineering [1–5].

Due to the lack of deep understanding of rockburst, engineers may design the high-strength and high-stiffness support in tunnel to control the risk of rockburst, which contradicts the generally accepted principle of releasing rockburst energy. This may lead to the failure of the surrounding rock mass to give full play to the self-stability in the stress adjustment, thus increasing the accumulation of strain energy of surrounding rock and the destructiveness of rockburst. For example, when the initial support system was strengthened by shortening the spacing of the steel arch, the rockburst in the Bamiao tunnel of Taoba expressway intensified, and the initial lining near the tunnel face appeared

large area exfoliation. Reinforced (rigid) support system has been carried out in the rockburst section of Micangshan tunnel of Bashan expressway, which poses a significant impact on the characteristics of rockburst and microseismicity.

To date, most of the researches on the influencing factors of rockburst, such as geo-stress, stratigraphic lithology, rock mass structure, topography, hydrology, excavation, and so on, have achieved outstanding results [6–11]; however, very limited studies have explored the impact of supporting structures on rockburst. For instance, Fan et al. [12] explored the influence of tunneling methods on the strainburst characteristics during the excavation. Hu [13] analyzed the response of support thickness to rockburst through numerical simulation, suggesting that support exerts an inhibitory effect on rockburst, but excessive support thickness might promote rockburst. Li et al. [14] determined the mechanical effects of rockburst by numerically changing the supporting parameters. Chen [15] investigated the rockburst under different densities of anchor arrangement, and thought that the rockburst under high density anchoring would lead to the overall damage of surrounding rock. In addition, Ortlepp [16, 17] described the characteristics and extent of rockburst failure under different support strength, and he thought it is futile to improve the support strength to resist rockburst when strong rockburst may occur. Huang [18] investigated the rockburst development under different support strengths through numerical simulation and field tests. The above researches reveal to some extent the effect of supporting system on rockburst, but these conclusions are mostly qualitative or semi-quantitative.

The development of rockburst accompanies a series of microfracture (microseismic event). The microseisms determine the failure characteristics and mechanism of rockburst [19–24]. To date, the interactive mechanism between microseismic activity and supporting structure remains less investigated, and the microseismic activity is rarely used to guide support strategy. In some representative studies, support system was determined based on the microseismic data in the underground cavern of a hydropower station [25]. Hu et al. [26] used the microseismic monitoring to investigate the deformation and failure of surrounding rock in an underground laboratory, and proposed reasonable schemes of excavation and support. Gale [27] enhanced the support structure by comparing microseismic data and numerical simulation of different mining areas. In fact, the initial support structure of the tunnel (such as support type, support strength, support stiffness, and support timing) exerts marked impact on the microseismic activity and rockburst. It is imperative to study the influence mechanism of the support system on fractures or microseismic activities of the surrounding rock mass.

To investigate the impact of the initial support system on rockburst, this study aims to explore the rockburst characteristics and microseismic activity under weak and strong stiffness of support based on the phenomena and data collected in the Micangshan tunnel of the Sichuan-Shaanxi expressway, combined with numerical simulation to elucidate the mechanism of the supporting structure affecting rockburst characteristics and intensity. This study will provide practical data and theoretical guidance for the reasonable strategy of supporting the rockburst and the consideration of the rockburst warning criterion affected by the support stiffness. The relevant results are helpful to reveal the rockburst mechanism under deep engineering activities and to effectively prevent and control underground engineering disasters.

2. Rockburst Influenced by Tunnel Initial Support

2.1. Composite Stiffness Assessment of Tunnel Support and Surrounding Rock. In order to distinguish the rockburst characteristics corresponding to different support stiffness, it is necessary to establish a method to determine the support stiffness. However, because the initial support of the tunnel is a composite system composed of a variety of supporting structures (such as shotcrete and steel arch frame), it is very challenging to propose a quantitative method for evaluating the composite stiffness. For this reason, This work is based on the empirical judgment of the effectiveness of various support types and support parameters in the actual construction of Micangshan tunnel (which may change due to engineering characteristics and geological types), a semi quantitative evaluation method of composite system stiffness considering both surrounding rock stiffness and initial support mode is proposed. As shown in Table 1, the stiffness evaluation method consists of two parts: the basic value A and the construction parameter B. Of these, The basic value A is the empirical value considering the support type and support specification for stiffness. the construction parameter B considers the contribution of the engineering dosage of each support type to the stiffness. The stiffness evaluation of surrounding rock has no basic value, which depends on the contribution of lithology quality grade to stiffness [28].

Specification of structure: steel arch- type I18, height 180mm, width 94mm and thickness 10.7mm; anchor- diameter 22mm and length 3m; shotcrete- type C20. The determination of A/B value should also refer to the specific geological conditions of each project.

2.2. Rockburst Characteristics Affected by the Tunnel Initial Support. The Micangshan extra-long tunnel of Sichuan-Shaanxi expressway is about 13.8 km in length, which was designed as the second longest expressway tunnel in China and the third longest in the world. In the excavation of K46+170-K45+800 mileage section of the tunnel, rockburst hazards caused by the high ground stress occurred frequently. As shown in Figure 1, “12.17” rockburst, “12.29” rockburst, “01.14” rockburst, “03.12” rockburst and so on. The rockburst areas have the following conditions: the buried depth is 530-760 m and the lithology is mainly gabbro and tectonic granulite; the grade of surrounding rock mass is mainly grade III (medium), and grade II (better) or grade IV (poor) in local; the gabbro and tectonic granulite are interlaced and rockburst generally occurs in the location of tectonic granulite. According to the identification, the

Table 1: Stiffness score of support and surrounding rock in Micangshan tunnel [28].

Type	Basic value/ A	Construction parameter/ B	Score
Steel arch	10	Spacing (m)	A × (1/B)
Strengthened steel arch	15	Spacing (m)	A × (1/B)
Anchor	1	Anchor number per steel arch	A × B
Shotcrete	2	Thickness (cm)	A × (B/10)
Pre-grouting	3	Volumes (m^3)	A × B
Pressure release blasting	2	Number of boreholes	−A × B
Surrounding rock mass	–	Grades (I-V)	I- 50 ; II- 40 ; III- 30 ; IV- 20 ; V- 10

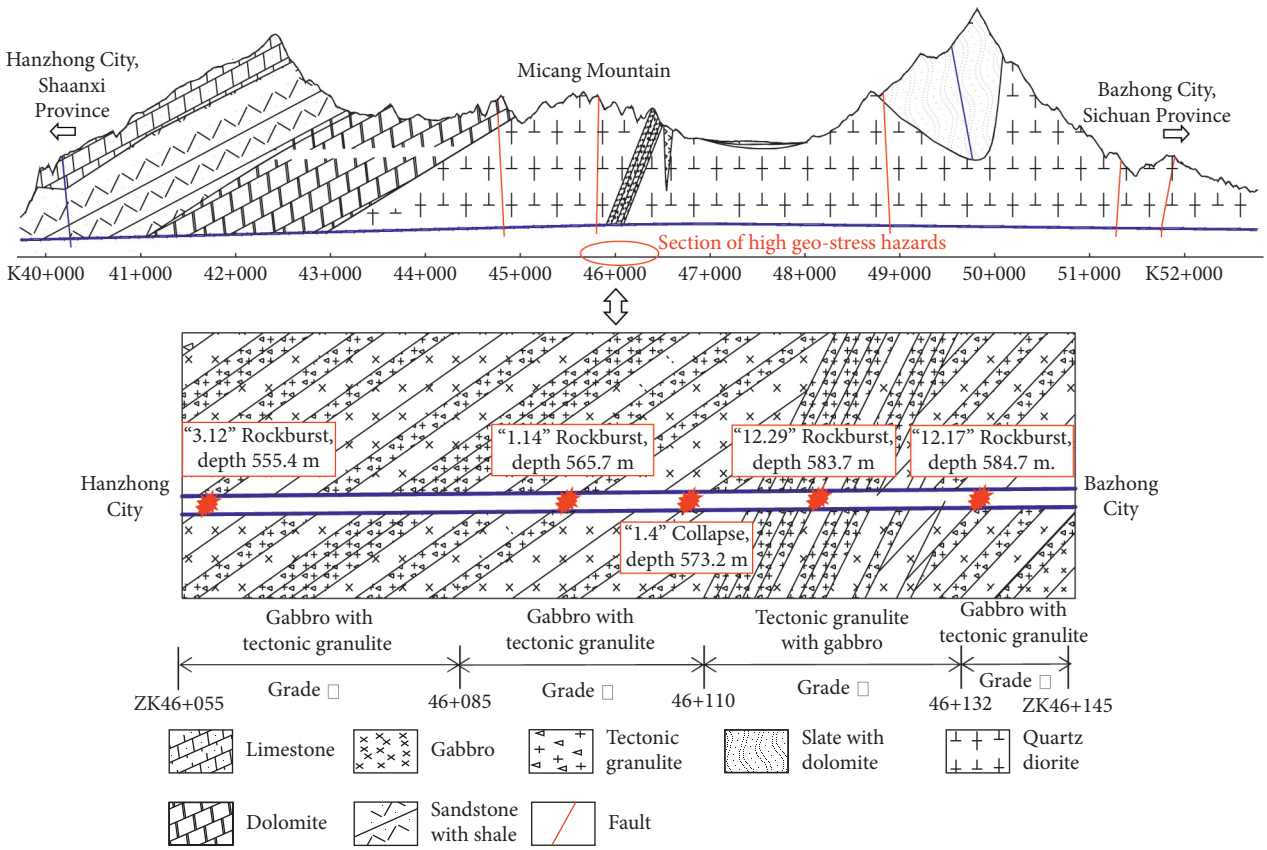

Figure 1: The geological cross-section along the Micangshan tunnel, China [28].

original rock of tectonic granulite should be gabbro, which undergo compressive rupture and recrystallize to form granulite. There are many microfractures in the rock mass, but it still has high residual ground stress, which satisfies the occurrence conditions of rockburst. Due to the occurrence of different degrees of rockburst, various support measures have been adopted in the construction site. In order to distinguish the stiffness changes of various support measures and study the influence of initial support stiffness on the characteristics of rockburst, the comprehensive stiffness evaluation method in Table 1 is used to evaluate the stiffness changes of "12.17" rockburst, "12.29" rockburst, "01.14" rockburst and "03.12" rockburst. As shown in Table 2, in comparison, the score of surrounding rock-support composite stiffness of "1.14" rockburst and "3.12" rockburst is higher than that of 12.17 "rockburst and" 12.29 "rockburst. Therefore, the "12.17" rockburst and the "12.29" rockburst is simply expressed as weak stiffness rockbursts, and the "1.14" rockburst and "3.12" rockburst is simply expressed as strong stiffness rockburst.

Tunnel support can be divided into initial support and secondary support. The initial support is carried out immediately after the excavation of the tunnel, and is the main structure to bear the pressure of surrounding rock. Experts suggest adopting flexible support system for the initial support of rockburst and following the principle of absorbing high energy, that is, the supporting structure should not only satisfy a certain strength but also can deform greatly, thus absorbing the kinetic energy of rockburst [17, 29]. However, high strength and high stiffness support are often used in rockburst due to the lack of comprehensive understanding of rock mass fractures. Such treatment lacks theoretical basis and is often controversial. For example, the Micangshan tunnel shows the rockburst intensity varying

Table 2: Composite stiffness of surrounding rock and support system in rockburst.

Hazards	Rockburst "12.17"	Rockburst "12.29"	Rockburst "01.14"	Rockburst "03.12"
Time span	2017/12/15-12/17	2017/12/26-12/29	2018/01/10-01/14	2018/03/08-03/12
Lithology	Gabbro with granulite interbedded, grade III	Granulite with gabbro interbedded, grade IV	Gabbro with granulite interbedded, grade III	Gabbro with granulite interbedded, grade III
Support structure and parameter	Steel arch: spacing 80 cm. Anchor: 12 per steel arch. Shotcrete: thickness 20 cm.	Steel arch: spacing 80 cm. Anchor: 12 per steel arch. Shotcrete: thickness 20 cm.	Strengthened steel arch: spacing 70 cm. Anchor: 20 per steel arch. Shotcrete: thickness 20 cm.	Steel arch: spacing 60 cm. Anchor: 12 per steel arch. Shotcrete: thickness 20 cm.
Stiffness score	58.50	48.50	75.43	62.67
Stiffness (For these four rockbursts)	Weak stiffness	Weak stiffness	Strong stiffness	Strong stiffness

with the change of initial support stiffness. In order to further explore this change law, a microseismic monitoring system was established in Micangshan Tunnel to capture microseismic events and rockburst evolution. As shown in Figure 2, The microseismic sensor array is deployed as three rows: two rows in the leading tunnel, one row in the following tunnel, and three sensors in each row, which ensures the precision of microseismic source location and the effectiveness of the source parameters.

Figure 3 records the rockburst evolution in the following tunnel of the twin-tube Micangshan tunnel. The three cases of rockburst disasters had developed in the period 2017/12/16–2018/01/14 (pentagram denotes the rockburst time). The first "12.17 rockburst" occurred in grade-III surrounding rock. The initial support was composed of steel arch and shotcrete anchor (weak stiffness). The rockburst occurs with a thunder-like bang and subsequent splitting sound, and the broken rocks are ejected or collapsed. Most of rockburst zones are controlled by a single set of dominant structural planes, or presents a wedge or fornix shape controlled by two or more sets of structural planes, with a maximum depth of up to 3m. The second "12.29 rockburst" occurred in grade-III or IV surrounding rock. The advanced grouting was used in the local broken surrounding rock, and the stiffness of the support system was slightly higher than that of the previous rockburst (weak stiffness). The maximum energy of microseismic event can reach one million joules, which is even comparable to the tunnel blasting. Strong energy releases impact on the equipment and surrounding rock mass of the tunnel, resulting in large mechanical shaking or overturning, cracking of the tunnel floor (floor heave), cracking of the sidewall (sidewall heave), and initial support failure. The third "01.14 rock burst" occurred in grade-II or III surrounding rock. Because of the frequent rockburst, the number of bolts in each construction period increased, the double-layer steel arch was adopted in local, and the support stiffness was the highest at this time. During the rockburst, the frequency of thunderous roar and splitting sound increased significantly, and the development period of the third rockburst was prolonged, the energy release was increased, and the crack range of lining caused by rockburst was enlarged.

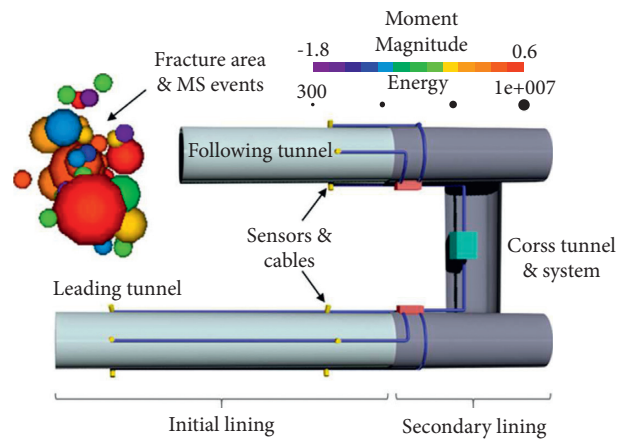

Figure 2: The layout of the microseismic monitoring system in the Micangshan tunnel.

2.3. Interpreting the Effect of Support Stiffness on Rockburst by Microseismic Characteristics. The microseismic indexes are introduced to elucidate the characteristics and mechanism of rockburst, and the process is divided as the developmental stage and occurrence stage. The occurrence time of rockburst is easily recorded by the microseismic monitoring system, and the period before rockburst is considered to be the developmental stage. For example, "12.29 rockburst" is a weak-stiffness rockburst and "1.14 rockburst" is a strong-stiffness rockburst. These rockbursts are developed in similar environment of lithology, buried depth and ground stress, and the space distance is close (Figure 1); therefore, we think that the main factor causing the change of rockburst intensity and characteristics is the support stiffness. Figure 4 shows the characteristics of the number of microseismic events and the incidence of high energy in rockburst process under strong and weak support stiffness. The seismic energy E denotes the elastic strain energy released by rock mass fracture:

$$E = \left(\frac{8}{5}\right)\pi\rho v R^2 \int_0^{t_s} \overline{u}_{\mathrm{corr}}^2(t)\mathrm{d}t. \quad (1)$$

ρ denotes the rock mass density; v denotes the microseismic velocity; R denotes the hypocentral distance; t_s denotes

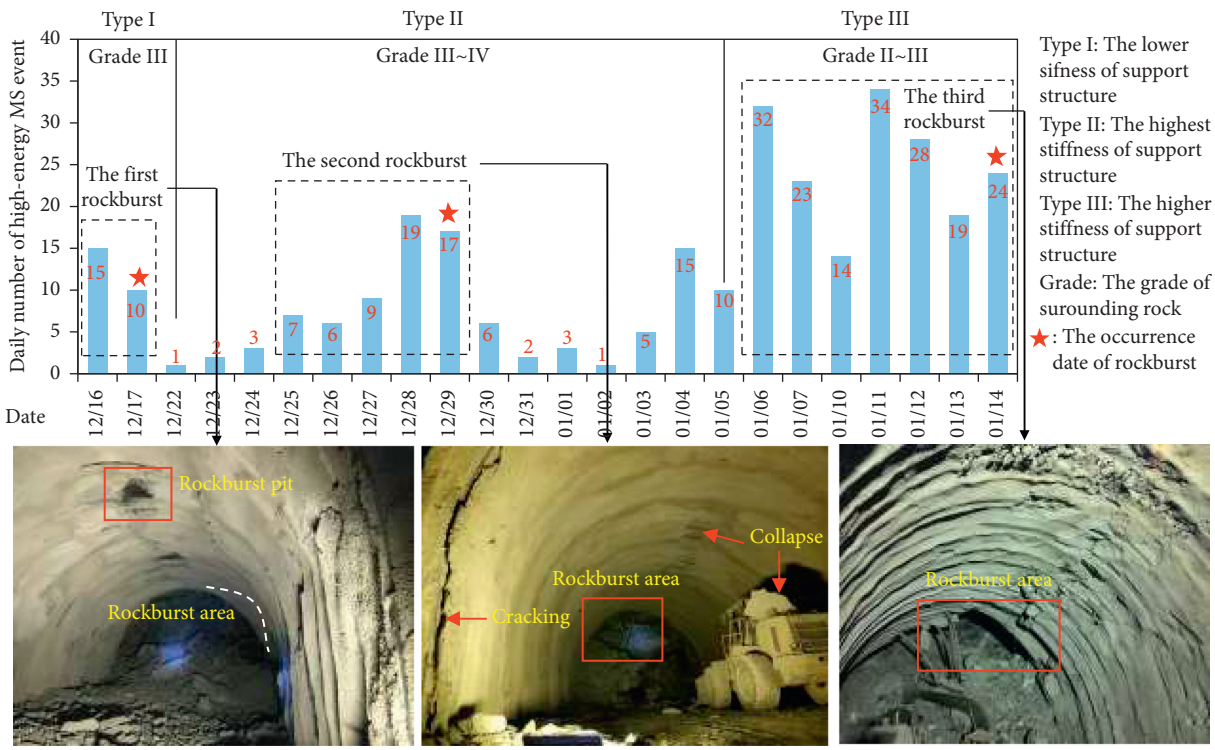

Figure 3: The record of the rockburst evolution during construction in the Micangshan tunnel (2017–2018).

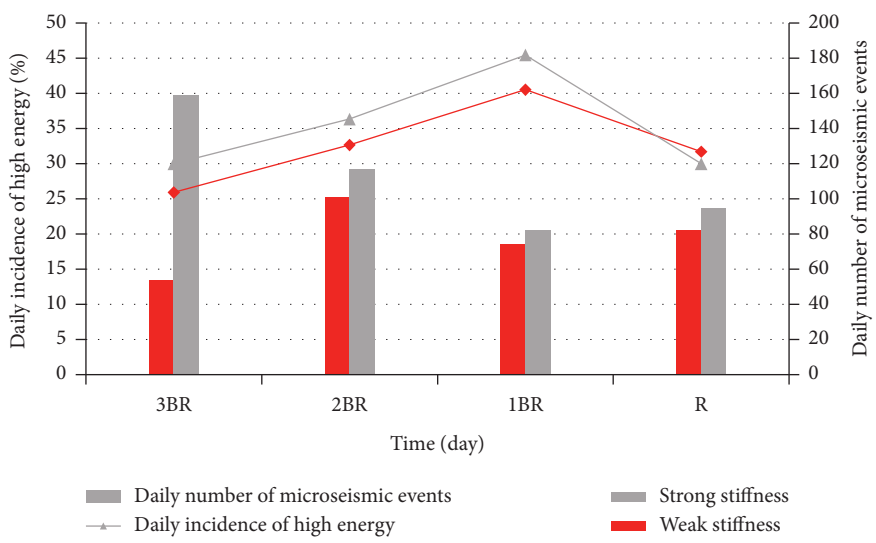

Figure 4: Characteristics of daily microseismic events and high energy incidence in rockburst process.

the time span of microseismic signal; u_{corr} denotes the displacement function of microseismic wave at the receiving end [25]. The number of daily cumulative microseismic events of rockburst under the condition of strong stiffness is obviously more than that of weak stiffness. The daily occurrence rate of high energy of rockburst is higher than that of weak stiffness under the condition of strong stiffness in the first 3 days before the occurrence of rockburst. But under the condition of strong stiffness on the day of rockburst, the daily incidence of high energy of rockburst is lower than that of weak stiffness.

Figure 5 shows the moment magnitude variation characteristics of microseismic events in rockburst process under strong support stiffness and weak support stiffness. Moment magnitude M_w is determined by seismic moment

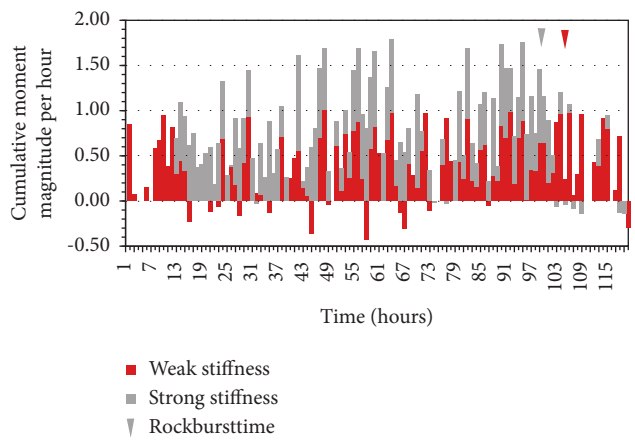

Figure 5: Characteristics of moment magnitude of microseismic events in rockburst process.

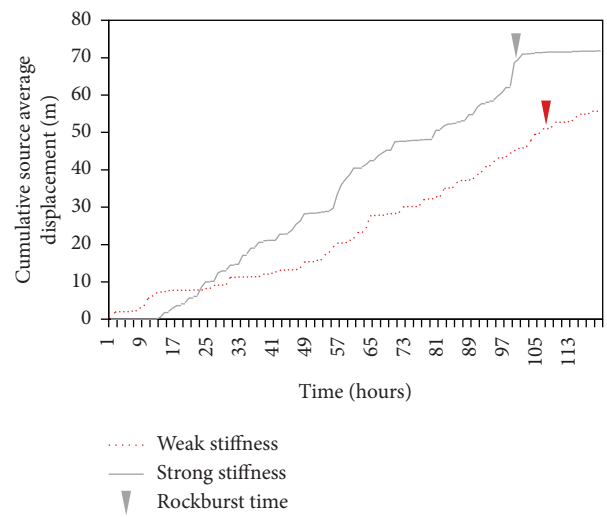

Figure 6: Characteristics of source average displacement in rockburst process.

calculation, which can directly represent the intensity of a microseismic event [30]:

$$M_w = \frac{2}{3} log_{10} M_0 - 6.0. \tag{2}$$

M_0 is the seismic moment, that is, the point source moment equivalent to the source fault dislocation that caused the earthquake ($N \cdot m$). In order to explore the characteristics of the moment magnitude of the microseismic event per hour before the rockburst, this study defines the sum of the moment magnitude of the microseismic event per hour as the hourly cumulative moment magnitude:

$$M_h = \sum_{i=1}^{n} M_w, \tag{3}$$

where M_h is the cumulative moment magnitude per hour, n is the number of microseismic events within one hour, and M_w is the magnitude of a single microseismic event. It can be found that the hourly cumulative moment magnitude of microseismic events under the condition of strong stiffness before rockburst (development period) is higher than that of weak stiffness condition. under the condition of weak stiffness after the occurrence of rockburst, the cumulative moment magnitude of microseismic events per hour of rockburst is obviously higher than that of strong stiffness. It is worth noting that the cumulative moment magnitude per hour after the occurrence of rockburst decreased obviously under both conditions.

Figure 6 reveals the characteristics of average displacement of microseismic source in rockburst process under strong support stiffness and weak support stiffness. The deformation caused by the rupture of source rock mass can be expressed by displacement, which can be expressed as follows:

$$\bar{D} = \frac{M_0}{\mu \pi r_0^2}. \tag{4}$$

μ is the shear modulus of rock mass, M_0 is the seismic moment, and r_0 is the radius of the fault plane [25]. It can be obviously found that the cumulative source average displacement of strong rigid rockburst is much higher than that of weak stiffness rockburst, and the trend characteristic of strong stiffness rockburst is more significant; after the occurrence of rockburst, strong stiffness rockburst basically does not change, weak stiffness rockburst continues to increase slowly.

Figure 7 shows the apparent volume series of rockburst developmental and occurrence stages under both strong and weak support stiffness. The apparent volume index V_A reflects the volume of inelastic shear deformation of rock mass:

$$V_A = \frac{M_0^2}{2\mu E}. \tag{5}$$

μ is the shear modulus of rock mass, M_0 is the seismic moment, and E is the microseismic energy [31]. In the developmental stage, the mean apparent volume of strong-stiffness rockburst (370 m^3) is higher than that of weak-stiffness rockburst (330 m^3). In the occurrence stage, the apparent volume of strong-stiffness rockburst increases obviously, but then decays rapidly, and the average value (397 m^3) is lower than that of the weak-stiffness rockburst (438 m^3).

Figure 8 describes the source parameter space of microseismic event during the developmental stage of rockburst; the abscissa of the microseismic parameter space is the apparent volume, the ordinate is the seismic energy, and the microseismic event (small dot) can be located in this space. When the stiffness of the support system changes from weak to strong, the microseismic events migrate toward the direction of arrow in the figure, indicating that the proportion of the small energy and the large apparent volume event increases. Based on the statistics in the development stage (Table 3), the proportion of small-energy events increases

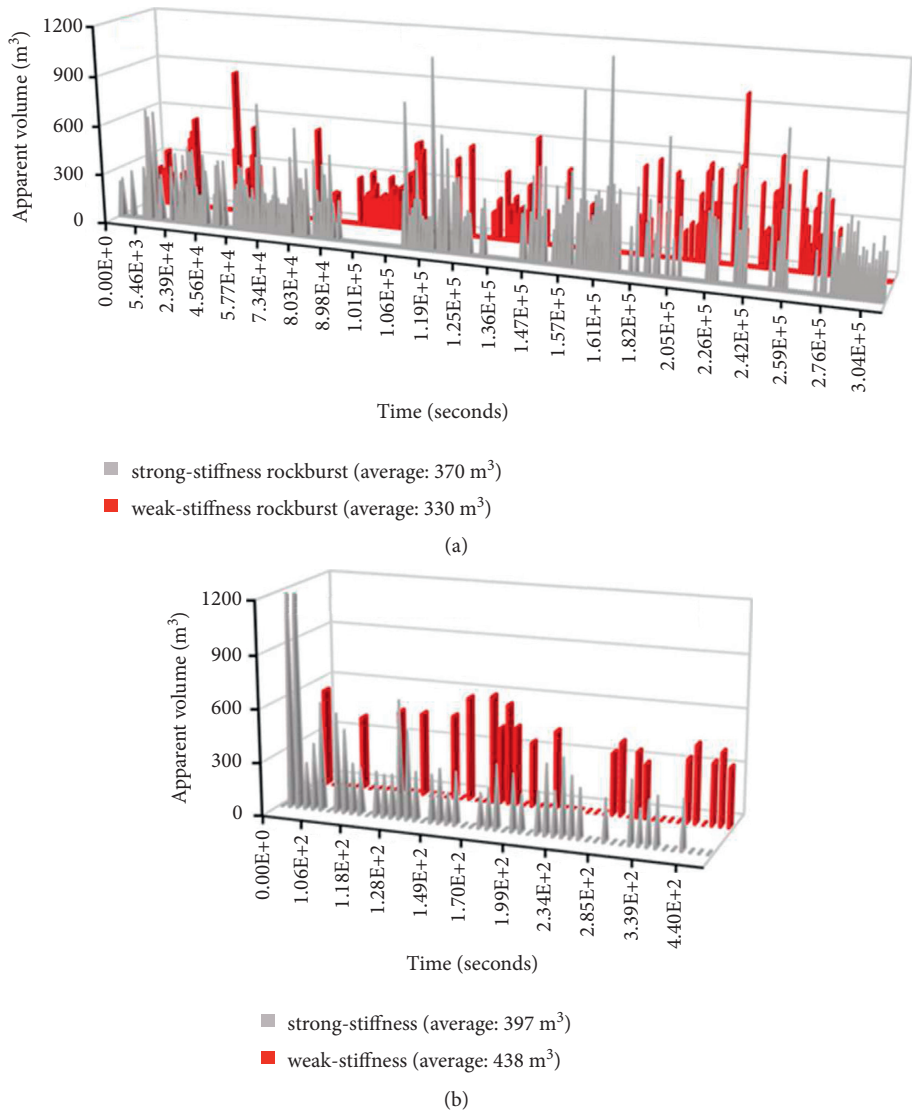

Figure 7: The apparent volume series of microseismic events during rockburst: (a) the development stage; and (b) the occurrence stage.

when the support stiffness changes from weak to strong, and the proportion of medium- and large-energy events decreases. Meantime, the proportion of small-volume events decreases, but the proportion of medium-volume events increases.

Classification of energy: small-energy event ($\leq 10^4$ J), medium-energy event (10^4 -10^5 J), and large-energy event ($\geq 10^5$ J) [32]. Classification of apparent volume: small-volume event ($\leq$ 200 m^3), medium-volume event (200 -400 m^3), and large-volume event ($\geq$ 400 m^3) [28].

According to the indexes summarized in Table 4, the support stiffness poses great influences on rockburst, and they can be described as follows:

(1) The reinforcement of the support stiffness imposes a more rigid constraint on the surrounding rock, which means a stronger confining pressure (support pressure) on the surrounding rock. In the process of rockburst, the high energy incidence of stress adjustment activities increased, the development time of rockburst prolonged and the number of microseismic events increased.

(2) with the increase of rigid constraint, the surrounding rock mass is easier to accumulate energy. The greater the moment magnitude of the microseismic event is in the process of stress adjustment.

(3) The reinforcement of the support stiffness indicates that the stress adjustment of surrounding rock requires a larger apparent volume of source. This is similar to the fact that the process of deformation, damage and near-critical failure of surrounding rock needs to be accompanied by large deformation by the increase of confining pressure. The average apparent

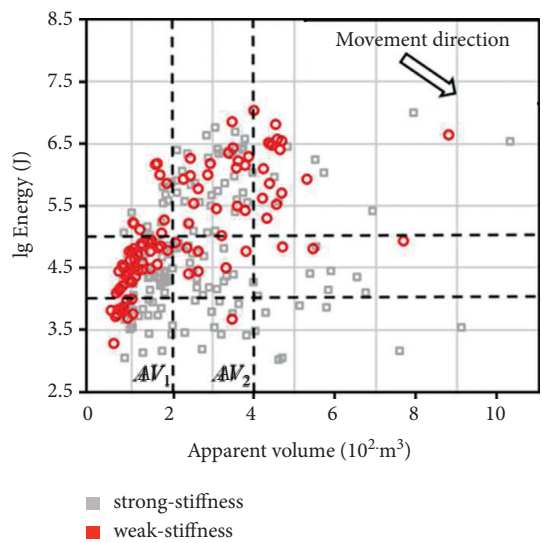

Figure 8: The source parameter space of the microseismic event during rockburst development stage. $(E)_1 = 4$ and $(E)_2 = 5$ are the threshold for small-energy events, medium-energy events, and large-energy events, respectively. $AV_1 = 200$ and $AV_2 = 400$ are the threshold for small-volume events, medium-volume events, and large-volume events, respectively.

Table 3: Statistics of microseismic event types in development stage of rockburst.

Rockburst	Event type by seismic energy			Event type by apparent volume		
	Small	Medium	Large	Small	Medium	Large
Low stiffness	13.0%	45.4%	41.6%	57.4%	25.0%	17.6%
High stiffness	25.2%	40.5%	34.3%	42.9%	41.7%	15.4%

volume during the rockburst development increases, and the average displacement of cumulative source also increases significantly.

(4) In the source parameter space composed of seismic energy and apparent volume, the motion path of microseismic events points to the lower right due to the enhancement of support stiffness, which indicates that the type of microseismic events changes and the proportion of events with both low energy and large apparent volume increases. The stress adjustment activities in the rockburst development tend to generate energy accumulation and energy transfer, and lead to stronger energy release in the occurrence stage of rockburst.

3. Numeric Simulation and Interpretation of Rockburst Effect

3.1. Modeling and Simulation Scheme. We established a tunneling model to simulate the rockburst affected by the drilling and blasting method in the Micangshan tunnel (Figure 9). Block-Dyna, a block-dynamic simulation software based on continuous-discontinuous method (CDEM), is used to simulate the whole process of damage and fracture of the tunnel surrounding rock under the action of static and dynamic loads. The software simulates the progressive failure process of materials by using the continuous medium characteristics of block characterization materials and the discontinuous medium characteristics of materials characterized by the interface between blocks. The software can simulate not only a variety of damage and failure processes of materials under static and dynamic loads, but also a series of mechanical processes of bulk after crushing. The overall size of the model is 50m (hight)×50m (width) and the tunnel size is 8m×12m, which includes the numbers of nodes and elements, 29302 and 54900, respectively. The tunnel length is 40m, which is designed as step by step excavation (5m per step). The model is composed of excavation body, surrounding rock mass and lining of the tunnel; the thickness of the lining is set to 20 cm and implemented immediately after the excavation step; the monitoring points for the lining and surrounding rock mass are set up. The actual stress conditions are applied to the model: the maximum principal stress σ_1 near the vertical direction is 25.2 MPa; the intermediate principal stress σ_2 near the axial direction of the tunnel is 13.1 MPa; the minimum principal stress σ_3 near the horizontal direction is 12.9 MPa. Finally, we designed the two schemes of rockburst simulation according to the actual engineering situation.

(1) Simulation of weak-stiffness rockburst under static load. Weak parameters of deformation and strength are used for lining support, and strain softening model is used for surrounding rock mass and lining. Rockburst occurs after the five-step excavation of the tunnel.

(2) Simulation of strong-stiffness rockburst under static and dynamic loads. Because strong stiffness support is also of high strength, rockburst does not generally occur under a single static loading condition, but needs to occur under the additional energy disturbance provided by dynamic load. In this simulation,

Table 4: Evolution of rockburst index with the strengthening of support stiffness.

Index	Rockburst stage	Stiffness condition	
		Weak stiffness	Strong stiffness
Event type by seismic energy	Development	The type of medium and large energy event is more, and the small energy event is less.	The type of medium, large energy event decreases, and the small-energy event increases.
	Occurrence	Mixed large and small energy events.	The large energy event is dominant.
Daily high energy rate	Development	The daily high energy rate increases gradually.	The daily high energy rate increases gradually and higher than weak stiffness.
	Occurrence	Daily high energy rate decreases.	Daily high energy rate decreases and lower than weak stiffness.
Cumulative moment magnitude per hour	Development	Increase of high moment magnitude.	Increase of high moment magnitude and the whole is higher than the weak stiffness.
	Occurrence	The cumulative moment magnitude per hour decreased obviously.	The cumulative moment magnitude per hour decreased obviously, but lower than weak stiffness.
Cumulative microseismic source average displacement	Development	Slow growth	Rapid growth and sudden increase.
	Occurrence	Slow growth	No significant changes.
Event type by apparent volume	Development	The type of small volume event is more, and the other types are less.	The type of small volume event decreases largely, and the medium volume event increases.
	Occurrence	Mixed extremely-larege, large and small volume event.	The large volume event is dominant.
Site characteristics of rockburst		Rockburst occurs on the excavation surface or tunnel roof, and is controlled by a single or multiple sets of structural plane, which could cause initial support cracking and fall of ground.	Rockburst possesses the features of strong energy release and large affected range, which can trigger side wall heave, floor cracking or floor heave in the same tunnel or adjacent tunnel.

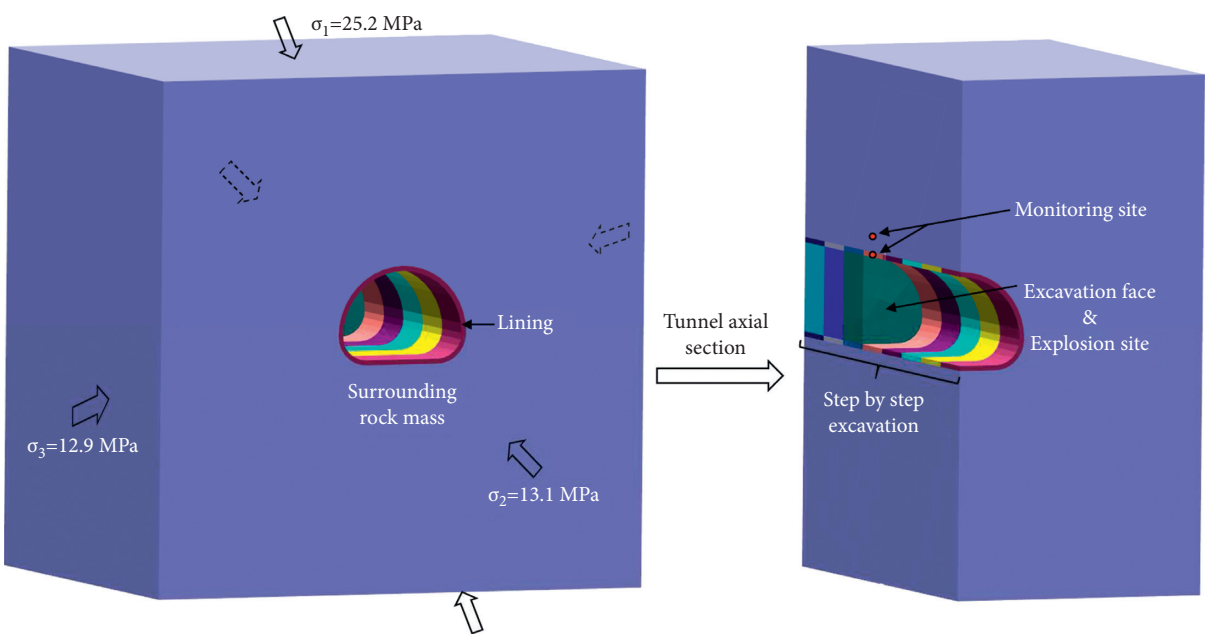

Figure 9: The excavation and blasting model of the Micangshan tunnel.

strong parameters of deformation and strength are used for lining support, and strain softening model is used for surrounding rock mass and lining. Rockburst occurs after the five-step excavation of the tunnel and the excavation face is blasted. The calculation parameters are presented in Table 5.

The Mohr-Coulomb strain softening model is introduced to describe the damage and fracture behavior of the rock mass:

$$C = \begin{cases} C_0\left(1 - \dfrac{|\gamma_p|}{\gamma_{\lim}}\right), & \left(|\gamma_p| < \gamma_{\lim}\right), \\ 0, & \left(|\gamma_p| \geq \gamma_{\lim}\right), \end{cases}$$
$$T = \begin{cases} T_0\left(1 - \dfrac{\varepsilon_p}{\varepsilon_{\lim}}\right), & \left(0 < \varepsilon_p < \varepsilon_{\lim}\right), \\ 0, & \left(\varepsilon_p \geq \varepsilon_{\lim}\right), \end{cases} \tag{6}$$

In the formula, C, C_0, T and T_0 represent the current and initial values of cohesion and tensile strength, respectively; γ_p, $\gamma_{\lim}$, ε_p and $\varepsilon_{\lim}$ represent the current and limit values of shear plastic strain and tensile plastic strain, respectively. According to the experiments and recommended values, $\gamma_{\lim} = 0.03$ and $\varepsilon_{\lim} = 0.01$. The strain softening model realizes the linear deterioration of the cohesion and the tensile strength with the plastic strain.

The Landau explosion source model is introduced to realize the tunnel blasting simulation:

$$\left.\begin{aligned} PV^{\gamma} &= P_0 V_0^{\gamma} \quad (P \geq P_k) \\ PV^{\gamma_1} &= P_k V_k^{\gamma_1} \quad (P \geq P_k) \end{aligned}\right\},$$
$$P_0 = \frac{\rho_w D^2}{2(\gamma + 1)}, \tag{7}$$
$$P_k = P_0 \left\{ \frac{\gamma_1 - 1}{\gamma - \gamma_1} \left[\frac{(\gamma - 1) Q_w \rho_w}{P_0} - 1 \right] \right\}^{(\gamma/\gamma - 1)}.$$

The blasting source model is based on the Landau–Stan Newkovic formula. $\gamma = 3$, $\gamma_1 = 4/3$; P, P_0, V and V_0 represent the current and initial values of explosive gas pressure and volume, respectively; P_k and V_k represent the pressure and volume of explosive gas on the boundary of two-stage insulation process; ρ_w denotes the charge density (kg/m^3); D denotes the explosion velocity (m/s); Q_w denotes the explosive heat per unit mass (J/kg). The time history curve of blasting dynamic load shown in Figure 10 is generated, by setting the blasting parameters $\rho_w = 1630$ kg/m^3, $D = 6930$ m/s, $Q_w = 4.23$ MJ/kg and the total charge 250 kg.

In the static calculation of tunnel excavation, horizontal displacement constraint is applied to the surrounding boundary and vertical displacement constraint is applied to the bottom boundary. In tunnel blasting calculation, the model boundaries are changed to viscous boundaries to eliminate the false reflection.

3.2. Simulation of Rockburst Affected by Support Stiffness. We introduce the stress evolution, damage factor and strain energy index in order to elaborate the rock failure and rockburst effect under static and dynamic loads. Figure 11 compares the simulation of rockburst effects by using the accumulated strain energy and damage factor (the deterioration of the strength parameters in the strain-softening model). Under the weak stiffness support (Figure 11(a)), the failure area of surrounding rock mass is concentrated on the tunnel excavation face and located on the tunnel floor and right tunnel roof. The strain energy of the surrounding rock near the tunnel surface is markedly decreased; that is, the release zone of strain energy, where the regional damage factor increases to 1 (a full failure of the surrounding rock). The strain energy concentration is transferred to the deep surrounding rock. Under the strong stiffness support (Figure 11(b)), the failure and damage range of the surrounding rock is progressively expanding. The energy release zone near the tunnel excavation face penetrates the tunnel roof, right sidewall and tunnel floor; the maximum energy release reaches 0.25 MJ/m^3.

In order to further reveal the fracture characteristics of rockburst disaster under the condition of strong and weak stiffness. The block velocity and fracture type of rockburst are simulated by discontinuous model (Figure 12). Under the condition of weak stiffness (Figure 12(a)), the rockburst occurs on the upper right and floor of the tunnel, and the maximum velocity of block ejection is 9.46 m/s. Under the condition of strong stiffness (Figure 12(b)), the failure strength and range of rockburst are obviously enhanced, and the maximum ejection velocity of the block is 13.9 m/s. In addition, in the fracture type diagram of rockburst block, the value 0 indicates no failure, the value 1 indicates tensile failure, and the value 2 indicates shear failure. It can be found that the main failure of rockburst is tension under the condition of weak stiffness, and the mixed failure type of tension and shear increases obviously under the condition of strong stiffness.

Figure 13 records the evolution of the maximum principal stress of the surrounding rock mass and lining. Under the weak stiffness support (Figure 13(a)), the maximum principal stress increases gradually during the five-step excavation and it declines after reaching the peak value. The lining stress drops behind the surrounding rock stress, which is affected by the damage and failure of rock mass. The surrounding rock further loses strength and has a secondary stress decline after the lining support fails. When the support stiffness is strengthened (Figure 13(b)), the maximum principal stress increases more severe than the weak-stiffness situation and reaches the peak value, followed by a rapid decline (representing the rockburst effect).

3.3. Mechanism Analysis. In order to interpret the rockburst effect under strong stiffness support, we categorize the stress evolution (Figure 13(b)) into three stages: the excavation stage A (static calculation), blasting vibration stage B (dynamic calculation) and rockburst stage C (static and equilibrium calculation). The surrounding rock mass completes step-by-step excavation and strong lining support at the excavation stage. The lining stress is highly concentrated and far exceeds the surrounding rock stress, which indicates the

Table 5: Mechanical parameters of rock mass and lining.

Mechanical parameters	Density (kg/m^3)	Elastic modulus (Pa)	Poisson's ratio	Cohesive strength (Pa)	Tensile strength (Pa)	Friction angle (°)	Shear expansion angle (°)
Rock mass (Tectonic granulite)	28.8	5.5×10^{10}	0.267	8×10^{6}	5×10^{6}	40.0	15
Weak-stiffness lining	28	2.5×10^{10}	0.2	1.5×10^{7}	1.3×10^{7}	35.0	0
Strong-stiffness lining	28	10×10^{10}	0.18	1.8×10^{7}	1.5×10^{7}	35.0	0

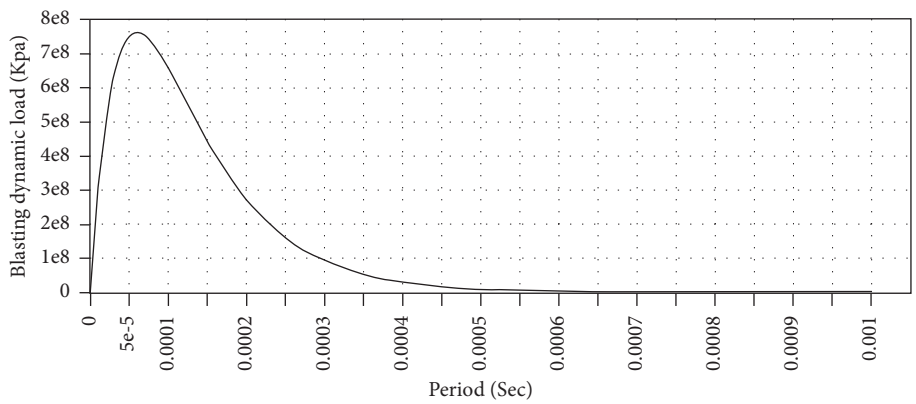

Figure 10: Time history curve of blasting dynamic load.

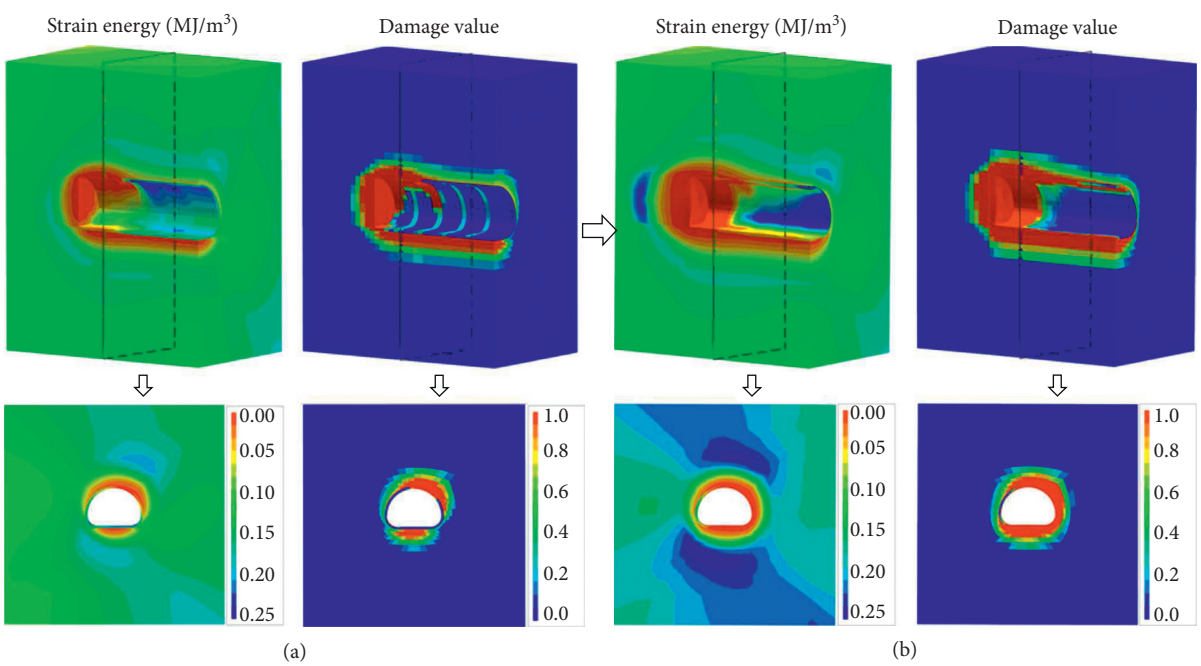

Figure 11: Simulation and comparison of rockburst effect (continuous model): (a) weak support stiffness; (b) strong support stiffness.

lining stress approaches the critical state of failure. In the blasting vibration stage, the lining has failed due to the stress fluctuation of blasting, and the lining stress decreases to a lower value. The failure of the lining causes the loss of support in the surrounding rock, which is similar to the sudden unloading effect in surrounding rock and results in the stress redistribution and rockburst stage.

Figure 14 presents the front stages (the excavation and blasting stages) of the strong-stiffness rockburst. The strong lining largely constrains the deformation of the surrounding rock at the excavation stage, and a large energy concentration occurs in the lining (the stress approaches the critical failure state); the damage value of the surrounding rock mass is not apparent. In the blasting vibration stage, the lining

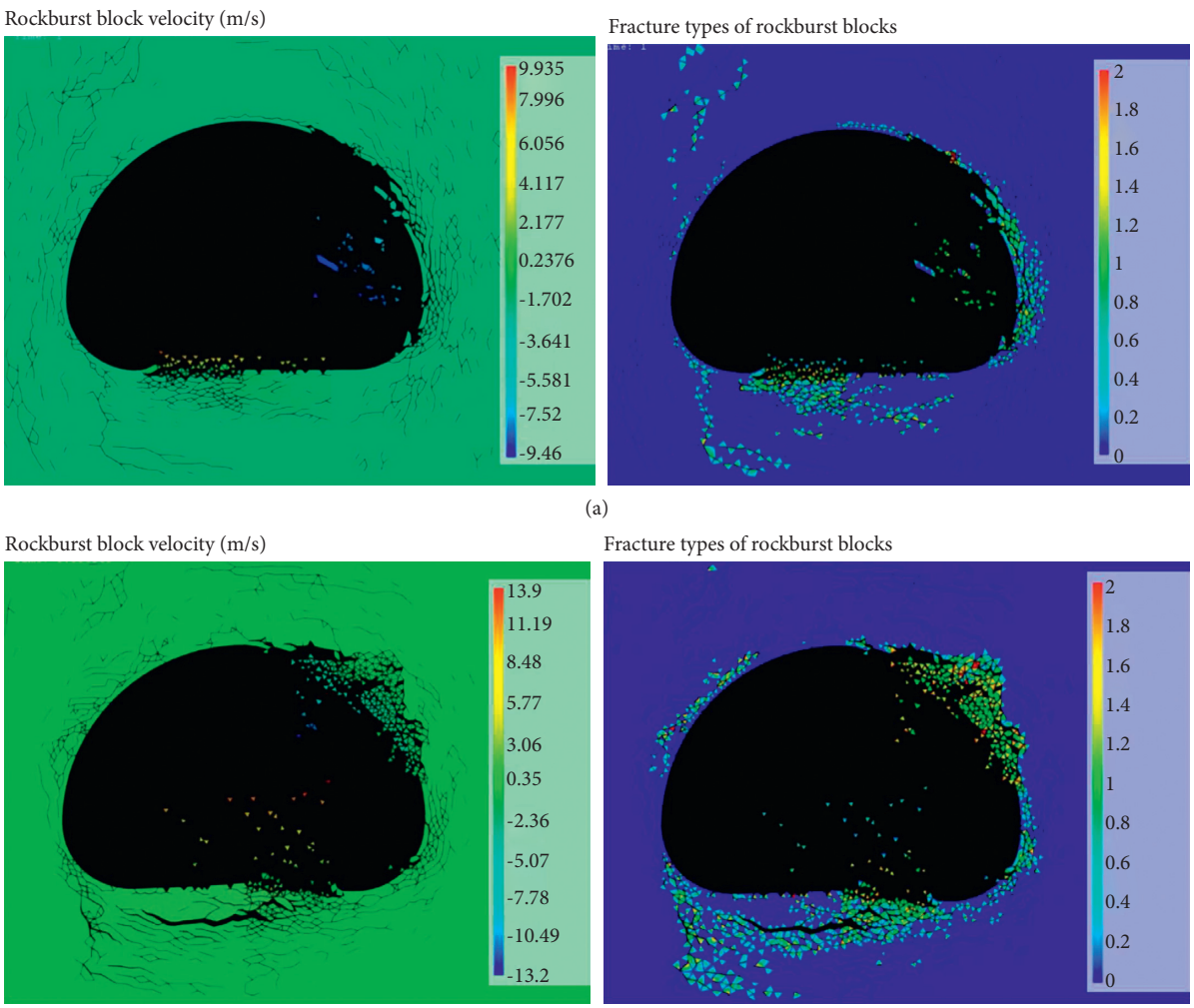

Figure 12: Simulation and comparison of rockburst disasters (discontinuous model): (a) weak support stiffness; (b) strong support stiffness.

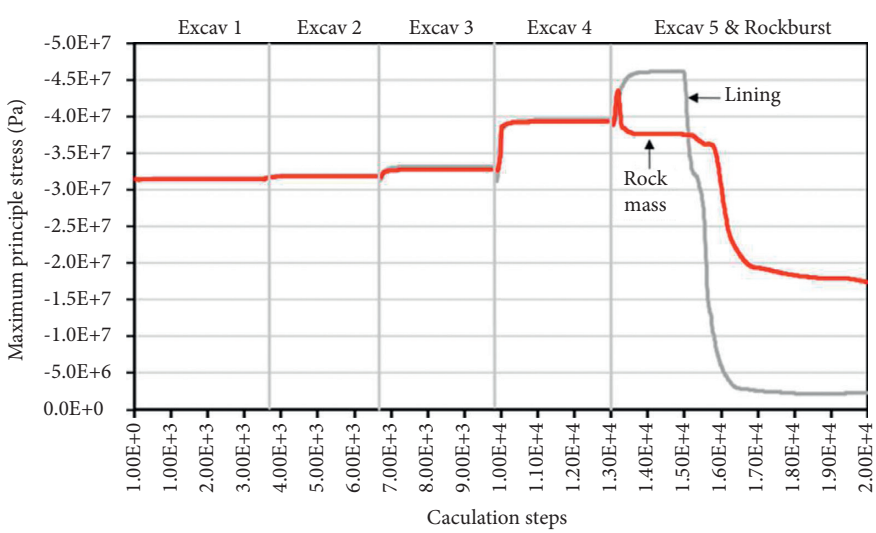

(a)

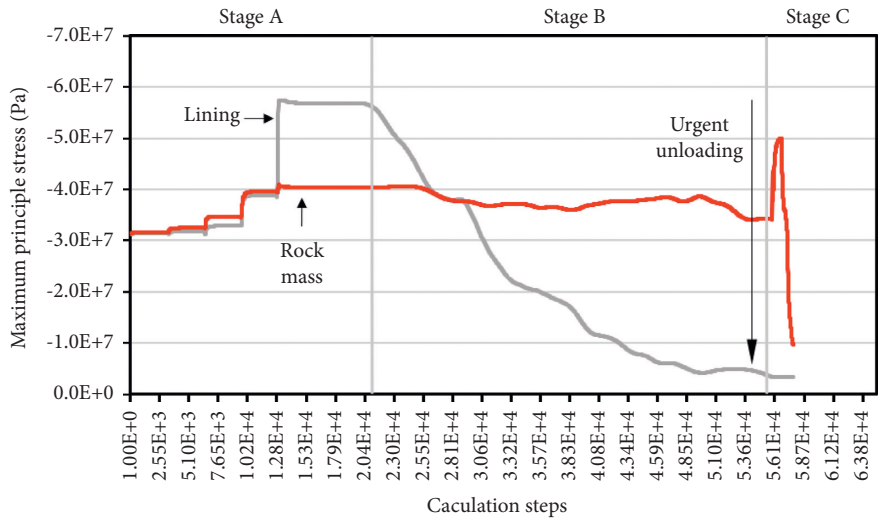

(b)

Figure 13: Stress monitoring of excavation and blasting during rockburst: (a) weak support stiffness; (b) strong support stiffness. Stage A is the excavation stage, stage B is the blasting vibration stage, and stage C is the rockburst stage.

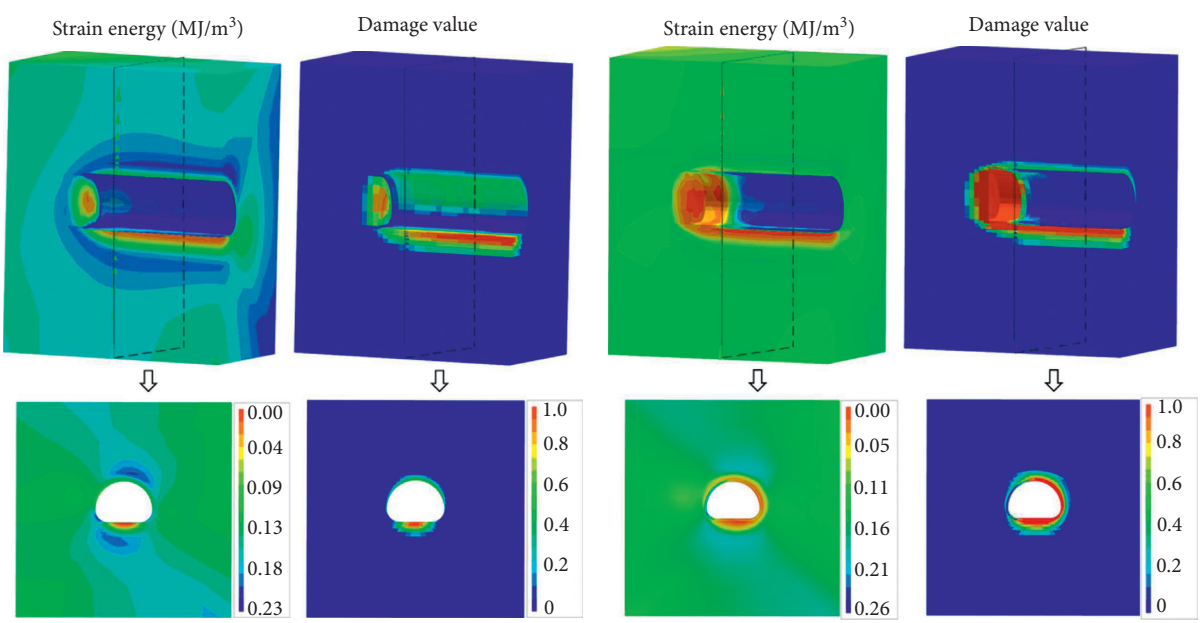

(a) (b)

Figure 14: The simulation of front stages of rockburst under strong-stiffness support(continuous model): (a) the excavation stage; (b) the blasting vibration stage.

cracks before the surrounding rock mass, and the crack number of the lining far exceeds that of the surrounding rock (Figure 15); the energy concentration of the lining is released and its damage value reaches one, which would result in sudden unloading and rockburst effect of the surrounding rock mass.

Figure 16 presents the site damage and failure of tunnel lining. The lining often cracks even in the absence of

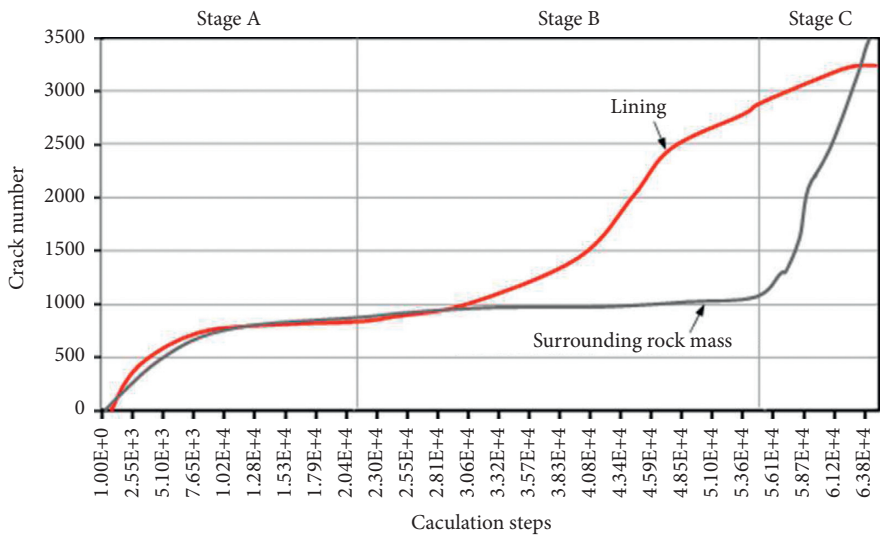

Figure 15: The evolution of crack number during strong-stiffness rockburst

Figure 16: The lining crack before and after rockburst: (a) before the rockburst; and (b) after the rockburst.

rockburst due to the strong stiffness support applied to the high-stress surrounding rock (Figure 16(a)), which provides evidence for the existence of the sudden unloading effect. When rockburst occurs, large-scale cracks of the surrounding rock and lining crack could occur, and its range could reach 30 m (Figure 16(b)), including the lining crack in the front stage of rockburst and the lining crack caused by the strong energy release of rockburst.

4. Conclusions

(1) The research shows that during the strong rock burst of Micangshan tunnel, the design of the initial support system greatly improves its strength and stiffness and poses a significant impact on the rockburst characteristics. The frequency of large-energy microseismic event and the developmental period of rockburst increases. The rockburst is characterized by high intensity, strong energy release and wide affected range.

(2) Rockbursts with unique fracture and microseismic characteristics are selected to evaluate the impact of support stiffness from weak to strong. Strong stiffness support makes the surrounding rock unable to give full play to its self-supporting capacity in the excavation, thus accumulating higher energy. In the development of rockburst, the frequency of microseismicity largely increases; the intensity of microseismic events increases obviously; the cumulative microseismic source average displacement increases significantly (or suddenly). The characteristics of these indicators can be used as precursors to potential strong rockburst.

(3) Understanding the correlation between support system and microseismicity of surrounding rock mass is helpful to judge the suitability of support system. Strong stiffness support changes the microseismic event type, and the proportion of events with both low energy and large apparent volume increases, which indicates the development of rockburst tend to generate energy accumulation and energy transfer. At the same time, the microseismic activity of surrounding rock results in greater surrounding rock pressure, and the supporting structure is in a high stress concentration and near failure state. These phenomena indicate that the selection of support system should make the surrounding rock exert its self-supporting capacity and release the pressure of the surrounding rock.

(4) The rockburst effect is numerically simulated to illustrate the influence of strong stiffness support on rockburst. The stress of lining is highly concentrated after tunnel excavation and the lining is easily failed under the impact of external loads (such as tunnel blasting), which causes an "sudden unloading" effect on the surrounding rock mass and results in a stronger effect of rockburst. The site photo confirms the unloading effect of the lining on the surrounding rock.

(5) This study is helpful to clarify the mechanism of deep underground engineering support system on surrounding rock fracture, establish the early warning and support criterion of deep engineering rockburst, which can ensure the safe and efficient engineering activities. However, our findings could be subject to the particularity of engineering and geological conditions. It is necessary to further explore the mechanical effects of support system on rockburst and reveal the interaction between support system and microseismicity.

Data Availability

The underlying data supporting the results of our study are unavailable.

Conflicts of Interest

No potential conflict of interest was reported by the authors.

Acknowledgments

The authors acknowledge the financial support from the Cooperative Project of National Defense Engineering Research Institute of Academy of Military Sciences (contract No. 2019-JKGF-C01-1003); National Natural Science Foundation of China (grant No. 41807255).

References

[1] G.-L. Feng, X.-T. Feng, B.-R. Chen, Y.-X. Xiao, and Y. Yu, "A microseismic method for dynamic warning of rockburst development processes in tunnels," *Rock Mechanics And Rock Engineering*, vol. 48, no. 5, pp. 2061–2076, 2015.

[2] T. Li, C. Ma, M. Zhu, L. Meng, and G. Chen, "Geomechanical types and mechanical analyses of rockbursts," *Engineering Geology*, vol. 222, pp. 72–83, 2017.

[3] H.-P. Xie, F. Gao, Y. Ju, R. Zhang, M.-Z. Gao, and J.-H. Deng, "Novel idea and disruptive technologies for the exploration and research of deep earth," *Engineering science and technology*, vol. 49, no. 1, pp. 1–8, 2017.

[4] Y. Yu, X.-T. Feng, C.-J. Xu, B.-R. Chen, Y.-X. Xiao, and G.-L. Feng, "Spatial fractal structure of microseismic events for different types of rockburst in deeply buried tunnels," *International Journal of Geomechanics*, vol. 20, no. 4, 2020.

[5] M.-W. Wang, Q.-Y. Liu, X. Wang, F.-Q. Shen, and J.-L. Jin, "Prediction of rockburst based on multidimensional connection cloud model and set pair analysis," *International Journal of Geomechanics*, vol. 20, no. 1, 2020.

[6] A. Keneti and B.-A. Sainsbury, "Review of published rockburst events and their contributing factors," *Engineering Geology*, vol. 246, pp. 361–373, 2018.

[7] F. Meng, H. Zhou, Z. Wang et al., "Experimental study of factors affecting fault slip rockbursts in deeply buried hard rock tunnels," *Bulletin of Engineering Geology and the Environment*, vol. 76, no. 3, pp. 1167–1182, 2017.

[8] C.-C. Ma, T.-B. Li, and H.-L. Xing, "Microseismic and precursor analysis of high-stress hazards in tunnels: a case comparison of rockburst and fall of ground," *Engineering Geology*, vol. 265, pp. 105–435, 2020.

[9] B.-A. Sainsbury and N. Kurucuk, "Impact of intact rock properties on proneness to rockbursting," *Bulletin of Engineering Geology and the Environment*, vol. 79, no. 4, pp. 1939–1946, 2020.

[10] N. W. Xu, T. B. Li, F. Dai, R. Zhang, C. A. Tang, and L. X. Tang, "Microseismic monitoring of strainburst activities in deep tunnels at the jinping II hydropower station, China," *Rock Mechanics and Rock Engineering*, vol. 49, no. 3, pp. 981–1000, 2016.

[11] H. Zhou, F. Meng, C. Zhang, D. Hu, F. Yang, and J. Lu, "Analysis of rockburst mechanisms induced by structural planes in deep tunnels," *Bulletin of Engineering Geology and the Environment*, vol. 74, no. 4, pp. 1435–1451, 2015.

[12] Y. Fan, W.-B. Lu, Y.-H. Zhou, P.-Z. Yan, D. Leng, and M. Chen, "Influence of tunneling methods on the strainburst characteristics during the excavation of deep rock masses," *Engineering Geology*, vol. 201, pp. 85–95, 2015.

[13] G.-Y. Hu, "Influence of support thickness on rockburst strength," *Inner Mongolia Science and Technology and Economics*, vol. 9, pp. 54–56, 2018.

[14] J. Li, L.-Q. Liu, G.-W. Miu, H.-X. He, and M.-H. Li, "Research and application of deep mining roadway support technology in Chener Gold Mine," *Gold*, vol. 39, no. 4, pp. 31–35, 2018.

[15] K. Chen, "Study of strainburst process under rockbolt support condition," Master's Thesis, Guangxi University, Nanning, China, 2017.

[16] W. D. Ortlepp, "High ground displacement velocities associated with rockburst damage," in *Proceedings of the Third International Symposium on Rockbursts and Seismicity in Mines*, Kingston, Ontario, 1993.

[17] W.-D. Ortlepp, *Rock Fracture and Rockbursts: An Illustrative Study*, The South African Institute of Mining and Metallurgy, Johannesburg, South Africa, 1997.

[18] G.-T. Huang, "Research on the prediction and prevention of rockburst of Cuihuashan super long tunnel in Qinling Mountain," Master's Thesis, Xi'an University of Architectural Science and Technology, Xi'an, China, 2013.

[19] J. M. Alcott, P. K. Kaiser, and B. P. Simser, "Use of microseismic source parameters for rockburst hazard assessment," *Pure and Applied Geophysics*, vol. 153, no. 1, pp. 41–65, 1998.

[20] G. K. Ghosh and C. Sivakumar, "Application of underground microseismic monitoring for ground failure and secure longwall coal mining operation: a case study in an Indian mine," *Journal of Applied Geophysics*, vol. 150, pp. 21–39, 2018.

[21] C. Ma, Y. Jiang, and T. Li, "Gravitational search algorithm for microseismic source location in tunneling: performance analysis and engineering case study," *Rock Mechanics and Rock Engineering*, vol. 52, no. 10, pp. 3999–4016, 2019.

[22] P.-M. Shearer, *Introduction to Seismology*, Cambridge: Cambridge University Press, Cambridge, UK, 2009.

[23] H. Zhang, C.-C. Ma, and T.-B. Li, "Quantitative evaluation of the "Non-Enclosed" microseismic array: a case study in a deeply buried twin-tube tunnel," *Energies*, vol. 12, no. 10, 2019.

[24] D. Zhuang, K. Ma, C. Tang, Z. Liang, Z. Wang, and F.-Q. Gong, "Microseismic monitoring of energy changes in deep tunnels during the TBM tunneling of the jinping II hydropower station," *Advances in Civil Engineering*, vol. 2018, Article ID 5364628, 15 pages, 2018.

[25] Y. Zhao, T. Yang, M. Bohnhoff et al., "Study of the rock mass failure process and mechanisms during the transformation from open-pit to underground mining based on microseismic monitoring," *Rock Mechanics and Rock Engineering*, vol. 51, no. 5, pp. 1473–1493, 2018.

[26] L. Hu, X.-T. Feng, Y.-X. Xiao et al., "Characteristics of the microseismicity resulting from the construction of a deeply-buried shaft," *Tunnelling and Underground Space Technology*, vol. 85, pp. 114–127, 2019.

[27] W.-J. Gale, K.-A. Heasley, and A.-T. Iannacchione, "Rock damage characterisation from microseismic monitoring," in *Proceedings of the 38th U.S. Rock Mechanics Symposium*, Washington, DC, USA, July 2001.

[28] C.-C. Ma, T.-B. Li, H. Zhang, Y.-X. Han, and X.-H. Zhou, "A preliminary study on the effect of the support system stiffness on the microseismic characteristics of rockburst," *Journal of rock mechanics and engineering*, vol. 38, pp. 2976–2987, 2019.

[29] C.-L. Li, "Rockburst conditions and rockburst support," *Journal of rock mechanics and engineering*, vol. 38, no. 4, pp. 1–9, 2019.

[30] T. C. Hanks and H. Kanamori, "A moment magnitude scale," *Journal of Geophysical Research*, vol. 84, no. B5, pp. 2348–2350, 1979.

[31] F. Dai, B. Li, N. Xu, and Y. Zhu, "Microseismic early warning of surrounding rock mass deformation in the underground powerhouse of the Houziyan hydropower station, China," *Tunnelling and Underground Space Technology*, vol. 62, pp. 64–74, 2017.

[32] H. Zhang, J. Zeng, J.-J. Ma et al., "Time series prediction of microseismic multi-parameter related to rockburst based on deep learning," *Rock Mechanics and Rock Engineering*, vol. 54, no. 12, pp. 1–23, 2021.

Hindawi
Advances in Civil Engineering
Volume 2022, Article ID 1917836, 10 pages
https://doi.org/10.1155/2022/1917836

Research Article

Dynamic Rock-Breaking Process of TBM Disc Cutters and Response Mechanism of Rock Mass Based on Discrete Element

Qinglong Zhang,[1] **Yanwen Zhu**,[1] **Canxun Du**,[2] **Sanlin Du**,[2] **Kun Shao**,[2] **and Zhihao Jin**[1]

[1]*Department of Civil Engineering, School of Civil and Resource Engineering, University of Science and Technology Beijing, Beijing 100083, China*
[2]*Huaneng Tibet Hydropower Safety Engineering Technology Research Center, Tibet, China*

Correspondence should be addressed to Qinglong Zhang; qlzhang@ustb.edu.cn

Received 9 December 2021; Accepted 27 December 2021; Published 11 January 2022

Academic Editor: Mingfeng Lei

Rock-breaking efficiency of full-face rock tunnel boring machine (TBM) is closely related to the performance of the disc cutter and the characteristics of the rock mass. In the point of view of mesomechanics, the particle flow code (PFC) is used to establish a numerical model of the rock mass and the disc cutter, and the process of TBM disc cutter intrusion into the rock mass is analyzed. The dynamic response mechanism and crack evolution process of the rock mass under the action of the disc cutter are studied on the basis of micromechanics, and the relationship between the rock mass crack, penetration, and cutting force during the intrusion of the disc cutter is revealed. The sensitivity analysis is carried out on the confining pressure conditions and the influence parameters of the disc cutter spacing. The results show that the rock breaking by disc cutter undergoes the transformation characteristics of compaction, shearing, and tension failure modes, and the failure process of the rock mass is the joint action of tension and shear. In the whole process of rock breaking, the disc cutter has the phenomenon of repeated loading-unloading alternation and leaping rock breaking; after the penetration of the disc cutter reached 9.0 mm, penetration creaks begin to appear on the surface of the rock mass; the penetration was obviously reduced with the increase of confining pressure, and it is mainly the penetration cracks on the surface; after the disc cutter spacing reaches 100.0 mm, there is no penetration crack between the two disc cutters. The research conclusion can provide a reference for the disc cutter optimization design.

1. Introduction

Full-face rock tunnel boring machine (TBM) has been widely used in mining engineering, water conservancy and hydropower tunnels, highway tunnels, and other projects. The disc cutter, at the foremost end of TBM, is an important part of TBM, which determines whether it can effectively break rock and directly generate load on the surrounding rock to cause dynamic damage to the rock mass. In order to better achieve the destructive effect, the generation, propagation, failure mechanism, and mode transformation of rock cracks have become a hot topic that many scholars pay attention to, and it is of great significance to how to optimize the design of the disc cutter for efficient rock breaking [1–5].

In terms of the interaction between the disc cutter and the surrounding rock, around the rock-breaking mechanism of the TBM disc cutter, the predecessors have carried out relevant research works from the perspectives of theoretical analysis, indoor linear cutting machine test, and numerical simulation [6–17]. However, due to the hypothetical limitations of theoretical analysis, the high cost of laboratory tests, and the difficulty in dynamically observing crack propagation changes, it is difficult to effectively analyze the rock-breaking mechanism and interaction process of the disc cutter. Numerical software has been gradually applied to scientific research due to its low computational cost, easy real-time observation of the state, and multifactor simulation experiments [18, 19]. Some scholars have achieved some research results by using the discrete medium mechanics method

[20–26]. Oñate and Rojek [27] analyzed the dynamic behavior of cutting geological rocks by the discrete element method. Kou et al. [28, 29] made a comprehensive study on the rock failure mode, the chip formation process, and the relationship between cutting force and displacement. Gong et al. [30] studied the rock fragmentation mode under the action of the disc cutter through the disc cutter intrusion discrete element model. Kong et al. [31] operated the particle flow code (PFC) to establish a rock-cutting model and then analyzed the effects of different joint orientations. Moon and Oh [32] simulated the crack formation process induced by multi-indenters to study the optimum cutting conditions by PFC-2D. Choi and Lee [33] employed PFC to simulate three-dimensional dynamic fracturing failure of rock.

In terms of failure mechanism, many researchers have put forward different explanations, mainly including three theories of shear mechanism, tension mechanism, and comprehensive action mechanism. Some scholars believe that it is a composite process of shear failures and tensile failures. In 1966, Maurer [34], Cheatham and Gnirk [35], and Gnirk [36] revealed that there are both shear failure and tensile failure when the disc cutter acts on rocks. In 1975, Lawn and Wilshaw [37] believed that the brittle materials formed a block due to cracks caused by stretching under the action of the indenter. Cook et al. [38] simulated the rock intrusion process of the circular flat heads through a two-dimensional symmetric linear elastic finite element model.

In terms of rock-breaking simulation with TBM disc cutter, the particle discrete element method focuses on the analysis of the damage and fracture mechanism of materials from the perspectives of the mesoscale mechanism, which can realize the numerical experiment and analysis of the meso-brittle fracture mechanism and progressive failure process of rock materials [39]. In the rock-breaking simulation of the disc cutter, the accurate simulation of the crack generation and propagation process is particularly important for revealing the rock-breaking mechanism. The existing simulation studies mostly use the development of the plastic zone instead of the rock crack range [7, 40–44], which cannot truly reflect the generation and propagation of radial and longitudinal cracks and the separation process between rock slices after the disc cutter is pressed into the rock. In this paper, the particle flow code (PFC) [45], which can better simulate the crack propagation of rock (body), is adopted. Based on the study and analysis of the rock-breaking mechanism of the TBM disc cutter, the dynamic response mechanism of rock mass under the action of the TBM disc cutter is studied by the particle discrete element method from the mesopoint of view. And the influence of the confining pressure conditions and the disc cutter spacing on the rock crack properties, quantity, disc cutter reaction force, rock-breaking effect, etc., are further simulated and analyzed. The research results can provide a reference for TBM type selection and disc cutter design.

2. Rock Parameter Calibration

As a numerical simulation method based on discontinuous medium theory and mesomechanics, the particle discrete element method can simulate the failure mechanism of rock materials from the perspective of mesomechanics and simultaneously reflect the micro-mesostructure characteristics and macromechanical behavior of materials. The simulation of the physical prototype by the particle flow method is mainly completed by defining the meso-parameters and macroboundary conditions of particle bonding. However, its mesoparameters generally cannot be directly and simply connected with the macroscopic physical and mechanical parameters of the rock. The macro-parameters are affected by multiple mesoparameters. Currently, it is impossible to deduce the accurate quantitative relationship between macroparameters and mesoparameters from a theoretical perspective. Meanwhile, it is difficult to directly measure mesoparameters through laboratory or on-site tests. Therefore, it is necessary to calibrate the meso-parameters. Generally, uniaxial compression and Brazilian splitting tests can be used to determine the macroscopic parameters that characterize rock mechanical behavior, mainly including uniaxial compressive strength f_c, tensile strength t_c, elastic modulus E, and Poisson's ratio v.

It is calibrated using the results of uniaxial compression and the Brazilian splitting test of marble (diameter × height: 50 mm × 100 mm and 50 mm × 25 mm, respectively). The macrophysical and mechanical parameters of the marble in the laboratory test are shown in Table 1, and the meso-mechanical parameters of the calibrated particle flow model are shown in Table 2. The maximum and minimum particle radius ratio (R_{max}/R_{min}) is 2.0, and the minimum particle radius is 1.2 mm. Figure 1 shows the stress-strain curve and the failure of the rock sample in the uniaxial compression and Brazilian splitting tests under corresponding meso-parameters. It can be seen from the figure that the rock sample in the uniaxial compression numerical test has a conical splitting failure, while the rock sample in the Brazilian splitting numerical test has a central crack penetration failure. The stress-strain curve, failure shape, and peak strength are all consistent with the laboratory test results. The calibrated parameters can be used to analyze the rock-breaking mechanism of the disc cutter.

3. Simulation of Rock Fragmentation by TBM Disc Cutters

3.1. Results and Analysis. In the process of rock breaking, the disc cutter ring contacts the rock, and the rock is penetrated by the pressure of the cutter head, and cracks are generated to achieve the purpose of rock breaking. The commonly used 17-inch disc cutter is adopted, the wall combination is used to simulate the disc cutter ring, and the model is 200.0 mm wide and 100.0 mm high. Through the servo mechanism of the upper and lower walls, preloading consolidation is performed to simulate the natural formation process of the rock mass. The left, right, and bottom walls of the sample are all rigidly constrained to limit the displacement of the rock mass. After stabilization, the top rigid wall is deleted and the stress is released, which is consistent with the on-site TBM tunneling conditions [46]. The intrusion speed of the disc cutter is set to 0.5 mm/s and the final penetration to 15.0 mm, the macro- and microinformation of the rock

Table 1: Macroscopic physical and mechanical parameters of rock materials.

Density ρ (kg/m^3)	Elastic modulus E (GPa)	Uniaxial tensile strength f_c (MPa)	Tensile strength t_c (MPa)	Poisson's ratio ν
2420.0	24.0	93.5	10.9	0.24

Table 2: Mesomechanical parameters of the particle flow model.

Density ρ (kg/m^3)	Normal stiffness (GPa)	Tangential stiffness (GPa)	Normal strength (MPa)	Tangential strength (MPa)	Frictional coefficient
2420.0	18.0	18.0	55.0	35.0	0.5

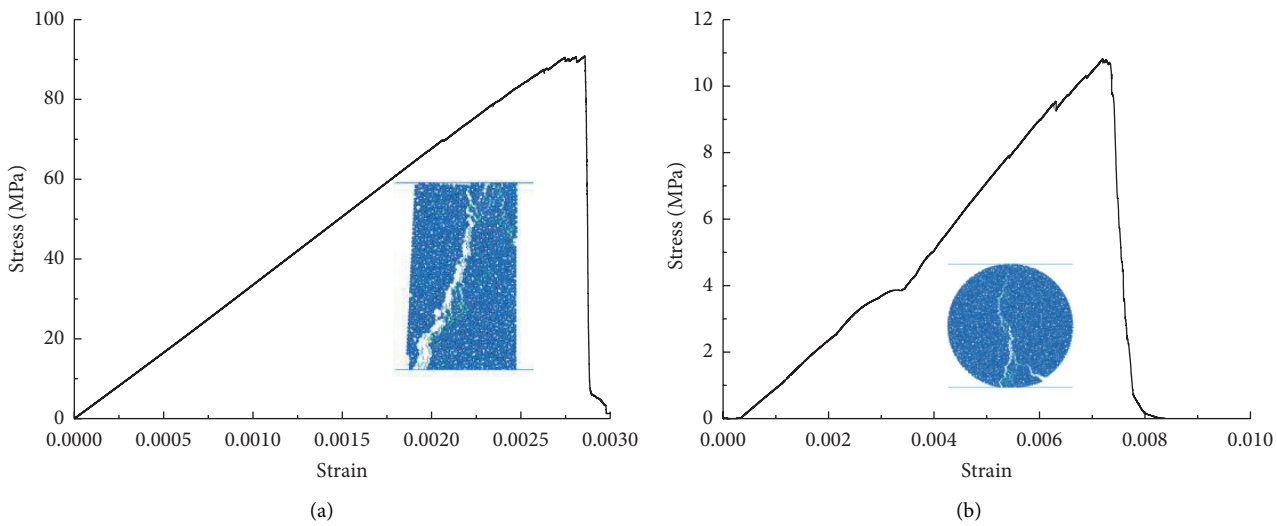

Figure 1: Calibration of mesoparameters of the particle flow model: (a) uniaxial compression compressive strength calibration; (b) Brazilian splitting tensile strength calibration.

sample are recorded during the entire intrusion process. Figure 2 shows the generation and expansion process of cracks and rock failure under the action of thrust at different penetration depths.

It can be seen from the figure that when the disc cutter penetrates 1.0 mm, microcracks are generated under the disc cutter. When the disc cutter penetrates 3.0 mm, the compressive stress is concentrated due to the obvious extrusion effect of the disc cutter on the rock mass, and the microcracks under the disc cutter begin to form penetrating diameter and lateral cracks. When penetrating 6.0 mm, the rock mass is continuously squeezed and fractured, and long cracks begin to form. This kind of fracture cannot reach the peeling off of the rock, but it is an inevitable process for the disc cutter to press into the rock. At 9.0 mm, a semicircular plastic failure zone is formed around the disc cutter, and a part of the lateral cracks gradually expands, and microcracks are formed on the surface of the rock without the action of the disc cutter, which intersects with the rock surface to form a through crack. At 12.0 mm, the large intact rock fragments on both sides of the disc cutter separated from the rock mass and began to fall off. With the increase of penetration, the increasing trend of failure area slows down to 15.0 mm, but the radial and lateral cracks still expand to a certain extent. In summary, after the penetration is 12.0 mm, the crack propagation effect is not obvious by increasing the penetration.

The change of vertical force of the disc cutter during penetration is shown in Figure 3. At the initial stage of penetration, the vertical force of the disc cutter increases nearly linearly with the increase of penetration. When the penetration reaches 1.0 mm, the vertical force drops abruptly, and the disc cutter begins to unload. However, the vertical force fluctuating up and down during the entire penetration indicates that the disc cutter has the alternating state of loading and unloading repeatedly, and the rock-breaking phenomenon of leaping forward is shown in the actual process. The main reason is that extrusion and collapse occur under the action of vertical force, and the resistance suddenly decreases. When the disc cutter continues to penetrate, the rock particles continue to peel off at the front end of the blade, and a small volume of rock debris falls out, resulting in a small range of fluctuation of vertical cutting force. In the vertical force curve, the rising stage of the curve indicates that the disc cutter penetrates the rock mass, and the disc cutter force continues to rise with the increase of penetration depth. In the meanwhile, the rock sample gradually forms broken zones, microcracks, and macrocracks and tends to penetrate. When the macrocracks penetrate to form the rock fragments and separate them from the rock mass, it causes the "void" phenomenon of the cutter, the disc cutter force dropped sharply, and a "leap forward" fracture of the rock occurs. After continuous small-

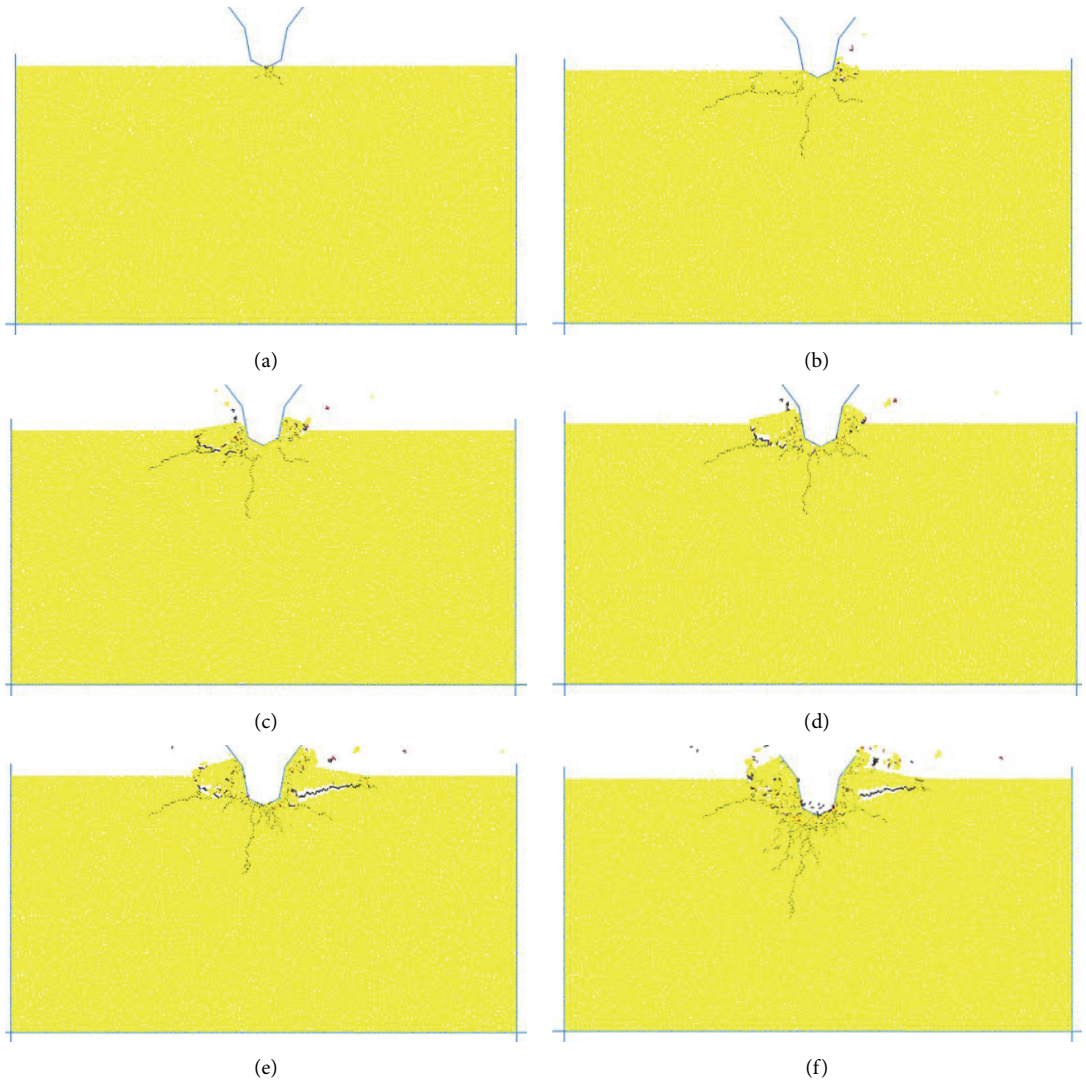

Figure 2: Failure characteristics of rock mass during rock breaking by disc cutter. (a) Intrusion 1.0 mm. (b) Intrusion 3.0 mm. (c) Intrusion 6.0 mm. (d) Intrusion 9.0 mm. (e) Intrusion 12.0 mm. (f) Intrusion 15.0 mm.

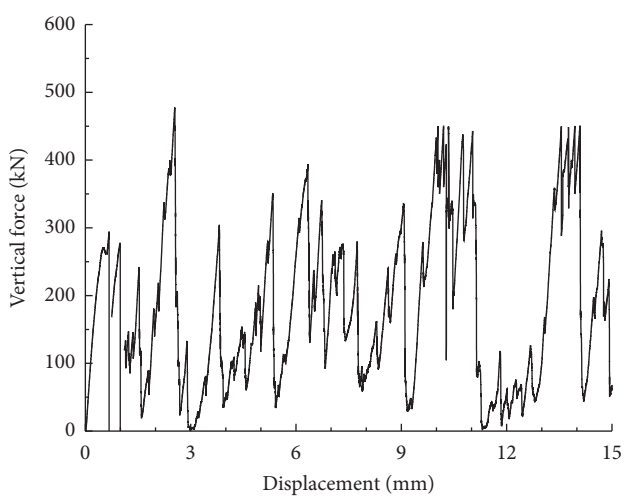

Figure 3: Vertical force in the rock-breaking process of disc cutter.

volume disintegration, the contact area between the disc cutter and the rock gradually increases, until the full-width contact is reached, and another large collapse occurs. Therefore, the process of the disc cutter intruding into the rock is a continuous cycle composed of several small collapses and one large collapse, which leads to the leap forward crushing of the rock under the action of the disc cutter.

3.2. Discussion on Mesomechanism of Rock Breaking by Disc Cutter. Compared with other numerical methods, PFC has unique advantages in the analysis of mesocharacteristics. It can monitor the mesoforce field and the development and evolution process of microcracks in the process of rock deformation and failure in real time and can reveal the mesomechanism of rock breaking by the disc-shaped disc cutter.

The change of the number of microcracks during the intrusion of the disc cutter is shown in Figure 4. During the initial penetration, the main result of the compression under the disc cutter is the formation of a dense core. Meanwhile, the number of cracks is small. With the increase of the penetration load, microcracks increase sharply. In a certain period, the cracks increase by leaps, and the phenomenon of leaping growth becomes more obvious in the later period of penetration, indicating that the cracks expand rapidly to form a large number of broken rock blocks in the process of rock fracture. Both tensile and shear cracks appear in the rock-breaking process of the disc cutter, indicating that this process is a joint failure mode of tension and shear. The number of shear cracks is always greater than that of tensile cracks, and the final number of shear microcracks is nearly 5 times that of tensile microcracks. The whole rock-breaking process is dominated by shear microcracks.

Figure 5 shows the distribution characteristics of tensile and shear cracks in the process of rock mass rupture. Red represents tensile cracks, and black represents shear cracks. Tensile and shear cracks appear simultaneously in the failure area under the edge of the disc cutter, with more shear cracks and fewer tensile cracks. Under continuous loading, the cracks gradually extend downwards, and then, the tensile cracks and shear cracks under the disc cutter increase rapidly, forming a concentrated failure powder core area. The cracks far away from the disc cutter are mostly shear cracks, which are similar to uniaxial compression, indicating that the shear action in the rock-breaking process dominates the propagation and development of the cracks and ultimately leads to the deep failure of the rock mass and the generation of large rock slag. The rock breaking by the disc cutter undergoes the transformation characteristics of compaction, shear, and tension failure modes.

4. Sensitivity Analysis of Influencing Parameters

4.1. Different Confining Pressures. Confining pressure conditions affect the generation and propagation of cracks, lead to different fracture modes, and then macroscopically affect the rock-breaking effect of the disc cutter. To explore the rock-breaking mechanism and its influence on the rock-

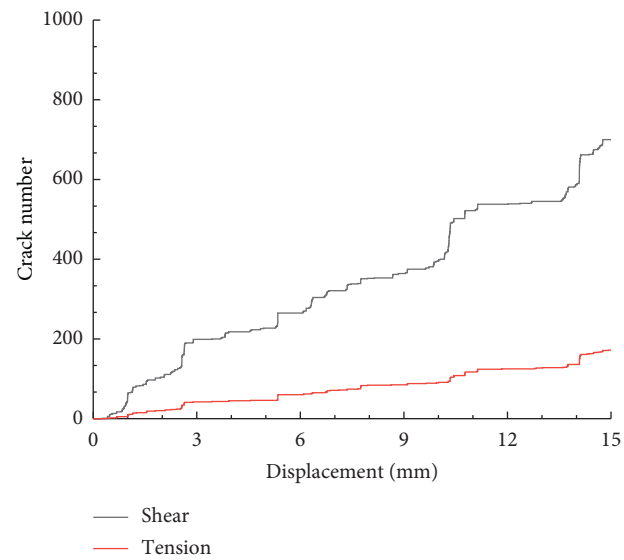

Figure 4: Number of cracks in the rock-breaking process of the disc cutter.

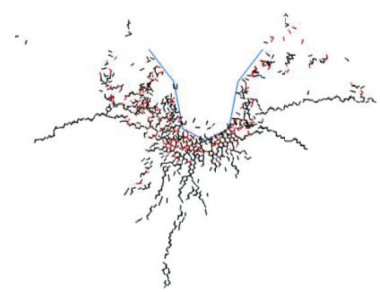

Figure 5: Failure characteristics of rock mass in the process of rock breaking by disc cutter.

breaking effect under different burial depths, the particle flow simulation of single disc cutter intrusion into fractured rock mass under different confining pressures was carried out. The confining pressure is set to 0.0, 10.0, 20.0, 30.0, and 40.0 MPa, respectively.

As shown in Figure 6, when the confining pressure is low, the longitudinal cracks develop obviously and develop deep into the rock mass, the damage depth of the rock mass is relatively large, and the development of transverse cracks is not obvious, mainly manifested in the fracture of the rock mass around the cutterhead. With the increase of the confining pressure, the longitudinal crack propagation is restrained, mainly to the transverse crack, the damage depth of the rock mass is small, and the transverse crack propagates obviously and gradually penetrates to form a large block falling off. Although high confining pressure is not conducive to the development of longitudinal cracks, it is more favorable to the development of lateral cracks. The cracks gradually extend to the free surface of the rock mass and are easy to intersect with the cracks generated by the adjacent disc cutters to generate exfoliated rock fragments. However, the radial crack expansion depth is small, and the overall rock-breaking effect is not ideal.

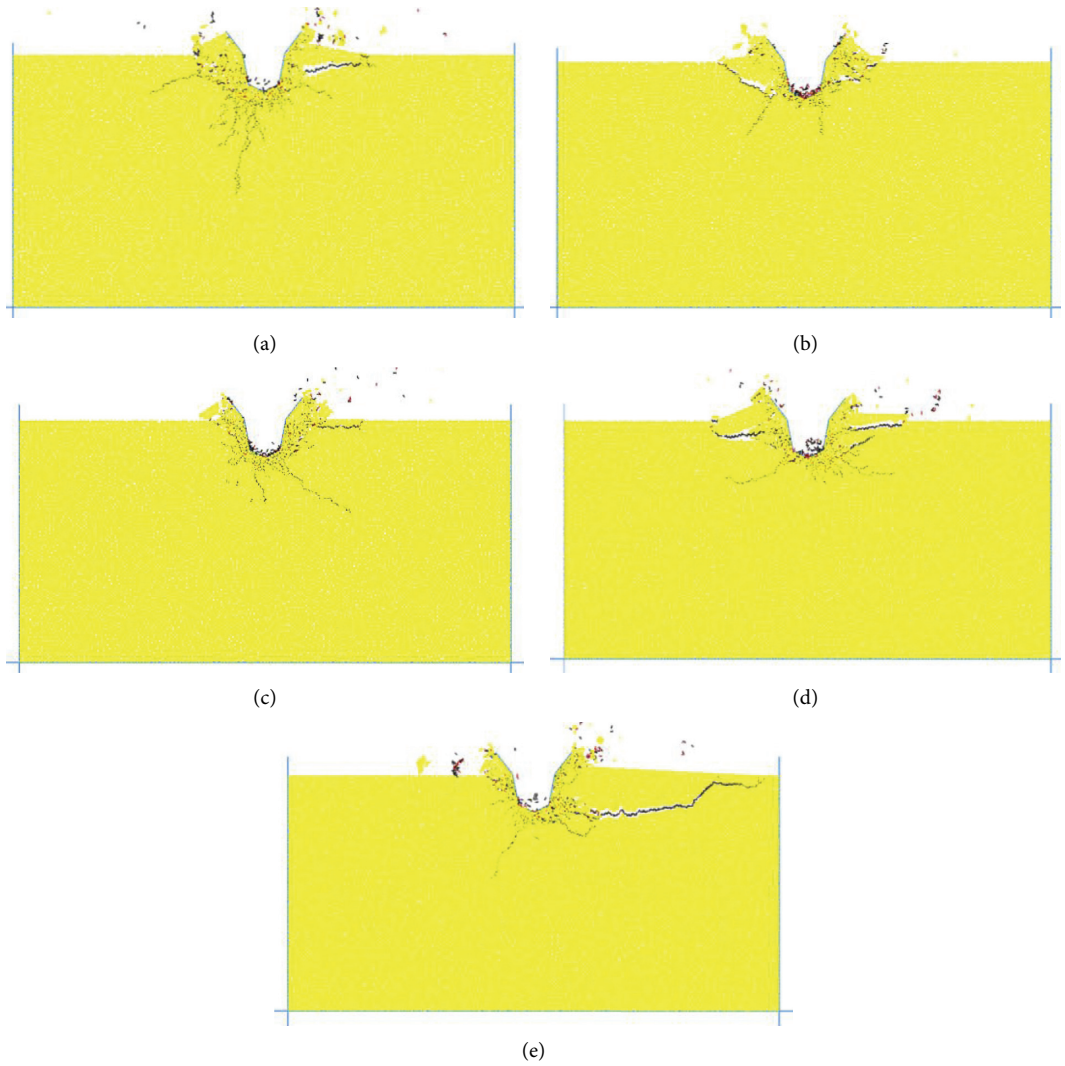

Figure 6: Failure characteristics of rock mass under different confining pressures: (a) 0.0 MPa, (b) 10.0 MPa, (c) 20.0 MPa, (d) 30.0 MPa, and (e) 40.0 MPa.

The number of microcracks under confining pressure is shown in Figure 7. The number of cracks under confining pressure is lower than that under no confining pressure. With the increase of confining pressure, the number of cracks gradually decreases. The vertical force of the disc cutter under confining pressure is shown in Figure 8. As the confining pressure increases, the disc cutter force gradually increases. This means that the confining pressure will limit the propagation of cracks. It is difficult to break the rock under confining pressure conditions than without confining pressure, and the degree of difficulty increases with the increase of confining pressure. The increase in confining pressure will inhibit the initiation of edge cracks and the propagation of the intermediate cracks in the crushing zone, and in the meanwhile, the depth of rock breaking will decrease, which is consistent with the conclusions obtained by Liu et al. [29] through theoretical derivation and laboratory experiments.

Synthesizing the rock-breaking modes of the disc cutter under different confining pressures, it can be obtained that the crack propagation has the following characteristics: (1) with the increase of the confining pressure, the depth of the crushing zone under the disc cutter becomes significantly smaller, that is, the increase in crustal stress will reduce the penetration depth of the disc cutter under the same disc cutter force; (2) the existence of confining pressure inhibits the longitudinal propagation of the central crack, which is beneficial to the propagation of transverse cracks; and (3) as the confining pressure increases, the depth and area of the crushing zone decrease, and the proportion of microcracks decreases.

4.2. Hob Spacing. Reasonable disc cutter spacing plays an important role in improving the rock-breaking ability of the disc cutter head and prolonging the service life of the disc cutter. In engineering, the disc cutter spacing of the cutter head is generally 60.0~120.0 mm. In this section, the research method of dual disc cutters invading rock samples at the same time is used to analyze the influence of the distance

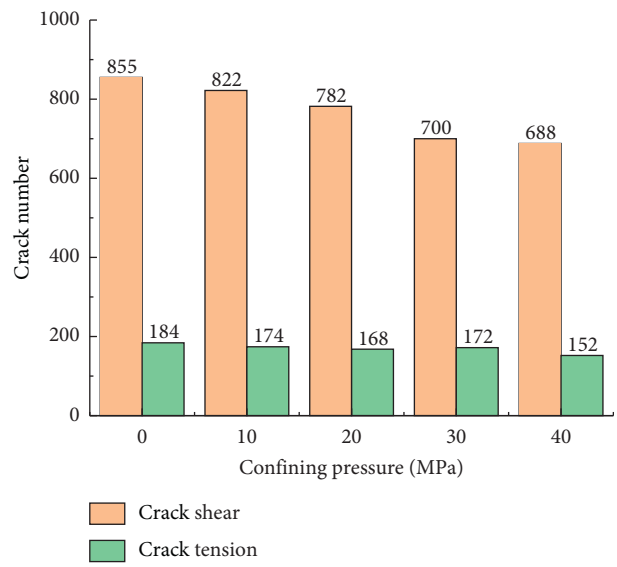

Figure 7: Statistics of the number of cracks under different disc cutter spacing.

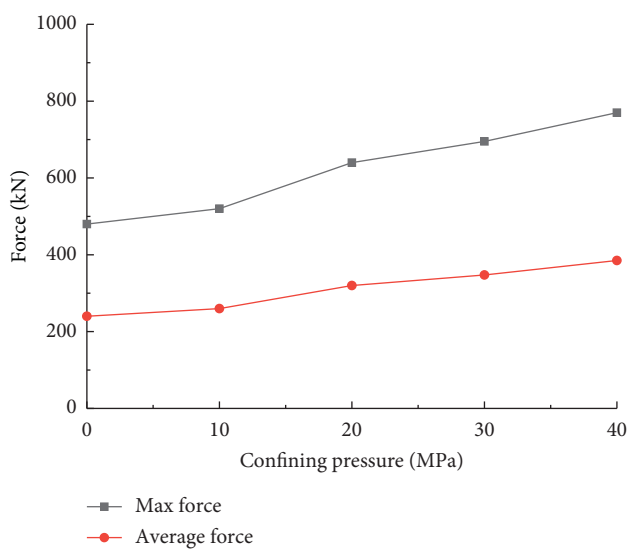

Figure 8: Vertical force of disc cutter under different confining pressures.

between the disc cutters on the rock-breaking process by means of numerical simulation.

When the distance between the disc cutters is small, the loaded energy causes the rock between the disc cutter edge to be broken, and the crack propagation mechanism is not fully utilized, resulting in low crushing efficiency (see Figure 9(a)). When the cutter spacing gradually increases but is less than 100.0 mm, the damage and fracture of the rock mass between the hobs will cause the crack to penetrate at a certain depth and form flaky rock ballast (see Figure 9(c)). The size of the rock ballast increases with the increase of the disc cutter spacing. When the disc cutter spacing is 120.0 mm, the damage caused by adjacent disc cutters did not cause the crack to penetrate, and the rock in the middle of the disc cutters forms an isolated rock ridge (see Figure 9(d)).

The number of cracks under different cutter spacing is shown in Figure 10. The number of cracks increases first and then decreases when the disc cutter spacing is from 60.0 mm to 120.0 mm. The number of cracks is the largest when the spacing is 80.0 mm. Therefore, if the disc cutter spacing is too large, the interaction between adjacent disc cutters cannot be fully utilized. In the process of cutting, there is an optimal disc cutter spacing, which makes the cutting specific energy consumption of the disc cutter lowest. When the disc cutters are arranged according to this optimal disc cutter spacing, taking the disc cutter spacing to an appropriate value will obtain higher cutting efficiency.

It can be seen from the figure that, within a certain range, the fragmentation of rock ballast increases with the increase of the disc cutter spacing. When the distance between the disc cutters is small, a large part of the rock between the two

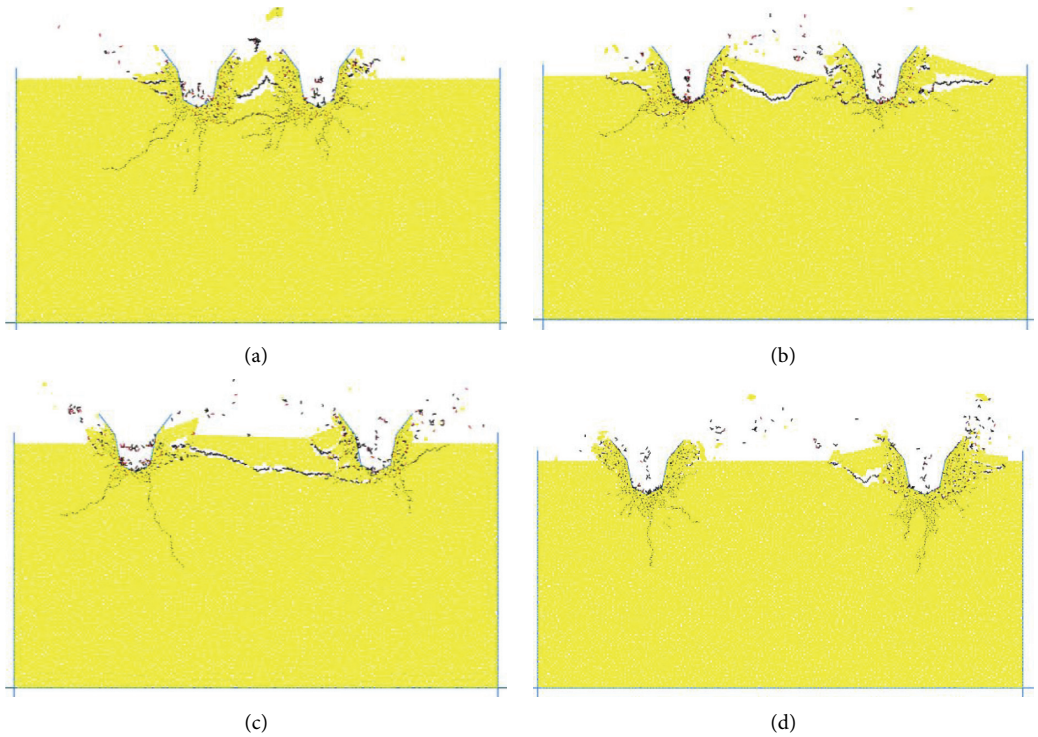

Figure 9: Crack propagation under different disc cutter spacing: (a) 60.0 mm, (b) 80.0 mm, (c) 100.0 mm, and (d) 120.0 mm.

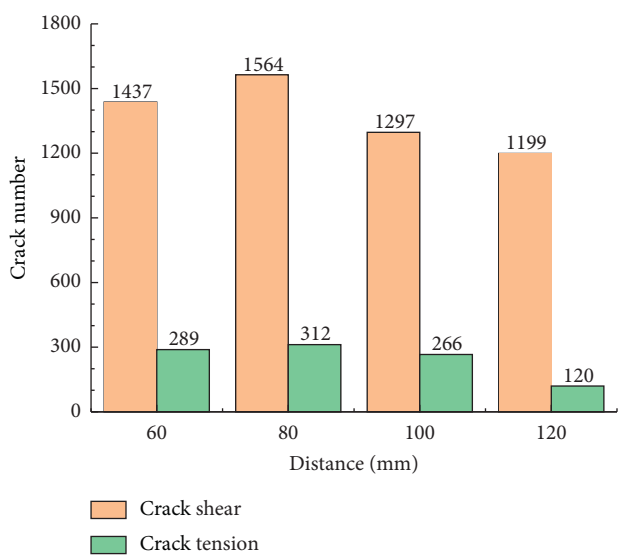

Figure 10: Statistics of the number of cracks under different disc cutter spacing.

disc cutters is still in the crushing zone, and the rock-breaking energy of the disc cutters fails to damage the deep rock, but to a large extent transforms into the crushing energy of the rock in the middle. When the disc cutter spacing is too large, the damage crack caused by a single disc cutter may be difficult to extend to 1/2 of the disc cutter spacing, resulting in that although the rock in the middle of the disc cutter has the trend of forming massive rock ballast, some rocks are not broken and cannot be completely separated from the parent rock. Therefore, if the disc cutter spacing is too large, the interaction between adjacent disc cutters cannot be fully utilized.

5. Conclusions

The following conclusions are drawn:

(1) Tensile and shear cracks appear simultaneously in the failure area under the edge of the disc cutter, with more shear cracks and fewer tensile cracks. The rock breaking by the disc cutter undergoes the transformation characteristics of compaction, shearing, and tension failure modes. The failure process of the rock mass is the joint action of tension and shear.

(2) In the initial stage of penetration, the vertical force of the disc cutter increases nearly linearly with the increase of penetration. When the penetration reaches 1.0 mm, the vertical force drops abruptly, the disc cutter begins to unload, and the disc cutter has repeated loading-unloading alternate and rock breaking by leaping.

(3) After the penetration of the disc cutter reaches 9.0 mm, penetration cracks begin to appear on the surface of the rock mass, the complete rock block is separated, and the falling rock block is formed.

(4) With the increase of confining pressure, the penetration is significantly reduced, mainly manifested as surface penetration cracks. The increase of confining pressure will inhibit the initiation of cracks at the edge of the crushing zone and the propagation of intermediate cracks, and in the meanwhile, the rock-breaking depth will be reduced.

(5) After the disc cutter spacing reaches 100.0 mm, there are no penetration cracks between the two disc cutters, and the rock in the middle of the disc cutters forms an isolated rock ridge. If the disc cutter spacing is too large, the interaction between adjacent disc cutters cannot be fully utilized.

Data Availability

The data used to support the findings of this study are included within the article and can be available from the corresponding author upon request.

Conflicts of Interest

The authors declare that there are no conflicts of interest regarding the publication of this study.

Acknowledgments

This work was supported by Fundamental Research Funds for the Central Universities (Project no. FRF-TP-20-043A1), Open Research Fund Program of the State Key Laboratory of Hydroscience and Engineering (Project no. sklhse-2021-C-04), and the Science and Technology Project of Huaneng Group Headquarters (Project no. HNKJ19-H15). The costs to publish in open access have been covered by the funding.

References

[1] S. F. Zhai, S. H. Cao, M. Gao, and Y. Feng, "The effects of confining stress on rock fragmentation by TBM disc cutters," *Mathematical Problems in Engineering*, vol. 2019, Article ID 5432470, 13 pages, 2019.

[2] G. Wang, T. Ren, and G. Zhu, "The influence of confining stresses on rock fragmentation, thrust force, and penetration energy in sandstone indentation tests using disc cutters," *Advances in Civil Engineering*, vol. 2021, Article ID 5541538, 13 pages, 2021.

[3] C. Cao and K. Zhang, "Systematic performance evaluation of shield TBM cutters for excavating multiple soft rock," *Advances in Civil Engineering*, vol. 2021, Article ID 4026283, 10 pages, 2021.

[4] L. Lin, Y. Xia, and D. Wu, "Multiobjective optimization design for structural parameters of TBM disc cutter rings based on FAHP and sampga," *Advances in Civil Engineering*, vol. 2019, Article ID 8438639, 13 pages, 2019.

[5] Q. Liu, Y. Pan, and P. Deng, "Mechanical and acoustic emission responses of rock fragmentation under disc cutter penetration," *Advances in Civil Engineering*, vol. 2021, Article ID 8829046, 17 pages, 2021.

[6] L. J. Yin, Q. M. Gong, H. S. Ma, J. Zhao, and X. B. Zhao, "Use of indentation tests to study the influence of confining stress on rock fragmentation by a TBM cutter," *International Journal of Rock Mechanics and Mining Sciences*, vol. 72, no. 2, pp. 261–276, 2014.

[7] J.-W. Cho, S. Jeon, H.-Y. Jeong, and S.-H. Chang, "Evaluation of cutting efficiency during TBM disc cutter excavation within a Korean granitic rock using linear-cutting-machine testing and photogrammetric measurement," *Tunnelling and Underground Space Technology*, vol. 35, no. 4, pp. 37–54, 2013.

[8] X. B. Zhao, X. H. Yao, Q. M. Gong, H. S. Ma, and X. Z. Li, "Comparison study on rock crack pattern under a single normal and inclined disc cutter by linear cutting experiments," *Tunnelling and Underground Space Technology*, vol. 50, pp. 479–489, 2015.

[9] J. Hassanpour, "Development of an empirical model to estimate disc cutter wear for sedimentary and low to medium grade metamorphic rocks," *Tunnelling and Underground Space Technology*, vol. 75, pp. 90–99, 2018.

[10] J.-H. Yang, X.-P. Zhang, P.-Q. Ji et al., "Analysis of disc cutter damage and consumption of tbm1 section on water conveyance tunnel at lanzhou water source construction engineering," *Tunnelling and Underground Space Technology*, vol. 85, pp. 67–75, 2019.

[11] Z. Zhang, M. Aqeel, C. Li, and F. Sun, "Theoretical prediction of wear of disc cutters in tunnel boring machine and its application," *Journal of Rock Mechanics and Geotechnical Engineering*, vol. 11, no. 1, pp. 111–120, 2019.

[12] R. Gertsch, L. Gertsch, and J. Rostami, "Disc cutting tests in Colorado red granite: implications for TBM performance prediction," *International Journal of Rock Mechanics and Mining Sciences*, vol. 44, no. 2, pp. 238–246, 2007.

[13] L. Wang, Y. Kang, X. Zhao, and Q. Zhang, "Disc cutter wear prediction for a hard rock TBM cutterhead based on energy analysis," *Tunnelling and Underground Space Technology*, vol. 50, pp. 324–333, 2015.

[14] W. C. Maurer and J. S. Rinehart, "Impact crater formation in rock," *Journal of Applied Physics*, vol. 31, no. 7, pp. 1247–1252, 1960.

[15] B. Chiaia, "Fracture mechanisms induced in a brittle material by a hard cutting indenter," *International Journal of Solids and Structures*, vol. 38, no. 44-45, pp. 7747–7768, 2001.

[16] Q. Geng, Z. Wei, and J. Ren, "New rock material definition strategy for FEM simulation of the rock cutting process by TBM disc cutters," *Tunnelling and Underground Space Technology*, vol. 65, pp. 179–186, 2017.

[17] J. Liu and J. Wang, "The effect of indentation sequence on rock breakages: a study based on laboratory and numerical tests," *Comptes Rendus Mecanique*, vol. 346, no. 1, pp. 26–38, 2018.

[18] Q.-M. Gong, J. Zhao, and Y.-Y. Jiao, "Numerical modeling of the effects of joint orientation on rock fragmentation by TBM cutters," *Tunnelling and Underground Space Technology*, vol. 20, no. 2, pp. 183–191, 2005.

[19] Q. M. Gong, Y. Y. Jiao, and J. Zhao, "Numerical modelling of the effects of joint spacing on rock fragmentation by TBM cutters," *Tunnelling and Underground Space Technology*, vol. 21, no. 1, pp. 46–55, 2006.

[20] P. A. Cundall and O. D. L. Strack, "A discrete numerical model for granular assemblies," *Géotechnique*, vol. 29, no. 1, pp. 47–65, 1979.

[21] M. J. Jiang, H.-S. Yu, and D. Harris, "A novel discrete model for granular material incorporating rolling resistance," *Computers and Geotechnics*, vol. 32, no. 5, pp. 340–357, 2005.

[22] M. Jiang, Z. Shen, and J. Wang, "A novel three-dimensional contact model for granulates incorporating rolling and twisting resistances," *Computers and Geotechnics*, vol. 65, pp. 147–163, 2015.

[23] M. J. Jiang, J. Liu, Z. F. Shen, and B. L. Xi, "Exploring the critical state properties and major principal stress rotation of sand in direct shear test using the distinct element method," *Granular Matter*, vol. 20, pp. 1–18, 2018.

[24] M. J. Jiang, Y. N. Liao, H. N. Wang, and Y. S, "Distinct element method analysis of jointed rock fragmentation induced by TBM cutting," *Eur. J. Environ. Civ. En.*vol. 22, no. suppl.1, pp. s79–s98, 2018.

[25] H. Huang, B. Lecampion, and E. Detournay, "Discrete element modeling of tool-rock interaction I: rock cutting," *International Journal for Numerical and Analytical Methods in Geomechanics*, vol. 37, no. 13, pp. 1913–1929, 2013.

[26] H. Huang and E. Detournay, "Discrete element modeling of tool-rock interaction II: rock indentation," *International Journal for Numerical and Analytical Methods in Geomechanics*, vol. 37, no. 13, pp. 1930–1947, 2013.

[27] E. Oñate and J. Rojek, "Combination of discrete element and finite element methods for dynamic analysis of geomechanics problems," *Computer Methods in Applied Mechanics and Engineering*, vol. 193, no. 27-29, pp. 3087–3128, 2004.

[28] S. Q. Kou, P.-A. Lindqvist, C. A. Tang, and X. H. Xu, "Numerical simulation of the cutting of inhomogeneous rocks," *International Journal of Rock Mechanics and Mining Sciences*, vol. 36, no. 5, pp. 711–717, 1999.

[29] H. Y. Liu, S. Q. Kou, P.-A. Lindqvist, and C. A. Tang, "Numerical simulation of the rock fragmentation process induced by indenters," *International Journal of Rock Mechanics and Mining Sciences*, vol. 39, no. 4, pp. 491–505, 2002.

[30] Q. M. Gong, J. Zhao, and A. M. Hefny, "Numerical simulation of rock fragmentation process induced by two TBM cutters and cutter spacing optimization," *Tunnelling and Underground Space Technology*, vol. 21, no. 3-4, pp. 263–270, 2006.

[31] X. X. Kong, Q. Liu, Y. F. Zhao, Y. Pan, and J. P. Liu, "Numerical simulation on the effect of joint orientation on rock fragmentation by TBM disc cutters," *Journal of China Coal Society*, vol. 40, pp. 1257–1262, 2015.

[32] T. Moon and J. Oh, "A study of optimal rock-cutting conditions for hard rock TBM Using the discrete element method," *Rock Mechanics and Rock Engineering*, vol. 45, pp. 837–849, 2012.

[33] S.-O. Choi and S.-J. Lee, "Three-dimensional numerical analysis of the rock-cutting behavior of a disc cutter using particle flow code," *KSCE Journal of Civil Engineering*, vol. 19, no. 4, pp. 1129–1138, 2015.

[34] W. C. Maurer, "The state of rock mechanics knowledge in drilling," in *Proceedings of the 8th Symposium on Rock Mechanics*, pp. 355–395, University of Minesota, Minneapolis, MI, USA, September 1966.

[35] J. B. Cheatham and P. F. Gnirk, "The mechanics of rock failure associated with drilling at depth," in *Proceedings of the 8th Symposium on Rock Mechanics*, pp. 410–439, University of Minesota, Minneapolis, MI, USA, September 1966.

[36] P. F. Gnirk, "An experimental study of indexed single bit-tooth penetration into dry rock at confining pressures of 0 to 7500 psi," in *Proceedings of the 1st Congress International Society on Rock Mechanics*, pp. 121–129, International Society of Rock Mechanics, Lisbon, Portugal, September 1966.

[37] B. Lawn and R. Wilshaw, "Indentation fracture: principles and applications," *Journal of Materials Science*, vol. 10, no. 6, pp. 1049–1081, 1975.

[38] N. G. W. Cook, M. Hood, and F. Tsai, "Observations of crack growth in hard rock loaded by an indenter," *International Journal of Rock Mechanics and Mining Sciences & Geomechanics Abstracts*, vol. 21, no. 2, pp. 97–107, 1984.

[39] M. Jiang, N. Zhang, L. Cui, and S. Jin, "A size-dependent bond failure criterion for cemented granules based on experimental studies," *Computers and Geotechnics*, vol. 69, pp. 182–198, 2015.

[40] J. H. Ren, Z. Y. Wei, and Q. Geng, "New rock material definition strategy for FEM simulation of the rock cutting process by TBM disc cutters," *Tunnelling and Underground Space Technology*, vol. 65, pp. 179–186, 2017.

[41] J.-W. Cho, S. Jeon, S.-H. Yu, and S.-H. Chang, "Optimum spacing of TBM disc cutters: a numerical simulation using the three-dimensional dynamic fracturing method," *Tunnelling and Underground Space Technology*, vol. 25, no. 3, pp. 230–244, 2010.

[42] E. Oñate and J. Rojek, "Combination of discrete element and finite element methods for dynamic analysis of geomechanics problems," *Computer Methods in Applied Mechanics and Engineering*, vol. 193, pp. 3087–3128, 2004.

[43] C. Labra, J. Rojek, and E. Oñate, "Discrete/Finite element modelling of rock cutting with a tbm disc cutter," *Rock Mechanics and Rock Engineering*, vol. 50, no. 3, pp. 621–638, 2017.

[44] F. Wang, S. Liu, and K. Ji, "Numerical study on abrasive machining of rock using FDEM method," *Simulation Modelling Practice and Theory*, vol. 104, Article ID 102145, 2020.

[45] M. J. Jiang, W. Liu, B. L. Xi, and S. L. Jin, "Preliminary DEM analysis on micro-mechanical behavior of the composite cemented granules under complex stress conditions," in *Proceedings of the 7th International Conference on Discrete Element Methods*, vol. 188, pp. 525–534, Dalian, China, December 2016.

[46] M. J. Jiang, J. M. Konrad, and S. Leroueil, "An efficient technique for generating homogeneous specimens for DEM studies," *Computers and Geotechnics*, vol. 30, no. 7, pp. 579–597, 2003.

Hindawi
Advances in Civil Engineering
Volume 2022, Article ID 8102488, 15 pages
https://doi.org/10.1155/2022/8102488

Research Article

Research on the Reuse of Discharged Soil from EBP Shield Tunnels in Synchronous Grouting Material

Guijun Luo,[1] Chao Xiao,[1] Yuan Liu,[2] Kejun Feng,[2] and Qingguo Ren[1]

[1]*CCFED Civil Engineering Co., Ltd., Changsha 410004, China*
[2]*Hunan University, Changsha 410082, China*

Correspondence should be addressed to Chao Xiao; xiaochao317@qq.com

Received 7 November 2021; Accepted 10 December 2021; Published 10 January 2022

Academic Editor: Yu Liang

Great practical significance and engineering application value can be achieved when the large amount of discharged soil produced by EPB shield tunnels is recycled and comprehensively utilized. As one of the key processes of shield construction, synchronous grouting needs a large amount of bentonite, cement, fly ash, sand, and other materials. The research on the reuse of shield muck as synchronous grouting material is carried out based on Zhengzhou subway project. The physical properties and phase of the discharged soil from EPB shield tunnels are studied by using laboratory tests and XRD. The statistics show that the shield muck meets the performance requirements of bentonite and fine sand in synchronous grouting materials. The optimal grout ratio of the reused muck is obtained based on the optimization idea of multiobjective programming by MATLAB. Considering the combined effect of seepage field, stress field, and the timeliness of the grout, the influences of grouting pressure and the filling rate of synchronous grouting on surface settlement, plastic zone of strata, and segment deformation are analyzed by using finite difference method. The results prove that the surface settlement and segment deformation can be better controlled when the grouting pressure is at 0.18 MPa and the grouting rate is at 120%–150%.

1. Introduction

EPB shield method has become the most widely used construction method in urban subway construction in China. A large amount of muck is generated during shield construction. The shield muck not only occupies a large amount of land, reduces soil quality, and affects air and water quality but also has certain security risks. Besides, it is expensive to transport the muck directly to waste disposal area. Therefore, the research on the reuse of shield muck is of great practical significance and practical value.

Presently, some researches on the reuse of shield muck have been carried out, including the following aspects: (1) engineering grout treatment technology. Zha et al. [1] studied a formula for converting wastewater-based drilling fluid into environmentally friendly soil. The treatment process can achieve harmless treatment and effective utilization of drilling waste. Through data analysis of the unconfined compressive strength, triaxial compressive strength, indirect tensile strength, humidity sensitivity, and seismic modulus, Shon et al. [2] conclude that it is feasible to use modified drilling waste as a basic material for road construction. Whitaker et al. [3] studied the effects of drilling mud application rate on soil salt accumulation and leaching, and the effects of applying time and rate of the drilling mud on wheat production are discussed. Dong [4] studied the treatment technology on drilling mud and explored the solidification treatment technology on drilling waste through laboratory research. Peng et al. [5] systematically analyzed and studied several main harmless treatment methods (solidification treatment, secondary utilization of waste grout) in China. (2) Reuse of shield muck: through the treatment process of grout in Weser river tunnel excavation, Grohs [6] found that the separated sand can be used as the load-bearing layer, sound insulation wall's cover layer, and filling material of highway subgrade according to the different particle content. Zhong et al. [7] studied the reuse of excavated silty fine sand in shield synchronous grouting. He

et al. [8] used shield muck sand (modulus at 1.88) from Shuangdun Station to Wangjiadun Center Station of Wuhan Metro Line 3 as fine aggregate to prepare environmentally friendly single-liquid synchronous grouting material with high performance through optimizing experimental mix proportion. In summary, although scholars have achieved fruitful results in the reuse of shield muck, there are few studies on the reuse of EPB shield muck as synchronous grouting material, and systematic research results have not been reported. Synchronous grouting is one of the key links in shield construction. Usually, grout is injected into the gaps between shield tail and segment to fill the gap and control strata deformation [9–12]. At the same time, the grouting protection layer is formed around the tunnel to improve the impermeability of shield tunnel [13–15]. The stratum that the shield passes through is usually soft soil stratum containing lots of clay particles and fine sand. If proper treatment is carried out, the discharged soil is one of the high quality raw materials for synchronous grouting.

In view of this, based on the construction example of a section crossing silty clay stratum and clayey silt stratum with sandy silt in Zhengzhou Metro, this paper discusses the feasibility about the reuse of shield muck, and the best synchronous grouting proportion with the reused shield muck is obtained. Moreover, the influences of grouting pressure and filling rate on surface settlement, soil plastic zone, and segment deformation are studied. The research results are expected to provide reference for similar projects.

2. Project Overview

The main strata of a certain section of Zhengzhou Metro are clayey silt stratum with sandy silt, and the local strata are silty clay stratum and clayey silt stratum with sandy silt. According to geological prospecting, 56% of the strata traversed by the tunnel are silty clay, 38% are fine sand, and 6% are silty clay mixed with sandy silt, as shown in Figure 1.

Two Earth pressure balance shield machines with a diameter of 6250 mm were used for construction. Reinforced concrete segments are used as tunnel lining. The segment has an outer diameter of 6.2 m, a thickness of 0.35 m, and a width of 1.5 m. The theoretical muck output per ring is 49.4 m^3. The theoretical grouting volume per ring is 4.1 m^3, and the filling factor is 1.5–2.0.

3. Feasibility of Shield Muck as Grouting Material

3.1. Engineering Features Test of the Shield Muck. The detailed composition and phase analysis of shield muck, mainly including density, water content, specific gravity, limit moisture content, void ratio, saturation, and grading feature and other physical characteristics tests, are carried out. Shield muck sample is shown in Figure 2.

3.1.1. Basic Physical Properties. Basic physical properties of shield muck can be obtained by physical property measurement, and the results are listed in Table 1.

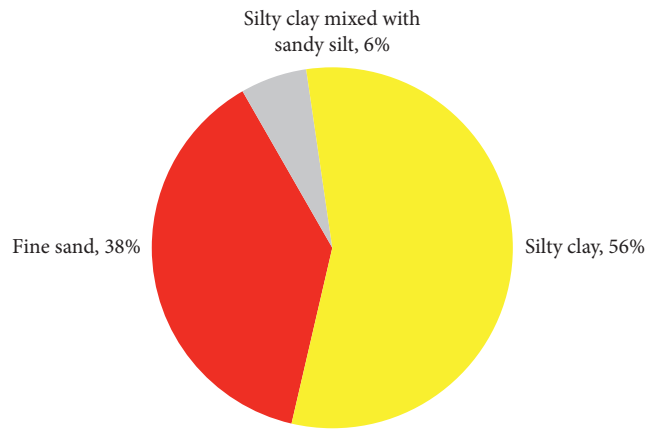

Figure 1: The proportion of strata that the shield crosses.

According to the measurement results, the muck sample has moderate moisture content and a viscosity index of 0.5. The soil sample is a low-liquid limit silty clay in a plastic state.

3.1.2. Grading Curve of the Muck. In the analysis of particle size composition, the particle size distribution of soil above 0.075 mm was determined by sieving method, and the particle size distribution of soil below 0.075 mm was measured by densimeter method considering the existence of fine particles in the muck of silty clay. The particle size composition of the muck is manifested in Table 2. The grading curve is portrayed in Figure 3.

According to Table 2 and Figure 3, the particle size distribution of silty clay samples is uneven, and the particle gradation is good. There are a lot of fine particles in the sample. The fine particles with particle size less than 0.075 mm account for 39.32%, and the clay particles with particle size less than 0.005 mm account for 8.45%.

Only the sieving method is used to determine the particle size distribution, and the fineness modulus and mud content are used to evaluate the quality of sand samples in the analysis of particle size composition of fine sand in muck. The particle size composition of the fine sand in muck is shown in Table 3, and the gradation curve is demonstrated in Figure 4.

According to Table 3 and Figure 4, the particle size distribution of fine sand samples is uniform and poor, mostly in the range of 0.6–0.15, and the composition is mostly composed of medium sand and fine sand.

3.1.3. Mineral Composition Analysis of the Muck. Multipurpose X-ray diffractometer (XRD) is applied to analyze the phase of silty clay and fine sand. The mineral composition of silty clay in muck is mainly composed of quartz (21.35%), feldspar (16.38%), and montmorillonite (31.03%). The mineral composition of fine sand mainly consists of quartz (35.03%) and feldspar (27.35%).

3.2. Feasibility Analysis of Shield Muck as Grouting Material. The clay mineral composition of the silty clay in muck is high with favorable water absorption and expansion properties.

(a) (b)

Figure 2: Shield muck sample: (a) fine sand, (b) silty clay.

Table 1: Basic physical properties of shield muck.

Soil sample	Water content (%)	Wet density (g)	Dry density (g)	Specific gravity	Plasticity limit (%)	Liquid limit (%)	Plasticity index	Void ratio	Degree of saturation
Silty clay	18.76	2.055	1.722	2.634	13.25	24.468	11.218	0.788	63.3
Fine sand	4.83	1.928	1.836	—	—	—	—	—	—

Table 2: Particle size composition of silty clay in muck.

Sample name	Contents of particles smaller than a certain size (mm) (%)						Uniformity coefficient	Curvature coefficient
	1	0.25	0.075	0.01	0.005	0.001		
Silty clay	94.68	69.46	39.32	11.63	8.45	3.56	26.00	1.73

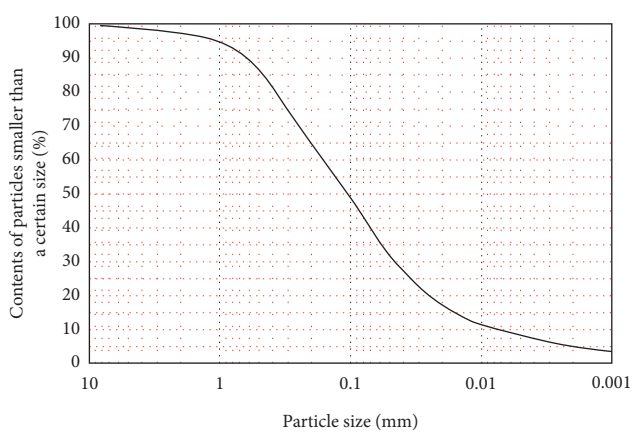

Figure 3: Grading curve of silty clay in muck.

Table 3: Particle size composition of fine sand in muck.

Sample name	Contents of particles smaller than a certain size (mm) (%)						Fineness modulus	Mud content (%)
	4.75	2.36	1.18	0.6	0.3	0.15		
Fine sand	99.86	99.25	98.05	91.15	42.99	9.36	1.61	9.11

Besides, the particle size of soil sample is small, and the specific surface area of soil particles per unit mass is large, which can effectively improve the viscosity and stability of the grouting liquid. Therefore, it is feasible to replace the bentonite in the raw materials of synchronous grouting liquid based on the features like physical properties, mineral composition, and particle size composition of the muck in the section of Zhengzhou Metro. Moreover, the mineral

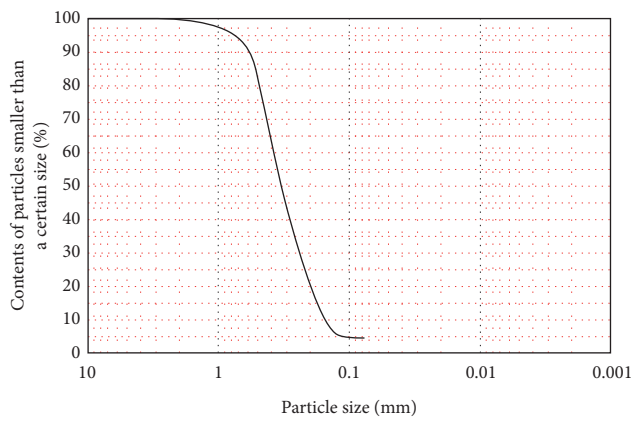

Figure 4: Grading curve of fine sand in muck.

components of the fine sand in muck are mainly quartz and feldspar with little mud content. It has the basic conditions for recycling and the utilization as engineering sand, so it is feasible to replace the fine sand in the raw materials of synchronous grouting liquid.

4. Optimization of Ratio of the Reused Muck Grout

Based on the engineering situation of the shield section, cement, fly ash, silty clay in muck (substitute for bentonite), fine sand in muck (substitute for river sand), bentonite, and water are chosen as single-liquid grouting materials with active cement mortar.

By using the basic theory and method of uniform design, a large number of tests can be effectively avoided. Uniform design was initiated by Chinese statistician Professor Fang Kaitai and member of Chinese Academy of Sciences Wang Yuan, and it is the premier method to conduct multifactor and multilevel experimental design. It can complete the research and development of complex scientific research projects and new products with fewer experiments. The biggest feature is that the number of experiments can be equal to the maximum level number, rather than the square of the number of experimental factors. Moreover, the number of experiments is only related to the number of factors to be investigated. However, the number of trials should be about 3 times the number of experimental factors, which is conducive to modeling and optimization.

The synchronous grouting liquid is a kind of hard single liquid, and its influencing factors can be generally divided into four properties, namely, water-binder ratio, binder-sand ratio, bentonite-water ratio, and fly ash-cement ratio. The water-binder ratio is the ratio of water to cementitious materials. The bentonite-water ratio is the ratio of bentonite to water. The cement-sand ratio is the ratio of cementitious materials to the sand. The fly ash-cement ratio is the ratio of fly ash to cement. To analyze the influence of each influencing factor on the construction performance of the grout and design the optimal mix proportions, five levels of tests were set for each influencing factor, and the number of tests was three times the actual level of the test. Therefore, 15 groups of tests were arranged, namely, the uniform design of 4 factors and 15 levels. Referring to Appendix I of Fang Kaitai's *uniform design and uniform design table* [16], the uniform design was carried out by choosing columns 1, 2, 4, and 6 of U15 ∗ (157). The material proportions of the uniform design are listed in Table 4. The items of the grouting material performance test mainly include specific gravity test, consistency test, fluidity test, bleeding rate test, setting time test, stone shrinkage test, and unconfined compression test. The test results are presented in Table 5.

Based on the results of uniform test, SPSS software was used for regression analysis with regression method, and quadratic multiple regression model was adopted to analyze the interaction among variables.

$$y = b_0 + \sum_{k=1}^{5} b_k x_k + \sum_{j=1}^{5} \sum_{k=j}^{5} b_{jk} x_j x_k + \varepsilon, \quad (1)$$

where x_i and x_k are test factors, b_0, b_k, and b_{jk} are coregression coefficients, x_1 is the water-binder ratio, x_2 is the binder-sand ratio, x_3 is the bentonite-water ratio, and x_4 is the fly ash-cement ratio. The regression equation of each factor is obtained according to the test results.

Based on the results of regression analysis, each influencing factor of grouting material and each performance of grout are analyzed. The factor was changed within its value range, and the influences of this factor on the specific gravity of mortar, stone shrinkage rate, initial fluidity, 3 h bleeding rate, setting time, and compressive strength are studied. Simultaneously, the range of independent variables in the multiobjective programming problem is determined according to the level interval of uniform test factors, and the fmincon function in MATLAB optimization toolkit is used to solve the multiobjective programming problem with ideal point method. The optimal proportions of synchronous grouting material prepared from shield muck are listed in Table 6. The performances of the grouting material with the optimal proportion are listed in Table 7.

Table 4: Material proportions of uniform experimental design (6.5 kg for each group).

Number	Ratio					
	C (cement) (kg)	F (fly ash) (kg)	S (sand in muck) (kg)	B (silty clay in muck) (kg)	W (water) (kg)	Ratio (C : F: S : B: W)
1	0.558	1.675	2.659	0.268	1.340	1 : 3: 4.76 : 0.48 : 2.4
2	0.420	1.765	2.601	0.184	1.530	1 : 4.2 : 6.19 : 0.44 : 3.64
3	0.626	1.502	2.533	0.136	1.702	1 : 2.4 : 4.05 : 0.22 : 2.72
4	0.420	1.513	2.479	0.348	1.740	1 : 3.6 : 5.9 : 0.83 : 4.14
5	0.674	1.214	2.421	0.302	1.888	1 : 1.8 : 3.6 : 0.45 : 2.8
6	0.482	1.736	2.844	0.106	1.331	1 : 3.6 : 5.9 : 0.22 : 2.76
7	0.713	1.283	2.772	0.335	1.397	1 : 1.8 : 3.89 : 0.47 : 1.96
8	0.490	1.470	2.722	0.251	1.568	1 : 3: 5.56 : 0.51 : 3.2
9	0.372	1.562	2.686	0.139	1.741	1 : 4.2 : 7.22 : 0.37 : 4.68
10	0.509	1.222	2.623	0.415	1.731	1 : 2.4 : 5.15 : 0.82 : 3.4
11	0.389	1.635	3.067	0.194	1.215	1 : 4.2 : 7.88 : 0.5 : 3.12
12	0.579	1.391	2.985	0.165	1.379	1 : 2.4 : 5.15 : 0.29 : 2.38
13	0.386	1.390	2.961	0.341	1.421	1 : 3.6 : 7.67 : 0.88 : 3.68
14	0.620	1.115	2.891	0.312	1.561	1 : 1.8 : 4.67 : 0.5 : 2.52
15	0.429	1.287	2.861	0.206	1.717	1 : 3: 6.67 : 0.48 : 4

Table 5: Test results.

Number	Specific gravity	Stone shrinkage rate (%)			Consistency (cm)	Initial fluidity (cm)	3h bleeding rate (%)	Initial setting time (h)	Compressive strength (MPa)
		1d	7d	28d					7d
1	2.005	3.9	4.1	4.1	13.9	13.8	3.0	8.92	0.81
2	1.878	6.1	6.2	6.2	16.2	21.0	3.0	9.25	0.38
3	1.810	7.2	7.3	7.3	15.2	27.3	5.0	9.93	0.62
4	1.789	8.5	8.7	8.7	13.5	27.0	6.0	21.22	0.30
5	1.720	11.8	12.0	12.0	13.8	26.5	8.0	17.88	0.60
6	1.945	4.2	4.4	4.4	14.1	17.0	3.0	11.58	0.64
7	1.940	4.3	4.4	4.4	12.2	18.0	4.0	9.73	1.01
8	1.825	5.2	5.3	5.3	13.1	22.5	4.0	12.17	0.40
9	1.635	12.4	12.3	12.3	13.0	30.3	12.0	27.95	0.18
10	1.753	10.3	20.5	10.5	13.4	25.5	7.0	17.75	0.36
11	1.925	4.6	4.8	4.8	12.7	17.7	2.0	11.03	0.37
12	1.935	5.7	5.7	5.7	15.0	20.3	3.0	11.42	0.67
13	1.825	6.4	6.5	6.5	13.7	22.3	4.0	15.57	0.32
14	1.783	4.1	4.3	4.3	12.4	15.1	4.0	15.26	0.61
15	1.724	7.1	7.3	7.3	12.7	19.3	6.0	20.13	0.36

Table 6: Optimal proportions of synchronous grouting material prepared from shield muck.

Water-binder ratio	Binder-sand ratio	Bentonite-water ratio	Fly ash-cement ratio	Mass of components per 6.5 kg of grout (kg)				
				Cement	Fly ash	Silty clay in muck	Fine sand in muck	Water
0.74	0.84	0.11	2.75	0.574	1.578	0.184	2.562	1.603

Table 7: Grouting material properties with the optimal proportions.

Specific gravity	Stone shrinkage rate (%)			Initial fluidity (cm)	3h bleeding rate (%)	Initial setting time (h)	Compressive strength (MPa)		
	1d	7d	28d				1d	7d	28d
1.878	5.57	5.77	5.78	22.5	3.6	10	0.62	1.81	5.17

5. Numerical Simulation Research on the Effect of Shield Muck Synchronous Grouting

5.1. Calculation Model and Parameters. The 201 ring to 210 ring of the left line in the interval are used as the test section of muck reuse. The tunnel section at the 205 ring of the left line is chosen as the calculation section to carry out the sensitivity analysis of synchronous grouting construction parameters by using FLAC3D finite difference software. Based on the geological survey data of this project, the main tunneling strata are fine sand and silty clay. The specific stratum parameters are shown in Table 8. The buried depth of underground stable water level is about 16 m, and the tunnel roof is 18 m away from the surface. The distance between the two lines at the section is about 13.5 m. Only the influence of grouting construction in the left line is considered in the calculation considering that the right line has been excavated.

According to the parameters of the shield machine, it can be calculated that the theoretical overbreak gap (25 mm) is half of the difference between the cutter diameter (6480 mm) and the outer diameter of the shield tail. The theoretical gap (70 mm) in shield tail is half of the difference between the inner diameter of the shield tail and the outer diameter of the segment (6200 mm). The theoretical thickness of the ring filled by grout is half of the difference between the cutter diameter and the outer diameter of the segment (140 mm).

Due to the randomness and complexity in the physical and mechanical properties of geotechnical materials, the following calculation conditions and assumptions are used in the numerical simulation: assuming that the thickness of each stratum is uniform and there is no mutual intrusion, surrounding rock and supporting structure are homogeneous and isotropic materials; the strata below groundwater depth are permeable; the water level remains unchanged during tunnel excavation; the grout is incompressible, isotropic, and nondilutable and does not block.

According to the Saint-Venant principle, the displacement and stress changes caused by excavation can be ignored outside the excavation area with 3 to 5 times the tunnel span. Therefore, the left, right, upper, and lower dimensions of the tunnel excavation area are not less than 3–5 times the tunnel span in the actual numerical simulation process. The calculation model is shown in Figure 5. The boundary constraints are the horizontal constraints on the front, back, left, and right of the model, the vertical constraints at the bottom of the model, and the free boundary on the top of the model. For the fluid boundary in seepage, the fluid exchange in the left, right, and bottom boundaries is constrained, and no fluid constraints are imposed on the front and back boundaries.

The stratum soil is simulated with solid element, and it obeys the M-C failure criterion. The shield segment is simulated with solid element, and it conforms to the elastic constitutive model. The segment joint is considered by setting the stiffness reduction coefficient as 0.7. The steel plate of shield machine is simulated by shell element in line with the elastic constitutive model. The grouting layer is simulated by solid element in accordance with elastic constitutive model and is regarded as permeable material. Since the grout is used to fill the gaps between the excavation diameter and the shield body, the filling layer is simulated with solid element with the elastic constitutive model, and it is regarded as impermeable material.

5.2. Simulation Steps of Construction. The calculation steps simulate the three stages of shield construction: (1) shield machine passing stage: the shield shell unit and the overexcavation filling layer in the model are activated; (2) segment out of the shield tail stage: the shield shell element and the overexcavated filling layer are passivated, and the shield tail grouting layer and the segment lining in the model are activated. The grouting pressure of the whole ring in shield tail is applied. Considering the shear movement and consolidation of the grout (the change rate of the grout parameters in the early stage of consolidation is huge), attention should be paid to change the hardening parameters of the grouting layer at the appropriate time and reduce the grouting pressure. (3) Grout hardening stage: time-dependent hardening parameters of grouting layer should also be applied at this stage.

To simulate the field construction more accurately, the three stages of shield construction are divided into six calculation steps (Table 9) according to the hardening process of grouting body considering the construction stage and the influence on surface deformation. In the calculation process, different stratum stress release coefficients are set for different construction steps.

5.3. Calculation of Time-Dependent Parameters of the Grout. To obtain the time-dependent hardening parameters of the materials in this study, the relationships between the elastic modulus and Poisson's ratio of the grout and time are fitted according to the measurement results of the grout performance parameters at different ages, and the relationships are as follows:

$$\begin{aligned} E &= 40 \times \ln(t) + 70, \\ \lambda &= -0.05 \times \ln(t) + 0.38, \end{aligned} \tag{2}$$

where E is elastic modulus, MPa, λ is Poisson's ratio, and t is the curing days of the grout for 0–28 d.

The hardening parameters of the grout are obtained (Table 10) according to the consolidation time point in construction simulation steps 2~6.

5.4. Construction Effect Analysis under Different Grouting Pressure

5.4.1. Range and Vertical Distribution of Grouting Pressure. It is assumed that the grouting pressure and grout are evenly distributed in the whole ring with a diffusion way of filling method. The filling rate of the shield tail void is 100%. To reasonably and fully study the influence of grouting pressure on tunnel structure and surface deformation, the range of

Table 8: Physical mechanics parameters for each stratum of the calculated section.

Stratum name	Permeability coefficient ($cm \cdot s^{-1}$)	Natural unit wet ($kN \cdot m^{-3}$)	Void ratio	Modulus of compression (MPa)	Force of cohesion (kPa)	Angle of friction (°)	Poisson's ratio	Buried depth (m)
Miscellaneous fill	—	18.5	—	5.4	10	15	0.33	0–2.5
Silty sand	—	20.5	—	18	0.1	30	0.25	2.5–7
Clayey silt	0.1	19.6	0.68	6	22.4	19.2	0.30	7–18
Fine sand	10	20.3	0.535	25	0.1	32	0.24	18–22
Silty clay	0.05	20.1	0.639	6.5	32	21	0.32	22–32
Calcareous cemented sandy soil	1.5	21.2	0.4	45	25	36	0.22	32–66

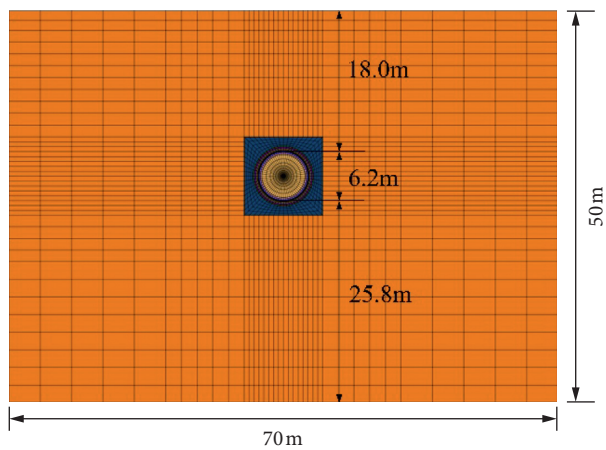

Figure 5: Calculation model.

Table 9: Stratum stress release coefficient at each stage of construction.

Construction simulation steps	1	2	3	4	5	6
Corresponding tunneling stage	Passing stage	Segment off the ring for 0~8h	Segment off the ring for 8~16 h	Segment off the ring for 16~24 h	Grouting hardening for 1~7 d	Grouting hardening for 7~28 d
Settlement stage	Passing settlement	Off-ring settlement			Subsequent settlement	
Release coefficient (%)	15 15	30	25 70	15	10 15	5

Table 10: Hardening parameters of the grout.

Hardening parameters of the grout	Simulation step 2 Off ring for 0~8 h	Simulation step 3 Off ring for 8~16 h	Simulation step 4 Off ring for 16~24 h	Simulation step 5 Off ring for 1~7 d	Simulation step 6 Off ring for 7~28 d
E/MPa	5	15	30	100	200
λ	0.45	0.42	0.37	0.32	0.24
ρ/$kg \cdot m^{-3}$	1900	1900	1900	1900	1900

uniform grouting pressure in the whole ring is set to 0.10 MPa~0.30 MPa, and the linear gradient is 0.04 MPa with a total of 6 working conditions.

Due to the circumferential and longitudinal shear movement of the grout when grouting, and the grout consolidating over time, it is considered that the grouting

pressure is almost reduced to 0 within 1 d after the detachment of the ring (i.e., 9 m away from the shield tail) combined with the engineering practice and literature research. The reduction coefficients of longitudinal grouting pressure are listed in Table 11.

5.4.2. Analysis of Numerical Simulation Results

(1) Surface Settlement. The surface settlement under different grouting pressures is shown in Figure 6. The lateral surface settlement curves under different grouting pressures are basically the same and nearly in line with the characteristics of Gaussian curve. The change of grouting pressure has a great influence on surface settlement. The maximum surface settlement gradually decreases with the increase of grouting pressure, but the width of settlement trough remains unchanged. When the grouting pressure is greater than 0.22 MPa, the uplift occurs at the surface about 25 m away from the axis on both sides of the shield, and the uplift increases with the increase of grouting pressure.

As shown in Figure 7, the segment deforms elliptically and sinks as a whole under the effect of water-soil pressure and grouting pressure. The segment deformation of the feature points changes greatly under different grouting pressure, and the overall settlement of the segment decreases with the increase of grouting pressure. The change values of segment convergence are manifested in Figure 8. With the increase of grouting pressure, the vertical convergence of segment gradually increases, while the horizontal convergence of segment shows a trend of first increasing and then decreasing. When the grouting pressure is set as 0.18 MPa, the horizontal convergence of segment reaches the maximum value of 4.16 mm.

(2) Distribution of Plastic Zone. Table 12 shows the distribution of the soil plastic zone under different grouting pressures. The plastic zone is mainly distributed on both sides of the tunnel, and the size decreases with the increase of grouting pressure. When the value of grouting pressure is less than 0.18 MPa, there are stretched failure units around the tunnel.

The control value of surface settlement in tunnel monitoring project is 10 mm according to the technical specifications of monitoring on urban rail transit engineering and the first-level requirements of engineering monitoring. Figure 6 shows that the minimum grouting pressure is 0.18 MPa. Figure 8 presents that, with the increase of grouting pressure, the convergence of segment clearance gradually increases. Excessive grouting pressure can easily lead to segment dislocation and cracking, so the uniformly distributed grouting pressure in the whole ring should be set to 0.18 MPa.

5.5. Construction Effect Analysis with Different Grouting Quantity

5.5.1. Filling Grouting

(1) Simulation Method. The convergent units are set up in the calculation model in order to simulate the effect that the grout incompletely fills the gaps of the shield tail. As demonstrated in Figure 9, when the segment is just separated from the shield tail, the soil tends to converge to the tunnel. It is assumed that when the grout fills 80% of the shield tail clearance, the remaining 20% is occupied by the convergent soil. To ensure the continuity of the grid in the numerical simulation, the convergent units are used to replace the empty units, and these units are given small strength parameters for approximate simulation.

(2) Working Conditions. Assuming the filling and grouting rate is 80%~100%, the specific conditions are shown in Table 13.

(3) Analysis of Numerical Results

① Surface settlement.

The surface settlement under different backfill grouting conditions is shown in Figure 10. The curves of horizontal surface settlement under different backfill grouting rates are basically the same, which is nearly in line with the feature of Gaussian. The change of backfill grouting rate has a great influence on surface settlement. With the increase of backfill grouting rate, the maximum value of surface settlement decreases gradually, and the variation is considerable. The width of the setting tank remains unchanged when the backfill grouting rate changes.

② Segment deformation.

Figure 11 shows the deformation of segment under different backfill grouting conditions. The segment deforms elliptically and sinks as a whole under the effect of water-soil pressure and grouting pressure. The segment deformation of the feature points changes greatly under different grouting pressure, and the overall settlement of the segment decreases with the increase of grouting pressure.

The relationship between backfill grouting rate and segment convergence is portrayed in Figure 12. With the increase of backfill grouting rate, the vertical convergence and horizontal convergence of the segment show an increasing trend; that is, the ellipticity of segment increases with the increase of backfill grouting rate.

③ Plastic zone distribution.

Table 14 is the distribution of soil plastic zone without backfill grouting. The plastic zone is mainly distributed on the left and right sides of the tunnel, and the size decreases with the increase of filling grouting rate. The plastic deformation areas above the left and right of the tunnel are large when the backfill grouting rate is less than 100%, and it is easy to cause the instability of the soil above the tunnel.

The control value of surface settlement in tunnel monitoring project is 10 mm according to the technical specifications of monitoring on urban rail transit engineering and the first-level requirements of engineering monitoring. Figure 10 shows that when the backfill grouting rate is less than 100%, the maximum surface settlement is greater than 10 mm. Considering the surface settlement and

Table 11: Reduction coefficient of longitudinal grouting pressure.

Construction stage	The circumferential grouting pressure after longitudinal reduction/MPa					Reduction coefficient
Initial grouting pressure	0.1	0.14	0.18	0.22	0.26	0.3
Off ring for 0~8 h	0.08	0.112	0.144	0.176	0.208	0.24
Off ring for 8~16 h	0.04	0.056	0.072	0.088	0.104	0.12
Off ring for 16~24 h	0.02	0.028	0.036	0.044	0.052	0.06

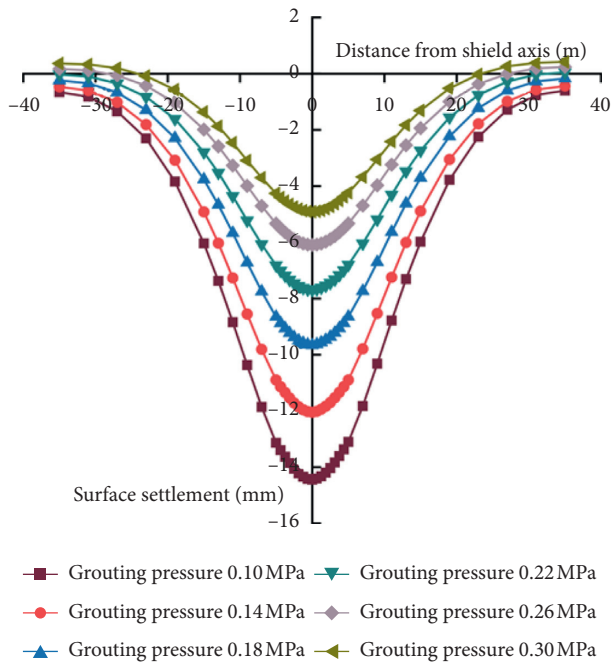

Figure 6: Surface settlement curve under different grouting pressures.

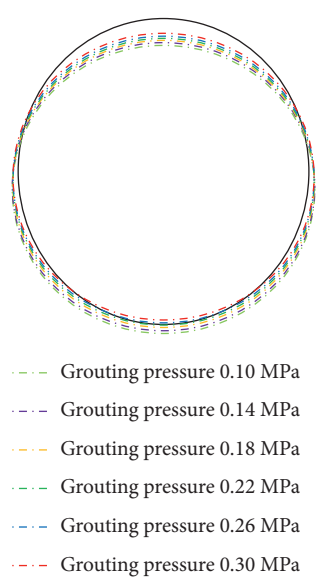

Figure 7: Segment deformation under different grouting pressures.

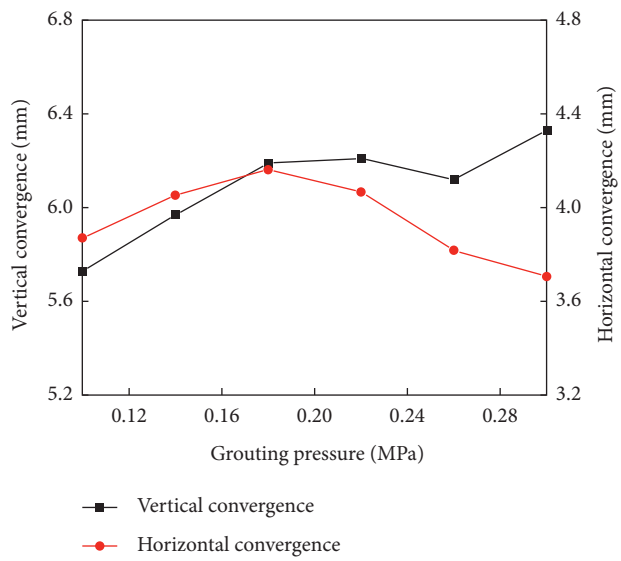

Figure 8: Variation of segment convergence under different grouting pressures.

Table 12: Distribution of plastic zone under different grouting pressures.

Grouting pressure (MPa)	Plastic zone distribution
0.10	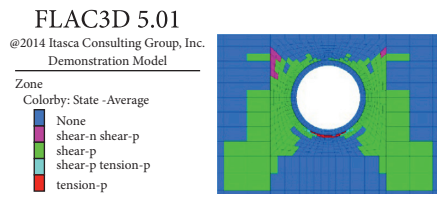
0.14	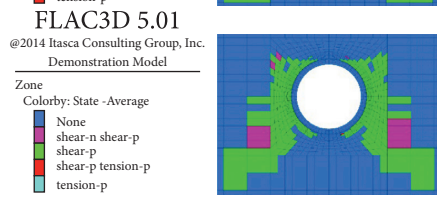
0.18	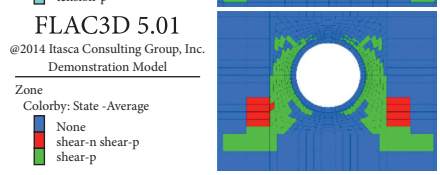
0.22	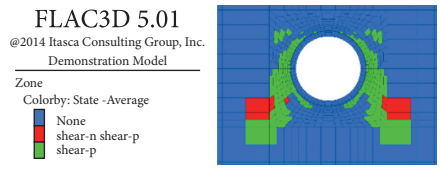
0.26	
0.30	

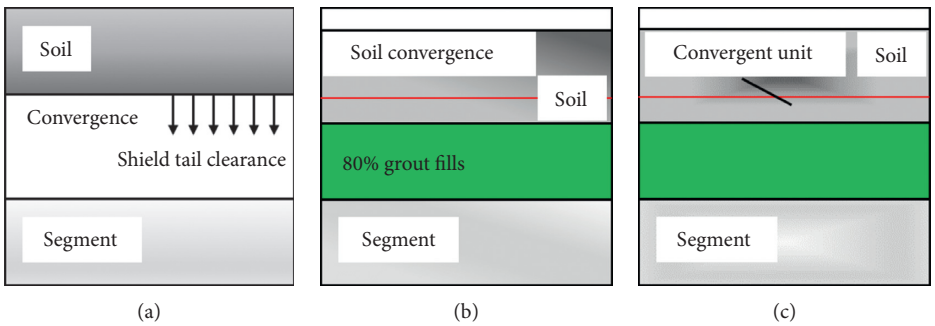

Figure 9: Simulation diagram of grout filling in shield tail gaps. (a) The segment off the ring. (b) Incomplete grout filling. (c) Convergent unit simulation.

Table 13: Conditions of uniform filling grouting.

Uniform grouting pressure on the whole ring/MPa			0.18		
Uniform filling grouting rate/%	80	85	90	95	100

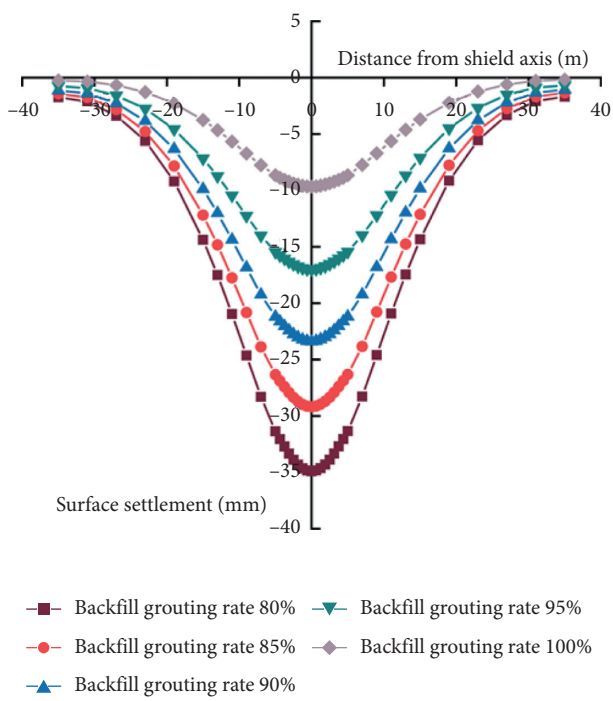

Figure 10: Surface settlement curve under different backfill grouting conditions.

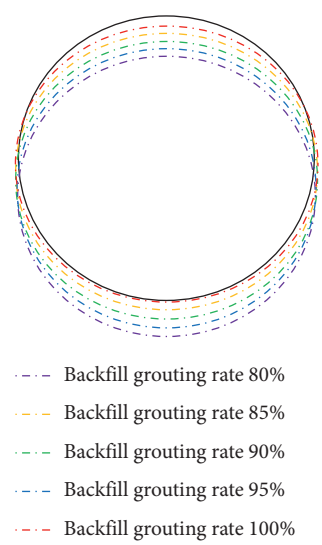

Figure 11: Segment deformation under different backfill grouting conditions.

plastic zone distribution, the backfill grouting rate should be 100%.

5.5.2. Penetration Grouting. The influences of the change of grout injection rate on surface settlement, segment deformation, and plastic zone distribution are simulated simultaneously, and the grout injection rate of 100%–200% is set for calculation and analysis. It is assumed that when the grout injection rate exceeds 100%, penetration grouting happens, and the whole ring is uniformly penetrated. Meanwhile, based on the method in Lei et al. [17], the elastic modulus of grout-soil mixture can be roughly calculated according to (3), and Poisson's ratio is adopted according to grout of corresponding calculation stage. The specific conditions are presented in Table 15.

$$E_3 = E_1 + n_f \times E_2, \tag{3}$$

where E_3 is the elastic modulus of grout-soil mixture, MPa, E_1 is the elastic modulus of the stratum soil where the tunnel is located, MPa, E_2 is the elastic modulus of the corresponding grout, MPa, and n_f is the effective porosity of the soil stratum where the tunnel is located, which is 25.44%.

The simulation results are shown in Figures 13-15. The simulation results indicate that the change of grout injection rate has little effect on surface settlement, segment deformation, and plastic zone distribution. With the increase of grout injection rate, the maximum surface settlement

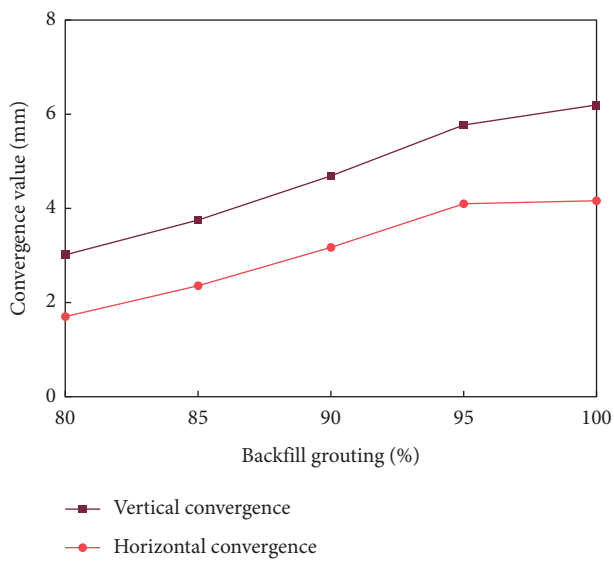

Figure 12: Changes of segment convergence without backfill grouting.

Table 14: Distribution of soil plastic zone without backfill grouting.

Backfill grouting rate (%)	Plastic zone distribution
80	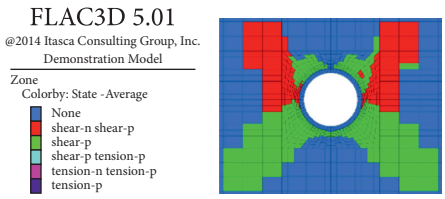
85	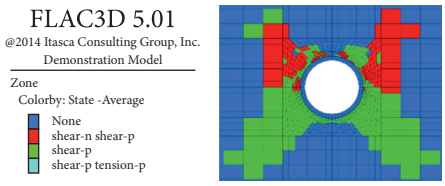
90	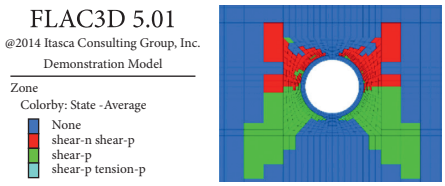
95	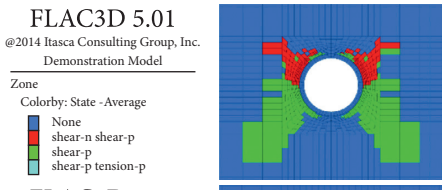
100	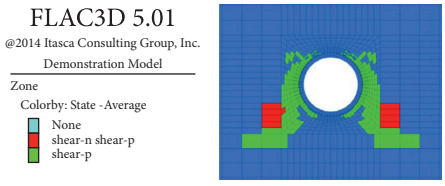

Table 15: Seepage grouting conditions.

Grouting pressure uniformly distributed on the whole ring (MPa)	0.18					
Injection rate of the grout (%)	100	120	140	160	180	200
Thickness of permeable grout-soil mixed layer (m)	0.000	0.106	0.209	0.308	0.405	0.500

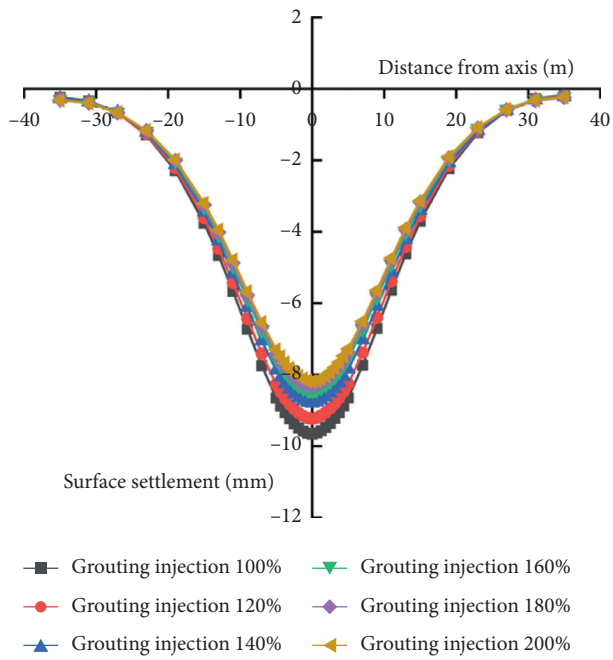

Figure 13: Surface settlement under different grout injection rate conditions.

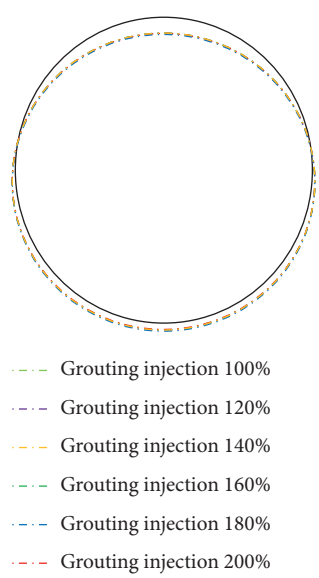

Figure 14: Segment deformation under different grout injection rate conditions.

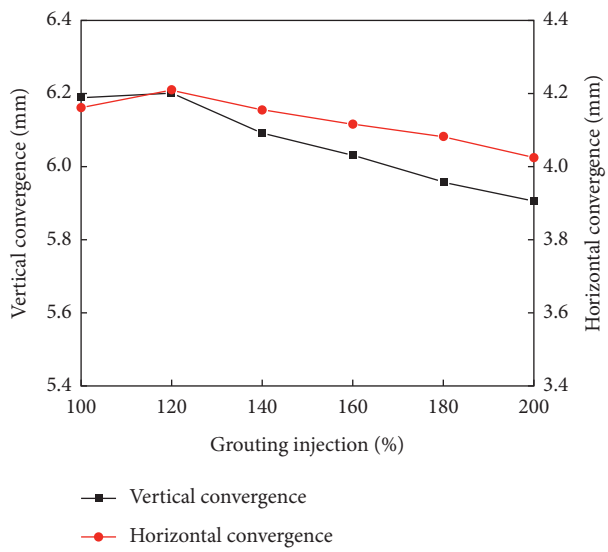

Figure 15: Variation of the convergence value of the segment under different grout injection rate conditions.

decreases. The ellipticity of the segment increases and then decreases with the increase of grout injection rate. When the grout injection rate is 120%, the vertical convergence and horizontal convergence of the segment reach the maximum.

6. Conclusions

(1) The mineral composition of silty clay in the shield muck is mainly composed of quartz (16.38%), feldspar (21.35%), and montmorillonite (31.03%). The mineral composition of fine sand mainly consists of quartz (35.03%) and feldspar (27.35%). It is feasible to use the silty clay and fine sand in shield muck to replace the bentonite and fine sand in raw materials of synchronous grouting, respectively.

(2) Based on the uniform test results, the SPSS multiple regression analysis and MATLAB are used to solve the nonlinear programming problem. The optimal proportions of shield muck synchronous grouting material are water-cement ratio of 0.74, binder-sand ratio of 0.84, bentonite-water ratio of 0.11, and fly ash-cement ratio of 2.75.

(3) The finite difference method is used to analyze the influences of the grouting pressure and the filling rate by considering the combined action of the seepage field, the stress field, and the time-dependent properties of the grout. From the perspective of calculation results and economic benefits, when the grouting pressure is constraint at 0.18 MPa and the grouting rate is arranged at 120%~150%, the surface settlement and the deformation of the segment are better controlled when muck grout is adopted.

Data Availability

The data used to support the findings of this study are available from the corresponding author upon request.

Conflicts of Interest

The authors declare that they have no conflicts of interest.

Acknowledgments

This work was sponsored by the State Key Program of National Natural Science of China (no. 51938005). The authors are grateful to this institution for the support.

References

[1] X. Zha, X. Liao, X. Zhao, F. Liu, A. Q. He, and W. X. Xiong, "Turning waste drilling fluids into a new, sustainable soil resources for landscaping," *Ecological Engineering*, vol. 121, no. 1, pp. 130–136, 2018.

[2] C.-S. Shon, C. K. Estakhri, D. Lee, and D. Zhang, "Evaluating feasibility of modified drilling waste materials in flexible base course construction," *Construction and Building Materials*, vol. 116, pp. 79–86, 2016.

[3] A. Whitaker, C. Penn, and J. Warren, "Surface application of a saline-sodic oil & gas drilling waste to winter wheat (*Triticum aestivum* L.)," *Geoderma*, vol. 274, pp. 97–103, 2016.

[4] Y. Dong, *Study on Solidification Treatment Technology of Waste Drilling Mud*, Chang ' an University, Xian, China, 2009.

[5] Y. Peng, Y. Xu, and C. Sun, "The overview of the way to recycle municipal domestic refuse," *Environmental science and management*, vol. 32, no. 4, pp. 102–104, 2007.

[6] H. Grohs, "Cost-efficient regeneration of bore slurry for driving of weser tunnel," *Tunnel Construction*, vol. 27, no. 6, pp. 47–51, 2007.

[7] X. Zhong, Z. Jia, Q. Liu, and Y. W. Han, "Reuse of excavated fine sand for back grouting of shield tunneling," in *Proceedings of the The 5th National Symposium on Geotechnical Engineering*, Iran, Tehran, December 2008.

[8] L. He, M. Xiao, L. Deng, Y. Liang, and Q. Ding, "Development and application of grouting material with shielded sediment and industrial residue," *The World of Building Materials*, vol. 36, no. 1, pp. 1–5, 2015, (in chinese).

[9] R. K. Rowe, K. Y. Lo, and G. J. Kack, "A method of estimating surface settlement above tunnels constructed in soft ground," *Canadian Geotechnical Journal*, vol. 20, no. 1, pp. 11–22, 1983.
[10] F. Ye, C. Gou, Z. Chen, and J. H. Mao, "Ground surface deformation caused by synchronous grouting of shield tunnels," *Chinese Journal of Geotechnical Engineering*, vol. 36, no. 4, pp. 618–624, 2014.
[11] J. Zhang, T. Feng, J. Yang, F. Yang, and Y. Gao, "Upper-bound finite-element analysis of characteristics of critical settlement induced by tunneling in undrained clay," *International Journal of Geomechanics*, vol. 18, no. 9, Article ID 04018110, 2018.
[12] J. Zhang, T. Feng, J. Yang, F. Yang, and Y. Gao, "Upper-bound stability analysis of dual unlined horseshoe-shaped tunnels subjected to gravity," *Computers and Geotechnics*, vol. 97, pp. 103–110, 2018.
[13] H. Feng and X. Chang, "Analysis of structural disasters in shield tunnels and measures and suggestions for waterproofing," *Modern tunnelling technology*, vol. 53, no. 6, pp. 36–43, 2016.
[14] F. Wang, Y. Fan, and C. Guo, "Practice of non-water-reacting polymer grouting treatment to seepage," *Journal of Hydroelectric Engineering*, vol. 37, no. 10, pp. 1–11, 2018.
[15] P. Song, J. Wang, and Y. Zhou, "Properties of high performance synchronous grouting material of water-resistance property and impermeability," *Bulletin of the Chinese Ceramic Society*, vol. 36, no. 2, pp. 438–442+448, 2017.
[16] K. Fang, *Uniform Design and Uniform Design Table*, Science Press, Beijing, China, 1994.
[17] J. Lei, F. Liu, Q. Wang, G. Peng, and Y. Jiang, "Diffusion characteristics and reinforcement mechanics of grouting in non-homogeneous soil strata," *Geotechnical Engineering Journal*, vol. 37, no. 12, pp. 2245–2253, 2015.

Hindawi
Advances in Civil Engineering
Volume 2021, Article ID 1595321, 10 pages
https://doi.org/10.1155/2021/1595321

Research Article

The Construction Countermeasures of Shallow-Buried Small Spacing Tunnel Undercrossing Cultural Relic Buildings: A Case Study

Li Wan,[1] Jiajia Shen,[1] Changan Zhang,[1] Zanquan Lin,[2] and Hu Zhang[2]

[1]*Shandong Provincial Communications Planning and Design Institute Group Co., Ltd., Jinan 250031, China*
[2]*School of Civil Engineering, Central South University, Changsha, China*

Correspondence should be addressed to Zanquan Lin; 204811092@csu.edu.cn

Received 14 October 2021; Accepted 25 November 2021; Published 18 December 2021

Academic Editor: Yu Liang

Based on the background of the reconstruction project from Changqing Chenzhuang-Pingyin section of G220 east-deep line in China, a special tunnel structure and construction plan was carried out according to the construction measures of the shallow-buried small spacing tunnel passing underneath cultural relic buildings, and a comprehensive deformation control scheme of "CRD construction method single-arm excavation + surface grouting prereinforcement + advanced large pipe shed presupport" was put forward. The results of numerical simulation and on-site construction monitoring showed that the overall deformation of aqueduct foundation generally increases first, then decreases and increases again, and finally tends to be stable. The effects of surface grouting prereinforcement and advance large pipe shed presupport are obvious. The comprehensive deformation control scheme can ensure the safety of the existing construction and meet the safety prevention and control requirements.

1. Introduction

With the increasing urban traffic pressure and the saturation of existing road traffic, urban underground transportation has become the main way to relieve traffic pressure. Due to the influence of the surrounding buildings, the construction of urban underground transportation projects will inevitably encounter existing buildings (structures) such as cultural relics which are often extremely sensitive to stratum deformation. As a result, various types of proximity construction, such as the penetration of new projects, are faced with stringent control requirements [1, 2].

As for the underpass construction of nearby existing sensitive buildings, domestic and foreign scholars have carried out a wealth of research work in the field monitoring [3, 4], numerical simulation [1, 5, 6], theoretical analysis [7–10], and other aspects. For example, Wang [11] studied the advantages and disadvantages of the underpassing scheme of jacking frame culvert and the underpassing scheme of shallow-buried tunnels in the project of Shanxi Yushen Expressway underpassing the Qin Great Wall ruins and pointed out that the shallow-buried underexcavation method can effectively restrain the deformation of the surrounding rock. It has the advantage of controlling ground subsidence. Yu [12] studied the influence of different excavation procedures, excavation methods, and buried depth of shallow-buried excavation method on the ground settlement above the excavation boundary based on the model test method with the background of Shenzhen undercrossing Longgang ramp project. Li et al. [13] focused on the control of stratum deformation, starting with the concept of reducing, blocking, and controlling stratum deformation, and proposed safety control measures for the construction of the underpassing building project between the Cuobuling Station and Qingjiang Road Station of Qingdao Metro Line 3. In addition, scholars have also established a variety of analysis models for the ground subsidence caused by tunnel construction [14–16] and proposed feasible control measures [17–20].

The above research expounded the law of land subsidence and surrounding rock deformation caused by tunnel proximity construction and played a positive role in guiding the actual engineering construction. However, most of them

are in the case of single hole or separated double hole, lacking the case of small spacing tunnel with more significant influence for reference. Based on the reconstruction project of the G220 Dongshen Line from Changqing Chenzhuang to Pingyin—Dongfeng Aqueduct Tunnel—which underpasses through the cultural relic Dongfeng Aqueduct, this paper conducts a specific study on the construction method of the small clear tunnel underneath the existing cultural relics. It is hoped to ascertain the impact of the underpass construction of the new tunnel project on the existing cultural relics and propose reasonable construction control methods to ensure the safety of the existing sensitive buildings [21].

2. Engineering Situations

The Dongfeng Aqueduct Tunnel is a reconstruction project from Changqing Chenzhuang to Pingyin boundary section of the G220 Dongshen Line. It is specially designed for the Dongfeng Aqueduct to penetrate the cultural relics. Taking into account the distribution and structural characteristics of the existing cultural relics, the tunnel is designed as two left and right. The mileages of both the left and the right lines are K288 + 608~K288 + 658. The length is 50 m, and the clear distance between the tunnels is about 6 m, which is a short tunnel with a small clear distance. The positional relationship between the Dongfeng Aqueduct Tunnel and the existing cultural relic Dongfeng Aqueduct is shown in Figure 1.

Dongfeng Aqueduct was built in 1970. It is an important part of Xiaoli Dongfeng Irrigation Station and Dongfeng Aqueduct, the fourth batch of municipal cultural relic protection units in Jinan. The aqueduct spans National Highway 220 and Ji-He Expressway, connecting the east and west sides of the mountain slopes, with a total of 34 holes and stone arch structure. The main span is 11.08 m, and the side span is 6.75~6.8 m. The buried depth of the aqueduct pier foundation is 1.3~2 m. The proposed Dongfeng Aqueduct tunnel passes through the main span of the aqueduct (crossing angle: 77°). The left-line tunnel passes under pier 2, and the right-line tunnel passes under pier 3 and pier 4. The aqueduct above the tunnel is 16.2 m high, and the vault is 13.2 m away from the pavement. The buried depth of the tunnel is about 7 m, as shown in Figure 1.

According to the relevant content of Code for design of irrigation and drainage system buildings (SL482-2011) and the purpose of protecting cultural relics, the settlement control of the aqueduct pier in the cross section in this project was carried out based on the settlement control standard used on the operation period. The allowable maximum settlement of the aqueduct pier structure is 20 mm, and the allowable maximum settlement difference of the adjacent pier is 10 mm.

3. Design and Construction Scheme

According to engineering geological mapping and exploration, the stratum of the tunnel site is the quaternary residual slope deposit and the Cambrian shale, limestone and marl thin layer. The hydrogeology is simple, and the surrounding rock conditions of Dongfeng Aqueduct tunnel are classified as V grade surrounding rock by comprehensive geological parameters, as shown in Figure 2.

Furthermore, comprehensively considering the terrain and geology of the intersection of G220 Dongshen Line with Dongfeng Aqueduct and the existing design experience, the proposed tunnel lining structure is a three-center circular curved wall structure. The supporting parameters are shown in Figure 2. At the same time, in order to solve the settlement control of shallow tunnel construction in sensitive environments and to avoid the uneven settlement exceeding the limit value of the foundation of the Dongfeng Aqueduct in the cross section after tunnel excavation, the 40 m long φ 152 mm advanced large pipe shed was planned to be used for prereinforcement in the tunnel undercrossing section. Besides, the CRD method and the cantilever roadheader excavation method are adopted, as shown in Figure 3. The specific construction techniques are as follows:

(1) *Surface Grouting Reinforcement*. In order to improve stratum stability, surface grouting reinforcement should be carried out within the influence range of aqueduct. The grouting pipe is a seamless steel pipe with a diameter of 42 mm and a wall thickness of 4 mm, and the steel bar with a diameter of 8 mm is welded as the stiffening hoop. The spacing between grouting pipes was 100 cm, the plum-shaped arrangement was adopted for the longitudinal spacing of 100 cm, as shown in Figure 3. The slurry used for grouting is cement-water glass slurry, which is blended strictly in accordance with the cement slurry water-cement ratio of 0.8 : 1. Water glass is 5% of the cement weight. The grouting pressure is strictly controlled according to the actual situation during grouting.

(2) *Pipe Shed Construction*. Firstly, the aqueduct is temporarily reinforced with full framing, and then the large pipe shed is constructed. The pipe shed is 40 m long, the diameter is 152 mm, and the wall thickness is 6 mm. Two rows of φ12 mm plum blossom-shaped grouting holes are drilled around. The elevation angle of pipe shed (1°) is parallel to the middle line of the route, as shown in Figure 4.

(3) *Mechanical Excavation of Main Tunnel by CRD Method*. The main tunnel is excavated by CRD method + cantilever roadheader, and the left and right tunnels are excavated separately. The excavation sequence is strictly observed and the footage is controlled. First, the small duct advance support of the right main tunnel is carried out. After the advance support, the upper bench of the right pilot tunnel is excavated. Initial support is provided promptly after excavation. Secondly, the excavation and initial support of the lower stage of the right pilot tunnel are carried out. At the same time of the initial

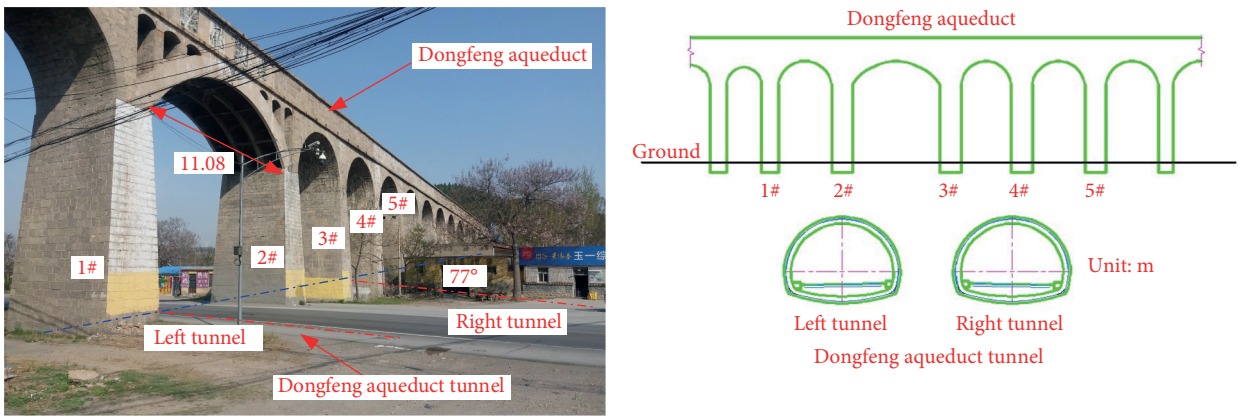

(a) (b)

Figure 1: Location map of Dongfeng Aqueduct tunnel: (a) spatial position; (b) facade.

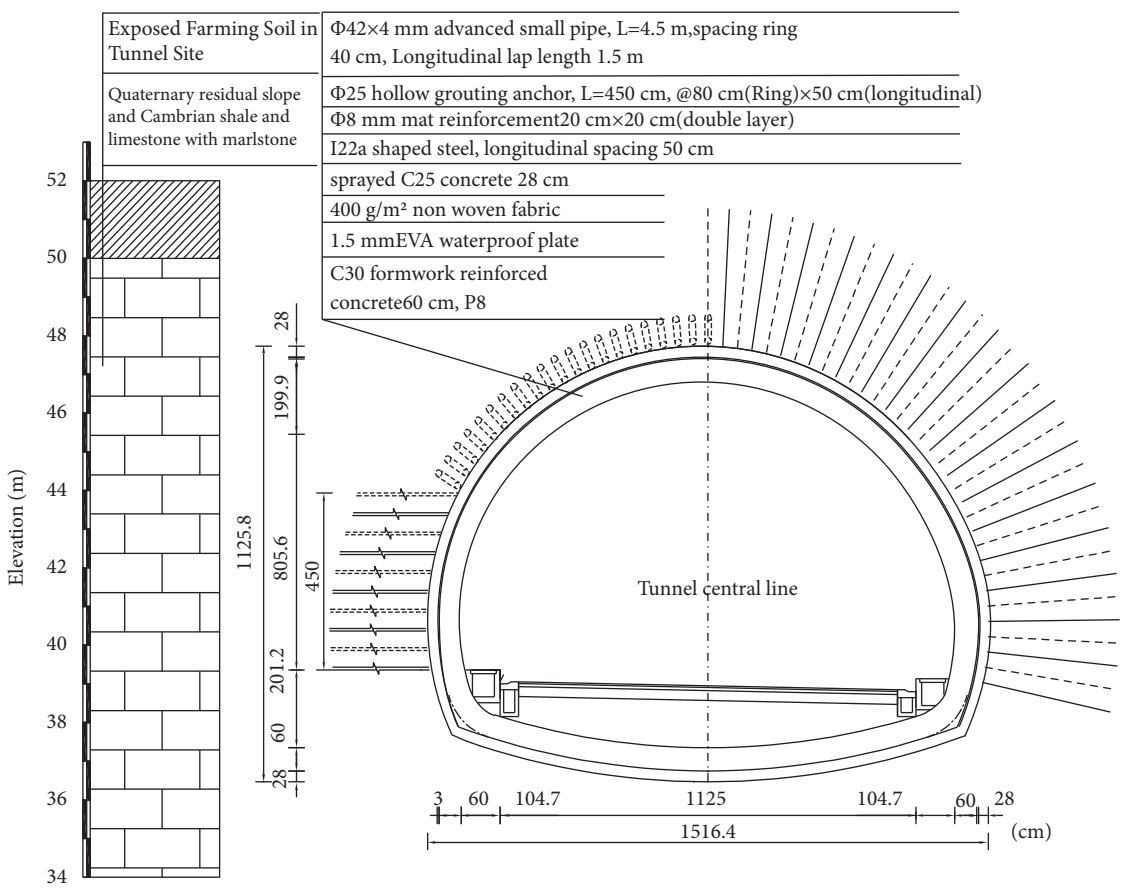

Figure 2: Geological conditions of tunnel site and section map of tunnel design.

support, a small grouting pipe is set up for the middle rock column to reinforce the middle rock. In the same way, the left pilot hole was excavated, as shown in Figure 5. After the initial support of the left pilot tunnel was completed, temporary support should be removed, and inverted arch and secondary lining were applied. The right tunnel adopts the same construction method.

4. Feasibility Analysis of the Scheme

In order to accurately analyze the influence of new tunnel undercrossing construction on Dongfeng Aqueduct and master the surrounding surface settlement law induced by tunnel excavation, seven span piers which have the greatest influence on the aqueduct in the process of tunnel excavation were selected as the research objects. The finite

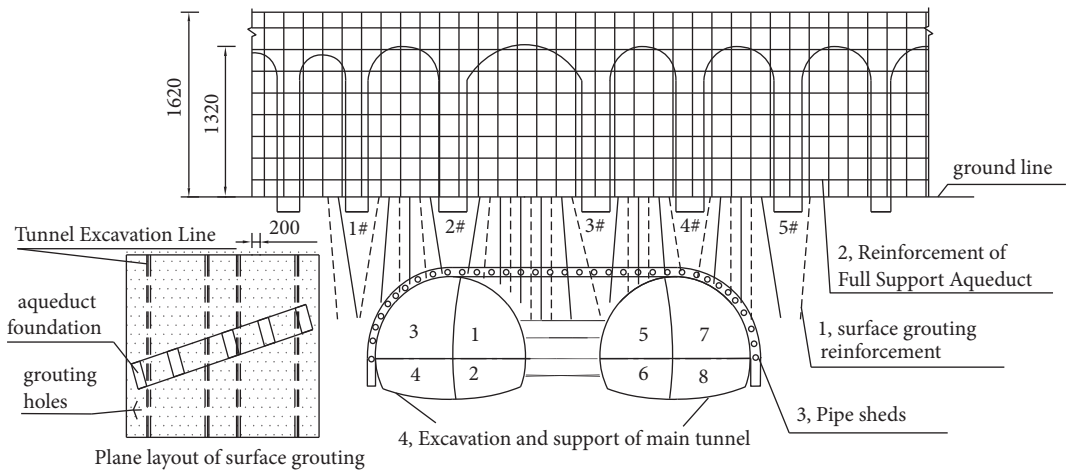

Figure 3: Excavation scheme of Dongfeng Aqueduct tunnel (cm).

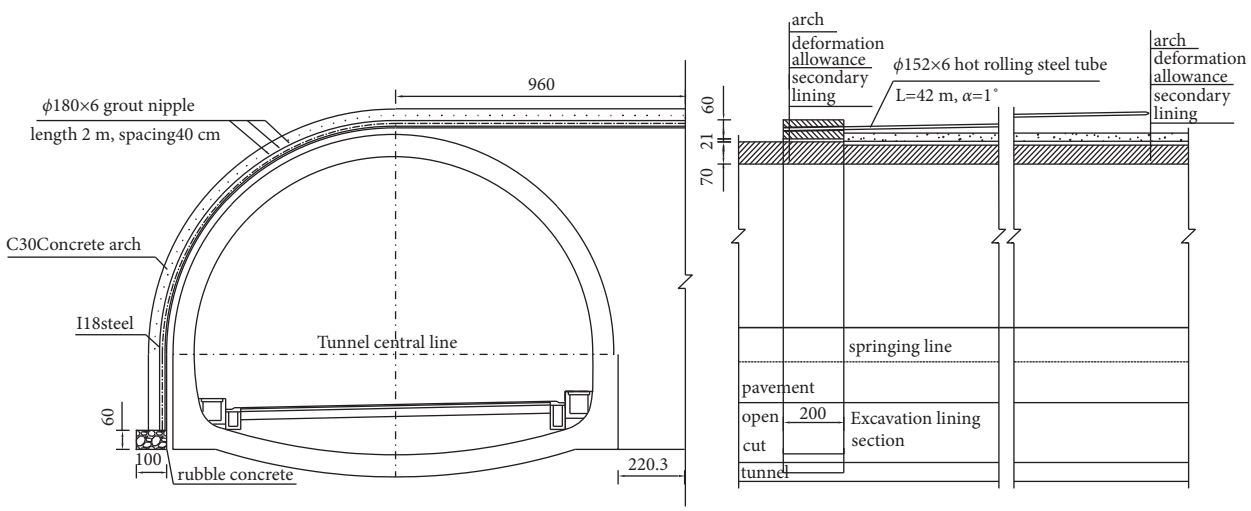

Figure 4: Pipe roof structure diagram (cm).

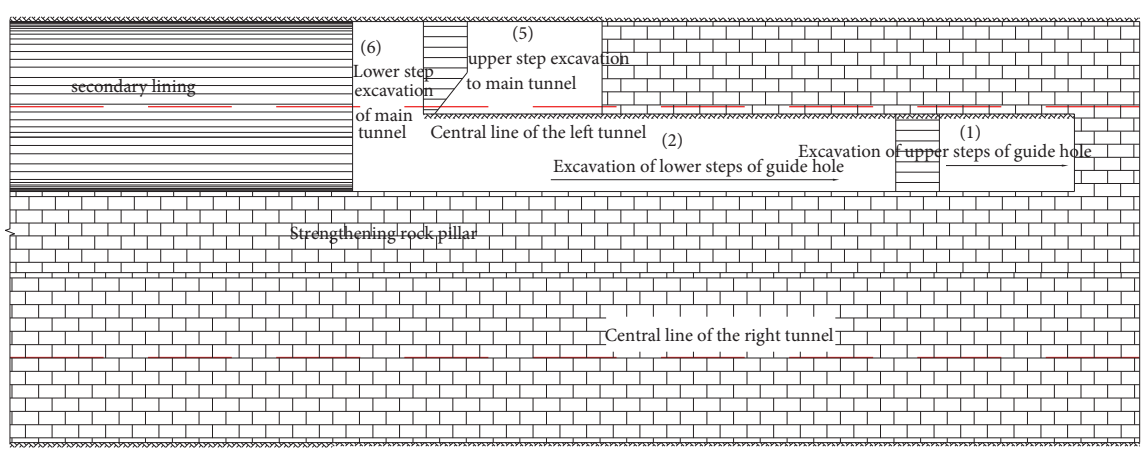

Figure 5: Excavation step diagram.

element model was established to investigate the influence of tunnel excavation on its deformation and internal force, and then the safety influence of tunnel undercrossing construction on the aqueduct was evaluated.

4.1. Modeling. In combination with the actual situation of the project, the left and right sides and the lower boundary of the model tunnel in the horizontal direction were all three times the diameter of the tunnel, and the left and right sides

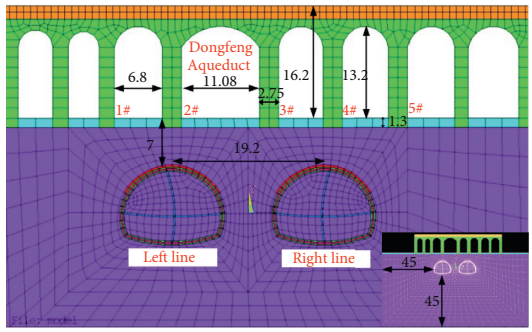

Figure 6: Calculation model (m).

Table 1: Values of calculation parameters for aqueduct structure.

Name	Elastic modulus (GPa)	Poisson's ratio	Volumetric weight (kN/m^3)	Shear transfer coefficient of open cracks	Shear transfer coefficient of closed cracks	Uniaxial tensile stress (MPa)
Flume structure	20000	0.25	25	0.35	0.9	0.75

Table 2: Calculation parameters of surrounding rock.

Surrounding rock	Modulus of deformation (MPa)	Poisson's ratio	Volumetric weight (kN/m^3)	Friction angle (°)	Cohesion (MPa)
Quaternary residual slope deposit	15	0.37	18	15	0.03
Medium weathered marlstone	3800	0.31	22	35	0.5
Advanced pipe shed	20000	0.25	24	50	1.5

of the aqueduct were symmetrical boundaries. The numerical model is shown in Figure 6.

4.2. Calculation Parameters. Since the aqueduct was built of reinforced concrete and mortar block stones, the strength of the joint mortar is lower than that of block stones and concrete. Besides, the aqueduct was built early, and its materials had different degrees of deterioration. When establishing the continuum model, its structural material adopts the concrete constitutive model. The material parameters of the aqueduct structure are shown in Table 1.

The surrounding rock adopts the Drucker–Prager constitutive model, and the supporting effect of the advanced pipe roof on the surrounding rock was considered by increasing the surrounding rock parameters, as shown in Table 2. The parameter values of the temporary support, initial support, and secondary lining of the tunnel are shown in Table 3.

4.3. Calculating Procedure. The method used for tunnel excavation is the CRD method, and the whole process of underpassing the tunnel may have an impact on the aqueduct. Therefore, it is necessary to establish a separate analysis step for each excavation step to consider. There were a total of 22 analysis steps in the calculation and analysis steps of this model. The general steps are as follows: step 1—initial stress field balance; step 2—soil reinforcement; steps 3–12—from left tunnel presupporting to completion of construction; and steps 13–22—from right tunnel presupporting to completion.

4.4. Result Analysis. Figures 7~10 show the calculation results of the deformation and force of each key part after the excavation of the Dongfeng Aqueduct tunnel. The analysis shows the following:

(1) After the excavation of the left tunnel, the surrounding rock and the upper aqueduct structure were deformed. However, due to the support effect of pipe roof and tunnel structure, the influence range of surrounding rock deformation was small. The deformation of aqueduct structure mainly occurred near No. 1 and No. 2 piers above the roof of the tunnel, as shown in Figure 7(a). After the excavation of both left and right tunnels, the influence range of surrounding rock deformation was further increased. The structural deformation of aqueduct mainly occurred in the range of piers 1–5 above the top of the tunnel, as shown in Figure 7(b). Through the deformation results of aqueduct structure, it can be found that during tunnel excavation, the deformation of the aqueduct is mainly vertical settlement with a slight twist, as shown in Figure 8. The settlement of aqueduct foundation was large above the vault and small on both sides. The settlement curve is

Table 3: Support parameter value.

Name	Material	Elastic modulus (GPa)	Poisson's ratio	Volumetric weight (kN/m^3)	Cross section	Geometry (m)	
Temporary support	C25 sprayed concrete	27.6	0.25	25	Rectangle	H B	0.20 1.0
Initial support	C25 sprayed concrete	28.3	0.25	25	Rectangle	H B	0.26 1.0
Secondary lining (including inverted arch)	Reinforced concrete	31	0.2	25	Rectangle	H B	0.60 1.0

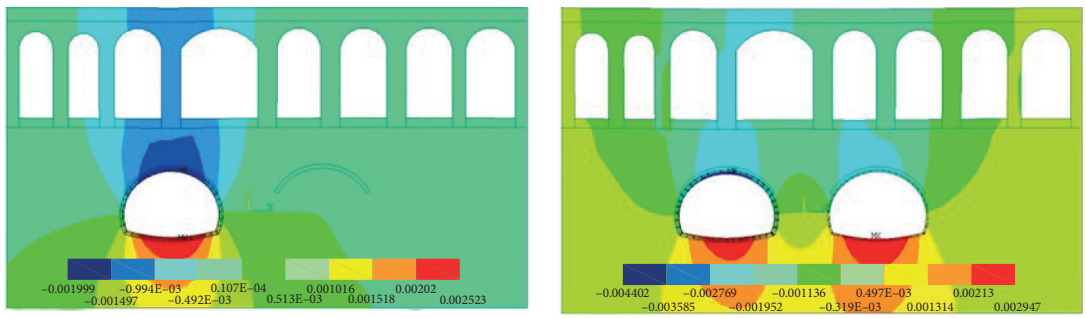

(a) (b)

Figure 7: Overall vertical deformation of the model. (a) After the excavation of the left tunnel. (b) After the excavation of the right tunnel.

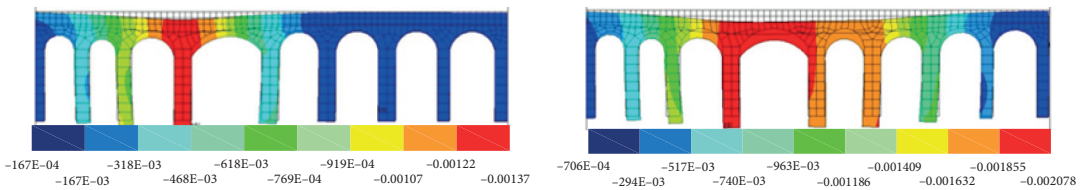

(a) (b)

Figure 8: Structural deformation of aqueduct. (a) After the excavation of the left tunnel. (b) After the excavation of the right tunnel.

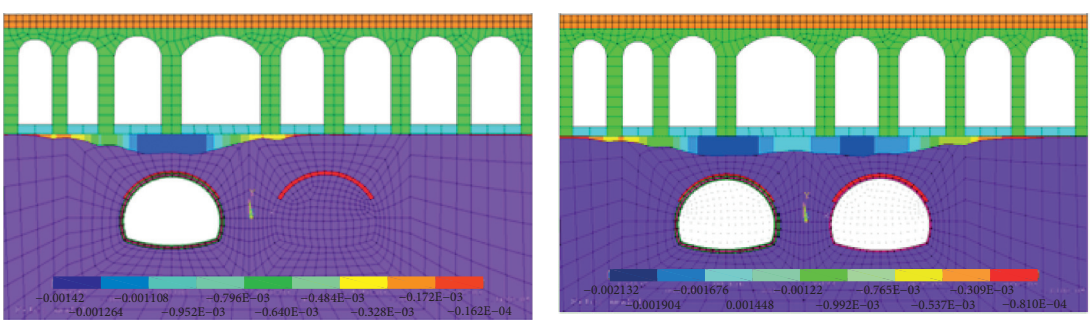

(a) (b)

Figure 9: Settlement of aqueduct foundation. (a) After the excavation of the left tunnel. (b) After the excavation of the right tunnel.

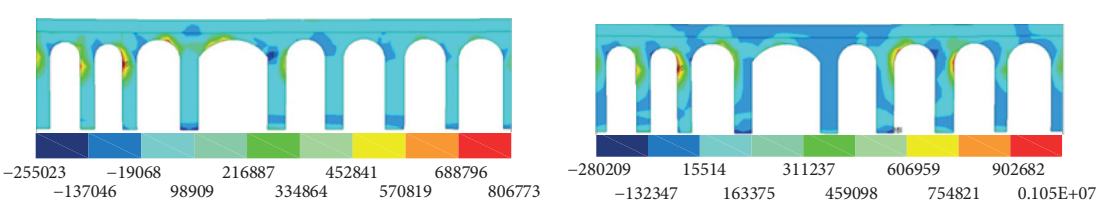

(a) (b)

Figure 10: First principal stress of aqueduct structure. (a) After the excavation of the left tunnel. (b) After the excavation of the right tunnel.

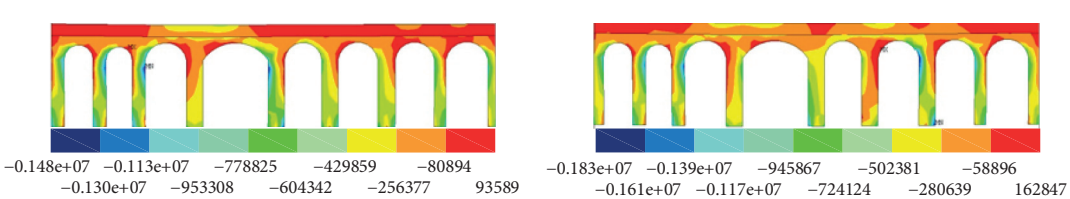

(a) (b)

Figure 11: Third principal stress of aqueduct. (a) After the excavation of the left tunnel. (b) After the excavation of the right tunnel.

Figure 12: Measuring point layout.

"W" shaped. The maximum calculation value of foundation differential settlement was about 7 mm, as shown in Figure 9.

(2) The stress of aqueduct structure was redistributed locally under deformation. After the left line excavation was completed, local tensile stress appeared near the arch ring connected with pier 1 and pier 2. The direction of tensile stress was basically tangent to the arch ring, and the maximum tensile stress was 0.57~0.81 MPa. After the excavation of the left and right lines, local tensile stress appeared near the arch ring connected with piers 1~5, and the maximum tensile stress was in the range of 0.6~1.1 MPa (Figures 10 and 11). The maximum tensile stress was lower than the bending tensile strength of stone and was greater than the strength of masonry cement mortar. Therefore, under the influence of tunnel construction, the aqueduct structure may have small range of masonry cracks. However, the tensile stress was mainly concentrated near the surface of the structure, the scale was small, the structure was not connected, and the internal stress of the structure was still dominated by compressive stress. Therefore, the masonry crack mainly occurs on the surface of the structure, which is not easy to develop into the internal structure and has little influence on the bearing capacity of the structure. So, it can be considered that the aqueduct structure was still in a safe state.

5. Engineering Application Effect

During the implementation of this project, measuring points were arranged on piers 1 to 5 to monitor the cumulative vertical displacement of aqueduct foundation. The arrangement of measuring points is shown in Figure 12, and the monitoring results of representative measuring points are shown in Figure 13. The analysis shows the following:

(1) The vertical displacement of aqueduct foundation generally showed a cumulative growth trend, except for a slight uplift in the period of surface grouting and pipe shed construction stage. In the presupport stage, the change of vertical displacement of foundation is relatively obvious, and in the left and right tunnel excavation stages, the vertical displacement gradually tended to be stable. In the process of slope construction, the cumulative vertical displacement of each measuring point was not large, and the maximum vertical displacement occurs in No. 2 foundation of −1.5 mm. The maximum value of cumulative vertical displacement in surface grouting engineering was −3.6 mm in foundation 3. The maximum cumulative vertical displacement of pipe shed during construction was −5.5 mm in No. 3 foundation. In the process of left and right tunnel excavation, the maximum cumulative vertical displacement also appeared in No. 3 foundation of −6.1 mm. In the construction process, the maximum differential settlement was 5.2 mm. It can be seen that in the process of presupport, the vertical displacement of aqueduct structure foundation was in a reasonable range and the differential settlement was also in the specified range.

(2) The horizontal displacement of aqueduct foundation generally showed a trend of cumulative shrinkage, with the exception of foundation No. 4 and foundation No. 5 slightly expanding in the period of surface grouting and pipe shed construction stage. In the presupport stage, the horizontal displacement of foundation changes significantly, and in the left and right tunnel excavation stages, the horizontal displacement gradually tended to be stable. In the process of slope construction, the cumulative horizontal displacement of each measuring point was not large, and the maximum horizontal displacement occurred in No. 3 foundation of −1.7 mm. The maximum value of cumulative horizontal displacement in surface grouting engineering was −3.1 mm in foundation 2. The maximum cumulative horizontal displacement during pipe shed construction appears on foundation No. 2 of −4.2 mm. In the process of left and right tunnel excavation, the

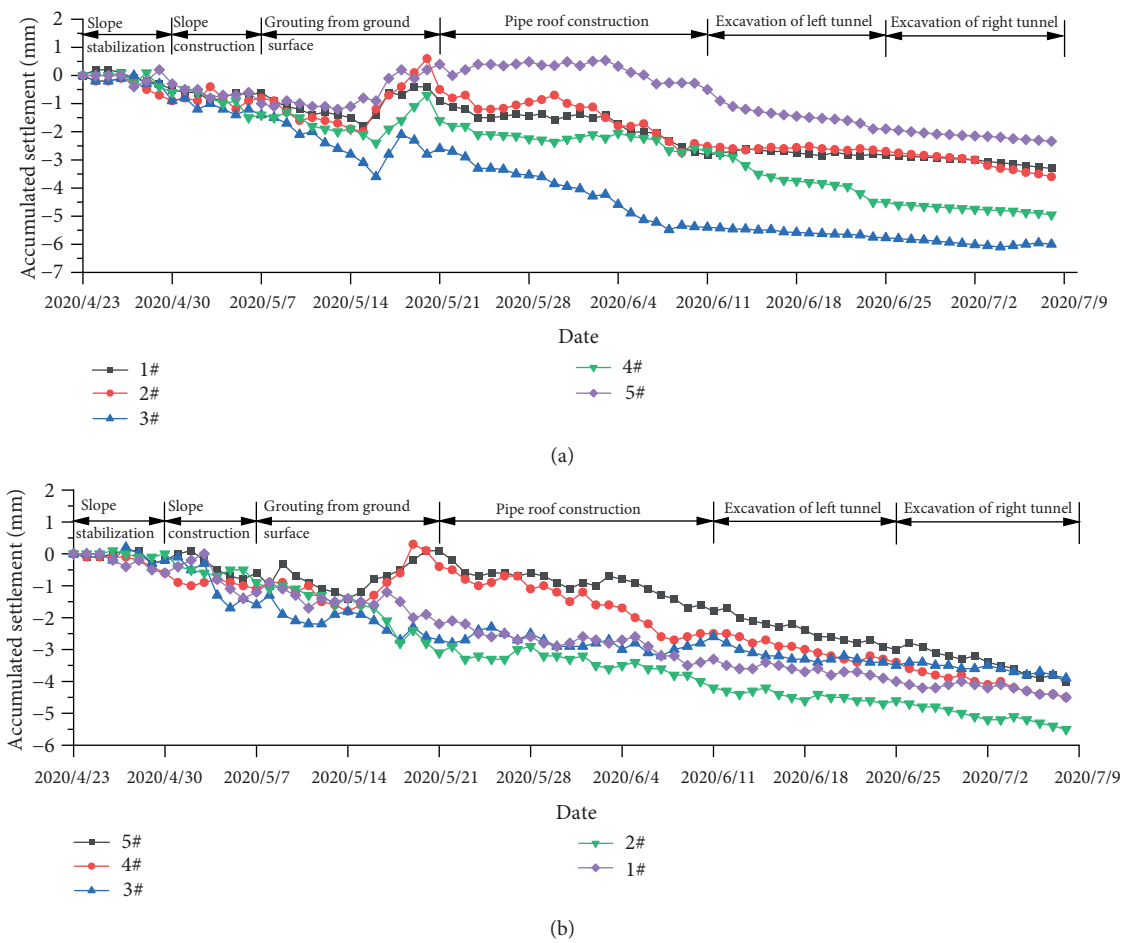

Figure 13: Monitoring data of representative measuring points. (a) Cumulative settlement map. (b) Cumulative horizontal displacement map (+: outward expansion; −: draw-in).

maximum cumulative horizontal displacement also appeared in No. 2 foundation of −5.5 mm. The cumulative horizontal displacement of each foundation during construction was also less than the warning value of 20 mm. It can be seen that in the presupport process, the horizontal displacement of the aqueduct structure foundation was in a reasonable range.

6. Conclusion

(1) Based on the reconstruction project of the section from Chenzhuang to Pingyin on the Dongshen line of G220, a special tunnel structure and construction plan design is carried out. The comprehensive deformation control scheme of "CRD single-arm tunneling + surface grouting prereinforcement + advanced large pipe shed presupport" is proposed, and the corresponding design parameters were obtained. This case can be used as reference for similar projects.

(2) The numerical simulation of mechanical behavior in the whole process of reinforcement treatment and excavation construction of Dongfeng Aqueduct tunnel was carried out. The results showed that the comprehensive deformation control scheme proposed by the project can ensure the safety of the existing construction, and the stratum deformation caused by the excavation of the new tunnel was small, which meets the requirements of safety prevention and control.

(3) The field monitoring scheme of the whole construction process was formulated and the real-time tracking observation was carried out. The results showed that the cumulative vertical displacement of the aqueduct foundation increases first, then decreases and increases again, and finally tends to be stable. The vertical displacement of the measuring point on the basis of No. 3 was the most significant, and the maximum value is −6.1 mm. The cumulative horizontal displacement of aqueduct foundation generally increased slowly except No. 4 and No. 5. From the completion of surface grouting to the pipe shed construction stage, the horizontal displacement was basically stable at other measuring points except for the expansion of foundation No. 4 and No. 5. The maximum cumulative horizontal displacement of No. 2 measuring point was −5.5 mm.

Data Availability

The data used to support the findings of this study are available from the corresponding author upon request.

Conflicts of Interest

The authors declare that they have no conflicts of interest.

Acknowledgments

This study was funded by the Transportation Department Science and Technology Research Project of Shandong Province, China (no. 2019B55).

References

[1] C. Zhao, M. Lei, C. Shi, H. Cao, W. Yang, and E. Deng, "Function mechanism and analytical method of a double layer pre-support system for tunnel underneath passing a large-scale underground pipe gallery in water-rich sandy strata: a case study," *Tunnelling and Underground Space Technology*, vol. 115, Article ID 104041, 2021.

[2] M. Lei, D. Lin, Q. Huang, C. Shi, and L. Huang, "Research on the construction risk control technology of shield tunnel underneath an operational railway in sand pebble formation: a case study," *European Journal of Environmental and Civil Engineering*, vol. 24, no. 10, pp. 1558–1572, 2020.

[3] M. Lei, L. Liu, C. Shi, Y. Tan, Y. Lin, and W. Wang, "A novel tunnel-lining crack recognition system based on digital image technology," *Tunnelling and Underground Space Technology*, vol. 108, Article ID 103724, 2021.

[4] Q. Tang, M. Lei, B. Zhu, L. Peng, W. Wu, and C. Shi, "Design and application of risk early warning system for subway station construction based on building information modeling real-time model," *Advances in Civil Engineering*, vol. 2021, pp. 1–12, Article ID 8898893, 2021.

[5] L. Huang, J. Ma, M. Lei, L. Liu, Y. Lin, and Z. Zhang, "Soil-water inrush induced shield tunnel lining damage and its stabilization: a case study," *Tunnelling and Underground Space Technology*, vol. 97, Article ID 103290, 2020.

[6] J. Liu, C. Shi, M. Lei, Z. Wang, C. Cao, and Y. Lin, "A study on damage mechanism modelling of shield tunnel under unloading based on damage-plasticity model of concrete," *Engineering Failure Analysis*, vol. 123, Article ID 105261, 2021.

[7] M. Lei, J. Li, C. Zhao, C. Shi, W. Yang, and E. Deng, "Pseudo-dynamic analysis of three-dimensional active earth pressures in cohesive backfills with cracks," *Soil Dynamics and Earthquake Engineering*, vol. 150, Article ID 106917, 2021.

[8] M. Lei, B. Zhu, C. Gong, W. Ding, and L. Liu, "Sealing performance of a precast tunnel gasketed joint under high hydrostatic pressures: site investigation and detailed numerical modeling," *Tunnelling and Underground Space Technology*, vol. 115, Article ID 104082, 2021.

[9] Q. Tang, F. Chen, M. Lei, B. Zhu, and L. Peng, "Study on the generalized displacement boundary and its analytical prediction for ground movements induced by shield tunneling," *Advances in Civil Engineering*, vol. 2021, Article ID 8858874, 18 pages, 2021.

[10] J. Liu, C. Shi, M. Lei, C. Cao, and Y. Lin, "Improved analytical method for evaluating the responses of a shield tunnel to adjacent excavations and its application," *Tunnelling and Underground Space Technology*, vol. 98, Article ID 103339, 2020.

[11] Y. Wang, "Scheme comparison and settlement control of shallow-buried double-span and large-section rectangular tunnel under the Great Wall site," *Sichuan Architecture*, vol. 33, no. 03, pp. 163–166, 2013, in Chinese.

[12] X. Yu, *Model Test Study on Urban Shallow-Buried Underground Tunnel Crossing Existing Bridge Piles*, Dalian University of Technology, 2019, in Chinese.

[13] Y. Li, D. Zhang, F. A. N. G. Qian et al., "Study on safety control technology of upper building crossed by shallow metro tunnel," *Journal of Civil Engineering*, vol. 48, no. S1, pp. 266–269, 2015, in Chinese.

[14] C. Camós and C. Molins, "3D analytical prediction of building damage due to ground subsidence produced by tunneling," *Tunnelling and Underground Space Technology*, vol. 50, pp. 424–437, 2015.

[15] D. Wu, T. Deng, R. Zhao, and Y. Wang, "THM modeling of ground subsidence induced by excavation of subway tunnel," *Computers and Geotechnics*, vol. 94, pp. 1–11, 2018.

[16] C. D. Garner and R. A. Coffman, "Subway tunnel design using a ground surface settlement profile to characterize an acceptable configuration," *Tunnelling and Underground Space Technology*, vol. 35, pp. 219–226, 2013.

[17] H. Cao, L. Peng, M. Lei, Q. Tang, L. Peng, and F. Chen, "Calculation model of supporting system for tunnel under shallow and weak surrounding rock considering the synergistic effects," *Geotechnical & Geological Engineering*, vol. 38, no. 2, pp. 1379–1388, 2020.

[18] J. Liu, C. Shi, C. Cao, M. Lei, and Z. Wang, "Improved analytical method for pile response due to foundation pit excavation," *Computers and Geotechnics*, vol. 123, Article ID 103609, 2020.

[19] C. Liu, M.-f. Lei, L.-m. Peng, and C.-h. Shi, "Cavity influence on fatigue performance of heavy haul railway Tunnel's bottom structure," *Construction and Building Materials*, vol. 251, Article ID 118886, 2020.

[20] Y. Cui, K. Kishida, and M. Kimura, "Prevention of the ground subsidence by using the foot reinforcement side pile during the shallow overburden tunnel excavation in unconsolidated ground," *Tunnelling and Underground Space Technology*, vol. 63, pp. 194–204, 2017.

[21] C. Jia, Q. Zhang, M. Lei, Y. Zheng, J. Huang, and L. Wang, "Anisotropic properties of shale and its impact on underground structures: an experimental and numerical simulation," *Bulletin of Engineering Geology and the Environment*, vol. 80, 2021.

Hindawi
Advances in Civil Engineering
Volume 2021, Article ID 9738820, 9 pages
https://doi.org/10.1155/2021/9738820

Research Article

Research on Visual Management Technology of Tunnel Construction Process Based on BIM Technology

Yue Zhou,[1] Chuang Wang,[1] Bingxiang Yuan,[2] Minjie Chen,[2] and Jianbing Lv[2]

[1]*Zhuhai Dahengqin Co., Ltd, Zhuhai, Guangdong 519000, China*
[2]*School of Civil and Transportation Engineering, Guangdong University of Technology, Guangzhou 510006, China*

Correspondence should be addressed to Bingxiang Yuan; yuanbx@gdut.edu.cn

Received 20 November 2021; Accepted 2 December 2021; Published 17 December 2021

Academic Editor: Ma Jianjun

In order to achieve more efficient management of BIM technology in the field of tunnel construction, this paper took Zhuhai Dahengqinshan No. 1 Tunnel as the project background and studied the visualization management technology of tunnel construction process based on BIM technology. Firstly, we created the 3D geological model and tunnel BIM model by using Revit, 3dsmax, and other software. Secondly, the detailed design was carried out, and there was no gap in the model after the detailed design was checked by ABAQUS software. Then, we checked the problems between disciplines and conducted collision inspection in the model. Finally, we carried out the 4D construction progress simulation to solve the conflict between time and space in the whole life cycle of tunnel construction. The results revealed that the deepening design could optimize the design scheme of tunnel construction engineering. Collision inspection directly exposed problems such as unscientific site layout. 4D construction schedule management could not only realize the visualization of field construction process but also improve the quality of project management compared with traditional means. The research results provide technical experience for the visualization management of tunnel construction.

1. Introduction

Since the beginning of the twenty-first century, the construction of traffic tunnels in China has developed rapidly [1, 2]. The large area of highway tunnels has broken the restrictions between urban areas, thus driving the economic development around the tunnel. At present, more than 35 cities in China have urban rail transit, mainly subway. There are more than 3000 stations and 169 planned lines in China, with a total mileage of more than 5000 km [3–5]. Up to 2017, 15000 km of railway tunnels have been put into use in China, and more than 16,000 highway tunnels have been operated, with a total length of 15000 km [6–8].

However, the tunnel project has the characteristics of concealment, large volume, long construction period, and high construction requirements. The traditional schedule management is largely dependent on the engineering experience of managers. It is often only to optimize the schedule in the early stage of the project, which cannot show the problems existing in the construction process. The lack of effective collaborative construction in each stage of the actual project is prone to delay the construction period [9–11].

BIM (Building Information Modeling) links the three-dimensional information model with schedule elements to realize visualization of the whole construction process and highly integrate project documents [12–14]. Compared with most projects only using PROJECT, P6, and other software for schedule management, BIM can better serve the visual management of tunnel construction by prefabricating site layout and formulating countermeasures in advance for problems encountered in the construction process [15–17].

Many scholars have applied BIM technology to the progress management of tunnel construction. IFC file can be used as the carrier of information interaction between platforms. Through 4DCAD technology, 3D terrain model, building model, and schedule can be combined to realize four-dimensional schedule management based on the IFC

standard [18, 19]. Wang et al. [20] introduced building information modeling and virtual reality technology into immersed tunnel engineering by combining with VR technology. Zhu et al. [21] proposed a standardized and refined modeling method for highway tunnels by using Civil3D, Revit, Dynamo, and other software, which solved the problem of spatial 3D surface modeling. This method is verified in the actual tunnel process. Song et al. [22, 23] introduced the role and advantages of BIM in design, construction, operation, and maintenance and provided guidance for integrated management based on practical engineering. Secondly, in view of the inconsistency of BIM standards in the whole life cycle of tunnel engineering, a BIM management platform for the whole life cycle is proposed to coordinate multiple levels, which lays the foundation for the application of the platform in practical engineering in the future.

On the basis of previous studies, taking Zhuhai Dahengqinshan No. 1 Tunnel as the project background, this paper carried out BIM technology application research on the establishment of three-dimensional geological model, tunnel model modeling, collision inspection, deepening design, and four-dimensional schedule management, which could realize the visualization of tunnel construction process. In this paper, we could formulate or optimize the construction scheme in advance for the conflicts in the construction. The research results provide experience reference for visual management of tunnel construction process.

2. Project Overview

Dahengqinshan Tunnel (phase I) is located in Hengqin Island, connecting Hengqin Avenue in the north and Qinhai South Road to be built in the south. It crosses Dahengqin Mountain, with a total length of 4.9 km. According to the plan, in the future, the tunnel will pass through Hengqin Avenue, connecting with Hengqin Tunnel in the north and with Zhuhai Avenue in the long term. It is one of the "aorta" of outreach in Hengqin Island. The design standard of Hengqinshan Tunnel is 60 km/h, which is a two-way 6-lane urban trunk road municipal tunnel. The section where the tunnel is located is the eroded residual hill landform, with residual soil (gravelly cohesive soil) covered on the surface of the mountain, and the basement is the granite of Yanshan Stage II-III. Dahengqinshan Tunnel is constructed by spray anchor support, composite lining, and CRD method. YK1 + 281 on the right and ZK1 + 289 on the left underpass the planned Zhuji urban rail tunnel. The vertical distance between the left line of Dahengqinshan Tunnel and Zhuji Tunnel is 4.36 m and 3.50 m on the right (Figure 1). According to the survey report, the topographic map of the survey area is shown in Figure 2.

3. Establishment of BIM Model

3.1. Tunnel Geological Model Modeling. In order to restore the real geological conditions of the geological model, this paper creates a three-dimensional geological model based on the 'point-surface-body' construction model of Civil 3D [24–26]. First of all, using the high and low irregular pile foundation information, namely, the original measurement data and geological drilling information data, we integrate them into a triangular network to form a triangular surface. Through the three-dimensional observer, the abnormal points are excluded in the elevation range. The processed data information is imported into the software platforms such as Revit and 3dsmax for secondary terrain utilization. According to the generated terrain surface, the tunnel plane route design, longitudinal section design, and assembly design are carried out. Finally, the geological rock and soil body surrounded by the surface are obtained by using the Civil3D surface creation and entity extraction function to surround the geological layer surface. The specific modeling technical route and the formed geological surface model are shown in Figures 3 and 4, respectively.

3.2. Tunnel Model Modeling. According to the geological information and route direction of the project, the BIM model of Dahengqinshan Tunnel is formed by cross section lofting along the central line of the route. When the superelevation part of the tunnel cross section appears, the superelevation value of the radius of the horizontal curve is given and loaded into the tunnel cross section. In this process, the cross section changes dynamically with the change of the pile number. Finally, the separated tunnel model is generated through component lofting (Figure 5).

3.3. Construction Monitoring Visualization. We compare the BIM model of each discipline with the drawings and model data provided by the owner for model integrity review. Problems between single specialty and multispecialty were found in the model inspection. Table 1 shows the single specialty model problem.

According to the process of BIM model deepening design, the model of the research object is optimized, including specialty internal deepening, multispecialty comprehensive optimization, and standardization of reserved holes. The principles and methods of model optimization are put forward (Table 2).

4. Analysis of Shield Tunnel Construction Scheme

4.1. Collision Check. The collision check function of BIM technology can allow quick identification of hard collision, soft collision, and duplicate items in the model [27–29]. Compared with the previous omissions caused by relevant personnel modifying the design scheme through two-dimensional drawings and personal spatial imagination, Navisworks' powerful "clash detective" function greatly improves the work efficiency. The resulting collision inspection report shows that there are 514 structural conflicts between different majors. Finally, the BIM model is modified according to the inspection results.

The errors can be divided into five types: collision between ① sprayed arch wall and arch wall lining; ② 3# plug

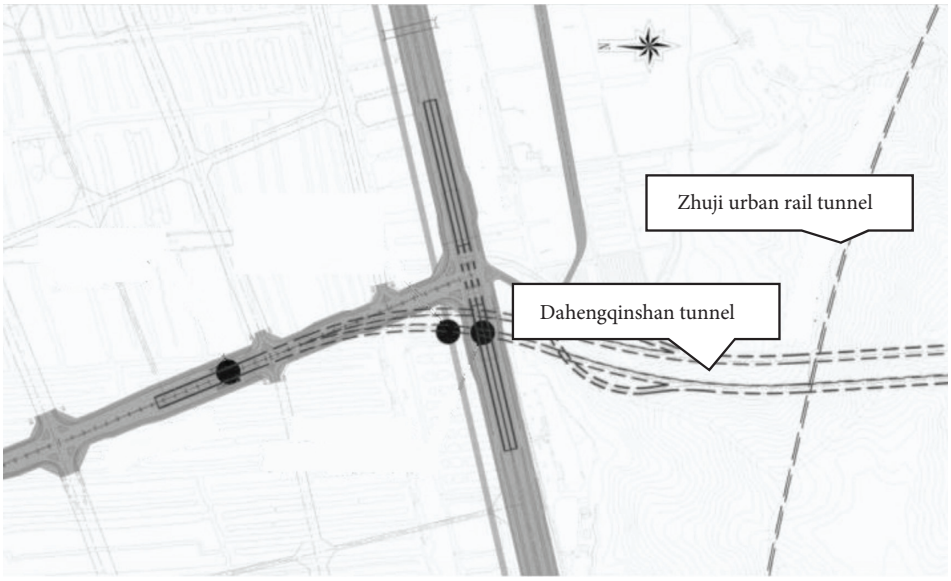

Figure 1: Plane position relationship between Dahengqinshan Tunnel and Zhuji Tunnel.

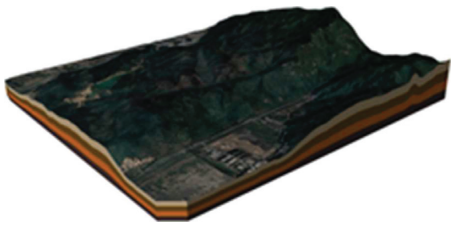

Figure 2: Topographic overview.

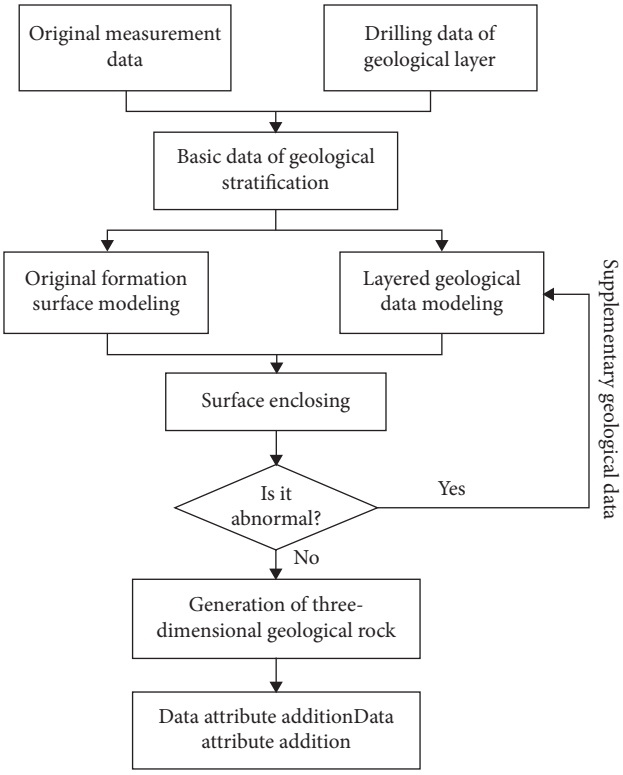

Figure 3: Modeling technology roadmap.

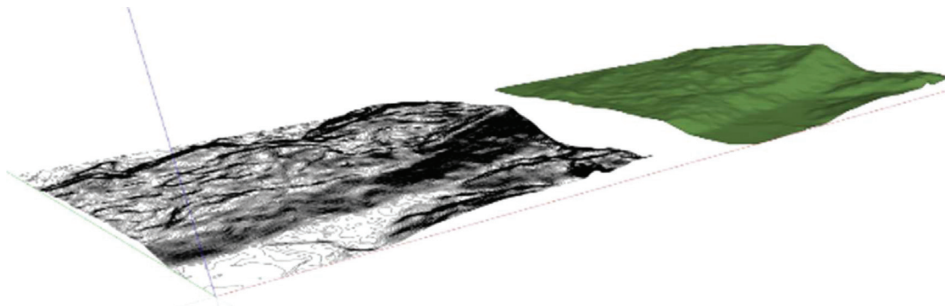

Figure 4: Geological model.

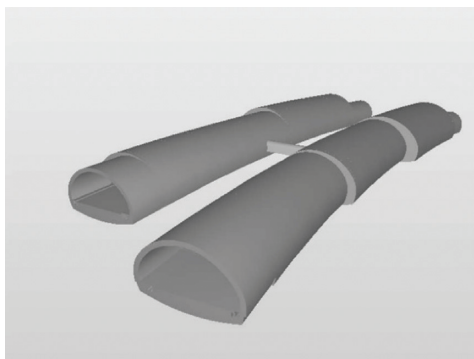

Figure 5: Tunnel model.

Table 1: Model problems.

Specialty	Problems
Comparison between civil engineering model and drawing	There will be overlaps and gaps between sprayed arch walls There will be overlaps and gaps between arch wall linings 3# plug wall of left line and sprayed arch wall cannot be closed There will be overlaps and gaps between invert arch linings There will be overlaps and gaps between shotcrete linings 3# plug wall of left line and arch wall lining cannot be closed 3# plug wall of left line and invert arch lining cannot be closed There is a gap between tunnel pipe sections, which cannot be closed Overlaps and gaps will be formed between inverted arch filling

wall of left line and sprayed arch wall; ③ 3# plug wall of left line and shotcrete lining; ④ invert arch lining and sprayed arch wall; and ⑤ shotcrete lining and 3# plug wall of left line.

Figure 6 shows the hard collision between several tunnel structures.

4.2. Visualization Analysis of Construction Monitoring. Based on the characteristics of BIM information integration and according to the layout scheme of measuring points of Dahengqinshan Tunnel at the intersection, the displacement sensors and velocity sensors arranged at the arch crown, arch bottom, and arch waist are visually displayed in the BIM model. The sensor model is created with the help of Revit software. At the same time, the sensor family is defined and the geometric appearance of the sensor entity is created. The sensors on the model are associated with the monitoring information collected in the field construction to facilitate the recording of monitoring data. Because the sensor model in this paper mainly realizes the function of information expression and three-dimensional positioning, in order to make the BIM model lightweight, the sensor entity is simplified. Figure 7 shows the layout and geometric appearance of sensors on the tunnel section. The visualization of construction monitoring can realize the automatic input of monitoring point information and monitoring data. Compared with the traditional manual data recording and excel table sorting and calculation, the BIM tunnel safety monitoring method can ensure the authenticity of the original data and greatly improve the efficiency of construction information processing.

Table 2: Professional internal deepening table.

Specialty	Optimization principle	Optimization reason
Tunnel structure	Tunnel joints close connection	Overlaps and gaps between tunnel sections
Optimization suggestion	Modify the model to make the tunnel element tightly connected	
Problem description	First process the tunnel model with Revit, modify the tunnel pipe joints so that there is no gap between the pipe joints, and then cut off the overlapping places of the tunnel pipe joints with ABAQUS to make the tunnel pipe joints closely connected	
Problem diagram	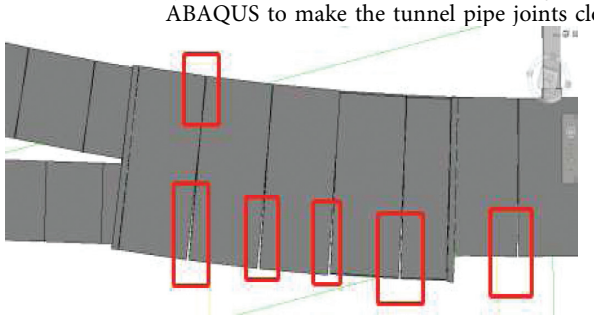	
Deepened model		

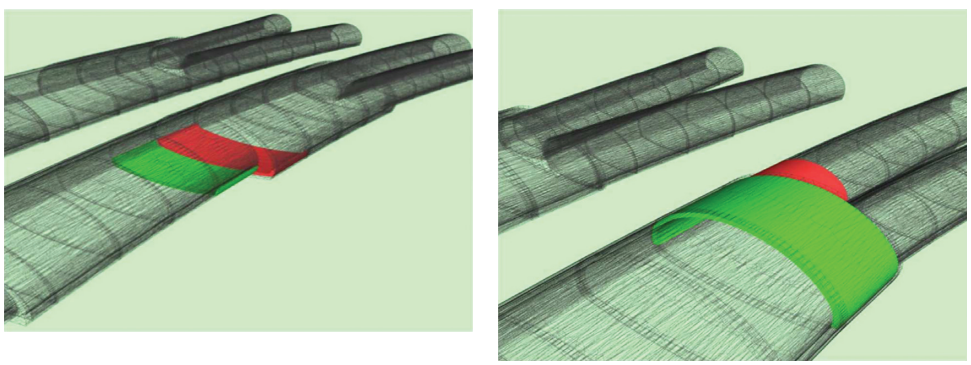

(a) (b)

Figure 6: Impact member display: (a) collision between sprayed arch wall and arch wall lining; (b) collision between invert arch lining and sprayed arch wall.

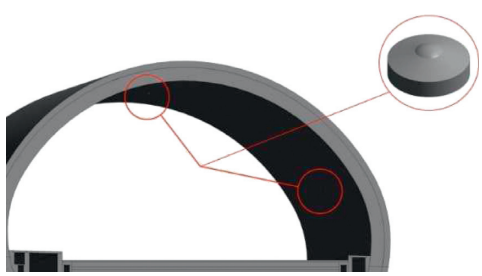

Figure 7: Sensor placement and geometric appearance.

5. 4D Construction Schedule Management of Shield Tunnel

In this paper, the construction process of A ramp and 1# tunnel right hole and B ramp and 1# tunnel left hole excavation in the construction organization design of Dahengqinshan Tunnel project is simulated in combination with the start and completion time of each work, and the corresponding progress analysis is carried out [30, 31].

5.1. 4D Construction Progress Simulation. In the process of project site schedule management, schedule tasks are decomposed according to WBS by introducing BIM technology. We use PROJECT software to create A ramp and 1# tunnel right hole, B ramp and 1# tunnel left hole excavation, and other stages of the construction process schedule. The BIM model and schedule is imported into Navisworks software for schedule simulation to show the dynamic change of overall schedule. In the actual construction, the plan is dynamically optimized and adjusted in real-time according to the actual construction progress so as to achieve the comprehensive, real-time, reasonable, and effective goal of schedule management. The main process is shown in Figure 8.

5.1.1. Preparation of Project Schedules at All Levels. (1) Establishment of WBS. According to the construction risk factors and management characteristics of the CRD method in Dahengqinshan Tunnel (phase I) project, each construction process is split and displayed. Taking the section as the basic unit, the tunnel project is divided into three basic works: extended support, initial support, and secondary lining structure construction. Finally, the overall schedule of Dahengqinshan Tunnel is obtained (Table 3).

(2) Preparation of Project Schedule. In this paper, the project management software is used to prepare the logical relationship and time arrangement of flow construction in the overall project and the three basic works according to the total construction period requirements and the total investment arrangement of the project, combined with the specific conditions such as the general layout, construction technical scheme, and construction process selection of the project. According to the overall plan of the project, the 4D schedule simulation schedule table of project management software is compiled, and the table is imported into Navisworks to form a schedule file.

5.1.2. Simulation of Four-Dimensional Construction Progress. The original 1 schedule (excavating the entrance tunnel body of ramp a tunnel and 1# tunnel right tunnel and carrying out initial support, with a single tunnel length of 1174.585 linear meters) is completed on September 8, 2018. Assuming that the actual progress of the project is on 30 September 2018, the actual completion time is delayed by 21 days compared with the planned time, which needs to be optimized.

The four-dimensional construction simulation based on BIM can optimize the management in two aspects: firstly, it can visually manage the whole construction process of tunnel engineering construction and then optimize the resource allocation; secondly, through construction simulation, we can study and obtain the technical key points that may affect the construction period in the whole construction process and optimize the construction scheme in advance, so as to ensure that the project is promoted as planned.

In the specific operation, in order to ensure that the progress plan can be accurately matched with the corresponding model construction, the progress information model of the plan is continuously generated in BIM according to the tunnel mileage pile number. At the same time, the Project file with construction progress data is exported to ".MPP" format. The "timeliner" function is used to connect each WBS task with each component one by one so as to realize the effective connection between BIM model and schedule task and establish the 4D model of BIM of tunnel engineering. Figure 9 shows the setting of the display effect at different stages in the four-dimensional simulation and the actual effect of the planned progress simulation.

5.1.3. Four-Dimensional Progress Control. The dynamic simulation of the whole construction process is carried out according to the set construction schedule. In the implementation process of specific projects, through the comparative analysis between actual progress and planned progress in the BIM growth model, combined with various possible influencing factors on the site, the progress plan can be updated and adjusted in a timely manner to ensure the realization of the duration goal.

5.2. Specific Results of 4D Simulation. On the basis of ensuring the seriousness of the progress plan, through four-dimensional progress simulation and progress control, combined with on-site progress feedback and dynamic adjustment, BIM application results are as follows:

(1) BIM visually shows the construction process of the tunnel in the form of animation so that the staff can clearly understand the operation of each period. Through on-site three-dimensional roaming (Figure 10), the problem of overlapping traditional two-dimensional graphic lines is solved, which reflects the characteristics of humanized design of BIM software modeling.

(2) Through the BIM model engineering quantity calculation and combined with the actual difficulty of engineering implementation, the engineering plan is prepared to improve the accuracy of the comprehensive construction plan. Through the four-dimensional construction progress simulation, it is foreseen that there are many problems in the implementation of the original plan, such as the conflict of work space and the unreasonable logical relationship of work, and an overall optimization and adjustment of the progress plan are carried out.

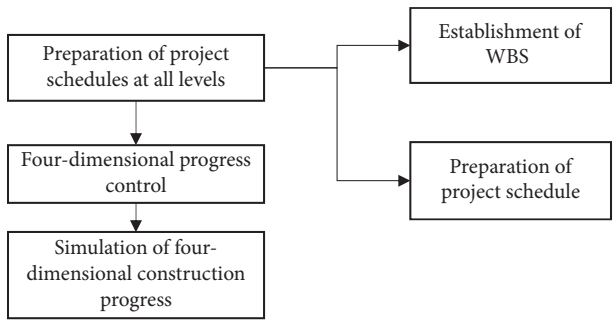

Figure 8: Construction progress simulation process.

Table 3: Overall project schedule.

Job content		Start time	Execution time
Tunnel engineering	Tunnel portal reinforcement	July 10, 2018	November 1, 2018
	Construction of 1# tunnel open cut section	October 20, 2018	May 17, 2019
	Tunnel body excavation and initial support of ramp A tunnel and right tunnel entrance of 1# tunnel (single tunnel length 1174.585 linear meters)	September 8, 2018	December 16, 2019
	The second lining, waterproof and drainage, and concrete pavement of ramp A tunnel and right hole entrance of 1# tunnel (single tunnel length 1174.585 linear meters)	November 8, 2018	March 31, 2020
	Tunnel body excavation and initial support of ramp B tunnel and left tunnel entrance of 1# tunnel (single tunnel length 1212 linear meters)	October 5, 2018	December 11, 2019
	The second lining, waterproof and drainage, and concrete pavement of ramp B tunnel and left hole entrance of 1# tunnel (single tunnel length 1212 linear meters)	December 5, 2018	March 31, 2020
	Excavation and initial support at the outlet of the right tunnel of 1# tunnel (single tunnel length 1232 linear meters)	November 16, 2018	December 9, 2019
	The secondary lining, waterproof and drainage, and concrete pavement at the outlet of the right tunnel of 1# tunnel (single tunnel length 1232 linear meters)	September 16, 2018	March 31, 2020
	Excavation and initial support at the outlet of the left tunnel of 1# tunnel (single tunnel length 1265 linear meters)	September 25, 2018	December 20, 2019
	The second lining, waterproof and drainage, and concrete pavement at the outlet of the left tunnel of 1# tunnel (single tunnel length 1265 meters)	November 25, 2018	March 31, 2020
	Excavation and initial support of right entrance of 2# tunnel (single tunnel length 1185 linear meters)	September 12, 2018	October 28, 2019
	The second lining, waterproof and drainage, and concrete pavement at the entrance of the right tunnel of 2# tunnel (single tunnel length 1185 meters)	November 12, 2018	March 31, 2020
	Excavation and initial support of left entrance of 2# tunnel (single tunnel length 1155 linear meters)	September 20, 2018	September 6, 2019
	The second lining, waterproof and drainage, and concrete pavement at the entrance of the left tunnel of 2# tunnel (single tunnel length 1155 meters)	November 20, 2018	March 31, 2020
	Excavation and initial support at the outlet of the right tunnel of 2# tunnel (single tunnel length 1036 linear meters)	November 1, 2018	October 3, 2019
	The secondary lining, waterproof and drainage, and concrete pavement at the outlet of the right tunnel of 2# tunnel (single tunnel length 1036 linear meters)	January 1, 2019	March 31, 2020
	Excavation and initial support at the outlet of the left tunnel of 2# tunnel (single tunnel length 1085.451 linear meters)	October 25, 2018	December 1, 2019
	The secondary lining, waterproof and drainage, and concrete pavement at the outlet of the left tunnel of 2# tunnel (single tunnel length 1085.451 linear meters)	December 25, 2018	March 31, 2020

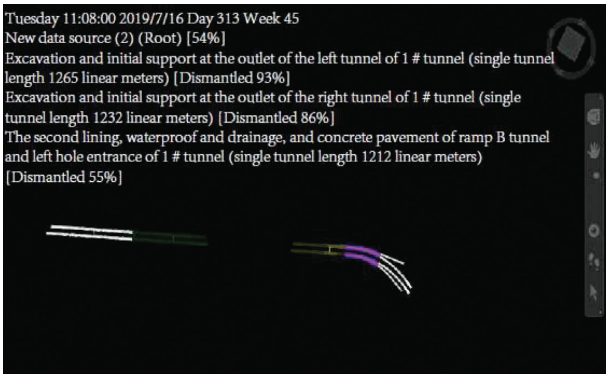

Figure 9: Four-dimensional construction schedule simulation process.

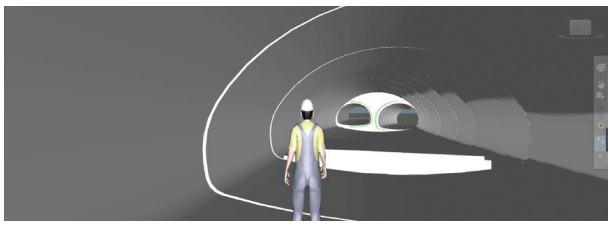

Figure 10: 3D roaming display of site construction.

6. Conclusions

Aiming at the problems of concealment, long construction period, and low construction efficiency in tunnel construction, combined with Dahengqinshan Tunnel project and based on BIM technology, this paper establishes a three-dimensional geological model and carries out three-dimensional modeling, deepening design, collision inspection, and 4D schedule management of the tunnel. The specific conclusions are as follows:

(1) We use BIM software to carry out three-dimensional tunnel modeling and deepen the design of the model to solve the problems of single discipline and multidiscipline. Compared with the traditional two-dimensional drawing design, the three-dimensional model ensures the integrity of the tunnel model. At the same time, BIM can make visual disclosure to help relevant personnel of later projects fully understand the four-dimensional construction process of the tunnel.

(2) Secondly, we carry out the structural collision inspection during the construction process and find a total of 514 structural conflicts. These structural conflicts are often difficult to find because they do not violate the design specifications. In this process, relevant personnel can optimize and adjust the design scheme in the model.

(3) Finally, the 4D construction technology management of Zhuji Tunnel is carried out to find the conflict between time and space in the construction process in advance. On this basis, the schedule is modified to ensure the construction progress. It is more conducive to command on-site construction than the traditional adjustment of the construction scheme based on the engineering experience of construction management personnel.

Data Availability

The data used to support the findings of this study are available from the corresponding author upon request.

Conflicts of Interest

The authors declare that they have no conflicts of interest regarding the publication of this paper.

Acknowledgments

The authors would gratefully like to acknowledge the support provided by the National Natural Science Foundation of China (No. 51978177) and by the Key R & D Projects of Zhuhai Dahengqin Co., Ltd. (No. SG88-2018-444B3).

References

[1] X. Que, Z. Zhu, and W. Lu, "Anisotropic constitutive model of pentagonal prism columnar jointed rock mass," *Bulletin of Engineering Geology and the Environment*, vol. 79, no. 1, pp. 269–286, 2020.

[2] K. Meng, C. Cui, Z. Liang, L. Haijiang, and P. Huafu, "A new approach for longitudinal vibration of a large-diameter floating pipe pile in visco-elastic soil considering the three-dimensional wave effects," *Computers and Geotechnics*, vol. 128, Article ID 103840, 2020.

[3] K. Hong, "Development and Prospect of tunnel and underground engineering in China in recent two years," *Tunnel construction*, vol. 37, no. 2, pp. 123–134, 2017.

[4] B. Yuan, Z. Li, Z. Zhao, H. Ni, Z. Su, and Z. Li, "Experimental study of displacement field of layered soils surrounding laterally loaded pile based on transparent soil," *Journal of Soils and Sediments*, vol. 21, no. 9, pp. 3072–3083, 2021.

[5] Y. Wu, J. Cui, J. Huang, W. Yoshimoto, and L. Wen, "Correlation of critical state strength properties with particle shape and surface fractal dimension of clinker ash," *International Journal of Geomechanics*, vol. 21, no. 6, Article ID 04021071, 2021.

[6] H. Lin, "Development and Prospect of tunnel and underground engineering technology in China," *Construction technology development*, vol. 47, no. 3, pp. 107-108, 2020.

[7] B. Yuan, Z. Li, Z. Su, Q. Luo, M. Chen, and Z. Zhao, "Sensitivity of multistage fill slope based on finite element model," *Advances in Civil Engineering*, vol. 2021, Article ID 6622936, 13 pages, 2021.

[8] B. Bai, Q. Nie, Y. Zhang, X. Wang, and W. Hu, "Cotransport of heavy metals and SiO_2 particles at different temperatures by seepage," *Journal of Hydrology*, vol. 597, Article ID 125771, 2021.

[9] X. Wang, K. Zhang, and X. Yin, "4D simulation based on BIM real-time construction model," *Journal of Guangxi University (Natural Science Edition)*, vol. 37, no. 4, pp. 814–819, 2012.

[10] F. Ji, D. Qu, and F. Shang, "Research on visual project schedule management under BIM scenario," *Construction economy*, vol. 35, no. 10, pp. 40–43, 2014.

[11] F. Wang, X. He, and H. Gao, "Research on visual management technology of construction process of high-speed railway continuous beam bridge based on BIM," *Journal of building science and Engineering*, vol. 1-9, 2021, http://kns.cnki.net/kcms/detail/61.1442.TU.20210827.1402.002.html.

[12] V. Valeria, E. M. Acerra, C. Lantieri, F. D. Vincenzo, G. Piacentini, and S. Pancaldi, "Building information Modelling (BIM) application for an existing road infrastructure," *Automation in Construction*, vol. 128, 2021.

[13] P. Huang, "Research on safety of operation and maintenance of utility tunnel based on BIM and computer technology," *Journal of Physics: Conference Series*, vol. 1815, no. 1, Article ID 012009, 2021.

[14] B. Yuan, Z. Li, Y. Chen et al., "Mechanical and microstructural properties of recycling granite residual soil reinforced with glass fiber and liquid-modified polyvinyl alcohol polymer," *Chemosphere*, vol. 268, Article ID 131652, 2021.

[15] Y. He, Y. Wang, and B. Xiao, "Research on rail transit EPC progress management based on BIM and engineering data," *Tunnel construction (Chinese and English)*, vol. 39, no. 10, pp. 1647–1656, 2019.

[16] L. Chen, P. Shi, Q. Tang, W. Liu, and Q. Wu, "Development and application of a specification-compliant highway tunnel facility management system based on BIM," *Tunnelling and Underground Space Technology*, vol. 97, no. C, 2020.

[17] H. Chen, Y. Shen, and H. Zheng, "Application of BIM + GIS in Expressway smart tunnel monitoring platform," *Highways*, vol. 66, no. 7, pp. 378–381, 2021.

[18] J. Zhang, M. Cao, and Y. Zhang, "Building construction 4D management system based on IFC Standard and engineering information model," *Engineering Mechanics*, no. S1, pp. 220–227, 2005.

[19] J. Zhang, T. He, and J. Lin, "Extraction and application of building space and equipment topology information based on BIM," *Journal of Tsinghua University*, vol. 58, no. 6, pp. 587–592, 2018.

[20] F.-Z. Wang, W. D. Kong, and H.-C. Sui, "Application of BIM + VR technology in immersed tunnel construction," *IOP Conference Series: Earth and Environmental Science*, vol. 798, no. 1, 2021.

[21] Y. Zhu, X. Zhang, and Z. Zhang, "Study on parametric modeling method of highway tunnel based on civil3d + Revit + dynamo," *Tunnel construction (Chinese and English)*, vol. 40, no. S2, pp. 109–115, 2020.

[22] Z. Song, G. Shi, and J. Wang, "Research on the architecture of tunnel collaborative management platform based on BIM technology," *Journal of geotechnical engineering*, vol. 40, no. S2, pp. 117–121, 2018.

[23] Z. Song, K. Xiao, and T. Cheng, "Research on tunnel life cycle management and application based on BIM Technology," *Journal of Xi'an University of Architecture and Technology*, vol. 52, no. 1, pp. 47–53, 2020.

[24] Z. Niu, G. Li, and L. Liu, "An improved method of 3D geological modeling based on civil 3D platform," *Water transportation engineering*, vol. 10, pp. 171–175, 2019.

[25] B. Yuan, M. Sun, Y. Wang, and Z. Lihua, "Full 3D displacement measuring system for 3D displacement field of soil around a laterally loaded pile in transparent soil," *ASCE International Journal of Geomechanics*, vol. 19, no. 5, Article ID 04019028, 2019.

[26] B. Bai, D. Rao, T. Chang, and Z. Guo, "A nonlinear attachment-detachment model with adsorption hysteresis for suspension-colloidal transport in porous media," *Journal of Hydrology*, vol. 578, Article ID 124080, 2019.

[27] B. Bai, G.-C. Yang, T. Li, and G.-S. Yang, "A thermodynamic constitutive model with temperature effect based on particle rearrangement for geomaterials," *Mechanics of Materials*, vol. 139, Article ID 103180, 2019.

[28] B. Yuan, M. Sun, L. Xiong, S. Prasad Pradhan, and H. Li, "Investigation of 3D deformation of transparent soil around a laterally loaded pile based on a hydraulic gradient model test," *Journal of Building Engineering*, vol. 28, no. 3, Article ID 1010124, 2020.

[29] B. Bai, R. Zhou, G. Cai, W. Hu, and G. Yang, "Coupled thermo-hydro-mechanical mechanism in view of the soil particle rearrangement of granular thermodynamics," *Computers and Geotechnics*, vol. 137, no. 8, Article ID 104272, 2021.

[30] X. Que, Z. Zhende, Z. Niu, and W. Lu, "Estimating the strength and deformation of columnar jointed rock mass based on physical model test," *Bulletin of Engineering Geology and the Environment*, vol. 80, pp. 1557–1570, 2021.

[31] C. Cui, K. Meng, C. Xu, Z. Liang, H. Li, and H. Pei, "Analytical solution for longitudinal vibration of a floating pile in saturated porous media based on a fictitious saturated soil pile model," *Computers and Geotechnics*, vol. 131, Article ID 103942, 2021.

Hindawi
Advances in Civil Engineering
Volume 2021, Article ID 7859284, 9 pages
https://doi.org/10.1155/2021/7859284

Research Article

Study on Development Risk of Overseas Transportation Infrastructure under the New Form Based on Interpretive Structure Model

Liang Ou,[1] **Chongsen Ma**,[1] **Yun Chen**,[1] **and Jing Zhang**[2]

[1]*School of Traffic & Transportation Engineering, Changsha University of Science and Technology, Changsha 410000, Hunan, China*
[2]*Hunan Kunqiao Engineering Project Management Co., Ltd., 410000 Hunan, China*

Correspondence should be addressed to Liang Ou; 3055471394@qq.com

Received 17 November 2021; Accepted 2 December 2021; Published 16 December 2021

Academic Editor: Mingfeng Lei

With the improvement of China's comprehensive national strength, more and more construction enterprises began to undertake overseas construction projects. Under the premise of the epidemic situation and the increasingly severe international situation, it is of great significance to study the risk control of overseas transportation infrastructure construction. This paper constructs the risk influencing factor model of overseas transportation infrastructure development risk in the new form from six aspects, that is, decision-making risk, design and planning risk, construction risk, operation risk, government risk, and force majeure, and uses the interpretative structure model and fuzzy comprehensive evaluation method. The key factors affecting the risk of overseas transportation foundation design and development are studied, and the adaptive solutions are put forward.

1. Introduction

Construction of transportation infrastructure plays an important role in promoting economic growth and promoting the upgrading and development of the tertiary industry. In recent years, there have been many breakthroughs in the construction of transportation infrastructure, one of which is the increasing overseas construction of transportation infrastructure aboard. Meanwhile, a number of major livelihood and manufacturing projects in key fields have also made important progress. The breakthrough of overseas transportation infrastructure construction mainly stems from the new facing situation: (1) with the continuous development of the national Belt and Road Initiative strategy, Chinese enterprises are facing a major opportunity to go abroad to participate in the construction of overseas transport infrastructure. (2) Diverse construction content and enrichment of resources lead transportation infrastructure to a tertiary industry service facility construction. (3) With the increasing traffic demand all over the world, overseas transportation infrastructure construction has the characteristics of larger investment, long-scale construction duration, and policy uncertainty, which led to a greater risk. In particular, it also faces the influence of special risk factors such as poor control of construction land, political instability, and social conflict caused by the normalization of epidemic situation. (4) Transformation of ways to realize profit: the more profit attention is paying to operation duration from the original profit mainly relying on transportation infrastructure construction. Therefore, it is of great significance for Chinese infrastructure enterprises to research the risk assessment of overseas transportation infrastructure development and clarify the means to deal with the risk.

Construction enterprises can make full use of advanced experience in China's construction industry and export China's standards while developing overseas transportation infrastructure investment projects, which can not only establish a good image in the world and enrich China's experience in overseas investment, but also realize the "going global" policy of China's construction industry. Investment

in overseas transportation infrastructure is a very important part of China's overseas strategy, which is of great significance to drive the increase of China's exports, promote the peripheral economic growth, and realize the mutual progress with surrounding countries.

At present, the research on risk management of transportation infrastructure construction has attracted more and more attention of some scholars domestically and abroad. Since 2014, the research on risk management of transportation infrastructure has increased rapidly, which focuses on "Belt and Road Initiative risk rating," "the PPP risk allocation," and "risk assessment of financing securitization." The main research and evaluation methods include difference-in-difference model, analytic hierarchy process, and fuzzy set. The research content covers a wide mature range, but few study on development risk factors analysis of overseas transportation infrastructure.

Li et al. studied the risk assessment of cross-border transportation infrastructure construction projects and improved the fuzzy comprehensive evaluation method on the premise of considering the dual correlation effect [1]; Jin and Suo put forward a risk assessment method of transportation infrastructure construction based on stochastic DEMATEL-VIKOR considering relevance and randomness [2]; Chang studied the risks related to profits distribution in the process of transportation infrastructure construction and modified the profits distribution model based on Shapley value [3]; Zolfaghari and Mousavi proposed a combined decision-making model based on fuzzy set and Shapley value method to research risk assessment of transportation infrastructure construction projects [4].

The risk assessment of overseas transportation infrastructure development and construction has three characteristics: firstly, the increased diversity of risks. Due to the high construction project investment with long construction cycle characteristics, the corresponding risks have more diverse and uncertain characteristics. The second characteristic is the increased correlation of risks. In the process of transportation infrastructure development, various risks are interrelated and affect each other. If they are not handled properly in the process, the correlated risks may cause chain effect; thirdly, there are great differences in the development environment, which include great differences in the political system, economic development level, and cultural atmosphere of various countries that lead to different types of risks in different actual development process. Meanwhile, most of the existing studies focus on the risk of a specific stage in the development process, but less research on the impact of the corelated risks analysis from the whole process. In actual implementing condition, it is easy to ignore the direct correlation impact of risks, resulting in result deviation. Therefore, it is necessary to solve the above problems through the research on the whole process of overseas transportation infrastructure construction and development.

This research takes the advantages of the interpretive structure model with the fuzzy comprehensive evaluation and build the basic directed graph of risk impact factors through the interpretive structure model as a reference, solving the problems of numerous and complex, difficulties, and contradictions of expert scoring and index selection to put forward corresponding solutions according to identified risks. By combining interpretive structure model with fuzzy comprehensive evaluation, a directed topology hierarchy diagram of risk factors is provided to enable experts to have a general understanding of the relationship between various dimensions of many influencing factors to reduce the roughness and imprecision and improve reliability of results. At the same time, compared with the previous method of directly substituting the data of explaining the structural model into the calculation of fuzzy comprehensive matrix, it improves the correlation between the two different models, so that the model avoids rigid fusion in the process of application, which leads to more reasonable result. Therefore, the method adopted in this paper has better reliability and rationality.

2. Models and Methods

2.1. Interpretative Structural Modeling (ISM) Related Concepts. The concept of Interpretative Structural Modeling Method (ISM) is proposed by Professor Linstone. Interpretative Structural Modeling finds out the relationship between the elements of the system through certain technologies and means and classifies the complex relationships between the elements through the form of directed graphs, improving the researchers' understanding of the internal system and relationship of the subjects.

There exist many design risk factors with long duration, and many factors which are difficult to be quantified in the process of overseas transportation infrastructure development. Therefore, before factors analysis and model-building, this research selects the interpretative structural model to analyze the risk factors in the whole process of overseas transportation infrastructure development and establishes a preliminary directed graph through research, which helps solve the problems in the analysis process of fuzzy analytic hierarchy process, such as many influencing factors and heavy workload of filling data in the judgment matrix. The process of using ISM method to study the risk influencing factors development process of overseas transportation infrastructure is shown in Figure 1.

2.2. Fuzzy Analytic Hierarchy Process Related Concepts. Analytic Hierarchy Process (AHP) has been widely used in various evaluation methods dominated by subjective cognition. However, in the calculation process of traditional analytic hierarchy process, the construction of judgment matrix is greatly affected by subjective factors. The consistency test of judgment matrix is complex and cumbersome, and the rationality of consistency judgment rules is also controversial. In order to solve the above problems, scholars proposed to introduce the fuzzy consistent matrix into the AHP analysis. This method combining the analytic hierarchy process (AHP) with the fuzzy mathematics theory is called the fuzzy analytic hierarchy process (FAHP), which can well solve the decision-making of people's subjective fuzziness on the problem. For fuzzy analytic hierarchy process, in the

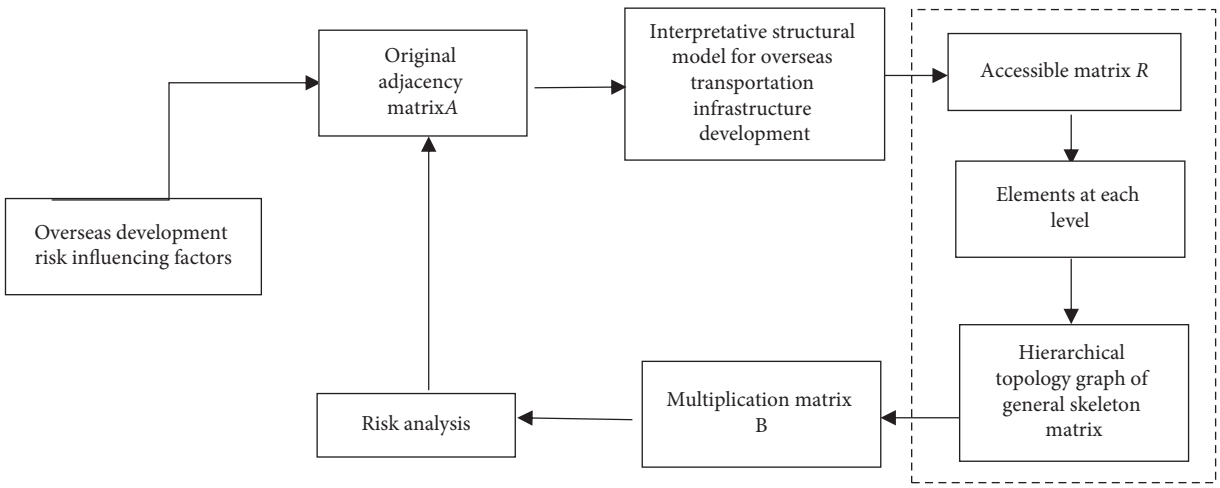

Figure 1: Steps of structural model calculation.

process of questionnaire filling, if the CI value does not meet the requirements of the request, the research would use particle swarm optimization algorithm to modify the questionnaire. On this basis, the questionnaire retains expert opinions to extremely extend and also meet the requirements of matrix calculation.

2.3. Concepts Related to Transport Infrastructure. Transportation infrastructure refers to the fixed assets public infrastructure facilities needed to complete passenger transport and logistics, mainly divided into the following five categories: railway transport infrastructure, road transport infrastructure, waterway transport infrastructure, air transport infrastructure, and pipeline transport infrastructure. Due to the difficulty of obtaining some data, this research mainly selects the risk factors of railway transport infrastructure and highway transport infrastructure as the research object, for which cross-border highways and high-speed railways, as an important part of the relevant infrastructure construction about the Belt and Road Initiative promoting infrastructure construction and realizing the interconnection between countries along the route, also make the research of this paper more practical.

The "new form" mentioned in this paper refers to the behavior of overseas infrastructure construction in response to the call of the "Belt and Road" and "going global" in the new stage of large construction enterprise development in order to obtain sustainable interests and expand the scale.

The new form is reflected in the following three points: firstly, with the saturation of the domestic market, overseas construction enterprises will continue to increase, and competition will become more intense; secondly, the scope of project construction continually expand not only for Chinese enterprises, but also for neighboring friendly countries that continue to cooperate and develop, to achieve a global layout; thirdly, with the continuous effect of coronavirus epidemics, the normalization of epidemic prevention and control will be gradually accepted. And in the development process of the project, it will be greatly affected by the level of epidemic prevention and control of the sovereign government of the construction site.

3. Quantitative Evaluation Research

3.1. Determination of Risk Evaluation Index

3.1.1. Selection of Risk Factors. The selection of risk factors is the premise of risk analysis of overseas transportation infrastructure development. The paper takes the following three steps to select risk factors:

(1) Based on the existing literature, the risk factors were preprocessed by manual screening.

(2) By seeking the internal relevance of the risk factors preliminarily determined, the seven criteria layer indicators of decision-making risk, construction risk, operational risk, government risk, investment and financing risk, legal risk, and force are finally determined, and the initial list of risk factors is finally formed.

(3) In the aspect of factor correction, relevant experts and relevant researchers from enterprises such as the Central South Institute of Chinese Municipalities are required to seek expert opinions through online surveys and revise the indicators. Finally, 24 evaluation layer indicators were determined. For risk factors of overseas transportation infrastructure development, see Table 1.

Key indicators indicate the following:

(1) Decision-making risk refers to the risk factors that may affect the completion of the project in the process of project decision-making, including decision-making conditions change risk, decision-making expertise, and decision-making information collection integrity of three indicators. The risk of decision-making condition change refers to the risk caused by the change of the main conditions that are dependent on in the decision-making process mainly

Table 1: Risk factors of overseas transportation infrastructure development.

Target level	Criterion level	Index level
Influencing risk factors of overseas transportation infrastructure development [5–11]	Decision-making risk	Decision-making conditions change risk
		Decision-making expertise risk
		Decision-making information collection integrity risk
	Construction risk	Quality of infrastructure construction
		Construction license convenience
		Safety awareness of local construction personnel
	Operation risk	Normative differences
		Labor efficiency difference
		Management talent reserve
		Local transport developments
		Labor cost of construction
	Policy risk	Eternal policy environment
		External policy environment
		Local government corruption situation
		Religion conflict
	Investment and financing risk	Currency risk
		Economic pattern risk
		Banks lending risk
		Local government debt default risk
	Legal risk	Government stability risk
		Risk of legal differences
		Justice of law enforcement
	Risk of force majeure	Risk of force majeure of political environment
		Risk of force majeure of social environment

due to the change of time and construction situation in the actual construction of the project.

(2) Construction risk refers to the construction risk caused by the construction party itself or external reasons in the process of project construction due to unpredictable factors. In this process, special attention should be paid on the inevitable use of overseas workers in overseas construction process. Therefore, the difference in labor efficiency domestic and abroad has a great impact on project implementation.

(3) Operational risk refers to the risk that occurs during the operation of the project from bidding to the end of the operation period, including relevant management talent reserves, local transportation situation, and construction labor costs. The labor cost of construction site not only refers to the personnel cost in the construction process but also includes the cost of the operation process. Throughout the whole development process, the difference of personnel costs domestic and abroad has a great impact on the success or failure of project operation. Therefore, the construction site labor costs should be attributed to operational risks.

(4) Government risk is also known as political risk. It includes four main influencing factors: internal environment (politics), external environment (politics), government corruption, and religious conflict risk. The stability of the regime in the construction site and the social stability have a great impact on the transportation infrastructure projects that focus on operation. Therefore, it is necessary to make a reasonable assessment of project risks.

(5) Investment and financing risks refer to the risks related to the economy in the process of investment and financing, including the selection of project investment and financing mode, the default risk of participants in the process, the risk of the debtor failure to perform relevant responsibilities, and macroeconomic impact risk. Due to the large investment, high development difficulty of transportation infrastructure construction projects, most of them need to select reasonable and proper financing mode for project construction. Therefore, reasonable control of this type of risk is of great significance for the completion of construction project.

(6) Legal risk refers to the risk related to legal issues in the whole life cycle of the project.

(7) Force majeure risk includes political environment force majeure risk and social environment force majeure risk.

In order to determine the final evaluation index, the paper makes a pretest on the determined initial index. The dimensions, reliability, and validity of the indicators were analyzed. The indicators are determined by questionnaire, online survey, and offline survey.

Table 2: Validity analysis.

Index item	Influencing factor loading coefficient						
	Factor 1	Factor 2	Factor 3	Factor 4	Factor 5	Factor 6	Factor 7
Decision-making conditions change risk				0.956			
Decision-making expertise risk				0.925			
Decision-making information collection integrity risk				0.896			
Quality of infrastructure construction		0.958					
Construction license convenience		0.815					
Safety awareness of local construction personnel		0.869					
Normative differences		0.876					
Labor efficiency difference		0.818					
Management talent reserve					0.944		
Local transport developments					0.879		
Labor cost of construction					0.887		
Eternal policy environment			0.954				
External policy environment			0.884				
Local government corruption situation			0.898				
Religion conflict			0.869				
Currency risk	0.961						
Economic pattern risk	0.893						
Banks lending risk	0.815						
Local government debt default risk	0.871						
Government stability risk	0.897						
Risk of legal differences							0.927
Justice of law enforcement							0.911
Risk of force majeure of political environment						0.948	
Risk of force majeure of social environment						0.944	
Latent root	4.008	3.923	3.387	2.688	2.570	1.849	1.816
Variance explained rate (%)	16.698	16.347	14.111	11.200	10.708	7.706	7.565
Cumulative variance (%)	16.698	33.045	47.156	58.356	69.065	76.770	84.335
Cronbach α				0.708			
KMO				0.690			
Bart value				1727.827			
df				276			
p				0.000			

The results of validity analysis are shown in Table 2.

This paper invited 100 relevant practitioners, researchers, and graduate students of related majors to conduct pretest analysis on the questionnaire. Finally, 86 valid questionnaires were collected. Through this analysis, it can be found that the *Cronbach* α coefficient is 0.708, greater than 0.7, and the data reliability quality is good, which can be further studied. At the same time, the *KMO* value of the data is 0.690, and the data validity is acceptable. In addition, the *KMO* value is 0.690, greater than 0.6, which means that the data is valid. In addition, the cumulative variance interpretation rate of seven factors after rotation was 84.335% > 50%, indicating that the information content of the study can be effectively extracted. Therefore, the questionnaire quality is good and can be further studied.

3.1.2. Preparation before Data Collection. Because there are many indexes in the evaluation layer, the experts may have contradictions when filling out the fuzzy analytic hierarchy process questionnaire. Therefore, before the formal start of the survey, some experts are invited to analyze the impact of the index categories. And get the original relation matrix A.

$$A = \begin{pmatrix} & & & & & & \\ & & & & & & \\ & & & & & & \\ & 1 & & & & & \\ & 1 & 1 & & & & \\ 1 & 1 & 1 & & & & \\ 1 & 1 & & & 1 & & \\ 1 & 1 & 1 & 1 & 1 & 1 & \end{pmatrix}. \quad (1)$$

And get its multiplication matrix B:

$$B = \begin{pmatrix} 1 & & & & & & \\ & 1 & & & & & \\ & 1 & 1 & & & & \\ & 1 & 1 & 1 & & & \\ 1 & 1 & 1 & & 1 & & \\ 1 & 1 & & & 1 & 1 & \\ 1 & 1 & 1 & 1 & 1 & 1 & 1 \end{pmatrix}. \quad (2)$$

The reachable matrix R:

$$R = \begin{pmatrix} 1 & & & & & & \\ & 1 & & & & & \\ & 1 & 1 & & & & \\ & 1 & 1 & 1 & & & \\ 1 & 1 & 1 & & 1 & & \\ 1 & 1 & 1 & & 1 & 1 & \\ 1 & 1 & 1 & 1 & 1 & 1 & 1 \end{pmatrix}. \quad (3)$$

The calculated general skeleton matrix S:

$$S = \begin{pmatrix} & & & & & & \\ & & & & & & \\ & 1 & & & & & \\ & & 1 & & & & \\ 1 & & 1 & & & & \\ & & & & 1 & & \\ & & & 1 & & 1 & \end{pmatrix}. \quad (4)$$

The results drawn from the general skeleton matrix S give priority to the directed topology hierarchy, as shown in Figure 2.

When using the fuzzy analytic hierarchy process to determine the weight, we must first establish a multilevel structure between the indicators. For overseas transportation infrastructure development risk, the risk index set is $U = \{U_1, U_2, \ldots, U_7\}$, and each index layer consists of n risk evaluation indexes. The index structure is constructed according to Table 1. The steps of using fuzzy analytic hierarchy process to calculate the weight are as follows:

(1) Through the established index system, a fuzzy judgment matrix is constructed for the criteria layer index and the index layer index. Through expert investigation, the indicators at the same level are compared with each other. The 9-level scale is used to reflect the importance of each index.

(2) Weight of each index is calculated through the relative importance of each index comparing. Due to the characteristics of overseas transportation infrastructure development, there are many considering influencing factors. In order to reduce inaccuracy and redundancy of expert filling data, in the investigation, the results calculated by the interpretative structural model are also provided as a reference for the priority directed topological hierarchy diagram. As the paper invited a number of experts to fill out the questionnaire, in order to fully reflect the true views of the experts, the data processing selected a group matrix method to summarize data filled out by experts.

(3) Test the consistency parameter of the judgment matrix, generally CI < 0.1; it is considered to meet the requirements. If the consistency CI value is greater than 0.1, the matrix needs to be adjusted.

3.2. Overseas Transportation Infrastructure Development Risk Analysis. This paper uses Mathis FAHP fuzzy analytic hierarchy process software to calculate the data. The established analysis model is shown in Table 1, and a five-level risk factor evaluation set r is established, corresponding to each other U = {lowrisk, lower risk, medium risk, higher risk, high risk}. A total of 80 relevant experts, project participants, and designers were invited to participate in the survey, and 74 valid questionnaires were collected. The fuzzy judgment matrix of criterion layer calculated by group matrix method is shown in Table 3. The adjusted CI value is 0.0994, meeting the requirements. Weight calculation results are shown in Table 4.

Through the analysis of the calculation results, it can be found that government risk, construction risk, and operation risk are more influencing risks in the construction of overseas transportation infrastructure, which should be paid more attention to. In the secondary index level indicators, the construction of labor costs, government corruption, and management talent reverse are more important.

3.3. Risk Response Strategies and Suggestions. Through the data analysis in Table 3, we can find that the risk distribution among various categories of indicators is relatively uniform, but the impact gap is large for the secondary evaluation level indicators. Therefore, in the actual development process of the project, taking targeted measures for key risks and influencing factors can better control the project development risk and promote the sustainable operation for the project. The paper puts forward strategies and suggestions for the risk disposal of overseas transportation infrastructure development based on the three stages of decision-making, construction, and operation of project development:

3.3.1. Project Decision Period

(1) During the project decision-making period, the biggest risk comes from the decision-making professionalism and management personnel reserve. Therefore, on the basis of fully collecting and possessing information, professional experts should be invited to make decisions to improve the accuracy and rationality of decision-making.

(2) During the project decision-making period, the possible changes in the operation of the project shall be fully considered, and the disposal plan shall be made for relevant changes to reduce the possible impact of unpredictable changes in conditions during decision-making on project development. Meanwhile, decision-making should also take into account the local government debt situation and consider the local government actual compliance ability. It is also important to reduce the impact of local government debt default on project construction and operation through contracts or mortgages [12–14].

(4) The bid price shall be reasonably determined on the basis of fully considering the differences in labor efficiency and labor cost domestic and abroad. For

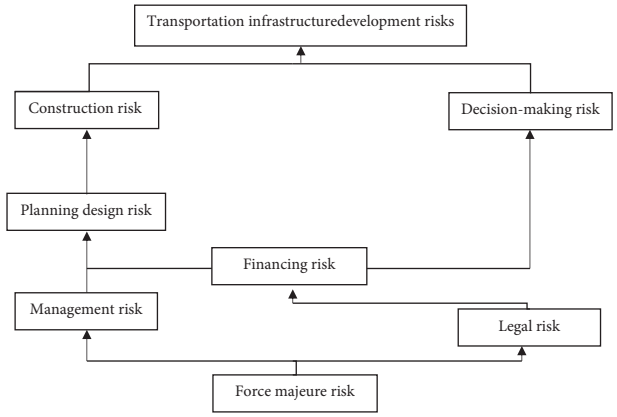

Figure 2: Results priority directed topological hierarchy graph.

Table 3: Fuzzy judgment matrix of criterion layer.

	Decision-making risk	Decision-making risk	Decision-making risk	Decision-making risk	Decision-making risk	Decision-making risk	Decision-making risk	Weight (wi)
Decision-making risk	0.5	0.7686	0.3243	0.2451	0.4483	0.274	0.5294	0.1233
Construction risk	0.2314	0.5	0.2916	0.5939	0.2548	0.4228	0.3871	0.1039
Operation risk	0.6757	0.7084	0.5	0.186	0.5666	0.7311	0.2862	0.1502
Policy risk	0.7549	0.4061	0.814	0.5	0.789	0.7277	0.5516	0.1925
Financing risk	0.5517	0.7452	0.4334	0.211	0.5	0.6007	0.7284	0.1557
Legal risk	0.726	0.5772	0.2689	0.2723	0.3993	0.5	0.4288	0.1273
Force majeure risk	0.4706	0.6129	0.7138	0.4484	0.2716	0.5712	0.5	0.1471

Table 4: Weight calculation results.

Index level indicator	Whole weight	Peer weight	Criterion level
Decision-making conditions change risk	0.0452	0.3667	Decision-making risk (0.1438)
Decision-making expertise risk	0.0452	0.3667	
Decision-making information collection integrity risk	0.0329	0.2667	
Quality of infrastructure construction	0.0197	0.19	Construction risk (0.1456)
Construction license convenience	0.026	0.25	
Safety awareness of local construction personnel	0.0145	0.14	
Normative differences	0.0239	0.23	
Labor efficiency difference	0.0197	0.19	
Management talent reserve	0.0451	0.3	Operation risk (0.1446)
Local transport developments	0.0451	0.3	
Labor cost of construction	0.0601	0.4	
Eternal policy environment	0.0545	0.283	Policy risk (0.1466)
External policy environment	0.0355	0.1845	
Local government corruption situation	0.0609	0.3163	
Religion conflict	0.0416	0.2162	
Currency risk	0.0325	0.2087	Financing risk (0.1418)
Economic pattern risk	0.0267	0.1717	
Banks lending risk	0.0337	0.2165	
Local government debt default risk	0.0214	0.1375	
Government stability risk	0.0414	0.2656	
Risk of legal differences	0.0382	0.3	Legal risk (0.1355)
Justice of law enforcement	0.0891	0.7	
Risk of force majeure of political environment	0.103	0.7	Force majeure risk (0.134)
Risk of force majeure of social environment	0.0441	0.3	

example, due to the different construction markets domestic and abroad, adopting reasonable low-price bidding strategy may be judged as low price dumping by the local government. Therefore, domestic construction enterprise should avoid low-cost bidding and reasonably evaluate the project cost. At the same time, we should fully consider the international market risks in the construction process, formulate reasonable risk response means, expand the scope of RMB settlement, and avoid unnecessary losses to the project due to changes in exchange rate.

(5) Early risk prevention strategy cannot fully cover all stage risks. For some overseas construction projects, early poor effect of negotiation, adjustment, and other measures can lead to uncontrollable failure result [15]. Therefore, in the process of project development, insurance institutions can be selected to provide guarantee for project construction to reduce the adverse impact of uncertain political factors on the project.

3.3.2. Project Construction Period

(1) During the project construction period, the influencing factors with high risk include the convenience and specification differences of construction license. Due to the different procedures and requirements for construction permit domestic and abroad, there may be some differences in the mandatory standards of construction specifications. Therefore, in the construction process, local standards should be observed on the basis of existing construction management experience.

(2) Meanwhile, due to the differences in labor efficiency of construction workers in different countries, the construction period shall be reasonably arranged to ensure the smooth completion of the project.

(3) During the project construction period, the local political situation should be paid more attention, and, according to this, the enterprise should reasonably arrange funds investment. And it is important to maintain good communication with banks and financial institutions to avoid bank lending and impact on project construction.

3.3.3. Project Operation Period

(1) During the operation period, the operation cost shall be fully considered [16–19]. If it is necessary to participate in the operation activity for construction enterprise of overseas transportation infrastructure, the operation cost shall be fully considered referring to the domestic project demonstration, and the correction calculation shall be carried out on the basis of integrating the operation cost of domestic projects and referring to the local development level, so as to ensure the smooth operation of the project.

(2) In the process of operation, there are many contacts with local people and government. In this process, local cultural factors and religious issues should be fully considered to avoid conflicts.

(3) Meanwhile, we must make contingency plans for force majeure, especially in the normalization management of *COVID-19*, make adequate preventive measures, and prepare early alerting measures for the impact of all kinds of force majeure on projects, so as to enhance the operational stability of the project.

4. Conclusion

At present, there is little research on the development risk of overseas transportation infrastructure under the new form. The research on the development risk of overseas transportation infrastructure under the new form combined with ISM and fuzzy analytic hierarchy process needs to be deepened further. This paper analyzes the risk of overseas transportation infrastructure development by combining ISM and fuzzy analytic hierarchy process. In the process of research, it can better solve the problems existing in the expert scoring process in the previous fuzzy analytic hierarchy process due to too much content of judgment matrix, strong randomness of expert scoring, and improve the reliability of the results.

Based on the previous research, this paper constructs 7 criteria level indicators and 24 indicator level indicators and realizes the multiangle judgment of the risk of overseas transportation infrastructure development. It can be found that government risk, construction risk, and operation risk are more important risk factors in the construction of overseas transportation infrastructure, which should be paid more attention. Among the secondary indicators, the labor cost of construction land, government corruption, and management talent reserve are more important.

For the judged main risk factors matrix, during the decision-making period of transportation infrastructure construction, it is necessary to increase the reserve of relevant talents, formulate a perfect risk plan and investigate the surrounding business environment, and make a scientific and reasonable prediction. In the process of project construction, we should pay full attention to the differences between domestic and foreign construction standards and labor rates, reasonably arrange the use of funds, maintain the relationship between financial institutions and enterprises, and ensure the source of project funds. In addition, we should try to establish an information platform shared by multiple enterprises to monitor the external risks in the construction process and ensure the operation of the project. During the operation of the project, the enterprise should pay attention to the political, religious, and cultural environment of the construction site and the operation site, avoid conflicts with aborigines during the construction process, and fully consider local customs and habits during the operation process.

Through the research on the development risk of overseas transportation infrastructure under the new form, this paper puts forward the important influencing factors

that may have a great impact on the development of overseas transportation infrastructure and relevant countermeasures, which can provide some reference for the construction of relevant projects and improve the investment efficiency. At present, there is still a need for further research on the relationship of risk factors contained in the study and the impact degree on the project caused by the relationship between them. Therefore, it is necessary to conduct in-depth research on the practical cases of the new form overseas transportation infrastructure construction projects.

The limitations of this paper are mainly reflected in the following two points.

(1) Since the construction and development of overseas transportation infrastructure in China is still in the development stage, and also due to the limitation of research method, the conclusion of the study is influenced by subjective factors. In future research, we will try to adopt empirical research, multisubject modeling, and other methods for further research to enhance the reliability of the research findings.

(2) This paper only analyzes the impact of each indicator on the development risk of overseas transportation infrastructure but does not consider the impact of the interaction of each influencing factor. In future research, we will further analyze the impact of the combination of influencing factors on the development risk.

Data Availability

The raw data supporting the conclusions of this article will be made available by the authors, without undue reservation.

Conflicts of Interest

The authors declared that they have no conflicts of interest regarding this work.

References

[1] J. Li, J. Zhang, and W. Suo, "Risk assessment in cross-border transport infrastructure projects: a fuzzy hybrid method considering dual interdependent effects," *Information Sciences*, vol. 488, pp. 140–157, 2019.

[2] Z. Jin and W. Suo, "Study on risk assessment method of traffic infrastructure construction considering risk correlation," *Management Assessment*, vol. 32, no. 06, pp. 45–55, 2020.

[3] L. Chang, *Research on Income Distribution of PPP Mode in Transportation Infrastructure Construction*, Beijing Jiaotong University, Beijing, China, 2018.

[4] S. Zolfaghari and S. M. Mousavi, "Construction-project risk assessment by a new decision model based on De-Novo multi-approaches analysis and hesitant fuzzy sets under uncertainty," *Journal of Intelligent and Fuzzy Systems*, vol. 35, no. 1, pp. 639–649, 2018.

[5] J. Charles and T. A. Falianty, "Managing leverage of infrastructure projects: aggregate and sectoral risk effect," *Journal of Asian Economics*, vol. 73, no. 3, Article ID 101284, 2021.

[6] Y. Yassien, M. Ezzeldin, M. Mohamed, and W. El-Dakhakhni, "Air transportation infrastructure robustness assessment for proactive systemic risk management," *Journal of Management in Engineering*, vol. 36, no. 4, Article ID 04020037, 2020.

[7] T. Rydén Sonesson, J. Johansson, and A. Cedergren, "Governance and interdependencies of critical infrastructures: exploring mechanisms for cross-sector resilience," *Safety Science*, vol. 142, no. 2, Article ID 105383, 2021.

[8] J. Guevara, M. J. Garvin, and N. Ghaffarzadegan, "The forest and the trees: a systems map of governance interdependencies in the shaping phase of road public-private partnerships," *Journal of Management in Engineering*, vol. 36, no. 1, Article ID 04019031, 2020.

[9] S. A. Thekdi and N. N. Joshi, "Prioritization of capacity investment projects with stakeholder divergence criteria for coordinated infrastructure development," *Journal of Infrastructure Systems*, vol. 22, no. 2, Article ID 04015019, 2016.

[10] K. Goh and J. Yang, "Importance of sustainability-related cost components in highway infrastructure: perspective of stakeholders in Australia," *Journal of Infrastructure Systems*, vol. 20, 2014.

[11] R. F. Herrera, O. Sánchez, K. Castañeda, and H. Porras, "Cost overrun causative factors in road infrastructure projects: a frequency and importance analysis," *Applied Sciences*, vol. 10, no. 16, p. 5506, 2020.

[12] L. Yang, J. Ma, Y. Zhang, C. Huang, and J. Zhou, "Research on the development strategy of highway traffic infrastructure along the Belt and road," *Engineering Science of China*, vol. 21, no. 4, pp. 14–21, 2019.

[13] H. Zhang, *Research on the Spatial Effect of Traffic Infrastructure Construction in the Silk Road Economic Belt*, Ji Lin University, Chaoyang, China, 2017.

[14] C. Jiang, "Failure causes and enlightenment of transportation infrastructure PPP project–based on the analysis of 25 typical PPP cases," *Journal of Beijing Jiaotong University*, vol. 15, no. 3, pp. 50–58, 2016.

[15] Y. Zhao, *Research on PPP Cooperation Mode between Government and State - Owned Enterprises in Transportation Infrastructure Construction Project[D]*, Chang'an University, Xi'an, China, 2016.

[16] L. Song, Q. Li, G. List, Y. Deng, and P. Lu, "Using an AHP-ISM based method to study the vulnerability factors of urban rail transit system," *Sustainability*, vol. 9, no. 6, p. 1065, 2017.

[17] M. K. Sen, S. Dutta, and G. Kabir, "An integrated approach for modelling and quantifying housing infrastructure resilience against flood hazard," *Journal of Cleaner Production*, vol. 288, 2020.

[18] B. T. B. Eshun and A. P. C. Chan, "An evaluation of project risk dynamics in sino-africa public infrastructure delivery; A causal loop and interpretive structural modelling approach (ISM-CLD)," *Sustainability*, vol. 13, no. 19, Article ID 10822, 2021.

[19] X. Jiang, K. Lu, B. Xia, Y. Liu, and C. Cui, "Identifying significant risks and analyzing risk relationship for construction PPP projects in China using integrated FISM-MICMAC approach," *Sustainability*, vol. 11, no. 19, p. 5206, 2019.

Hindawi
Advances in Civil Engineering
Volume 2021, Article ID 8628842, 10 pages
https://doi.org/10.1155/2021/8628842

Research Article

Shear Strength Deterioration of Compacted Residual Soils under a Wind Turbine due to Drying-Wetting Cycles and Vibrations

Yan-Ming Zhou,[1,2] Zong-Wei Deng,[2,3] Zi-Jian Fan,[1] and Wen-Jie Liu[4]

[1]*School of Civil Engineering, Changsha University of Science & Technology, Changsha 410114, China*
[2]*Hunan City University Design and Research Institute Co., Ltd., Changsha 410008, China*
[3]*College of Civil Engineering, Hunan City University, Yiyang 413049, China*
[4]*Hunan Communications Research Institute Co., Ltd., Changsha 410007, China*

Correspondence should be addressed to Zong-Wei Deng; dengzongwei@hncu.edu.cn

Received 19 October 2021; Accepted 11 November 2021; Published 13 December 2021

Academic Editor: Mingfeng Lei

The soil beneath a wind turbine withstands not only environmental impacts but also continuous vibrations transmitted from the superstructure. This paper presents an experimental study of the deterioration characteristics of shear strengths of residual soils affected by drying-wetting cycles and continuous vibrations. A series of triaxial tests were performed on compacted residual soil specimens after various drying-wetting cycles and vibrations. The influences of drying-wetting cycles and vibrations on the shear strengths of residual soils with different compaction degrees were analyzed. The results demonstrate that the shear strength and cohesion of compacted residual soils decreased as the number of drying-wetting cycles increased, and they tended to be stable after three drying-wetting cycles. The angle of internal friction decreased linearly with the reduction of compaction degree but was generally not affected by drying-wetting cycles. The shear strength of compacted residual soils also decreased because of continuous vibrations. After 10000 vibrations, the strength was stabilized gradually. Both the cohesion and angle of internal friction showed dynamic attenuation phenomenon. Finally, a modified Mohr–Coulomb strength equation considering the effects of drying-wetting cycles and vibrations was established. This equation could be used to predict the shear strength of compacted residual soils and further estimate the embedded depth of wind turbine foundations.

1. Introduction

Wind power generation technology has been developed rapidly in recent decades, making wind power the third largest power source after coal-fired power and hydropower. Although wind resources are more abundant in offshore areas, onshore wind farms have been a great concern because of their relatively low investment and mature technology [1]. For example, China has built 42,000 MW wind turbines in several provinces in the south, where hilly, plateau, and mountainous terrains exist, from 2016 to 2020 [2, 3]. Wind turbines in these regions are installed at the top of hills in order to gain sufficient wind energy (Figure 1). Thus, the foundations are often supported by strongly weathered rocks and residual soils. The mechanical properties of these materials are relatively weak and can be reduced under cyclic drying-wetting conditions [4, 5]. On the other hand, the major force on a wind turbine is the dynamic wind load, which could produce considerable vibrations on the structure. The continuous vibrations will further induce increased stresses, strains, and deformations in the foundation and subsoil [6]. Obviously, the combined effect of cyclic drying-wetting environment and continuous vibrations will greatly reduce the strength of the subsoil and cause instability of the wind turbine foundation.

Many studies have been carried out to investigate the performance of wind turbine foundations and the subsoil via theoretical analyses, numerical calculations, and field monitoring. Vahdatirad et al. [7] and Liu et al. [8] applied probabilistic reliability theory to the analysis of bearing

Figure 1: Wind driven generator at hilltop.

capacity and the stability of wind turbine foundations considering spatial variability of parameters. Pasten et al. [9] analyzed the responses of a foundation and its subsoil under cyclic loading using the mixed numerical method. It was found that the vertical settlement, horizontal displacement, footing rotation, and stress redistribution within the soil mass change with increasing number of load cycles. In addition, the displacement and rotation become more pronounced as the cyclic load amplitude increases. Madaschi et al. [10] conducted model tests on the dynamic behavior of shallow square foundation of a wind turbine under the rocking motion of the tower. The authors reported that the vibration of the wind turbine tower induces a sort of forced, damped harmonic excitation in the shallow foundation. Gao et al. [6] and Deng et al. [1] conducted numerical simulations and physical model tests on a 2 MW wind turbine subjected to random wind loads. Currently, there are also many unsaturated constitutive models that can reasonably predict the mechanical behavior of unsaturated soils under monotonic loading, such as those proposed by Russell and Khalili [11] and Li and Yang [12]. The results demonstrated that the dynamic amplification factor strongly depends on the wind speed and spatial position and that the responses of the shallow foundation of a wind turbine are significantly affected by dynamic wind loads.

The mechanical properties of soil subjected to a cyclic drying-wetting process or loading alone have also received much attention. Xu et al. [13], Rayhania et al. [14, 15], and Zhang et al. [16] reported that the desiccation cracking induced by a cyclic drying-wetting process is the main reason for the strength degradation of soils. Ng et al. [17] studied the effects of dry/wet ratio and stress ratio on unsaturated fully weathered tuff and found that the dry-wet cycle led to a nonlinear increase in the small strain shear modulus. Monghassem et al. [18] analyzed the influence of dry and wet cycles on clay in Izad Khast Castle, pointing out that the increase of suction will raise the effective friction angle and dilatancy of clay linearly. Pasculli et al. [19] indicated the change of water content in the dry-wet cycle would lead to the change of porosity by laboratory tests. In order to understand the influence of drying-wetting cycles on the saturated shear strength characteristics of undisturbed residual soil, Sayem [20] conducted consolidation drainage triaxial test and discovered that the cohesion and internal friction angle decreased with the increase in drying-wetting cycles, while proposing a function describing the attenuation rate of saturated shear strength of samples.

However, few studies are focused on the evolution of mechanical behavior of soil underlying the shallow foundation of wind turbines. The purpose of this study is thus to investigate the shear strength deterioration of compacted residual soils under a wind turbine affected by drying-wetting cycles and vibrations. Residual soil specimens are prepared at various compaction degrees. Then, different numbers of drying-wetting cycles and vibrations are imposed on the specimens. Afterward, triaxial shearing was performed under different confining pressures to determine the stress-strain relationships and shear strength parameters of residual soils. The effects of drying-wetting cycles and continuous vibrations on the shear strength were analyzed. On this basis, a modified Mohr–Coulomb strength equation considering those effects was developed and then employed to estimate the bearing capacity of the soil. The findings could provide guidance for the design of wind turbine foundations on residual soils.

2. Materials and Methods

2.1. Material Properties. The studied soil was collected from the Qiaoshi Wind Farm located in Guiyang County, Hunan Province, China. Many 2 MW horizontal-axis wind turbines were installed in this wind farm, and the total mass of each wind turbine was approximately 294.0 t. This region has a subtropical monsoon climate, with abundant rainfall and distinctive seasons. The landscape is characterized by low hills with an elevation of 400–580 m. The land is covered by a layer of 5.1–8.2 m thick residual soils. The bedrock is medium- and fine-grained sandstone with various weathering degrees.

Table 1 shows the physical properties of strata of the wind farm. The residual soil was sampled at the bearing stratum of a wind turbine foundation. The grain size distribution of the soil is presented in Figure 2, and relative parameters are shown in Table 2. The material can be classified as silty sand according to the Chinese specification GB/T 50123–2019 [21]. However, particles in the material with size <0.075 mm still accounts for about 35%, which results in obvious cohesive soil feature.

2.2. Specimen Preparation. The residual soil was used to prepare specimens with 50 mm in diameter and 100 mm in height in the laboratory (see Figure 3). Because the soil beneath a wind turbine foundation is usually compacted to meet the desired bearing capacity, the compaction method was used to form soil specimens. Firstly, the soil was mixed at the optimum water content (i.e., 12.55%). Then, it was added in a cylindrical mold and compacted by layers. The top surface of the soil was scraped to ensure uniformity of the specimen between every two layers. Three compaction degrees (i.e., 0.98, 0.95, and 0.92) were considered in order to simulate different compaction conditions of the soil.

Table 1: Physical properties of the soil and bedrocks.

No.	Stratum	Thickness, t (m)	Natural density, ρ (g/cm^3)	Optimum water content, wopt (%)	Maximum dry density, ρdmax (g/cm^3)
1	Residual soil	5.1–8.2	1.71	12.55	1.86
2	Strongly weathered sandstone	4.2–6.8	2.45	—	—
3	Moderately weathered sandstone	>16.7	2.55	—	—

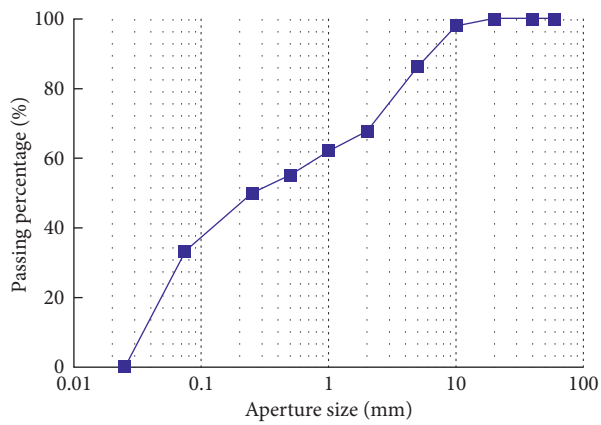

Figure 2: Grading curve of the residual soil.

Table 2: Grading parameters of the residual soil.

Parameter	Gravel and sand content (%)	Silt content (%)	Clay content (%)	Cu	Cc	D_{10} (mm)	D_{30} (mm)	D_{60} (mm)
Value	32.3	34.3	33.4	27	0.1	0.03	0.06	0.81

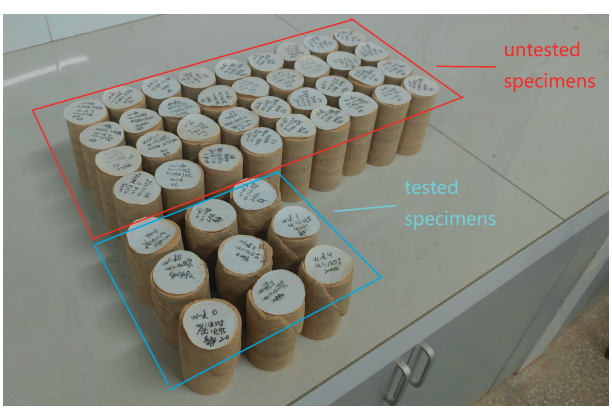

Figure 3: Cylindrical residual soil specimens.

Figure 4: GDS cyclic triaxial testing system.

2.3. Test Methods. Dynamic triaxial tests were performed to determine the shear strength of residual soils under cyclic drying-wetting and vibrating conditions. The instrument used in the tests was the GDS cyclic triaxial testing system (Figure 4). The tests could be divided into the cyclic drying-wetting phase, consolidation phase, and triaxial shearing phase when examining the influence of drying-wetting cycles on the shear strength. When the effect of vibrations was taken into account, a cyclic loading phase was introduced between the consolidation phase and triaxial shearing phase. The test schemes are shown in Table 3.

Preliminary tests were carried out to determine the drying and wetting time to achieve the target water content. The drying process was realized by drying the specimen in an oven at 104°C for 10 h, after which the water content was reduced down to 7%. The wetting process was achieved by soaking the specimen in water for 24 h after evacuation. The devices used in the wetting process are shown in Figure 5. The wetting process could cause the specimen to have a water content of 18% and a degree of saturation of about 90%. Every drying-wetting cycle consisted of a drying

Table 3: Test schemes.

Factor	Compaction degree, K	Number of drying-wetting cycle, n	Confining pressure, σ_3 (kPa)	Amplitude of cyclic load, $\Delta\sigma_1$ (kPa)
Drying-wetting cycle	0.98	0	20, 40, 60	0
		1	20, 40, 60	
		2	20, 40, 60	
		3	20, 40, 60	
		4	20, 40, 60	
	0.95	0	20, 40, 60	0
		1	20, 40, 60	
		2	20, 40, 60	
		3	20, 40, 60	
		4	20, 40, 60	
	0.92	0	20, 40, 60	0
		1	20, 40, 60	
		2	20, 40, 60	
		3	20, 40, 60	
		4	20, 40, 60	
Drying-wetting cycle and vibration	0.98	0	20, 40, 60	±5.0 kPa (1000, 5000, and 10000 vibrations)
		2	20, 40, 60	
		4	20, 40, 60	

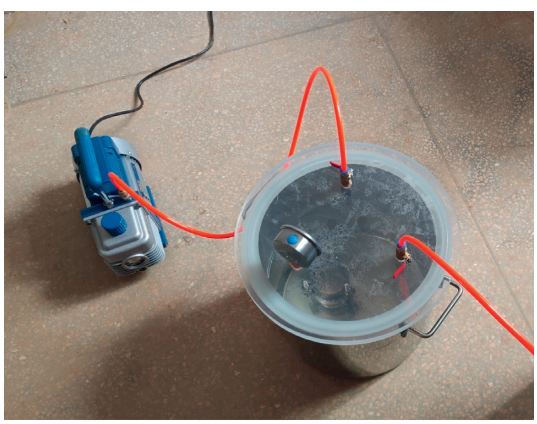

Figure 5: Devices used in the wetting process.

process and a wetting process, and the variation of water content was about ±5.5% relative to the optimum water content (12.55%). Different numbers of drying-wetting cycles (i.e., 0, 1, 2, 3, and 4) were imposed on the specimens, and a 2 h pause was considered between every two cycles.

Three levels of confining pressure (i.e., 20, 40, and 60 kPa) were employed in triaxial tests. The consolidation phase lasted 24 h at an isotropic confining pressure state. Three parallel tests were conducted for each test scheme. Triaxial shearing was performed under drained conditions at an axial strain rate of 0.003% (min). This loading rate was reduced if excess pore water pressure occurred. The shearing continues until the axial strain reached 10%. The axial strain and axial stress were monitored.

According to the field monitoring work reported by Gao et al. [6], the contact pressure between the wind turbine foundation and the subsoil can be broken down into a long-periodic static component and a short-periodic dynamic component. The latter can be simplified to be a low-amplitude sinusoidal pressure. In this study, a cyclic axial pressure with an amplitude of ±5 kPa and a frequency of 0.5 Hz was used to analyze the effect of vibration on soil strengths. Figure 6 presents the diagram of the axial loading applied in a triaxial test with vibration.

3. Results and Discussion

3.1. Stress-Strain Relationships. Figure 7 illustrates the stress-strain curves of soil specimens with different compaction degrees affected by drying-wetting cycles. It shows that the influence of drying-wetting cycles on the mechanical behavior of residual soil varies at different compaction degrees. When the compaction degree is 0.98, the stress-strain curves of all specimens are characterized by strain-softening behavior (Figure 7(a)). In this case, the maximum deviatoric stress generally occurs at an axial strain of 3%–4%. The specimens still show strain-softening behavior at a compaction degree of 0.95, but the curve peaks tend to be less obvious (Figure 6). When the compaction degree is reduced to 0.92, the specimens after zero, one, and two drying-wetting cycles exhibit strain-softening behavior, but those after three and four drying-wetting cycles show strain-hardening behavior (Figure 6). It is also noted that the failure mode of the specimens is affected by the confining pressure. As shown in Figure 8, the failure mode changes from a single failure surface to two intersected failure surfaces with increasing confining pressure.

The soil specimens were prepared at high compaction degrees ($K = 0.92$–0.98) while they were consolidated at relatively small confining pressures ($\sigma_3 = 20$–60 kPa), so they possess similar characteristics to overconsolidated soils. This is why all specimens before the cyclic drying-wetting process show strain-softening behavior. Since the residual soil contains a large number of clay minerals such as montmorillonite and illite, it shows shrinkage and expansion during the cyclic drying-wetting process. The repeated shrinkage and expansion will lead to crack development and destroy the internal

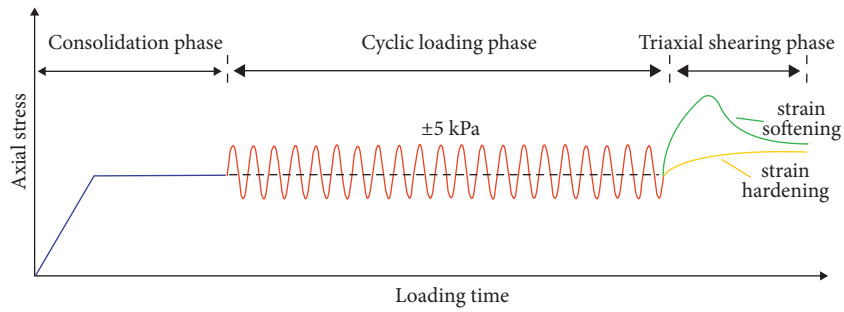

Figure 6: Loading diagram for triaxial tests on residual soil specimens with vibration.

structure of residual soils. As a result, the shear strength reduces during the cyclic drying-wetting process. The phenomenon is more prominent for the specimen of a smaller compaction degree. This is because the larger the compaction degree is, the smaller the initial porosity is and the stronger the contact between particles becomes, which can better restrain the development of cracks and protect the original structure of soil. Hence, the specimens with $K = 0.95$ and 0.98 always show strain-softening behavior although they experienced several drying-wetting cycles. By contrast, when the compaction degree is 0.92, the stress-strain curve is transferred from the strain-softening type to the strain-hardening type. The above phenomenon indicates that drying-wetting cycles will damage the internal structure of residual soils, and an increase in compaction degree can effectively inhibit the damaging effect.

Figure 9 depicts the influences of the drying-wetting cycle (n) and compaction degree (K) on the maximum deviatoric stress, ($\sigma 1 - \sigma 3$)max, of residual soil at different confining pressures. It is observed that drying-wetting cycles have an obvious deteriorative effect on the maximum deviatoric stress of compacted residual soil. At a given compaction degree, the maximum deviatoric stress reduces as the number of drying-wetting cycles increases, but the reduction becomes less obvious after three drying-wetting cycles. Meanwhile, the increase of compaction degree can restrain the deteriorative effect. For example, at a confining pressure of 40 kPa, the maximum deviatoric stress of the specimen with $K = 0.92$ reduces by 59.3% after four drying-wetting cycles; by contrast, when $K = 0.98$, the reduction of maximum deviatoric stress is only 34.1%. This suggests that the compaction degree of the soil should be strictly controlled in the construction phase; otherwise, the bearing capacity will degrade and cause instability of the wind turbine foundation due to the effect of cyclic drying-wetting environment.

3.2. Shear Strength Parameters. Figure 10 plots the change of shear strength parameters (i.e., cohesion c and angle of internal friction φ) as the drying-wetting cycle n and compaction degree K increase. The shear strength parameters were acquired from Mohr's circle.

As shown in Figure 10(a), when K is constant, the c value first shows an obvious decrease and then tends to be stable as the n value increases from 0 to 4. This indicates that the deteriorative effect of drying-wetting cycles on the cohesion is mainly manifested in the first three drying-wetting cycles. When n is constant, c decreases linearly with the reduction in K. Thus, c can be expressed as a function of n and K:

$$c = -137.42[1 + 0.08\ \ln(n+1) - 1.37K], \quad R^2 = 0.9023. \tag{1}$$

Figure 10(b) shows that the angle of internal friction is almost not affected by drying-wetting cycles, while it linearly increases with the increase in compaction degree. The relationship between the angle of internal friction and compaction degree can be fitted by the following equation:

$$\varphi = 123.2K - 86.8, \quad R^2 = 0.9257. \tag{2}$$

Figure 11 presents the photos of specimens with different compaction degrees (i.e., 0.92, 0.95, and 0.98) after shear failures. It is observed that the angle (αf) between the failure surface and the major principle stress direction reduces as the compaction degree increases. Theoretically, this angle can be expressed by the angle of internal friction:

$$\alpha_f = 45^\circ - \frac{\varphi}{2}. \tag{3}$$

Equation (3) shows that the larger the angle of internal friction, the smaller the angle αf. This confirms the positive correlation between the angle of internal friction and the compaction degree in Figure 10(b).

The cohesion of geomaterials usually comes from the cementing force, electrostatic force, van der Waals force, etc. [18], among which the cementing force is the most important component. The cyclic drying-wetting process continuously causes the development of microcracks in soil. This will reduce the cementing force and finally lead to a decrease in cohesion. As for the angle of internal friction, on the one hand, the existence of microcracks will reduce the angle of internal friction; on the other hand, cyclic drying-wetting process will cause fine particles to form aggregate, leading to the increase of interlocking force and friction. It is found that the angle of internal friction is almost not affected by drying-wetting cycles. This is probably due to the counterbalance between the above two effects.

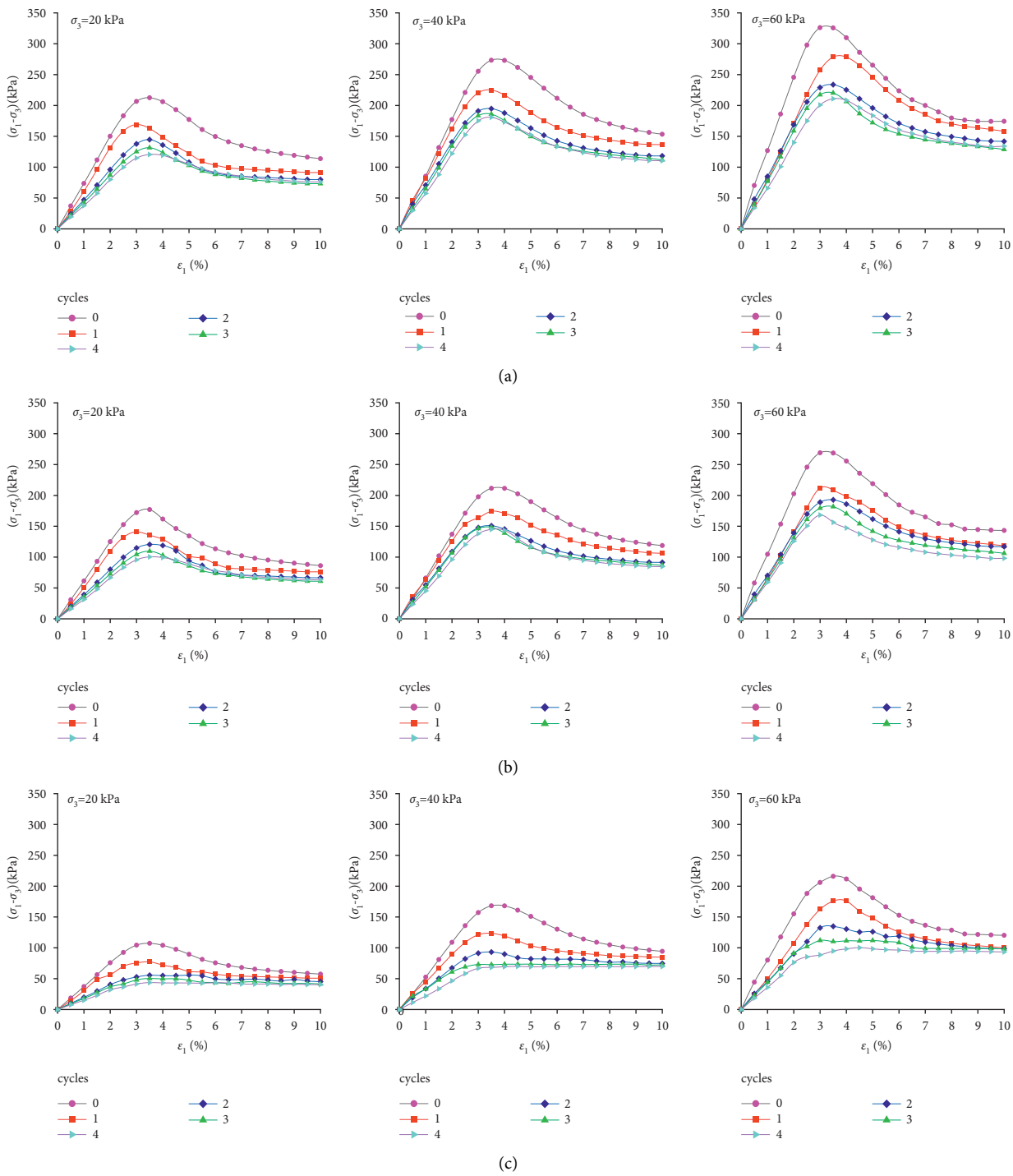

Figure 7: Stress-strain curves of compacted residual soil: (a) $K = 98\%$; (b) $K = 95\%$; (c) $K = 92\%$.

4. Effect of Vibrations on Shear Strengths

The influence of continuous vibrations on the mechanical behavior of residual soils is analyzed. Figure 12 shows the stress-strain curves of the specimens under a confining pressure of 20 kPa after cyclic drying-wetting process and continuous vibrations.

It is observed that continuous vibrations also have obvious deteriorative effects on the strength of specimens free of cyclic drying-wetting process (Figure 12(a)). The maximum deviatoric stress decreases by 23.2% after 1000 vibrations, but the decreasing rate slows down as the number of vibrations increases. When the vibrating number rises up to 10000, the stress-strain curve and maximum deviatoric stress begin to stabilize. In addition, as shown in Figures 12(b) and 12(c), the specimen that has undergone many drying-wetting cycles is not sensitive to continuous vibrations.

(a) (b) (c)

Figure 8: Failure mode of soil specimens with $K = 0.98$ and $n = 0$: (a) $\sigma_3 = 20$ kPa; (b) $\sigma_3 = 40$ kPa; (c) $\sigma_3 = 60$ kPa.

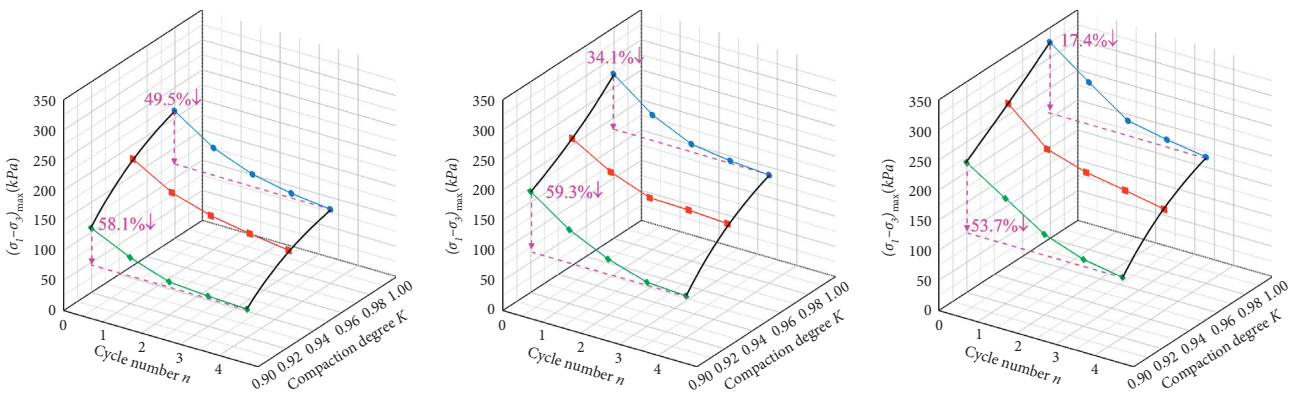

(a) (b) (c)

Figure 9: Strength variations of compacted residual soil: (a) $\sigma_3 = 20$ kPa; (b) $\sigma_3 = 40$ kPa; (c) $\sigma_3 = 60$ kPa.

Table 4 shows the shear strength parameters of specimens after 10000 vibrations. One can note that both the cohesion and angle of internal friction exhibit dynamic attenuation effects after continuous vibrations. Thus, the dynamic attenuation coefficients of cohesion and angle of internal friction are 0.5–0.7 and 0.8–0.9, respectively, considering that a lower compaction degree will lead to a stronger dynamic attenuation effect. Obviously, a larger coefficient should be taken when the compaction degree is high, and vice versa.

In general strength formulas of soils, such as the Mohr–Coulomb strength equation, the cohesion and angle of internal friction are regarded as constant. This is not necessarily applicable to soils suffering from cyclic drying-wetting process and continuous vibrations. Therefore, the Mohr–Coulomb strength equation is modified to consider the influences of drying-wetting cycle number, compaction degree, and dynamic attenuation coefficients:

$$\tau = c + \sigma \tan \phi, \tag{4}$$

$$c = 137.42\xi[1.37K - 0.08 \ln(n+1) - 1], \tag{5}$$

$$\phi = (123.2K - 86.8)\zeta, \tag{6}$$

where τ is the shear strength, σ is the normal stress on the shear surface, ξ is the dynamic attenuation coefficient of the cohesion, and ζ is the dynamic attenuation coefficient of the angle of internal friction.

Equation (4) not only reflects the evolution of shear strengths of compacted residual soil with drying-wetting cycles and compaction degrees, but also considers the continuous vibrating effect due to the wind-induced dynamic load transferred from the superstructure of wind turbine. Therefore, this equation can be used to calculate the stability of wind turbine foundation relying on residual soils.

5. Discussion on Bearing Capacity

A wind turbine is mainly composed of a wind rotor, a nacelle, a tower, and a foundation. Due to the eccentric center of the wind rotor and nacelle as well as the presence of horizontal wind loads, the subsoil is usually eccentrically compressed with an eccentricity e less than 0.033 b (b is the foundation width, and it is set to be 6 m when $b > 6$ m). Thus, the bearing capacity of the soil can be estimated by [22]

$$f_a = M_b \gamma b + M_d \gamma_m d + M_c c, \tag{7}$$

where f_a is the characteristic value of bearing capacity; M_b, M_d, M_c are bearing capacity parameters given in [22]; γ is the

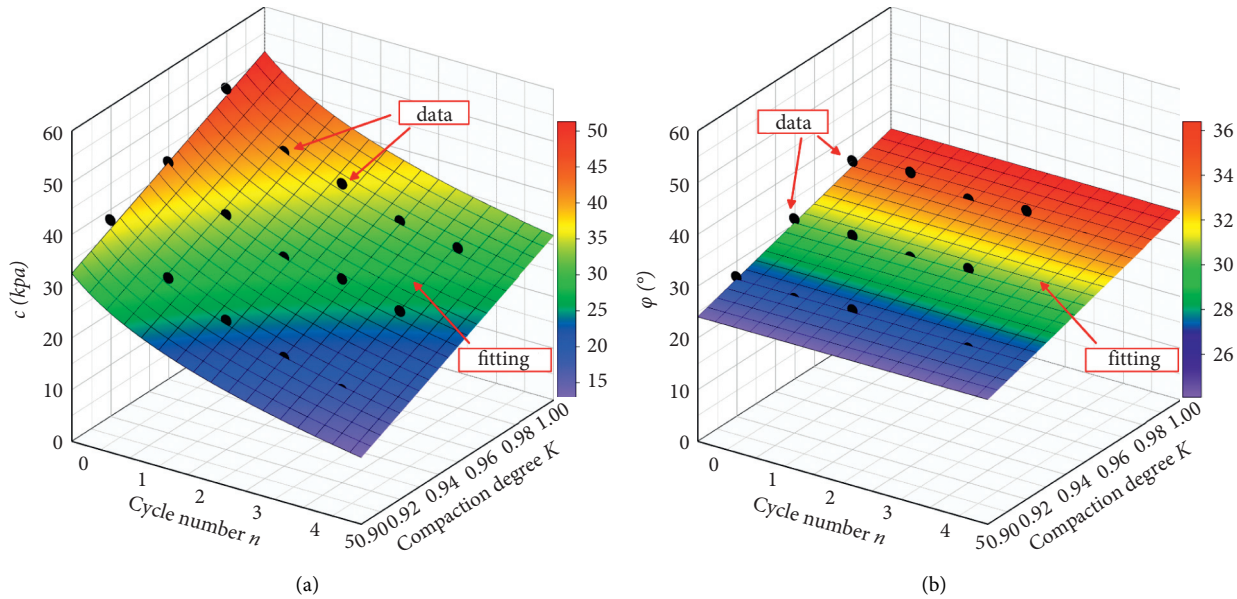

Figure 10: Influences of drying-wetting cycles and compaction degree on shear strength parameters: (a) cohesion; (b) angle of internal friction φ.

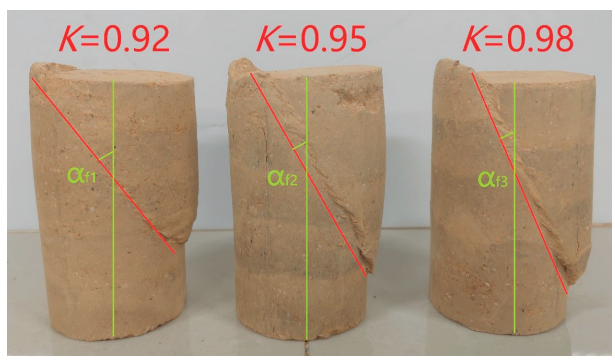

Figure 11: Angle between the failure surface and major principal stress direction ($n = 0$, $\sigma_3 = 20$ kPa).

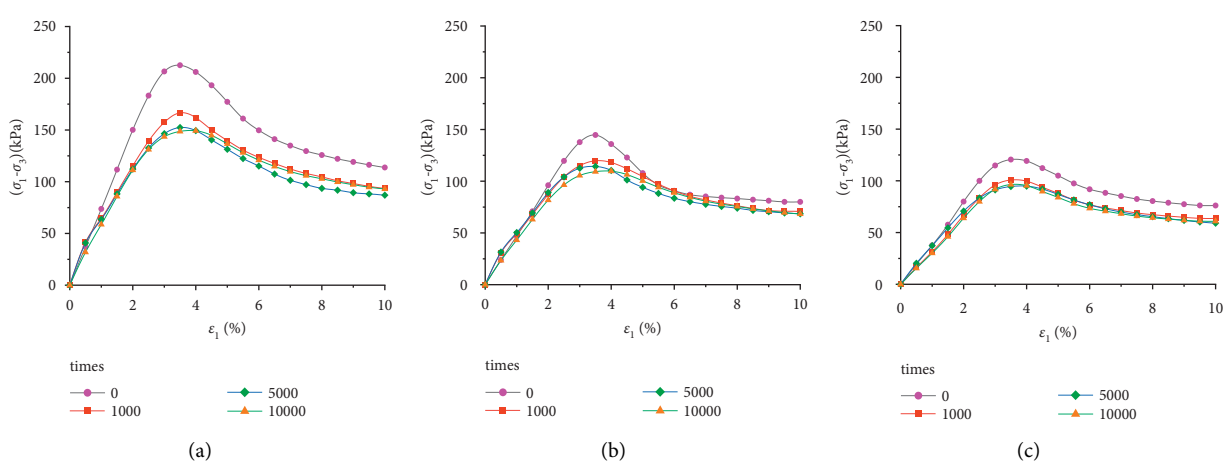

Figure 12: Stress-strain curves of the specimens under $\sigma_3 = 20$ kPa affected by vibrations: (a) $n = 0$; (b) $n = 2$; (c) $n = 4$.

Table 4: Variation of shear strength parameters after vibrations.

Compaction degree	Drying-wetting cycle, n	Cohesion, c (kPa)		Angle of internal friction, φ (°)	
		Value	Reduction	Value	Reduction
0.98	0	29.6	−39.5%	29.3	−16.3%
	2	24.2	−34.7%	29.1	−14.2%
	4	21.2	−31.7%	28.3	−14.3%

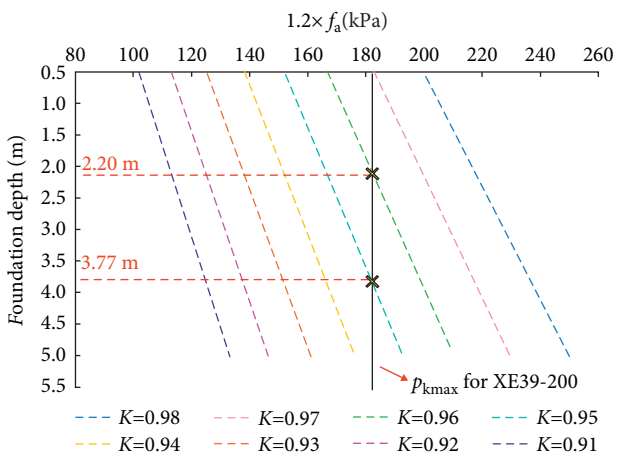

Figure 13: Relationship between the bearing capacity and embedded depth of foundation.

average unit weight of soil below the foundation; γ_m is the average unit weight of soil above the foundation bottom; d is the foundation depth; and c is the cohesion of the soil below the foundation bottom.

According to the Chinese specification [22], the maximum contact pressure should not be larger than $1.2f_a$ for compression with small eccentricity. With the consideration of the long-term variation of bearing capacity, n, ξ, and ζ are assumed to be 4, 0.6, and 0.85, respectively. Therefore, the cohesion and angle of internal friction of residual soil with different compaction degrees can be determined from (5) and (6). Finally, the bearing capacity of the soil is estimated based on (7). It is worth pointing out that almost all the foundation width of turbine surpasses 6 m, so b is supposed to be 6 m in the calculation.

Figure 13 presents the bearing capacity as a function of the embedded depth of the foundation. The maximum contact pressure ($p_{kmax} = 183.0$ kPa) below the shallow foundation of a typical 2 MW horizontal-axis wind turbine reported by [23] is also plotted in the figure. It is noted that if a compaction degree of 0.96 is used to treat the subsoil, the embedded depth of the foundation should be larger than 2.2 m; if a compaction degree of 0.95 is used to treat the subsoil, the embedded depth of the foundation should be larger than 3.77 m; otherwise, the subsoil will not be able to support the foundation steadily. The above results can provide guidance for the design of wind turbine foundations on residual soils considering both the cyclic drying-wetting environment and the continuous vibration of the wind turbine.

6. Conclusions

The following conclusions can be drawn:

The shear strength of compacted residual soil gradually reduces as the number of drying-wetting cycles increases, but it tends to be stable after three drying-wetting cycles. The drying-wetting cycle has a certain deteriorative effect on the internal structure of residual soil, and an increase in compaction degree can effectively restrain the deteriorative effect.

With the increase in drying-wetting cycle number, the cohesion decreases rapidly and then tends to be stable. The deteriorative effect of drying-wetting cycles on the cohesion is mainly manifested in the first three drying-wetting cycles. The angle of internal friction is not significantly affected by drying-wetting cycles, but it decreases linearly with the decrease in compaction degree.

After continuous vibrations, the strength of compacted residual soil decreases. When the vibrating number increases up to 10000, the stress-strain curve and strength begin to stabilize. However, the specimens that have been subjected to many drying-wetting cycles are not sensitive to continuous vibrations.

The dynamic attenuation coefficients of cohesion and angle of internal friction are recommended to be 0.5–0.7 and 0.8–0.9, respectively. A modified Mohr–Coulomb strength equation that considers the deteriorative effects of drying-wetting cycles and continuous vibrations is established. This equation can be used to predict the shear strength of compacted residual soils underlying wind turbines.

Based on the modified Mohr–Coulomb strength equation, the embedded depth of wind turbine foundations at different compaction degrees is estimated. The finding provides a reference for the design of wind turbine foundations in mountainous areas with the consideration of cyclic drying-wetting environment and continuous vibrations.

Data Availability

Because the data in the paper are still part of a project of the National Natural Science Foundation of China, they need to be used in the follow-up study of the project. Therefore, all the figures and tables data used to support the findings of this study were supplied by the corresponding author under license and so cannot be made freely available. Requests for access to these data should be made to Deng Zong-Wei, Hunan City University, No. 518, Yingbin East

Road, 413000, Yiyang, Hunan, China (e-mail: dengzongwei@hncu.edu.cn).

Conflicts of Interest

The authors declare that they have no conflicts of interest.

Acknowledgments

This work was supported by the Natural Science Foundation of Hunan Province, China (2020JJ4156 and 2021JJ50142); the National Natural Science Foundation of China (51674041 and 51474103); and the Changsha Municipal Natural Science Foundation (kq2014110).

References

[1] Z.-W. Deng, Q.-F. Gao, H. Dong, and L.-X. Li, "Dynamic responses of the shallow foundation of an onshore wind turbine," *International Journal of Physical Modelling in Geotechnics*, vol. 19, no. 5, pp. 247–260, 2019.

[2] X.-c. Fan and W.-q. Wang, "Spatial patterns and influencing factors of China's wind turbine manufacturing industry: a review," *Renewable and Sustainable Energy Reviews*, vol. 54, pp. 482–496, 2016.

[3] L. Li, X. Ren, Y. Yang, P. Zhang, and X. Chen, "Analysis and recommendations for onshore wind power policies in China," *Renewable and Sustainable Energy Reviews*, vol. 82, pp. 156–167, 2018.

[4] L. Zeng, F. Li, Q. F. Gao, X. Yao, and G. Wang, "Insight into the fracturing of silty mudstone in cyclic hydrothermal environments based on computed tomography," *Transportation Geotechnics*, vol. 26, Article ID 100432, 2021.

[5] P. Liu, R. P. Chen, K. Wu, and X. Kang, "Effects of drying-wetting cycles on the mechanical behavior of reconstituted granite-residual soils," *Journal of Materials in Civil Engineering*, vol. 32, no. 8, 2020.

[6] Q.-F. Gao, H. Dong, Z.-W. Deng, and Y.-Y. Ma, "Wind-induced dynamic amplification effects on the shallow foundation of a horizontal-axis wind turbine," *Computers and Geotechnics*, vol. 88, pp. 9–17, 2017.

[7] M. J. Vahdatirad, D. V. Griffiths, L. V. Andersen, J. D. Sørensen, and G. A. Fenton, "Reliability analysis of a gravity-based foundation for wind turbines: a code-based design assessment," *Géotechnique*, vol. 64, no. 8, pp. 635–645, 2014.

[8] M. M. Liu, M. Yang, and H. J. Wang, "Study on subgrade reaction and punching of circular spread foundation for onshore wind turbines," *Acta Energiae Solaris Sinica*, vol. 36, no. 5, pp. 1130–1135, 2015, (In Chinese).

[9] C. Pasten, A. M. Asce, H. Shin, and C. Santamarina, "Long-term foundation response to repetitive loading," *Journal of Geotechnical and Geoenvironmental Engineering*, vol. 140, no. 36, pp. 1–11, 2014.

[10] A. Madaschi, A. Gajo, M. Molinari, and D. Zonta, "Characterization of the dynamic behavior of shallow foundations with full-Scale dynamic tests," *Journal of Geotechnical and Geoenvironmental Engineering*, vol. 142, no. 38, pp. 21–30, 2016.

[11] A. R. Russell and N. Khalili, "A unified bounding surface plasticity model for unsaturated soils," *International Journal for Numerical and Analytical Methods in Geomechanics*, vol. 30, no. 3, pp. 181–212, 2006.

[12] W. G. Li and Q. Yang, "Hydromechanical constitutive model for unsaturated soils with different overconsolidation ratios," *International Journal of Geomechanics*, vol. 18, no. 2, Article ID 04017142, 2018.

[13] B. Xu, Z. Z. Yin, and S. L. Liu, "Experimental study of factors influencing expansive soil strength," *Rock and Soil Mechanics*, vol. 32, no. 1, pp. 44–50, 2011, (in Chinese).

[14] M. H. T. Rayhani, E. K. Yanful, and A. Fakher, "A.Physical modeling of desiccation cracking in plastic soils," *Engineering Geology*, vol. 97, no. 1-2, pp. 25–31, 2008.

[15] M. H. Rayhani, E. K. Yanful, and A. Fakher, "Desiccation-induced cracking and its effect on the hydraulic conductivity of clayey soils from Iran," *Canadian Geotechnical Journal*, vol. 44, no. 3, pp. 276–283, 2007.

[16] J. J. Zhang, B. W. Gong, and B. Hu, "Study of evolution law of fissures of expansive clay under wetting and drying cycles," *Rock and Soil Mechanics*, vol. 32, no. 9, pp. 2729–2734, 2011, (in Chinese).

[17] C. W. W. Ng, J. Xu, and S. Y. Yung, "Effects of wetting-drying and stress ratio on anisotropic stiffness of an unsaturated soil at very small strains," *Canadian Geotechnical Journal*, vol. 46, no. 9, pp. 1062–1076, 2009.

[18] M. Monghassem, M. Ajdari, S. M. Binesh, and F. Vahedifard, "Effects of suction and drying-wetting cycles on shearing response of adobe," *Journal of Materials in Civil Engineering*, vol. 133, no. 7, pp. 1–15, 2021.

[19] A. Pasculli, N. Sciarra, L. Esposito, and A. W. Esposito, "Effects of wetting and drying cycles on mechanical properties of pyroclastic soils," *Catena*, vol. 156, pp. 113–123, 2017.

[20] H. M. D. Sayem, "Effect of drying-wetting cycles on saturated shear strength of undisturbed residual soils," *American Journal of Civil Engineering*, vol. 4, no. 4, pp. 159–166, 2016.

[21] Ministry of Housing and Urban-Rural Development, *GB Chinese Specification for the Design of Building Foundations*, China Building Industry Press, Beijing, 2011, in Chinese.

[22] Ministry of Housing and Urban-Rural Development, *PRC, GB 50007-2011 Chinese Specification for the Design of Building Foundations*, China Building Industry Press, Beijing, China, 2011, in Chinese.

[23] Z. W. Deng, W. C. Peng, and Q. F. Gao, "Base pressure monitoring and flatness analysis for wind turbine spread subgrade," *Rock and Soil Mechanics*, vol. 36, no. 9, pp. 2659–2664, 2015, in Chinese.

Hindawi
Advances in Civil Engineering
Volume 2021, Article ID 9448436, 11 pages
https://doi.org/10.1155/2021/9448436

Research Article

Finite Element Analysis of Vertical and Horizontal Drainage Structures under Vacuum Combined Surcharge Preloading

Daqing Wang,[1] Dong Wei,[1] Guoyi Lin,[1] Jiannan Zheng,[1] Zhiting Tang,[1] Litao Fan,[2] and Bingxiang Yuan[2]

[1]*China Construction Fourth Engineering Bureau Limited, Guangzhou 510280, China*
[2]*School of Civil and Transportation Engineering, Guangdong University of Technology, Guangzhou 510006, China*

Correspondence should be addressed to Bingxiang Yuan; yuanbx@gdut.edu.cn

Received 28 October 2021; Accepted 13 November 2021; Published 27 November 2021

Academic Editor: Yu Liang

Combined vacuum and surcharge preloading has gradually been widely used because of its advantages of low cost, green environmental protection, and good treatment effect. The conventional prefabricated vertical drain presents obvious defects in vacuum preloading treatment, such as obvious silting, serious bending of the drainage board, large attenuation of vacuum degree of drainage board along the depth, long construction period, and so on, which affect the final reinforcement effect. In this paper, the MIDAS finite element simulation of combined vacuum and surcharge preloading of prefabricated vertical drains (PVDs) and prefabricated horizontal drains (PHDs) is established through the comparative experiment of the engineering field. The comparative experimental study is carried out from the aspects of the vertical settlement, horizontal displacement, and pore water pressure. The results show that under combined vacuum and surcharge preloading, the consolidation effect of soft soil with PHDs is better than that with PVDs. When PHDs are used, the vertical settlement increases by 7.2% compared with PVDs; the horizontal displacement is larger; and the pore water pressure dissipates faster. This is because when the PHDs are adopted, the consolidation direction of the soil is consistent with the direction of the vacuum suction, which is mainly caused by vertical settlement. With the consolidation, the spacing between PHDs is gradually shortened, and the drainage distance is reduced, which can effectively reduce the consolidation time and improve the reinforcement effect of the soil. In addition, the PHDs can move downward uniformly with the soil during the consolidation process and have almost no bending deformation, which makes the vacuum transfer more uniform and effective.

1. Introduction

The vacuum-surcharge preloading method is an economic and effective soft foundation treatment method, which has been widely used in large-area soft foundation treatment, and its advantages in foundation treatment are very obvious. As early as the 1980s, a large number of scholars in China have been exploring the application of vacuum combined surcharge preloading method to practical engineering. Through exploring and testing to solve the key problems in the process, the Scientific Research Institute of the First Aviation Administration has achieved success in the field test of large-area vacuum combined surcharge [1]. Shang [2] obtained the best consolidation effect and economic benefit of combined vacuum and surcharge preloading through field comparative tests. Subsequently, due to the update of theory [3–6] and the progress of construction technology, with the further development of indoor model test and finite element numerical simulation [7–9], the vacuum-surcharge preloading method is widely applied to practical engineering. Through engineering example and stress route analysis, Lou and Yi [10] put forward the necessity of graded loading for soft foundation strengthened by vacuum combined surcharge preloading. Yuan and Lu [11, 12] studied the deformation characteristics of micro prefabricated vertical drainage unit by changing the loading rate of heaped pressure and vacuum pressure so that the soft soil was consolidated more fully and the consolidation efficiency was

improved. Jin et al. [13] used vacuum combined surcharge preloading method to reinforce soft foundation with confined water and introduced the construction technology to prevent the penetration of confined water. Based on the combined surcharge preloading model test, the lateral pressure is applied to the internal air injection of the filled foundation, which has a significant effect on improving the consolidation degree of the soil [14, 15].

However, the engineering practice shows that the vacuum preloading method using PVDs has the following problems: the drainage plate is easy to silt up, and the soil column is formed around the drainage plate, leading to uneven settlement [16, 17]. The attenuation of vacuum along the PVDs leads to the poor treatment effect of deep soil [18–20] and a long construction period [21, 22]. This is mainly due to the fact that in the process of vacuum preloading, small particles are easily blocked in the filter membrane pores of the drainage plate, resulting in siltation of the drainage plate. Subsequently, fine particles continue to migrate to the drainage plate and accumulate near the drainage plate, forming soil columns with extremely poor permeability around the drainage plate, which greatly reduces the drainage rate and seriously affects the efficiency of drainage consolidation.

Therefore, the research on prefabricated horizontal drains (PHDs) is gradually carried out. In the early stage, Lee [23] used horizontal shallow sand-clay layer instead of vertical sand wells as drainage body to reinforce dredger fill silt and proved its feasibility. Jin et al. [24] used the laboratory test results of the middle well and soil box test to simulate the local installation of horizontal drainage pipe and discussed the estimation of the best negative pressure. Li [25] successfully completed vacuum dehydration using a horizontal geosynthetic drainage blanket, and the placement of a horizontal geosynthetic drainage blanket also enhanced the strength and stability of silt. In the domestic research, Bao et al. [26] research showed that horizontal integral drainage plate is more conducive to the transmission of vacuum in soil. By comparing the vacuum preloading effect of the vertical drainage plate and horizontal drainage plate, it is concluded that the physical and mechanical indexes of PHDs are better than those of PVDs, and the deformation of PHDs is smaller than that of PVDs [27, 28]. In addition, the PHD has a better reinforcement effect on dredged silt because its vertical spacing decreases with settlement, and drainage path is shorter [29, 30]. Wang et al. [31] proposed a method about combining vacuum preloading with electroosmosis using prefabricated horizontal drain (EPHD) to treat dredged fill sludge and compared it with combining vacuum preloading with electroosmosis using prefabricated vertical drain (EPVD). EPHD showed obvious advantages in drainage efficiency, reinforcement efficiency, and economy.

Based on the above analysis, PHDs + vacuum preloading method as a promising dredging sludge treatment method can effectively solve the traditional vacuum preloading consolidation stress limitation, vacuum attenuation along the depth, the reinforcement effect of deep soil that is not ideal, uneven settlement, and other shortcomings. In order to further explore the mechanism and effect of PHDs in soft foundation reinforcement, this paper simulates the actual project of vacuum combined surcharge preloading by MIDAS.GTS.NX finite element software. By comprehensively comparing the effects of PHDs and PVDs on the reinforcement effect of soft foundation, the advantages of PHDs + vacuum combined surcharge preloading method are discussed.

2. Project Profile

The first-stage project from Xinhuicheng to Yamen section of Guangfo River Expressway is located in the central and western part of Guangdong Province, China. The total area of foundation treatment is divided into 13 treatment areas, as shown in Figure 1, and the foundation treatment methods in areas 1, 3, and 6–10 are plastic drainage plate + vacuum combined surcharge preloading method. In this paper, area 1 is selected as the research object for simulation analysis. The soft foundation treatment area is 48 m × 106.9 m, and some of them are used as field experiments in this study. The silt soft soil in the region has the characteristics of "three high and one low," that is, high water content, high porosity ratio, high sensitivity, and low strength. Engineering properties are poor, so soft foundation treatment is needed to be developed and utilized. The basic physical and mechanical properties of the soil layer in the region are shown in Table 1.

According to the requirements of the construction design drawings, the first step is the preliminary preparation, such as leveling the site and digging the drainage ditch. Then lay the lower sand cushion, and then carry out the construction of plastic drainage board. The foundation treatment depth is about 13 m, and the buried depth of the plastic drainage plate is 12 m. The PVDs and PHDs are buried, respectively. After the plastic drainage board is completed, the upper sand cushion is laid, and vacuum preloading is started. The vacuum pressure under the membrane can be maintained at 85 kPa after 10 days of the vacuum pumping. When the reinforcement effect of vacuum preloading method was gradually weakened in the later stage, the stack preloading was carried out, and the accumulated loading was three levels. The vacuum preloading can be stopped after the settlement meets the design requirements by analyzing the settlement observation data. The vacuum pumping time of the whole test process is about 3 months.

2.1. Experimental Method and Finite Element Establishment

2.1.1. Theoretical Analysis of Consolidation. When Terzaghi studied the consolidation characteristics of soil in 1925, he proposed and established a one-dimensional consolidation differential equation, which laid the theoretical foundation of consolidation in classical soil mechanics. On this basis, Biot proposed the three-dimensional consolidation theory of soil in 1943. The consolidation problem of soil can be understood as the transformation process of effective stress in soil. Through the coupling effect of continuous conditions and compression conditions of the interaction between laminar pore water and

Figure 1: Aerial view of engineering site.

soil skeleton, the physical equation, geometric equation, and continuity equation of soil are constructed. The consolidation equation is solved by Darcy's law and boundary conditions.

In vacuum combined surcharge preloading, due to the existence of drainage plate, the drainage consolidation problem of foundation reinforced by vacuum combined surcharge preloading method is a three-dimensional problem. However, due to the dense drainage plate arranged in a soft soil foundation, it can be assumed that the drainage plate is connected into a plane in the longitudinal direction, and then it is simplified into a plane strain problem for processing. Therefore, Biot's consolidation equation can be simplified as follows:

$$\begin{cases} -G\nabla^2 w_x - \dfrac{G}{1-2\nu} g \dfrac{\partial \varepsilon_v}{\partial x} + \dfrac{\partial u}{\partial x} = 0, \\ -G\nabla^2 w_z - \dfrac{G}{1-2\nu} g \dfrac{\partial \varepsilon_v}{\partial z} + \dfrac{\partial u}{\partial z} = -\gamma, \\ \dfrac{\partial \varepsilon_v}{\partial t} + \dfrac{K}{\gamma_w} \nabla^2 u = 0, \end{cases} \tag{1}$$

where G is the soil shear modulus; v is Poisson's ratio; u is pore water pressure; K is the permeability coefficient, assuming that the permeability coefficient in the soil is the same in all directions; and γ_w and γ are the gravity of water and the gravity of soil, respectively. Under the plane strain condition, the Laplace operator and volumetric strain in the equation are expressed as follows:

$$\nabla^2 = \frac{\partial}{\partial x^2} + \frac{\partial}{\partial z^2}, \tag{2}$$

$$\varepsilon_v = -\left(\frac{\partial w_x}{\partial x} + \frac{\partial w_z}{\partial z}\right). \tag{3}$$

2.1.2. Equivalent Principle of Drainage Plate. Using vacuum combined surcharge preloading method to reinforce soft soil foundation, drainage plate should be inserted into the foundation. The function of the drainage plate is to drain and transfer vacuum negative pressure. The plastic drainage plate cannot be simulated in the plane calculation model of finite element, so the drainage plate is converted into the sand wall for processing. Firstly, the drainage plate is equivalent to sand well. The basic idea is to make the cylindrical sand well; the plastic drainage plate has the same drainage capacity; and the diameter of the sand well can be set as the equivalent diameter of the drainage plate. Hansbo (1979) first proposed that the equivalent diameter formula of plastic drainage plate can be expressed as [32]:

$$d_w = \alpha \frac{2(a+b)}{\pi}, \tag{4}$$

where d_w is the equivalent diameter of the drainage plate; a and b are the width value and thickness value of plastic drainage plate, respectively; and α is the conversion coefficient, usually 0.75~1.0.

The consolidation problem of sand wells should be calculated by a three-dimensional spatial model. However, due to the heavy workload of three-dimensional finite element analysis itself, coupled with dense sand wells, the mesh elements are greatly increased. The calculation can be greatly reduced by using two-dimensional plane finite element analysis. Therefore, on the basis of transforming plastic drainage plate into the sand well, the sand well is transformed into the sand wall, and the space problem is transformed into the plane problem to simplify the calculation. The relationship between permeability coefficient of converted sand wall and permeability coefficient of sand well is as follows [33]:

$$k_{xp} = D_x k_{xa}, \tag{5}$$

$$k_{zp} = D_z k_{za}, \tag{6}$$

where k_{xa} and k_{za} are the horizontal and vertical actual permeability coefficient of sand well foundation, respectively, and D_x and D_z are horizontal and vertical permeability coefficient adjustment coefficient, respectively; the calculation formula are as follows:

$$\begin{aligned} D_x &= \frac{4(\eta p - sp)^2 (1+v) L^2}{9\eta_p^2 \mu_a - 12\beta\left(n_p - s_p\right)\left(s_p - 1\right)(1+v)L^2}, \\ D_z &= \frac{2(1+v)}{3}, \end{aligned} \tag{7}$$

where

$\mu_a = n^2/n^2 - s^2 \ln n/s - (3n^2 - s^2)/4n^2 + k_{ra}/k_s (n^2 - s^2)/n^2$

In s; $L = B/r_e$ is the magnification of sand well spacing; B and r_e are half of sand wall spacing and effective drainage radius, respectively; β is the ratio of horizontal actual permeability coefficient (k_{xa}) to permeability coefficient of smearing area (k_{sp}); n_p is the ratio of half of sand wall spacing (B) to sand well radius (r_{wp}); s_p is the ratio of the distance from the center of sand well to the outer edge of smearing area (r_{sp}) to half of the thickness of the sand wall (r_{wp}); $n = r_e/r_{wa}$ is hole diameter ratio; r_{wa} is the radius of sand well; $s = r_s/r_{wa}$ is coating ratio; r_s is the smear radius; and v is Poisson's ratio of soil.

Table 1: Basic physical parameters of the soil layer.

Parameter	Sand cushion	Plain fill	Silt	Mucky soil	Silty clay
Depth (m)	1.0	1.0	8.0	4.0	6.0
Γ (kN/m^3)	18.7	17.0	16.6	18.4	20
υ	0.25	0.35	0.38	0.37	0.37
e_0	0.6	0.65	1.6	1.2	0.7
E (kPa)	12,000	3,590	2,380	2,650	4,270
C (kPa)	1	12	8	10	15
Φ (°)	20	15	4	12	17
K (m/s)	1.35×10^{-3}	3.75×10^{-5}	1.55×10^{-9}	6.26×10^{-8}	1.55×10^{-6}

Note: γ is the weight of the soil; υ is Poisson ratio; e_0 and E are initial void ratio and elastic modulus, respectively; C and Φ are the cohesion and internal friction angle of soil, respectively; and k denotes the permeability coefficient.

2.1.3. Establishment of MIDAS Finite Element. The consolidation problem of vacuum combined surcharge preloading is actually a three-dimensional consolidation problem. However, due to the existence of plastic drainage plates, the calculation cost of three-dimensional finite element analysis is too high. In addition, many scholars can get better results through the calculation of a two-dimensional finite element model. Therefore, this paper selects MIDAS.GTS.NX finite element numerical software to carry out two-dimensional plane strain finite element analysis of vacuum combined surcharge preloading. In this paper, the local area of 1 area is selected for finite element analysis. The reinforcement width of the model is 20 m, and the vacuum preloading can affect the soil below the bottom of the drainage plate and outside the reinforcement area. Therefore, the width and height of the calculation model are 80 mm and 20 m. The drainage plate size is 4.5 mm × 100 mm, and the embedded depth is 12 m. For the vertical drainage system, the spacing of the PVDs is 1 m. In order to ensure that the length of PHDs and PVDs in the experimental area is consistent, the spacing of the adjacent PHD in the horizontal drainage system is 1.2 m. The equivalent diameter and permeability coefficient of the plastic drainage plate can be calculated according to formulas (2)–6 The parameters of the drainage plate are shown in Table 2.

According to the basic parameters of the soil layer and the drain plate, the model and grid division can be obtained, as shown in Figure 2. The numerical simulation analysis of vacuum combined surcharge preloading with PVDs and PHDs is carried out, respectively. The load in the vacuum combined surcharge preloading is mainly the self-weight of the soil, the vacuum negative pressure in the drainage body, and the surcharge pressure acting on the surface of the soil in the reinforcement area. Therefore, the construction simulation mainly has the following three stages:

(1) Initial stress stage: activate all soil layers (including sand cushions), drainage plate, foundation boundary constraints, and weight. In the definition construction, check the displacement to zero and set the displacement in the initial stress stage to the initial value.

(2) Vacuum preloading stage: activate cushion drainage conditions and drainage plate drainage conditions. The vacuum load is set to negative node pressure head, duration of 30 days.

(3) Vacuum combined surcharge stage: activate the surcharge soil and its nonconsolidation conditions and carry out graded surcharge. After each stage of surcharge, it will stand for 10 days. After the end of the last stage of surcharge, it will stand until the consolidation effect is obviously weak.

3. Results and Analysis

3.1. Calculation and Analysis of Vertical Settlement Displacement. Figure 3 is the final settlement calculation cloud chart of vacuum combined surcharge preloading with two different drainage plates. It can be seen from the figure that whether PVDs or PHDs are used, the settlement deformation of the soil layer from top to bottom is concave. With the increase of depth, the settlement of soil is decreasing, and the settlement tends to be gentle. The settlement contour of soil at the bottom of the drainage plate is similar to a straight line. The settlement mainly occurs in the range of the reinforcement area, and there is a certain degree of influence outside the influence area. This is mainly because the soil in the reinforcement area moves to the influence area under the action of vacuum combined surcharge. Figure 4 shows the relationship between the depth at the center of the reinforcement area and the final settlement. It can be obtained that the soil settlement on the surface is the largest, and the maximum settlement of the soil in PVDs is smaller than that in PHDs. The maximum settlement of the two drainboards is 0.692 m and 0.742 m, respectively. This is because when the PHDs are used, the consolidation direction of the soil is consistent with the direction of the vacuum suction, that is, the vertical settlement is mainly caused. With the progress of consolidation, the distance between adjacent PHD is gradually shortened, and the drainage distance is reduced, which can effectively reduce the consolidation time and improve the soil reinforcement effect.

The surface central point of the preloading area is analyzed to obtain the surface subsidence-time curve of the central point (Figure 5). As shown in the figure, the two drainage modes have rapid settlement under the action of vacuum preloading, accounting for about 60% of the total settlement. In the early stage of vacuum preloading, the surface settlement changes almost linearly, while the later stage of the preloading gradually slows down. At the

Table 2: Equivalent parameters of drainage plates.

Parameters	E (kPa)	S (m)	υ	d_w (m)	K (m/s)	D_x	D_z	k_x (m/s)	k_z (m/s)
Value	6,000	1.0	0.25	0.06	5.8×10^{-6}	1.05	0.83	6.1×10^{-6}	4.8×10^{-6}

Note. E is elastic modulus; s and υ are the spacing and Poisson's ratio of drainage plates, respectively; d_w is the equivalent radius; k denotes the original permeability coefficient; D_x and D_z are the adjustment coefficients of horizontal and vertical permeability coefficients, respectively; and k_x and k_z are the adjusted horizontal and vertical permeability coefficients, respectively.

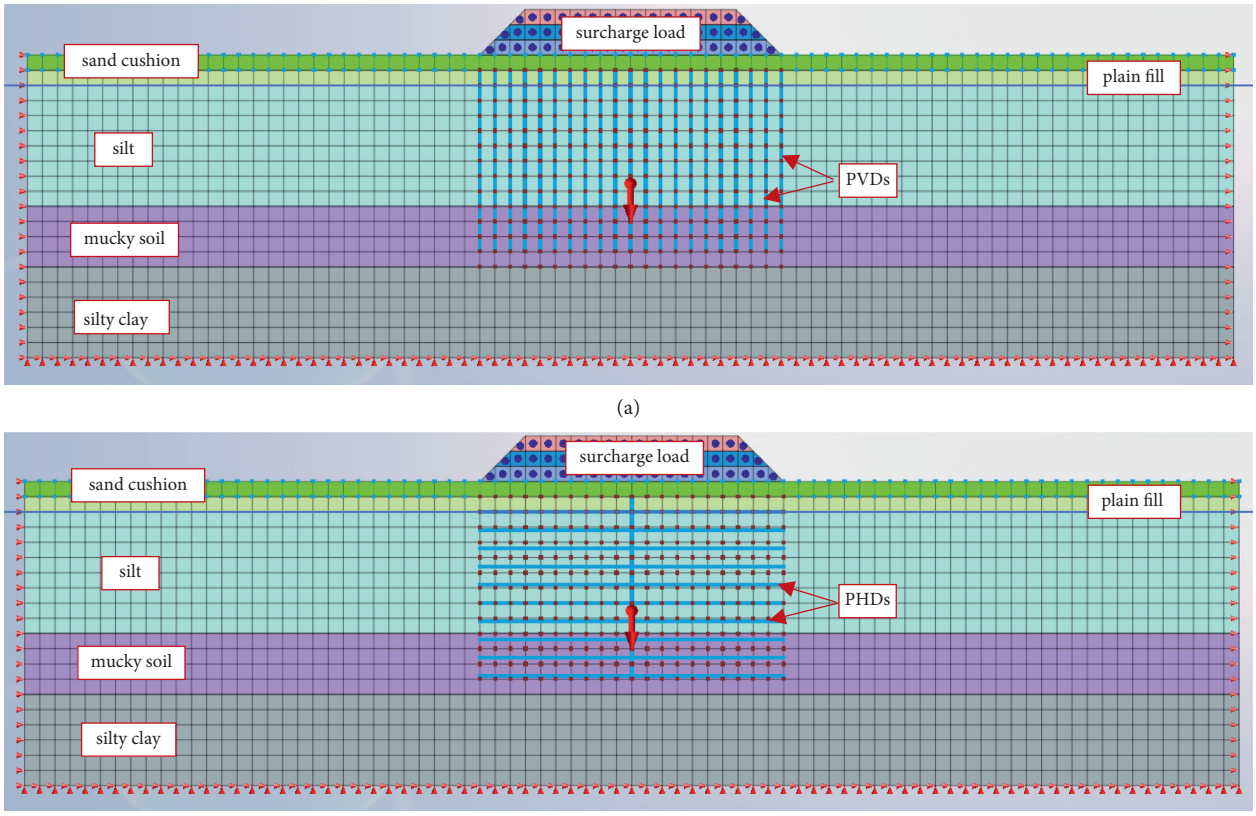

Figure 2: Finite element model of vacuum combined surcharge preloading: (a) PVDs and (b) PHDs.

beginning of preloading, the settlement increases significantly and then gradually slows down. The settlement in the last 30 days accounts for only 3% of the total settlement. This is because when the loading starts, the discharge rate of excess pore water is fast, the pore water pressure is converted into effective stress, and the pores in the soil are reduced. In the later stage, fine particles are easy to block the filter membrane of the drainage plate and continue to gather, forming a "soil column" near the drainage plate, resulting in the decline of drainage efficiency and slow settlement in the later stage.

In general, the surface settlement with the PHDs is larger than that with the PVDs. This is because in the process of consolidation with PVDs, due to the initial stress of the soil and the compression and bending of the plate, the drainage plate has serious deformation and obvious bending to one side. The distance between PVDs is getting farther and farther, and the drainage path is lengthened, so the consolidation drainage is more difficult. In the consolidation process with PHDs, the drainage plate can move down uniformly with the soil, and the plate has almost no bending deformation, which makes the vacuum transfer more uniform and effective. Figure 6 shows the displacement vector diagrams of the two drainage plates. Figure 6 shows the displacement vector diagrams of two kinds of drainage plates. It can be seen from the figure that the deformation of the drainage plate gradually decreases with the increase of depth. The drain plate with the largest displacement for analysis is taken, and the results shown in Figure 7 are obtained. The maximum displacement difference of the PHDs is 50 mm, and the maximum displacement difference of the PVDs is 80 mm, that is, the deformation of the horizontal drainage plate is smaller than the vertical drainage plate.

3.2. Calculation and Analysis of Horizontal Displacement. Figure 8 is the horizontal displacement cloud chart of vacuum combined surcharge preloading using two kinds of

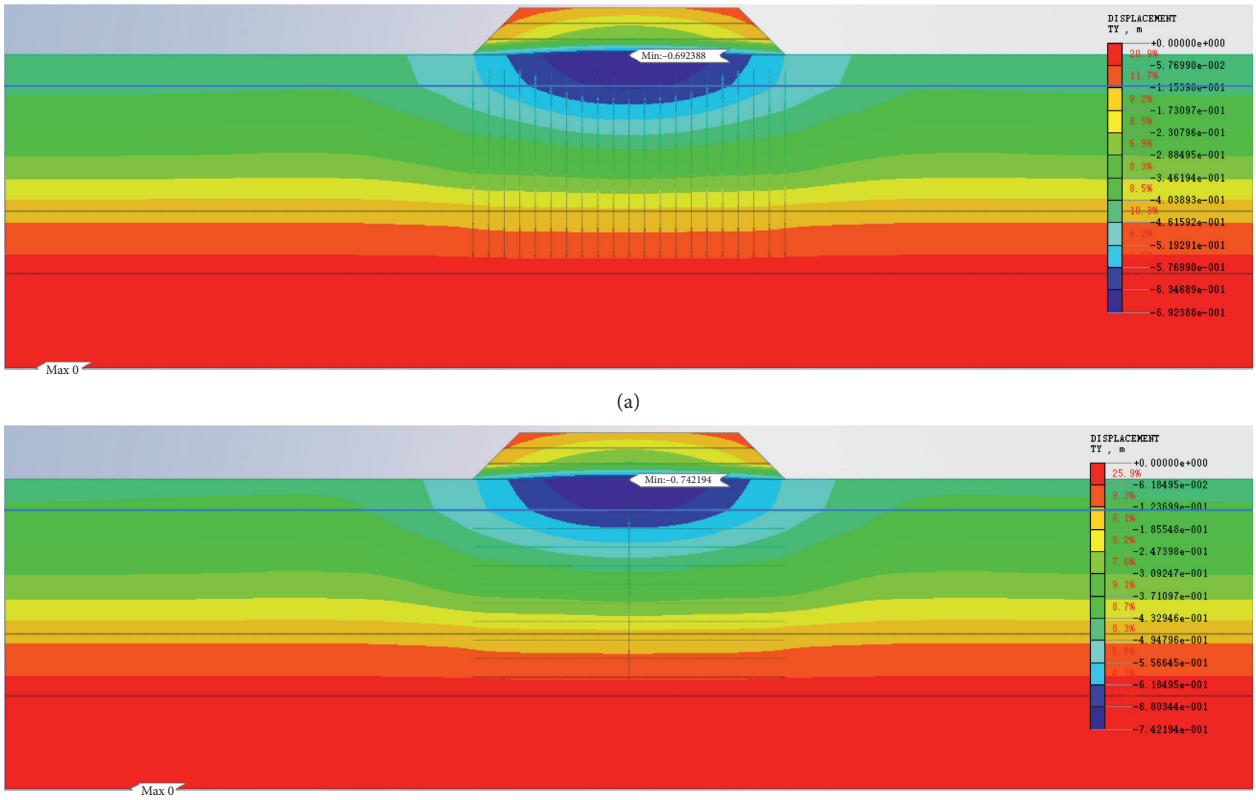

Figure 3: Vertical settlement nephogram of finite element: (a) vertical drainage and (b) horizontal drainage.

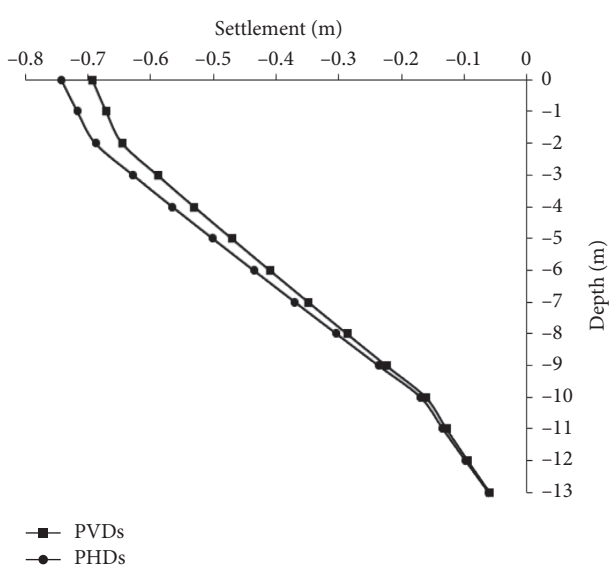

Figure 4: Relationship curve between depth and final settlement.

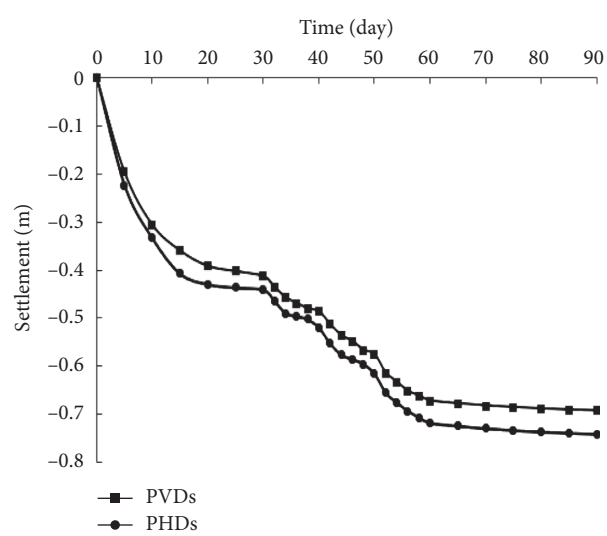

Figure 5: Central subsidence of surface and its relation curve.

drainage plates. It can be seen from the figure that the maximum positive and negative horizontal displacement occurs between the first and second layers of the soil during the vacuum combined surcharge preloading, and the influence range of the influence area is larger than that of the settlement area. The maximum horizontal displacement of the vacuum combined surcharge preloading with PHDs is larger than that with PVDs, which are 96.8 mm and 93.8 mm, respectively, and the difference is 3 mm. When the buried depth is 6 m, the horizontal displacement of the soil at the junction of the affected area and the reinforcement area is analyzed, as shown in Figure 9. In the process of vacuum loading, the soil in the affected area is

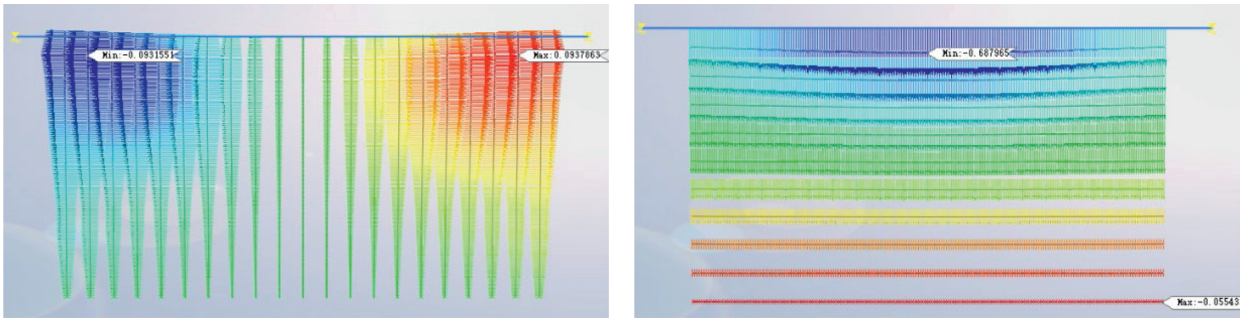

(a) (b)

Figure 6: Displacement vector diagram of drainage plate: (a) PVDs and (b) PHDs.

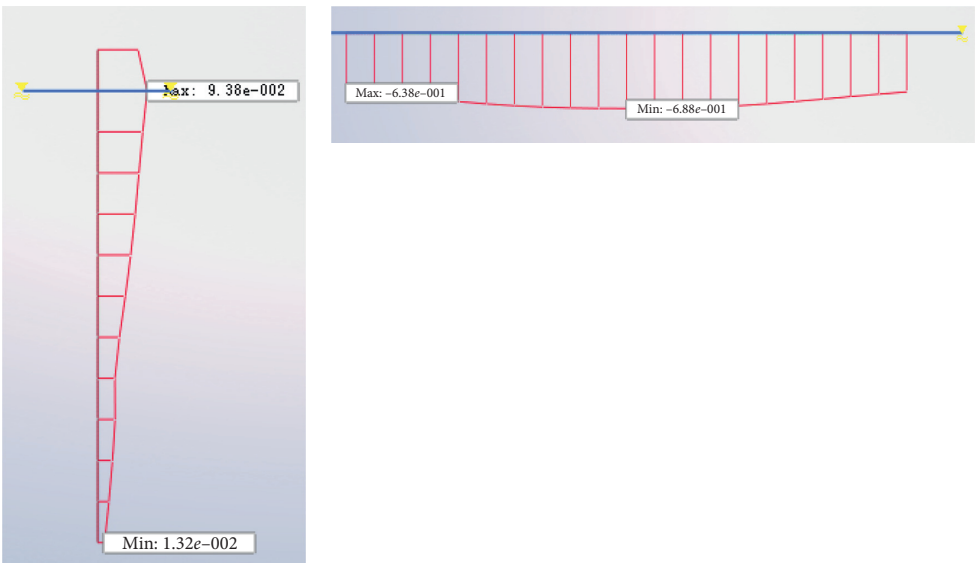

(a) (b)

Figure 7: Calculation value of displacement of drainage plate: (a) PVDs and (b) PHDs.

squeezed to the reinforced area (horizontal displacement is expressed as negative), while in the process of surcharge preloading, the trend of extrusion of soil from the reinforced area to the affected area (horizontal displacement is expressed as positive) is generated. In the early stage of vacuum preloading, the horizontal displacement in the direction of the reinforcement area increases linearly and rapidly and gradually slows down after reaching the maximum negative value. This is due to the beginning of vacuum pumping; the vacuum degree in the film increases rapidly; and the vacuum suction makes the soil in the influence area move to the reinforced area. Then, with the discharge of pore water, the effective stress of the upper soil increases, and the upper soil exerts pressure on the lower soil, resulting in a gradual decrease in the horizontal displacement. With the increase of surcharge preloading, the soil further slows down the lateral shrinkage deformation of soil under vacuum pressure and gradually produces lateral expansion deformation. The soil moves from the reinforcement area to the influence area.

Figure 10 is the relationship curve between horizontal displacement and depth of soil on the boundary between reinforcement area and influence area with two different drainage structures. From the surface to the bottom of the first layer of soil, the horizontal displacement gradually increases and reaches the maximum value. Then, as the reinforcement depth increases, the horizontal displacement of the soil gradually decreases, indicating that the horizontal displacement of the soil on the soft soil surface is large and is greatly affected by the drainage preloading. The deeper the depth, the less affected. In addition, the abrupt change position of the slope of the relationship curve is the junction between the soil layers, indicating that the horizontal displacement of the soil is greatly affected by the properties of the soil layer.

3.3. Calculation and Analysis of Pore Water Pressure. Figure 11 is the cloud diagram of pore water pressure calculation of vacuum combined surcharge preloading with

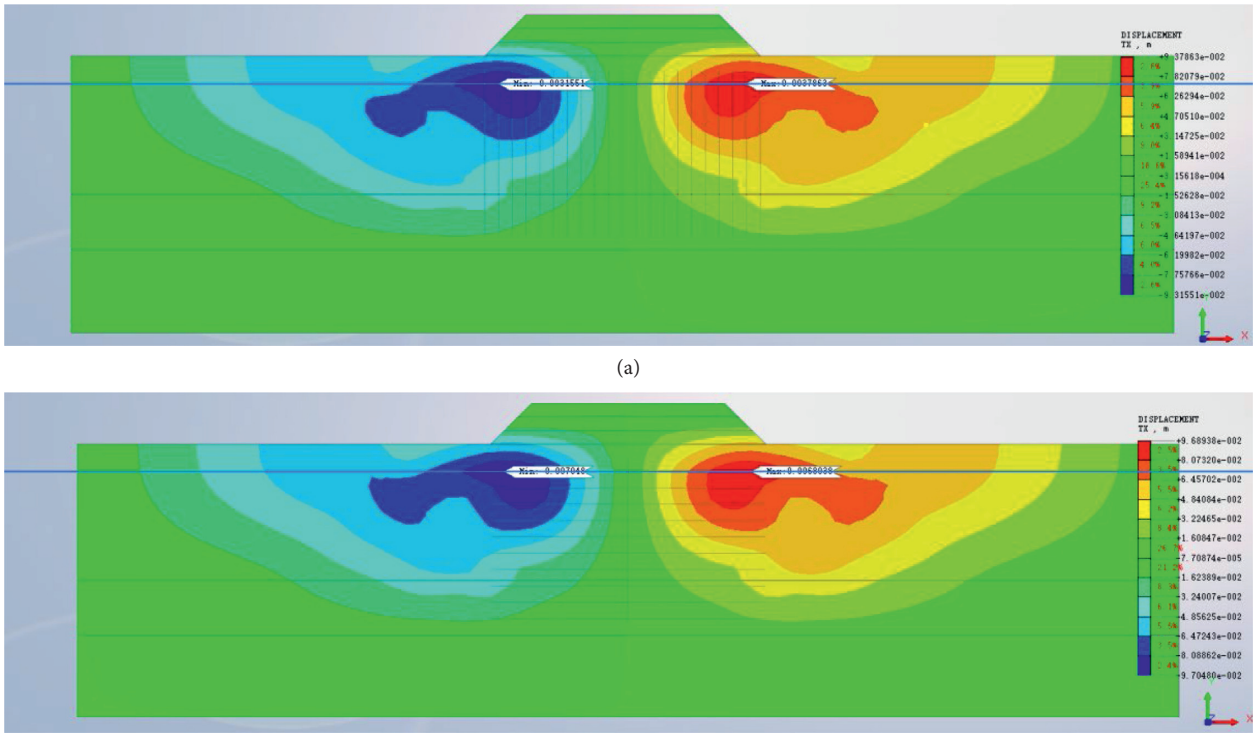

Figure 8: Cloud chart of horizontal displacement calculation: (a) PVDs and (b) PHDs.

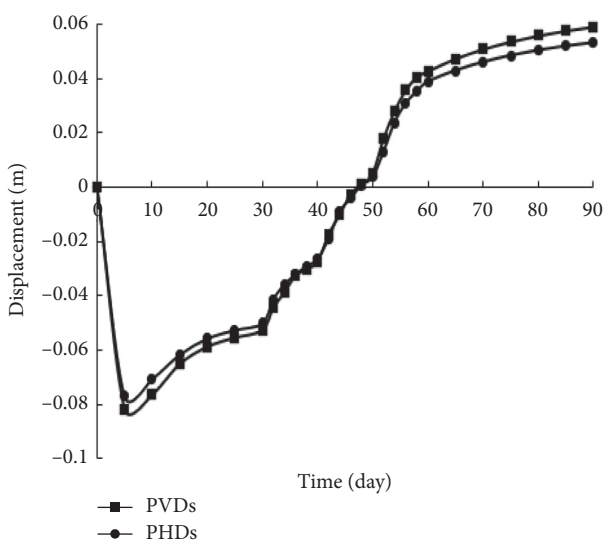

Figure 9: Relationship curve between horizontal displacement and time.

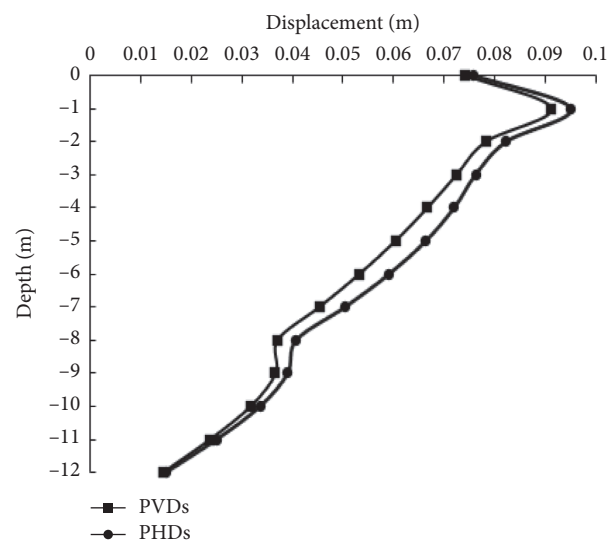

Figure 10: Relationship curve between horizontal displacement and depth.

two different drainage plates. It can be seen from the diagram that the pore water pressure considering the well resistance effect decreases with the increase of depth in the reinforcement area. The change curve is consistent with the function added when defining the node head. In addition, within the depth range of the drainage board, the pore water pressure is obviously affected by the vacuum load, which also has a certain impact on the pore water pressure below the drainage board and in the influence area. The contour line of the pore water pressure of the soil with PHDs is more gentle, indicating that the influence of the PHVs on the pore water pressure of the soil in the affected area is greater than that of the PVDs.

The surface center node of the reinforced area is analyzed, as shown in Figure 12. In the early stage of vacuum preloading, the pore water pressure rapidly dissipates and

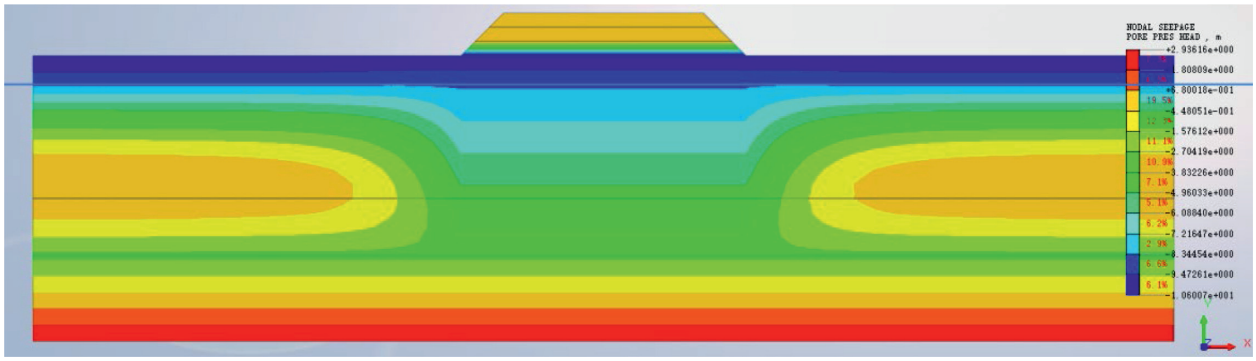

(a)

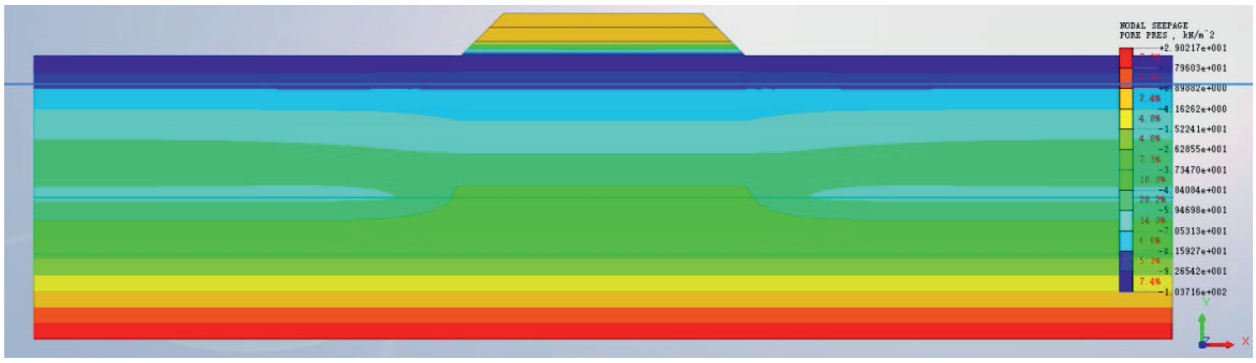

(b)

Figure 11: Calculation cloud chart of pore water pressure: (a) PVDs and (b) PHDs.

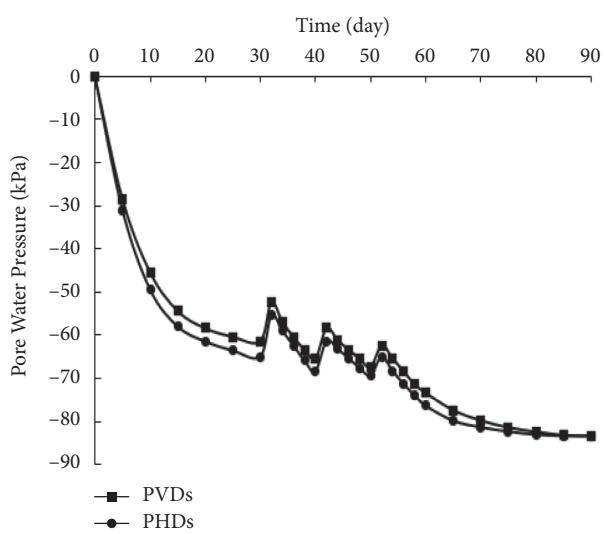

Figure 12: Relationship curve between pore water pressure and time.

then gradually slows down under the effect of vacuum negative pressure but still maintains the dissipation trend. Then when surcharge preloading starts, each level of preloading causes the pore pressure to increase suddenly and then dissipate gently. After the surcharge preloading is over, the pore pressure still slowly dissipates until it reaches about −85 kPa and then tends to be flat. In addition, the diagram shows that the dissipation rate of pore water pressure in the soil layer with PHDs is faster than that with PVDs, and the pore pressure value reaches coincidence in the final stage. This is because the bending deformation of the PHDs is small, and the drainage effect is better. The spacing of the PHDs is gradually reduced in the consolidation process; the drainage path is shortened; and the drainage efficiency is higher, so the pore pressure dissipation is faster. In the final stage, since the vacuum negative pressure set by the node head value of the model is the same, the pore water pressure of the last two is consistent.

4. Conclusions

Based on the field test of the first-stage project from Xinhuicheng to Yamen of Guangzhou-Foshan River Expressway, the calculation model of vacuum combined surcharge preloading was established by MIDAS finite element software. The reinforcement effect of the horizontal drainage plate and vertical drainage plate on soft soil such as local silt under vacuum combined surcharge preloading was compared and analyzed, and the following conclusions were obtained:

(1) In the vacuum combined surcharge preloading method, the vertical settlement, horizontal displacement, and pore water pressure with two different drainage plates are analyzed. It is found that the rules of soil consolidation and deformation caused by two kinds of drainage plates are basically

the same, but in general, the consolidation effect of PHDs is better than that of PVDs.

(2) The maximum vertical settlement of vacuum combined surcharge preloading with PHDs is 742 mm, which are 50 mm larger than that with PVDs, and the pore water pressure dissipates faster. This is because the spacing of PHDs decreases gradually in the consolidation process, the drainage path is shortened, the drainage efficiency is higher, and the settlement is larger. The maximum horizontal displacement of vacuum combined surcharge preloading with PHDs is larger than that with PVDs, which is 96.8 mm and 93.8 mm, respectively. The difference between the two is 3 mm, and the difference is not large.

(3) The force and deformation of the two drainage plates are analyzed. It is found that the maximum displacement difference of PHDs is 50 mm, and the maximum displacement difference of PVDs is 80 mm, that is, the deformation of PHDs is smaller than that of the PVDs. This leads to PVDs appearing to one side of the obvious bending; the distance between the drainage plate is farther and farther; drainage path lengthening and consolidation drainage more difficult; and PHDs can move down uniformly with the soil during the consolidation process. The drainage plate has a small bending deformation, which makes the vacuum transfer more uniform and effective.

Data Availability

The data used to support the findings of this study are available from the corresponding author upon request.

Conflicts of Interest

The authors declare that they have no conflicts of interest regarding the publication of this paper.

Acknowledgments

The authors would gratefully like to acknowledge the support provided by the National Natural Science Foundation of China (no. 51978177). The editorial help from Professor Galen Leonhardy of Black Hawk College is also greatly appreciated.

References

[1] Y. Tang, D. Jiao, and Y. Yang, "Experimental study on strengthening soft foundation by vacuum combined surcharge preloading," *Port engineering*, vol. 1986, no. 06, pp. 4–15, 1986.

[2] shizuo Shang, "Experimental study on vacuum combined surcharge preloading in a loading and unloading area in shanghai," *Port & Waterway Engineering*, vol. 1986, no. 03, pp. 1–08, 1988.

[3] B. Bai, D. Rao, T. Chang, and Z. Guo, "A nonlinear attachment-detachment model with adsorption hysteresis for suspension-colloidal transport in porous media," *Journal of Hydrology*, vol. 578, p. 124080, 2019.

[4] B. Bai, R. Zhou, G. Cai, W. Hu, and G. Yang, "Coupled thermo-hydro-mechanical mechanism in view of the soil particle rearrangement of granular thermodynamics," *Computers and Geotechnics*, vol. 137, p. 104272, 2021.

[5] K. Meng, C. Cui, Z. Liang, H. Li, and H. Pei, "A new approach for longitudinal vibration of a large-diameter floating pipe pile in visco-elastic soil considering the three-dimensional wave effects," *Computers and Geotechnics*, vol. 128, p. 103840, 2020.

[6] C. Cui, K. Meng, C. Xu, Z. Liang, H. Li, and H. Pei, "Analytical solution for longitudinal vibration of a floating pile in saturated porous media based on a fictitious saturated soil pile model," *Computers and Geotechnics*, vol. 131, p. 103942, 2021.

[7] B. Yuan, Z. Li, Z. Su, Q. Luo, M. Chen, and Z. Zhao, "Sensitivity of multistage fill slope based on finite element model," *Advances in Civil Engineering*, vol. 2021, pp. 1–13, 2021.

[8] B. Yuan, Z. Li, Z. Zhao, H. Ni, Z. Su, and Z. Li, "Experimental study of displacement field of layered soils surrounding laterally loaded pile based on transparent soil," *Journal of Soils and Sediments*, vol. 21, no. 9, pp. 3072–3083, 2021.

[9] B. Yuan, Z. Li, Y. Chen et al., "Mechanical and microstructural properties of recycling granite residual soil reinforced with glass fiber and liquid-modified polyvinyl alcohol polymer," *Chemosphere*, vol. 286, p. 131652, 2022.

[10] L. Yan and J. Yin, "Control of loading rate of vacuum combined surcharge preloading," *Highways*, vol. 2006, no. 08, pp. 287–290, 2006.

[11] X.-q. Yuan, Q. Wang, W.-x. Lu, W. Zhang, H.-e. Chen, and Y. Zhang, "Indoor simulation test of step vacuum preloading for high-clay content dredger fill," *Marine Georesources & Geotechnology*, vol. 36, no. 1, pp. 83–90, 2018.

[12] Y. Lu, J. Chai, and W.-Q. Ding, "Predicting deformation of PVD improved deposit under vacuum and surcharge loads," *Geotextiles and Geomembranes*, vol. 48, no. 1, pp. 32–40, 2020.

[13] X. Jin, J. Yu, X. Gong, D. Huang, and leixia Yang, "Experimental study on Vacuum Combined Surcharge Preloading reinforcement of soft foundation with confined water," *Chinese Journal of Geotechnical Engineering*, vol. 2007, no. 05, pp. 789–794, 2007.

[14] X. Li, hang Zhou, H. Liu, and xuanming Ding, "Model test study on consolidation of alluvial fill foundation by air bag pressurization combined with surcharge," *Chinese Journal of Rock Mechanics and Engineering*, vol. 39, no. S1, pp. 3085–3094, 2020.

[15] H. Lei, P. Wang, L. Xu, and L. Wang, "Analysis of reinforcement mechanism of pressurized vacuum preloading method based on gas migration law," *Rock and Soil Mechanics*, vol. 42, no. 4, pp. 943–953, 2021.

[16] Y. Wang and J. Wang, "Clogging mechanism of high moisture content dredged sludge drainage plate filter membrane," *Port & Waterway Engineering*, vol. 2015, no. 03, pp. 6–11, 2015.

[17] P. Chen, Z. Dong, and G. Zhang, "Formation mechanism and numerical analysis of "soil pile" in shallow surface reinforcement of new hydraulic fill sludge," *Port & Waterway Engineering*, vol. 2015, no. 02, pp. 88–94, 2015.

[18] G. Mei, K. Xu, Z. Jinmin, and Z. Yin, "Discussion on deformation mechanism of soft soil foundation strengthened by vacuum preloading," *Chinese Journal of Geotechnical Engineering*, vol. 28, no. 9, pp. 1168–1172, 2006.

[19] B. Indraratna, C. Bamunawita, and H. Khabbaz, "Numerical modeling of vacuum preloading and field applications," *Canadian Geotechnical Journal*, vol. 41, no. 6, pp. 1098–1110, 2004.

[20] J. C. Chai, J. P. Carter, and S. Hayashi, "Ground deformation induced by vacuum consolidation," *Journal of Geotechnical and Geoenvironmental Engineering*, vol. 131, no. 12, pp. 1552–1561, 2005.

[21] M. Tang and J. Q. Shang, "Vacuum preloading consolidation of Yaoqiang Airport runway," *Géotechnique*, vol. 50, no. 6, 2000.

[22] J.-C. Chai, J. P. Carter, and S. Hayashi, "Vacuum consolidation and its combination with embankment loading," *Canadian Geotechnical Journal*, vol. 43, no. 10, pp. 985–996, 2006.

[23] S. L. Lee, G. P. Karunaratne, K. Y. Yong, and V. Ganeshan, "Layered clay-sand scheme of land reclamation," *Journal of Geotechnical Engineering*, vol. 113, no. 9, pp. 984–995, 1987.

[24] J. Xiusan, H. Shangcai, J. Bingri, and J. Zhengji, "The effects of negative pressure and drain spacing in the horizontal method for an early settlement of dredged and filled grounds," *Journal of Korean Society of Coastal and Ocean Engineers*, vol. 15, no. 1, 2003.

[25] L. H. Li, Q. Wang, N. X. Wang, and J. P. Wang, "Vacuum dewatering and horizontal drainage blankets: a method for layered soil reclamation," *Bulletin of Engineering Geology and the Environment*, vol. 68, no. 2, pp. 277–285, 2009.

[26] S. Bao, Z. Dong, H. Mo, and P. Chen, "Field research and development of vacuum consolidation drainage system for recently dredged silt foundation," *Chinese Journal of Rock Mechanics and Engineering*, vol. 33, no. S2, pp. 4218–4226, 2014.

[27] Pukhov, Y. Pan, and D. Khoteja, "Model experimental study on treatment of high moisture content dredged sludge by flocculation horizontal vacuum two-stage dewatering method," *Rock and Soil Mechanics*, vol. 41, no. 5, pp. 1502–1509, 2020.

[28] J. Lin, S. Bao, and B. Zhang, "Analysis on main influencing factors of vacuum preloading reinforcement effect of recently dredged silt foundation," *Port & Waterway Engineering*, vol. 2015, no. 12, pp. 138–143, 2015.

[29] W. Zhang, X. Wang, J. Xie, B. Pan, J. Chen, H. Zhao et al., "Experimental study on treatment of hydraulic fill flow mud by vacuum preloading of horizontal drainage plate," *Port & Waterway Engineering*, vol. 2016, no. 07, pp. 122–127, 2016.

[30] Y. Zhou, Pukhov, Z. Li, Y. Pan, and D. Song, "Model experimental study on combined treatment of high moisture content dredged sludge with horizontal drain board and vacuum preloading," *Chinese Journal of Rock Mechanics and Engineering*, vol. 38, no. S1, pp. 3246–3251, 2019.

[31] L. Wang, Q. Chen, S. Liu, and Y. Fu, "Model test of soft clay treated by vacuum preloading combined with electroosmosis of horizontal drainage plate," *Chinese Journal of Rock Mechanics and Engineering*, vol. 39, no. S2, pp. 3516–3525, 2020.

[32] S. Hansbo, "Consolidation of clay by band-shaped prefabricated drains," *International Journal of Rock Mechanics and Mining Science & Geomechanics Abstracts*, vol. 12, no. 5, pp. 16–25, 1979.

[33] W. Zhao, Y. Chen, and Y. Gong, "Treatment method of sand well in plane strain finite element analysi," *Journal of Hydraulic Engineering*, vol. 1998, no. 06, pp. 54–58, 1998.

Hindawi
Advances in Civil Engineering
Volume 2021, Article ID 2255518, 10 pages
https://doi.org/10.1155/2021/2255518

Review Article

Dynamic Response of the Entrance Structure of an Elliptical Mountain Tunnel under the Action of SH Waves

Zhenyu Wang,[1,2] **Junsheng Yang**,[1] **and Xinghua Wang**[1]

[1]*Central South University, Changsha 410075, China*
[2]*Hunan University of Finance and Economics, ChangSha 410027, China*

Correspondence should be addressed to Zhenyu Wang; adiwangzy@qq.com

Received 21 September 2021; Accepted 27 October 2021; Published 24 November 2021

Academic Editor: Yu Liang

Generally, the surrounding rock at the entrance of a mountain tunnel is loose, and the entrance has more slopes due to topography, which causes the tunnel entrance section to be easily destroyed under an earthquake. Based on the established slope model with a single free surface, this paper adopted the elastic wave theory to derive the analytical solution of the strain at the entrance of the mountain tunnel when the SH wave is incident perpendicularly to the bottom of the tunnel; besides, the factors affecting strain were also analyzed. The tangential strain curve at each point of the entrance section takes the centre of the elliptical tunnel as the centre of symmetry, forming symmetry between the left and right sides and mirror symmetry between the top and bottom sides. Then, large-scale shaking table model experiments were conducted to model the actual working conditions, and the correctness of the analytical solution was verified. The research can provide a theoretical reference for the seismic design of the entrance section of the high-speed railway tunnel and greatly improve the understanding of its seismic response.

1. Introduction

In China, the mountainous area accounts for more than 60%, and most mountainous areas (such as the Qinghai-Tibet Plateau) are in the contact zone of the Eurasian Plate and the Indian Plate, where exists frequent seismic activity. With the continuous development of Chinese western development strategy, high-speed railways are also designed and constructed in this area; simultaneously, the anti-seismic problem of high-speed railway tunnels has attracted increasing attention. Moreover, the entrance section of the tunnel is an essential part of the tunnel and is prone to damage, making the entire tunnel unusable under the action of an earthquake. Due to the unique nature of high-speed railways, the tunnel is usually designed as a double-track single-hole similar to ellipse, with a relatively large span and a relatively large cross-sectional area, making the tunnel's entrance section more susceptible to earthquakes [1–5]. The method of studying the dynamic response of the tunnel entrance section includes theoretical analysis, numerical simulation, and shaking table model experiment. At present, researchers mainly adopt numerical simulation and shaking table model experiments, and the main research content is about the measures and effectiveness of anti-earthquake. During the research, the dynamic response of the entrance of the tunnel with a single cross-sectional structure is mainly considered, but the integrity of the tunnel and the three-dimensionality of the wave propagation are ignored [6–8]. The authors in [9, 10] only studied the dynamic response characteristics of the entrance section of the lower circular mountain tunnel under the effect of the SH wave and used the elliptical tunnel model to conduct shaking table tests to verify the analytical solution. The most significant difference between the tunnel entrance section and the tunnel body is that the tunnel entrance section has a free surface, while the tunnel body section can be regarded as a structure without an open surface. Based on the wave theory and the characteristics of the open surface at the tunnel entrance, the reflected wave was superimposed on the central axis of the tunnel to form a complex wave field, which makes the tunnel structure more complicated [11–18].

In this paper, the model of the entrance section of the mountain tunnel was simplified to a simple slope with a single surface, and it is believed that the structure of the tunnel does not affect wave propagation. Using the elastic wave propagation theory, when the SH wave was incident perpendicularly from the bottom of the tunnel, the dynamic stress along the axis of the elliptical mountain tunnel was derived. Then, the elliptical tunnel structure was regarded as a three-dimensional thin-walled shell to derive the analytical solution of the displacement of the tunnel structure under the action of SH wave. Finally, the shaking table model of the mountainous elliptical tunnel was conducted to verify the previous theoretically analyzed results and to summarize the deformation mechanism of the entrance section of the elliptical mountain tunnel.

2. Theoretical Derivation

To analyze the dynamic response of the entrance section of the elliptical mountain tunnel, it is first assumed that when the SH wave is incident perpendicularly from the bottom of the mountain, there is only the effect of the reflection of SH wave from the slope of the mountain, and the generated stress field at the axial of the tunnel is calculated. Then, while simplifying the tunnel into a three-dimensional thin-walled shell structure, the interaction between the surrounding rock and the tunnel is ignored to solve the displacement distribution of the tunnel structure under the action of the stress field.

2.1. Basic Assumptions. In the theoretical derivation process, the following assumptions are made:

(1) The ratio between the size of the surrounding rock mass and the size of the tunnel structure is so large that the influence of the existence of the tunnel structure on the dynamic response of the surrounding rock can be ignored.

(2) The link between the surrounding rock and the structure is tight, and there is no mutual displacement.

(3) The approximately elliptical tunnel of the high-speed railway is simplified to a standard elliptical structure.

(4) All structures are assumed to be a uniform elastic body.

2.2. Analytical Solution of Axial Displacement of Elliptical Model Tunnel. Figure 1 shows a single-sided slope model. According to the wave propagation theory, it can be known that SH waves are incident perpendicularly from the bottom, travel along O1B to point B on the slope, and then are reflected; the reflected waves propagated along BA to point A, where it superimposed with the incident SH wave that directly travels along O2A (Figure 2). According to the wave propagation theory, the reflection angle (α) of the SH wave is equal to the slope angle (α) of a single-sided slope, the speed of the incident wave is equal to the reflected wave, and their amplitudes are equal [19].

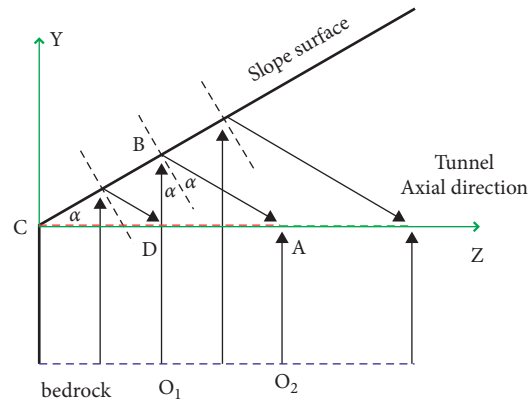

Figure 1: SH wave propagation model.

The function of the displacement of the incident wave is supposed to be

$$u_x = A \times \sin\left[\frac{2\pi}{L}\left(y - v_s t\right)\right], \tag{1}$$

where A is the amplitude, L is the wavelength, and Vs is the shear wave velocity. If a single-sided slope is regarded as a free boundary, the function of the reflected wave displacement is

$$u_x = A \times \sin\left[\frac{2\pi}{L}\left(z\prime - v_s t'\right)\right], \tag{2}$$

where $t' = t - t0$, in which $t0$ is the time when SH wave propagates from point D to point A through the slope reflection (see Figure 1).

In Figure 2, the origin of the coordinates is point C, the coordinate of point A is (0, Z), and the delayed time of the reflected wave reaching point A is

$$t_0 = \frac{Z \sin(2\alpha)}{v_s}. \tag{3}$$

According to the research of Kuesel [20], the SH wave reflected by the mountain slope is equivalent to the following two waves.

The SH wave propagating along the tunnel axis (Z direction) has a wavelength of $L/\cos(\pi/2 - 2\alpha)$, a wave speed of $v_s/\cos(\pi/2 - 2\alpha)$, and an amplitude of A. The SH wave propagating in the cross-sectional direction (Y direction) has a wavelength of $L/\sin(\pi/2 - 2\alpha)$, a wave speed of $vs/\sin(\pi/2 - 2\alpha)$, and an amplitude of A. Therefore, the wavefield at point A is the superposition of the above three waves (incident SH wave, SH wave propagating in the directions of axial, and cross section).

2.2.1. The Strain of Tunnel Structure While Superimposing the Wavefield. To solve the dynamic response of the tunnel structure, the tunnel is simplified as a thin-walled elliptical cylindrical shell, as shown in Figure 3. Because the thickness of the cross section of the thin-walled elliptic cylindrical shell is very small, only three strains of the structure, including axial strain, hoop strain, and tangential strain, need to be considered.

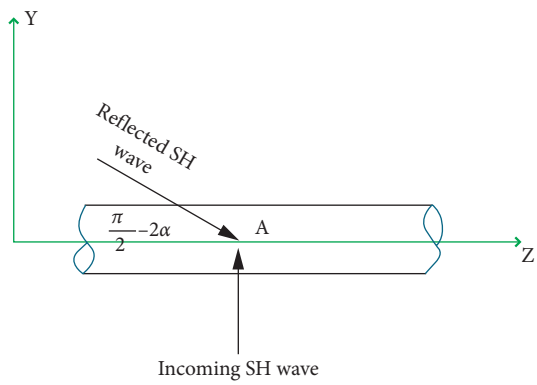

Figure 2: The illustration of the superposition of axial displacement at A point.

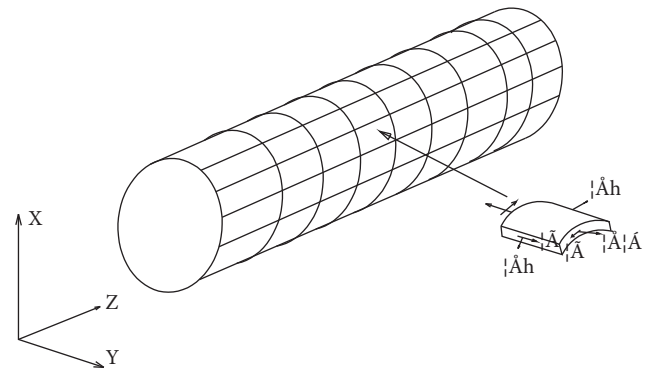

Figure 3: Tunnel lining strain of thin-walled elliptical cylindrical shell.

The calculation formulas of axial strain, hoop strain, and tangential strain are, respectively,

$$\varepsilon_\alpha = \varepsilon_z = \frac{\partial u_z}{\partial z}, \tag{4}$$

$$\varepsilon_h = \varepsilon_{\theta\theta} = \frac{1}{r(\theta)}\frac{\partial u_\theta}{\partial \theta} + \frac{u_{r\theta}}{r(\theta)}, \tag{5}$$

$$\gamma = \gamma_{\theta z} = \frac{1}{r(\theta)}\frac{\partial u_\theta}{\partial \theta} + \frac{\partial u_\theta}{\partial z}. \tag{6}$$

In the cylindrical coordinate system, the elliptic equation is

$$\frac{r^2(\theta)\sin^2\theta}{a^2} + \frac{r^2(\theta)\cos^2\theta}{b^2} = 1,$$
$$r(\theta) = \frac{ab}{\sqrt{b^2\sin^2\theta + a^2\cos^2\theta}}, \tag{7}$$

where $r(\theta)$ is the radius of the ellipse, $2a$ and $2b$ are the long and short axes of the elliptical tunnel, respectively, and uz, $u\theta$, and ur are the components of displacement induced by the shear wave in the cylindrical coordinate system.

Therefore, under the impact of the superimposed displacement field, the total strain of the tunnel structure is equal to the superposition of the strain generated by each wave alone. At point A of the tunnel structure, the strain caused by the three waves is calculated as follows.

In the elliptic cylindrical coordinate system shown in Figure 4, the coordinates of point X of the double-track single-hole structure of the high-speed railway are

$$\frac{x^2(\theta)}{a^2} + \frac{y^2(\theta)}{b^2} = 1,$$
$$\frac{x(\theta)'x(\theta)}{a^2} + \frac{y(\theta)'y(\theta)}{b^2} = 0, \tag{8}$$

where $(`x(\theta), `y(\theta)) \perp (x(\theta)/a^2, y(\theta)/b^2)$.

$$(`x(\theta), `y(\theta))\left(\frac{y(\theta)}{b^2}, -\frac{x(\theta)}{a^2}\right)(\text{mark as } \overrightarrow{1}), \tag{9}$$

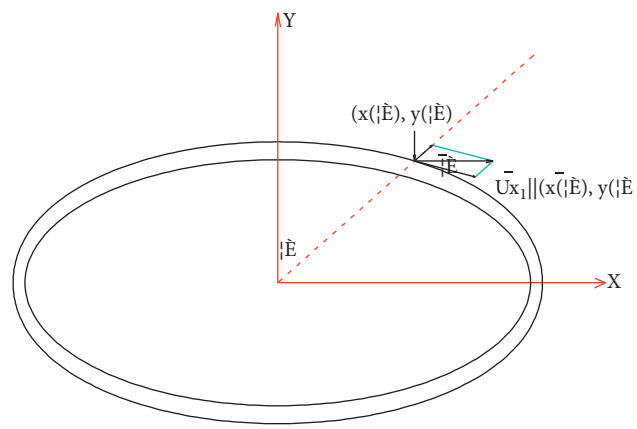

Figure 4: Figure ellip[[parms resize(1),pos(50,50),size(200,200),bgcol(156)]]ical cylindrical coordinates.

and therefore

$$\cos\tilde{\theta} = \frac{a\cos\theta}{\sqrt{b^2\sin^2\theta + a^2\cos^2\theta}},$$
$$\sin\tilde{\theta} = \frac{b\sin\theta}{\sqrt{b^2\sin^2\theta + a^2\cos^2\theta}}. \tag{10}$$

(1) Reflected SH Wave Propagating along the Tunnel Axis (Z Direction). The propagation of the reflected SH wave along the Z direction in the XOZ plane is reflected by the displacement of the surrounding rock:

$$u_x = A \times \sin\left[\frac{2\pi}{L/\cos(\pi/2 - 2\alpha)}\left(z - \frac{v_s t_1'}{\cos(\pi/2 - 2\alpha)}\right)\right]. \tag{11}$$

According to the cylindrical coordinate system in Figure 4, the tunnel displacement can be decomposed into the tangential and radial displacement, and the corresponding functions are

$$u_x = A \times \sin\left[\frac{2\pi}{L/\cos(\pi/2 - 2\alpha)}\left(z - \frac{v_s t_1'}{\cos(\pi/2 - 2\alpha)}\right)\right], \tag{12}$$

$$u_\theta = A\frac{a\cos\theta}{\sqrt{b^2\sin^2\theta + a^2\cos^2\theta}}\sin \cdot \left[\frac{2\pi}{L/\cos(\pi/2 - 2\alpha)}\left(z - \frac{v_s t'}{\cos(\pi/2 - 2\alpha)}\right)\right]. \tag{13}$$

By substituting formulas (12) and (13) into formulas (2)~(4), the strain expression can be sorted and obtained as

$$\left.\begin{aligned} \varepsilon_h = \varepsilon_\theta &= A \times A_1 \times A_2 \sin\left[A_3\left(Z - \frac{v_s t'}{A_4}\right)\right], \\ \gamma &= A \times A_5 \times A_3 \cos\left[A_3\left(z - \frac{v_s t'}{A_2}\right)\right], \\ \varepsilon_\alpha &= 0, \end{aligned}\right\} \tag{14}$$

where

$$\begin{aligned} A_1 &= \frac{1}{(ab)}, \\ A_2 &= \frac{\sin\theta\left(b^3\sin^2\theta + a^2 b\cos^2\theta - ab^2\right)}{b^2\sin^2\theta + a^2\cos^2\theta}, \\ A_3 &= \frac{2\pi}{L/\cos(\pi/2 - 2\alpha)}, \\ A_4 &= \cos\left(\frac{\pi}{2} - 2\alpha\right), \\ A_5 &= \frac{a\cos\theta}{\sqrt{b^2\sin^2\theta + a^2\cos^2\theta}}. \end{aligned} \tag{15}$$

(2) Reflected SH Wave Propagating in the Y Direction. The displacement function corresponding to the reflected SH wave propagating in the Y direction is

$$u_x = A \times \sin\left[\frac{2\pi}{L/\sin(\pi/2 - 2\alpha)}\left(-y - \frac{v_s t'}{\sin(\pi/2 - 2\alpha)}\right)\right]. \tag{16}$$

Similarly, the function of the tangential and radial displacement can be, respectively, obtained:

$$u_r = A\frac{b\sin\theta}{\sqrt{b^2\sin^2\theta + a^2\cos^2\theta}} \cdot \sin\left[\frac{2\pi}{L/\sin(\pi/2 - 2\alpha)}\left(-y - \frac{v_s t'}{\sin(\pi/2 - 2\alpha)}\right)\right], \tag{17}$$

$$u_\theta = A\frac{a\cos\theta}{\sqrt{b^2\sin^2\theta + a^2\cos^2\theta}} \cdot \sin\left[\frac{2\pi}{L/\sin(\pi/2 - 2\alpha)}\left(-y - \frac{v_s t'}{\sin(\pi/2 - 2\alpha)}\right)\right]. \tag{18}$$

By substituting formulas (17) and (18) into formulas (2)~(4), the strain expression can be sorted and obtained as

$$\begin{aligned} \varepsilon_h = \varepsilon_\theta = A \times A_1 \Bigg\{ & A_6 A_7 \cos\left[A_7\left(-y - \frac{v_s t_1'}{A_8}\right)\right] \\ & + A_2 \sin\left[A_7\left(-y - \frac{v_s t_1'}{A_8}\right)\right]\gamma = \varepsilon_\alpha = 0\Bigg\}, \end{aligned} \tag{19}$$

where

$$\begin{aligned} A_6 &= \frac{a^2 b^3 \sin\theta\cos\theta}{\left(b^2\sin^2\theta + a^2\cos^2\theta\right)^{3/2}}, \\ A_7 &= \frac{2\pi}{L/\sin(\pi/2 - 2\alpha)}, \\ A_8 &= \sin\left(\frac{\pi}{2} - 2\alpha\right). \end{aligned} \tag{20}$$

(3) Incident SH Wave Propagating in the Y Direction. The displacement function corresponding to the incident SH wave propagating in the Y direction is

$$u_x = A \times \sin\left[\frac{2\pi}{L}(y - v_s t)\right]. \tag{21}$$

After decomposing the displacement function of the wave along with the tangential and radial directions, their functions can be obtained as

$$u_r = A\frac{b\sin\theta}{\sqrt{b^2\sin^2\theta + a^2\cos^2\theta}}\sin\left[\frac{2\pi}{L}(y - v_s t)\right], \tag{22}$$

$$u_\theta = A\frac{a\cos\theta}{\sqrt{b^2\sin^2\theta + a^2\cos^2\theta}}\sin\left[\frac{2\pi}{L}(y - v_s t)\right]. \tag{23}$$

By substituting formulas (22) and (23) into formulas (2) to (4), the strain expression can be sorted and obtained as

$$\left.\begin{aligned} \varepsilon_h &= A_1\{A_2\sin[A_9(y - v_s t)] - A_9 A_6\cos[A_9(y - v_s t)]\}, \\ \gamma &= \varepsilon = 0, \end{aligned}\right\} \tag{24}$$

where

$$A_9 = \frac{2\pi}{L}. \tag{25}$$

After superimposing the tunnel structure strain caused by the above three SH waves and eliminating the time term t', the total strain of the tunnel structure can be obtained:

$$\begin{aligned}
&\varepsilon_\alpha = 0,\\
&\gamma = A \times A_5 \times A_3 \cos\left[A_3\left(2z - \frac{v_s t}{A_4}\right)\right],\\
&\varepsilon_h = A_1\left(A_2\left\{\sin\left[A_3\left(2Z - \frac{v_s t}{A_4}\right)\right] + \sin\left[A_7\left(ztg2\alpha - y - \frac{v_s t}{A_8}\right)\right] + \sin\left[A_9\left(y - v_s t\right)\right]\right\},\right.\\
&\quad\left. + A_6\left\{B_3 \cos\left[A_7\left(ztg2\alpha - y - \frac{v_s t}{A_8}\right)\right] - A_9 \cos\left[A_9\left(y - v_s t\right)\right]\right\}\right).
\end{aligned} \tag{26}$$

It can be seen from formula (26) that under the action of the SH wave incident vertically at the bottom, the axial strain of the tunnel structure is 0, the hoop strain is generated by the SH wave propagating along the Y-axis (parallel cross section), and the tangential strain is generated by SH waves propagating in the Z-axis direction (axial direction). The above three equations are the expressions of the total strain of the entrance section of the elliptical mountain tunnel. When the tunnel structure is a circle, which means the long and short axes are equal, formula (26) will degenerate into the form in literature [9].

3. Analysis of the Influencing Factors of the Dynamic Response of the Entrance Section

To analyze the influence of various factors on the dynamic response of the entrance section of the mountain tunnel, firstly, the displacement function of the incident wave is assumed:

$$f(t) = A \sin(2\pi f t), \tag{27}$$

where the frequency f is 2 Hz and the amplitude A is 0.3 m. According to formulas (26) and (27), the dynamic strain of the elliptical tunnel structure can be calculated.

The parameters are as follows: the long axis of the elliptical tunnel is $2a = 11.2$ m, the short axis $2b = 8.6$ m, and the thickness is 0.48 m. The parameters of the surrounding rock and lining are shown in Table 1, and the studied scope in the axial direction of the tunnel is taken as 100m ($z = 100$ m), and the portal angle is set to 70° to facilitate comparison with the shaking table model test results.

Figure 5 shows the tangential strain curve of each position of the mountain tunnel opening section when the SH wave is incident from the bottom of the tunnel; it can be known that all the tangential strain curves are similar to a sine curve, and when the slope is 45°, the amplitude of the strain curve is the largest, which appears at the arch base and the vault, and their absolute value is equal to $\mathcal{E} = 6.283\varepsilon\mu$, but the sign is opposite. The strain at the left (right) arch waist is zero, and the tangential strain at each position of the tunnel entrance section is mirror-symmetric with the axis of the tunnel as the centre; when the slope of the mountain slope is greater than or equal to 60°, the tangential strain curve of each position of the opening section begins to reverse, and the largest absolute value of the strain still appears at the vault and arch bottom of the tunnel, but when the slope is 89°, the tangential strain at each position of the tunnel opening section is almost zero.

Figure 6 shows the relationship between the tangential strain at each position of the tunnel opening section and the slope of the mountain slope; it can be seen that when the slope is 45°, the absolute value of the tangential strain at each position of the tunnel opening section is the largest; as the slope of the slope increases, this absolute value decreases, and the tangential strain decreases to 0 at about 60°. With the continuous increase of the slope, the absolute value of the tangential strain keeps increasing and reaches the maximum when the slope is 70°. When the slope continues to increase, the absolute value of the tangential strain begins to decrease and tends to 0 when the slope is 89°. Besides, it can also be seen that the tangential strain curve at each position of the mountain tunnel entrance section is symmetrical with the centre of the elliptical tunnel as the centre; combining Figures 5 and 6, it can also be known that this tangential strain is mirror-symmetric at the top and bottom sides.

Figure 7 shows the relationship between the tangential strain at each position of the entrance section and the distance from the entrance, which further verifies the symmetry of the tangential strain curve; in the range of 100 m from the cave opening, each tangential strain curve undergone 6 times of phase inversion. Figure 8 shows the relationship between the tangential strain at the right shoulder of the tunnel entrance and the ratio of the long axis to the short axis (a/b); it can be seen that as the value of a/b increases, the tangential strain at the right shoulder of the tunnel also increases, but the increment varies with the slope of the mountain slope. Only when the slope is 45°, the strain is positive; at this time, the increment is the largest (from 4.649 $\varepsilon\mu$ to 5.620 $\varepsilon\mu$), which is followed by the slope of 70°; when the slope is 89°, the tangential strain increases from $-0.095\varepsilon\mu$ to $-0.114\varepsilon\mu$.

4. The Preparation of a Large-Scale Shaking Table Test Model

To verify the theoretical analysis result, a large-scale shaking table experiment was designed to model the on-site working condition. To objectively and truly reflect the characteristics of the prototype, a similar design is required. Other physical parameters are shown in Table 2.

Table 1: Mechanical parameters of lining and rock materials.

		Bulk density, γ (kN/m^3)	Elastic modulus, E (GPa)	Poisson's ratio
Wall rock	Soft rock	17.09	0.65	0.22
	Hard rock	22.3	31.5 (23.4 MPa)	0.23
Tunnel lining	25	29.8	0.23	

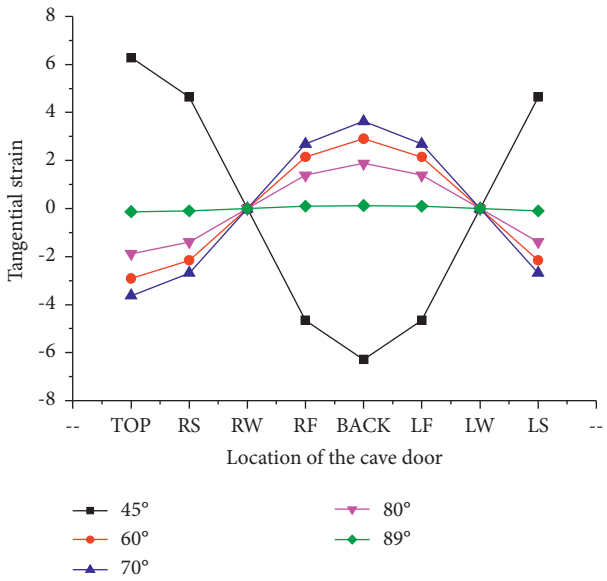

Figure 5: Tangential strain of opening section.

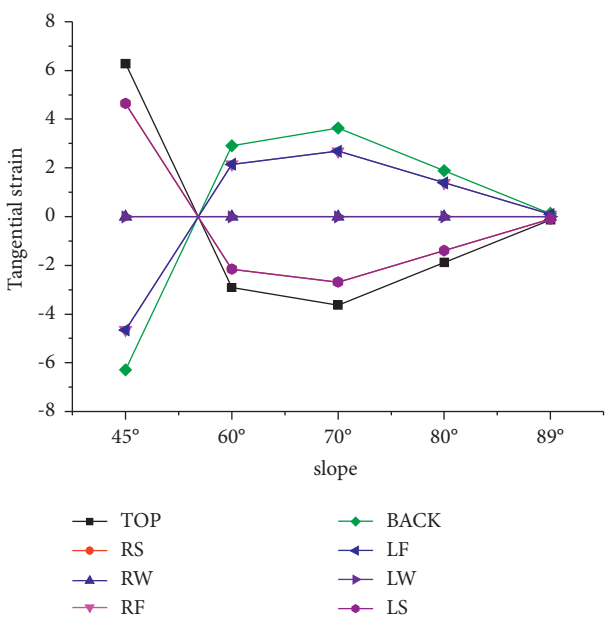

Figure 6: The influence of mountain slope.

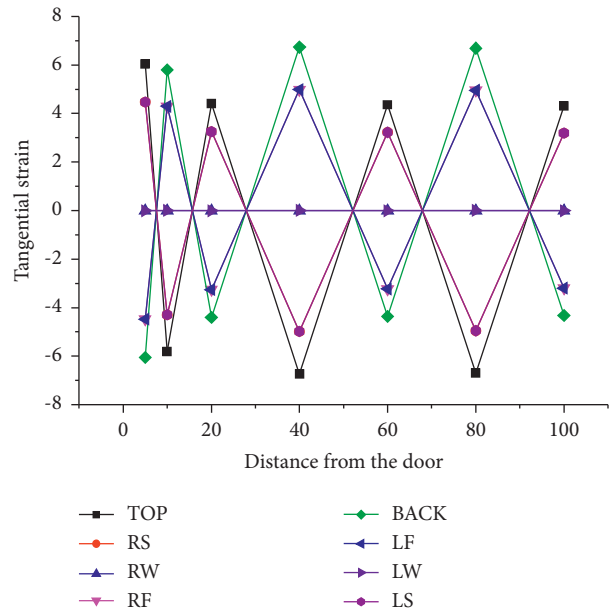

Figure 7: The influence of tunnel opening distance.

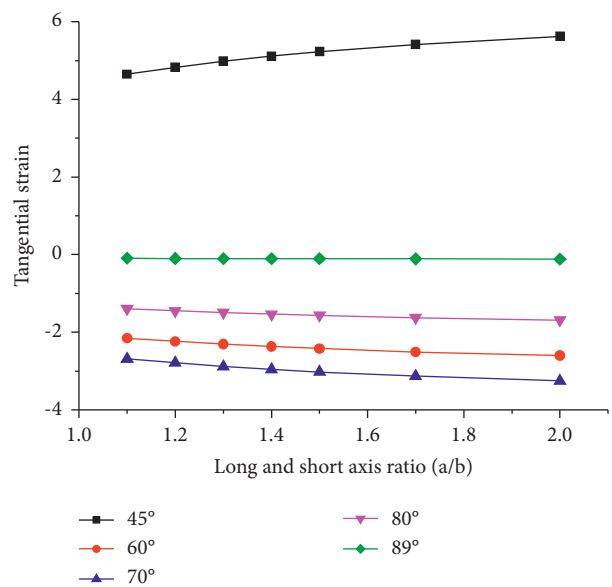

Figure 8: The influence of the long and short axes.

4.1. The Preparation of the Elliptical Tunnel Model and Monitoring Plan. As shown in Figures 9 and 10, considering the size of the vibrating table and its ultimate bearing capacity, the size of the model box is set as 9300 mm (length) × 3700 mm (width) × 2500 mm (height), and the total weight is 3.8 tons.

In the tunnel model test, along the axial direction of the tunnel, from left to the right, they are mainly arranged at the

Table 2: Physical dimension and similarity relation of model test.

Physical quantity	Dimension	Similarity ratio
Length	C_l	1/8
Mass density	$C\rho$	1/1
Elastic modulus	C_E	1/1
Time	$C_t = C_l^{1/2}$	0.353
Poisson's ratio	—	1
Stress	$C\sigma = CE\ C\varepsilon$	1
Cohesion	$C\sigma = CE\ C\varepsilon$	1
Coefficient of viscosity	$C_\gamma = C_E C_t$	0.353
Internal friction angle	—	1
Strain	$C\varepsilon$	1
Displacement	$C\mu$	0.125
Velocity	$C_v = C_l C_t^{-1}$	0.353
Acceleration	$C_\alpha = C_l C_t^{-2}$	1
Strength	$C_F = C_\gamma C_l^3$	0.0 15625
Frequency	$C_N = C_t^{-1}$	2.828
Damping coefficient	$C_\varsigma = C_\gamma C_l^2 C_t$	0.04418

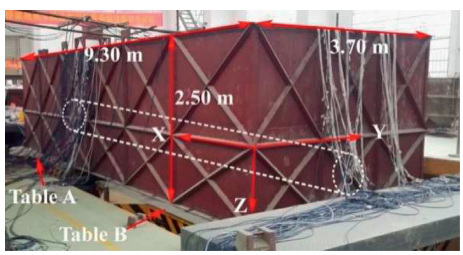

Figure 9: Outside of the model box.

Figure 10: Oval tunnel lining model.

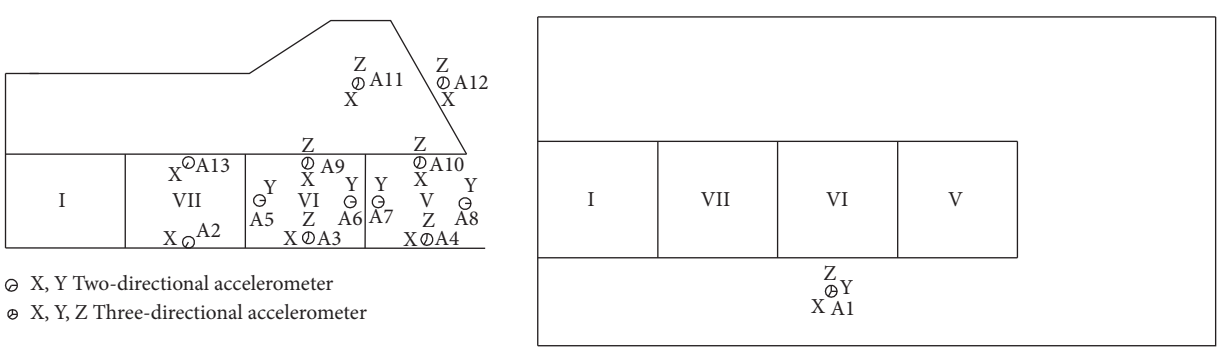

Figure 11: Schematic diagram of the longitudinal section and bottom of the elliptical tunnel opening section.

Figure 12: External view of the oval tunnel opening.

Figure 13: Oval tunnel opening map.

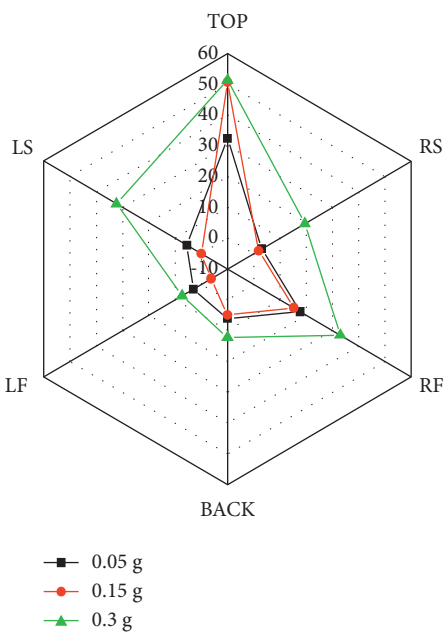

Figure 14: Circumferential strain inside the tunnel portal (4Hz).

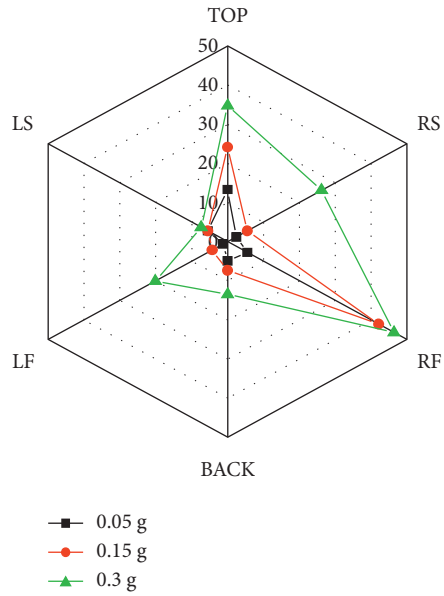

Figure 15: Circumferential strain inside the tunnel portal (7.237Hz).

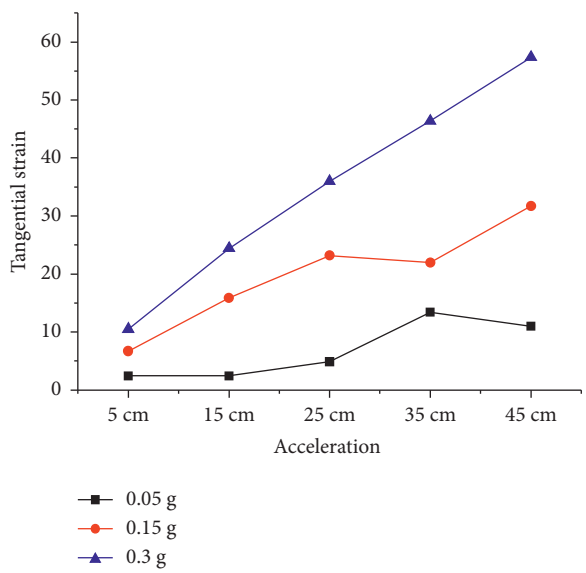

Figure 16: Longitudinal strain curve of vault exterior (6.383Hz).

positions of VII-VII, VI-VI, and IX-IX and the periphery of the tunnel, as shown in Figures 11–13.

4.2. Analysis of Model Test Results. For different seismic intensities, the strain development of the tunnel is the same. The change of the hoop strain of the tunnel entrance section is as shown in Figures 14 and 15.

It can be known that when a sinusoidal seismic wave is input, the most dangerous parts of the tunnel are the right arch foot and the vault. When the seismic frequency is 4 Hz, the maximum strain appears on the vault (acceleration is 0.3 g and strain is 51.27 $\mu\varepsilon$); when the seismic frequency is 7.237 Hz, the maximum strain appears on the right arch foot (acceleration is 0.3 g and strain is 46.39 $\mu\varepsilon$).

Figures 16 and 17 show the longitudinal strain of the tunnel vault outside when the sinusoidal seismic wave is input, and it can be seen that as the seismic acceleration increased, the strain of the tunnel also increases; this variation has nothing to do with the frequency of the input seismic wave. When the frequency of the seismic wave is relatively small (6.38 Hz), the strain of the tunnel increases with the increase of the distance from the opening; when the frequency is relatively large (13 Hz), the strain of the tunnel

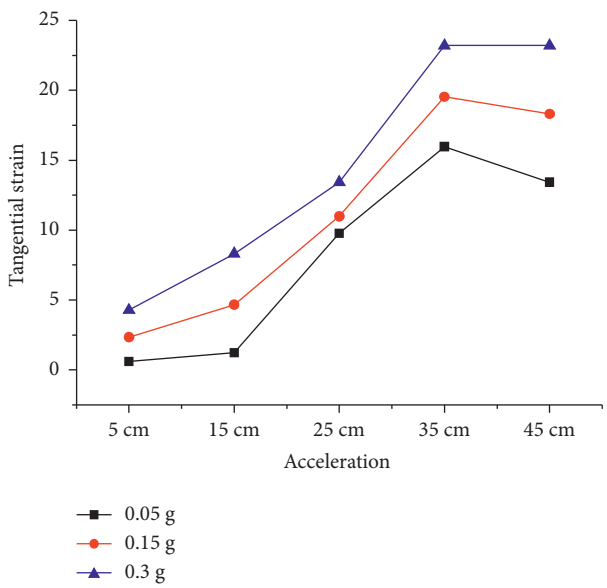

Figure 17: Longitudinal strain curve of vault exterior (13Hz).

Figure 18: Destruction diagram of the right spandrel at the entrance of the tunnel.

Figure 19: Destruction diagram of the right arch foot of the tunnel entrance section.

still increases with the increase of the distance from the opening, but the most dangerous section is 35 cm from the entrance of the cave. Under the action of the axial seismic wave, horizontal shear deformation occurs along the axial direction of the tunnel, and a large rigid displacement appears at the tunnel entrance, which makes the right shoulder and right foot easily undergo destruction (Figures 18 and 19).

The test results above preliminarily verify the theoretical analysis results.

5. Conclusions

In this paper, under the effect of the SH wave incident from the bottom of the tunnel, the strain at the entrance of the elliptical mountain tunnel was simplified and deduced theoretically; at the same time, a large-scale shaking table model test was carried out to verify the analytical results.

(1) By simplifying the slope of the mountain into a slope with a single surface, when the SH wave is incident vertically at the bottom, an analytical solution for the deformation at the entrance of the elliptical mountain tunnel is obtained. By analyzing the parameter, it is known that when the sinusoidal SH wave is input, the curve of tangential strain at the tunnel entrance section is symmetric, with the centre of the tunnel as the centre. The strain curves at the left and right of the tunnel are symmetrical, while the strain curves at the top and bottom of the tunnel are mirror-symmetrical, and their values are equal with opposite signs.

(2) Through parameter analysis, it can be confirmed that as the ratio of the long axis to the short axis of the elliptical tunnel increases, the tangential strain at the right shoulder of the tunnel portal section increases slowly, and the magnitude of the increment varies with the slope of the mountain slope. When the slope is 45°, the strain is positive, and other slopes are negative; when the slope is 45°, the increment is the largest (0.971 $\varepsilon\mu$), followed by 70°; when the slope is 89°, the tangential strain increases from −0.095 $\varepsilon\mu$ to −0.114 $\varepsilon\mu$, which only increases by 0.019 $\varepsilon\mu$.

(3) With the large-scale shaking table model, considering the seismic wave reflection effect, the rationality of the theoretical model of the single-surface slope at the tunnel entrance is verified. It is proved that when the frequency of the earthquake is different, the most dangerous position is also different. For example, when the frequency is 4 Hz, the most dangerous position is the vault (the strain is 51.27 $\mu\varepsilon$ and the acceleration is 0.3 g), and when the frequency is 7.237 Hz, the maximum strain appears at the right arch (acceleration is 0.3 g and strain is 46.39 $\mu\varepsilon$), which is also confirmed by the failure results of the test model.

(4) The dynamic response is regarded as the superposition of the dynamic response in the direction of the tunnel cross section and longitude; the cross section is prone to shear deformation, making the shoulders and feet be the vulnerable parts during seismic. This phenomenon increases slowly along the axial direction, which is caused by SH waves propagating parallel to the cross section of the tunnel structure.

Data Availability

The data used to support the findings of this study are available from the corresponding author upon request.

Conflicts of Interest

The authors declare that they have no conflicts of interest regarding the publication of this paper.

Acknowledgments

This study was supported by the Key Project of China Railway (2014G010-G).

References

[1] M. Gan, "Investigation of earthquake diseases on tunnel engineering," *Investigation and Study of Earthquake Disease on Hanchuan Earthquake Engineering*, vol. 6, 2009.

[2] Y. Yu, *Seismic Damage Mechanism of Secondary Lining of Mountain tunnel*, China Earthquake Administration, Harbin, China, 2013.

[3] Li Lin, *Research on Seismic Response and Seismatic Design of Tunnel Grossing fault*, Southwest Jiaotong University, Chengdu, China, 2009.

[4] C.. Jiao, *Analysis on Earthquake Dynamic Response of Compound Tunnel anchorage of Suspension bridge*, Southwest Jiaotong University, Chengdu, China, 2008.

[5] S. Huang, *Research of Failure Mechanism and Seismic Measure for Underground Engineering under High Intensity earthquake*, Wuhan Institute of Rock &Soil Mechanics Chinese Academy of Sciences, Wuhan, China, 2020.

[6] M. Yang, *Study on the Influence Elements of Seismic Dynamic Response of the portal of Mountain Tunnel in High Intensity Seismic zone*, Beijing Jiaotng University, Beijing, China, 2011.

[7] X. Chao, *Research on Dynamic Response at portal Section of Mountain Tunnel under Intense Earthquake and Shock Absorption measeure*, Lanzhou Jiaotong University, Lanzhou, China, 2013.

[8] Ke. Tang, *Study on the Influence Elements of Seismic Dynamic Response of portal of Mountain tunnel*, Southwest Jiaotong University, Chengdu, China, 2006.

[9] S. Hou and L. Tao, "Dynamic response of portal section of mountain tunnel under seismic SH wave action," *Chinese Journal of Rock Mechanics and Engineering*, vol. 34, no. 2, pp. 340–348, 2015.

[10] T. Lian-jin and S. Hou, "Large-scale shaking table test for dynamic response in the portal section of mountain tunnel with different gradients of upward slope," *Rock and Soil Mechanics*, vol. 35, no. S1, pp. 91–98, 2014.

[11] V. W. Lee and J. Karl, "Diffraction of SV waves by underground, circular, cylindrical cavities," *Soil Dynamics and Earthquake Engineering*, vol. 11, no. 8, pp. 445–456, 1992.

[12] V. W. Lee and J. Karl, "Diffraction of elastic plane P waves by circular, underground unlined tunnels[J]," *European Earthquake Engineering*, vol. 6, no. 1, pp. 29–36, 1993.

[13] V. W. Lee, S. Chen, and I. R. Hsu, "Antiplane diffraction from canyon above subsurface unlined tunnel," *Journal of Engineering Mechanics*, vol. 125, no. 6, pp. 668–675, 1999.

[14] C. A. Davis, V. W. Lee, and J. P. Bardet, "Transverse response of underground cavities and pipes to incident SV waves," *Earthquake Engineering & Structural Dynamics*, vol. 30, no. 3, pp. 383–410, 2001.

[15] V. W. Lee, L. Hao, and L. Jianwen, "Diffraction of anti-plane SH waves by a semi-circular cylindrical hill with an inside concentric semi-circular tunnel," *Earthquake Engineering and Engineering Vibration*, vol. 3, no. 2, pp. 249–262, 2004.

[16] C. Yi, P. Zhang, D. Johansson, and U. Nyberg, "Dynamic response of a circular lined tunnel with an imperfect interface subjected to cylindrical P-waves," *Computers and Geotechnics*, vol. 55, pp. 165–171, 2014.

[17] C. P. Yi, W. b. Lu, P. Zhang, D. Johansson, and U. Nyberg, "Effect of imperfect interface on the dynamic response of a circular lined tunnel impacted by plane P-waves," *Tunnelling and Underground Space Technology*, vol. 51, pp. 68–74, 2016.

[18] H. F. Kara, "A note on response of tunnels to incident SH-waves near hillsides," *Soil Dynamics and Earthquake Engineering*, vol. 90, pp. 138–146, 2016.

[19] H. Dai, *Mechanics of Elasticity*, Vol. 8, Hunan University Press, , Changsha, China, 2014.

[20] T. R. Kuesel, "Earthquake design criteria for subways," *Journal of the Structural Division*, vol. 95, no. 6, pp. 1213–1231, 1969.

Hindawi
Advances in Civil Engineering
Volume 2021, Article ID 6594889, 8 pages
https://doi.org/10.1155/2021/6594889

Research Article

Study on Mechanical Properties and Damage Evolution of High-Porosity Concrete under Cyclic Loading and Unloading

Dong Zhang,[1] Ai-hong Lu,[2] Xia Wang,[1] Yu Xia,[2] Si-yu Gong,[1] Lei Sun,[3] Ran-fang Zuo,[1] and Yang Dong[1]

[1]*National Institute of Clean-and-Low-Carbon Energy, Beijing 102211, China*
[2]*School of Mechanics and Civil Engineering, China University of Mining and Technology, Xuzhou 221116, China*
[3]*State Key Laboratory of Coal Resources and Safe Mining, China University of Mining and Technology, Xuzhou 221116, China*

Correspondence should be addressed to Ai-hong Lu; xzlah@163.com

Received 13 October 2021; Accepted 3 November 2021; Published 19 November 2021

Academic Editor: Ma Jianjun

Understanding the mechanical properties and energy response of high-porosity concrete under the cyclic loading and unloading is the foundation of road construction in sponge city. In this study, the concrete with the porosity of 15% was taken as the research object, and the cyclic loading and unloading tests on the high-porosity concrete were performed under the stress amplitude of 25 MPa, 30 MPa, and 35 MPa in the elastic stage. The effects of stress amplitude and cycle number on the mechanical characteristics and damage evolution law of concrete were obtained. The experimental results show the following. (1) With the increase of cycle number, the loading and unloading elastic modulus of concrete under different stress amplitudes first increases and then decreases; the greater the stress amplitude, the faster the growth and deceleration of the loading and unloading elastic modulus. (2) With the increase of the cycle number, the peak strain and residual plastic deformation increase. (3) The greater the stress amplitude, the higher the damage of concrete; with the increasing number of cyclic loading and unloading, the damage of concrete is enhanced gradually. When the damage variable value is 1, the relationship between the cycle number and the initial stress amplitude satisfies a negative exponential function.

1. Introduction

Sponge city construction is an important opportunity and challenge in China's new urbanization construction, and it is also an important way to solve the water shortage, water environment deterioration, and flood disasters in the current new urbanization construction [1]. Due to the good permeability of permeable concrete, permeable concrete has been widely used in the construction of sponge cities [2]. The application of permeable concrete not only meets the needs of environmental protection but also effectively utilizes urban water resources and alleviates the urban heat island effect [1, 3].

At present, the effect of loading mode on the mechanical properties of concrete has been extensively studied [4]. Cook and Chindaprasirt [5] investigated the effect of loading history on the compressive properties of concrete. It is found that the compressive performance of concrete is slowly rising in the early stage; after reaching a certain strength (about 10% of the theoretical value), the compressive performance of concrete decreases rapidly with the occurrence of damage. Subsequently, Cook and Chindaprasirt [6] explored the effect of loading history on the tensile properties of concrete. Akutagawa et al. [7] found that the loading history on the compressive performance of concrete not only affects its compressive performance but also affects the elastic modulus and Poisson's ratio of concrete. Through the MTS 815 program-controlled servo test system, Xing et al. [8] conducted a uniaxial compression test on concrete cylindrical specimens under cyclic loads and studied the effects of the initial load, cyclic frequency, and the increased amplitude of cyclic stress on the mechanical behavior of concrete specimens. It is concluded that under the same initial load and increased amplitude of cyclic stress, cyclic

frequency has little effect on the strength of concrete. Under the same initial load and cycle frequency, the strength of the specimen decreases with the increase of the increased amplitude of cyclic stress. Under the same cycle frequency and the same increased amplitude of cyclic stress, the strength of concrete tends to decrease with the increase of initial load [9]. By using a large multifunctional dynamic and static triaxial apparatus, Hu et al. [10], Wang et al. [11], and Liang et al. [12] treated the damage characteristics as the research objective, analyzed the constitutive model of concrete under cyclic load, and then obtained the damage law. According to the research result of Song et al. [13], concrete will have much more fatigue strain under cyclic load than monotonic load. They also found that the damage accumulation caused by internal microcrack is the result of the irreversible deformation of concrete material and the change of various mechanical parameters [14]. Song et al. [13, 15] analyzed the destruction of concrete under cyclic load in the way of the hysteretic characteristics of dissipated energy. They also researched the failure mode of concrete under monotonic load and cyclic load and then found that the size and type of crack are directly related to the loading method. At the same time, the energy loss during loading increases with the increase of load level and simultaneously reaches the maximum. Ma et al. [16] studied the crushing characteristics and seepage characteristics of gangue concrete samples under different stresses and proposed a method to predict the evolution of permeability using fractal dimensions. Jiang et al. [17] compared and analyzed the fatigue damage characteristics of concrete through three types of cyclic action of concrete and evaluated the fatigue life based on the damage variables. Xiao et al. [18] established a damage accumulation model with mathematical equation and physical significance for rock under cyclic load and verified it with data.

Scholars have used different experimental methods to study the relationship between porosity and physical and mechanical properties of concrete and achieved rich results [19–25]. Balshin [22] and Hasselman and Fulrath [23] investigated the influence of porosity change on compressive strength of the porous concrete through experiments and obtained the relationship between compressive strength and porosity change. Knudsen [24] conducted a series of seepage experiments to explore the influence of fluid scouring behavior on sample porosity and permeability. Ma et al. [26] explored the relationship between porosity and compressive strength of cement foamed concrete and developed a mathematical model to describe the relationship between porosity and strength of concrete. Deng and Li [27] adopted expanded polystyrene (EPS) particles with a diameter of about 1-2 mm as the approximate pore structure in concrete and obtained the compressive strength, splitting tensile strength, and static compressive elastic modulus of C15, C20, and C30 concrete with the porosity of 0, 1%, 3%, and 5%. It is reported that under the same strength grade, the compressive strength, split tensile strength, and static compressive elastic modulus of concrete decrease with the increase of porosity. Xia et al. [28] discussed the influence of porosity on the energy dissipation of artificial rock from the perspective of impact load and found that under the action of impact load, the energy dissipated by concrete increases with the increase of concrete porosity.

In the research on the mechanical properties of concrete, mechanical properties of concrete with different porosity under uniaxial compression are mainly studied, as well as the concrete test without considering the porosity factor. However, the roads of sponge cities are constructed on high-porosity permeable concrete, and vehicles have a typical cyclic loading and unloading effect on the roads. At present, there are few studies on the mechanical properties of high-porosity concrete under cyclic load [29]. To this end, the experimental method was used to analyze the effects of cyclic number, cyclic load amplitude, and other parameters on the mechanical properties and energy dissipation of high-porosity concrete in this study.

2. Test Equipment and Test Scheme

2.1. Sample Preparation. The raw materials of concrete samples in this test were cement, stone, and water. The PO 32.5 grade ordinary Portland cement was produced by Xuzhou China United Cement Corporation. The limestone gravel with the particle size of 5–13 mm was used as coarse aggregate. The apparent density of limestone gravel was 3010 Kg/m^3, the content of elongated and flaky particles was 5.25%, the mud content was 0.26%, and the water content was 0.24%.

The cubic concrete samples with high porosity of $P = 15\%$ and the size of $100\,\text{mm} \times 100\,\text{mm} \times 100\,\text{mm}$ were prepared. According to the previous studies [30], the mixed proportion of water, cement, and stone was determined. Then, concrete mixed by the mixer was injected into the mold, and the surface was smoothed after shaking by the shaking table. The concrete was cured in the curing room (temperature $20 \pm 2^{\circ}$C) for 24–48 hours and watered every 8 hours. After that, the mold was removed, and the demoulded concrete was placed in the curing room (temperature $20 \pm 2^{\circ}$C, humidity ≥95%) and cured for 28 days. Figure 1 shows a part of the processed concrete samples. The water saturation method was used to remove the specimens that did not meet the porosity requirement. Finally, 40 pieces of specimens were processed for the subsequent study.

2.2. Experimental Equipment. The universal testing machine of the State Key Laboratory for Geomechanics and Deep Underground Engineering of China University of Mining and Technology was used as the loading equipment in the test. This system consists of four parts: control valve system, dynamic loading system, data acquisition system, and computer control system. The data acquisition system consists of two parts. One is the displacement load acquisition system carried by the test loading equipment; the other part is the ASMB2-8 super static signal acquisition instrument. Figure 2 shows the main test instruments. During the test, horizontal and vertical strain gauges were attached to the side of the sample, as shown in Figure 2.

Figure 1: Processed concrete samples.

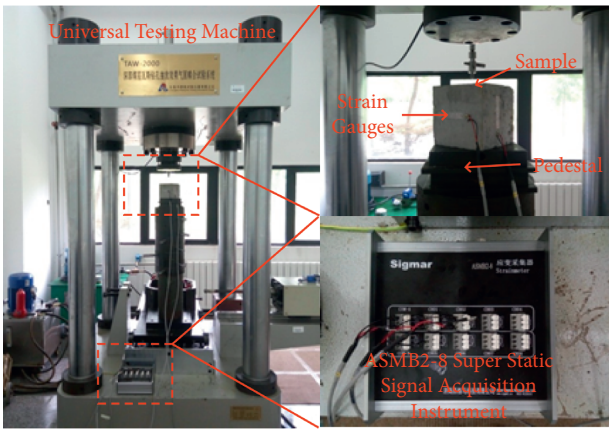

Figure 2: Test instrument diagram.

2.3. Test Scheme. Firstly, the uniaxial compression test of high-porosity concrete was carried out, and its full stress-strain curve was obtained, as shown in Figure 3. Secondly, the deformation process of high-porosity concrete was divided into different stages: (I) initial compaction process $((d^2\sigma/d\varepsilon^2) > 0)$, (II) approximate linear elastic stage $((d^2\sigma/d\varepsilon^2) = 0)$, (III) microcrack evolution stage $((d^2\sigma/d\varepsilon^2) < 0)$, and (IV) failure stage $((d\sigma/d\varepsilon) < 0)$.

In the test, 50%, 60%, and 70% of the peak stress of concrete under uniaxial compression, i.e., 25 MPa, 30 MPa, and 35 MPa, were selected as the stress amplitude of low cyclic loading. The three stress amplitudes were in the approximate linear elastic stage (stage II) in Figure 3. During the test, the corresponding stress amplitudes were loaded by 0.002 mm/s displacement loading and then unloaded to 5 MPa (the boundary point between compaction stage and linear elastic stage) by 0.002 mm/s displacement unloading. This process was called a cycle. A total of 60 cycles were performed under the stress amplitude of each group to analyze the influence of stress amplitude σ_M and cycle number C on the mechanical properties and damage evolution of concrete.

3. Mechanical Properties of High-Porosity Concrete under Different Stress Amplitudes in Cyclic Loading and Unloading

3.1. Variation Law of Stress-Strain Curve with Stress Amplitude. Figure 4 shows the similarities and differences of concrete stress-strain curves under cyclic loading and unloading with different stress amplitudes. With the increase of the cycle number, the peak strain and residual plastic deformation under different stress amplitudes gradually increase. However, the changes of peak strain and residual plastic deformation under different stress amplitudes are different. The greater the stress amplitude, the larger the increase of the residual plastic deformation and the peak strain. When the stress amplitude is 30 MPa and 35 MPa, the density of the stress-strain cycle curve changes from sparse to dense and then to sparse, while when the stress amplitude is 25 MPa, the density of the stress-strain cycle curve changes from sparse to dense. This is can be explained as follows. Before loading, there are original pores and cracks in the high-porosity concrete, and the concrete is more prone to deformation; under the action of the load, these pores and cracks are gradually and partially closed, leading to the denser concrete. Thus, the stress-strain cycle curve shows a process from sparse to dense. When the concrete undergoes multiple cyclic loading and unloading, internal pores of the concrete are damaged, leading to the generation of new cracks. At the same time, coupled with the development of the original cracks, the integrity of the internal structure of concrete becomes worse and the compressive capacity becomes weaker. Thus, the stress-strain cycle curve changes from dense to sparse. When the stress amplitude is 25 MPa, there is no change from dense to sparse in stress-strain cycle curves. It indicates that the internal structure of the sample is relatively complete after 60 cyclic loading and unloading cycles at the stress amplitude of 25 MPa. Besides, the concrete can generally withstand the action of multiple alternating loads if the applied load is relatively small.

3.2. Variation Law of Mechanical Properties of Concrete with Stress Amplitude. Under different loading stress amplitudes and number of cycles, the variation laws of different loading stress amplitudes and cycle number on the loading elastic modulus EF, unloading elastic modulus EC, and peak strain ε_F and residual plastic deformation ε_C (the strain corresponding to unloading to 5 MPa during unloading) of the concrete are shown in Figure 5.

After the concrete is loaded, the initial microcrack will expand. When the load is small, the length and width of the initial interface crack will increase and form a new interface crack. As long as the load does not exceed a certain value, the crack will stop expanding due to constant load or unloading. However, when cyclic loading is repeated, the crack will continue to expand and the mechanical properties of the concrete will be changed; the greater the applied load, the faster the crack propagation. Therefore, when concrete is subjected to cyclic loading, its mechanical properties will be changed accordingly.

As shown in Figures 5(a) and 5(b), the influence of stress amplitude and cycle number on loading and unloading elastic modulus can be obtained. Under the same stress amplitude, the loading elastic modulus and unloading elastic modulus first rise and then decline with the increase of cycle number. The greater the stress amplitude, the faster the rising rate and the faster the decline rate. When the stress

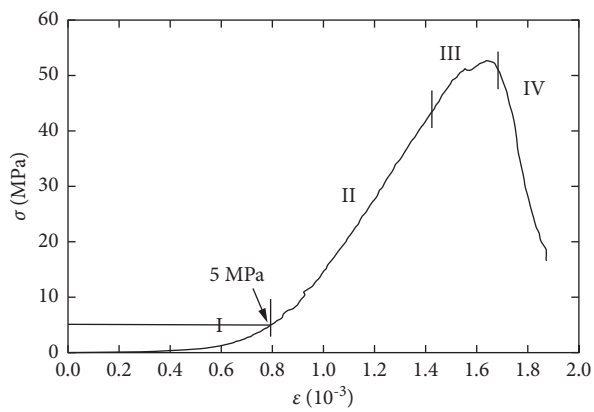

Figure 3: Stress-strain curve segmentation of high-porosity concrete.

amplitude is 25 MPa, 30 MPa, and 35 MPa, there are different cycle numbers required for reaching the peak of loading and unloading elastic modulus. The cycle numbers of 55, 35, and 15 are required for the peak of loading elastic modulus, and the cycle numbers of 50, 30, and 15 are required for the peak of unloading elastic modulus, respectively. In other words, the greater the stress amplitude, the less the cycle number required for the maximum of loading and unloading elastic modulus. When the stress amplitude is 25 MPa and 35 MPa, the maximum values of loading elastic modulus are 59.07 GPa and 58.12 GPa, respectively, and the maximum values of unloading elastic modulus are 63.71 GPa and 64.2 GPa, respectively. Therefore, the larger the stress amplitude, the smaller the maximum value of loading elastic modulus and the larger the maximum value of unloading elastic modulus.

Figures 5(c) and 5(d) show the influence of stress amplitude and cycle number on peak strain and residual plastic deformation. It can be concluded that the greater the stress amplitude, the greater the corresponding peak strain and residual plastic deformation at the same cycle number. With the increase of the cycle number, the peak strain and residual plastic deformation under the three stress amplitudes linearly increase. Under different stress amplitudes, there are different increasing rates of peak strain and residual plastic deformation with the increase of cycle number. When the stress amplitude is 35 MPa, the increasing rate of peak strain and residual plastic deformation is the largest with the increase of cycle number; when the stress amplitude is 25 MPa, the increasing rate is the smallest.

4. Damage Evolution Law of High-Porosity Concrete

4.1. Definition of Damage Variable. High-porosity concrete is an elastic-plastic material. In the process of cyclic loading and unloading, the damage evolution process of concrete is closely related to the strain amplitude of concrete and cycle number [31]. Under the same stress amplitude, the unloading process is a slow process. Only when the damage threshold of porosity accumulation is reached after a certain number of cycles, the mechanical properties of the concrete during the unloading process will be attenuated. Before attenuation, in each cycle, the strength and elastic modulus of concrete may be greater than or equal to the initial elastic modulus of concrete. At this time, if the damage of concrete is defined according to the traditional elastic modulus method, the damage variable will be negative or the damage variable will be 0.

Therefore, the previous definition of damage to elastic materials is not applicable in this study, and a new definition of damage is introduced for the elastic-plastic body. For a single cycle of concrete, the deformation modulus at the damage is

$$\widetilde{E} = \frac{\sigma}{\varepsilon}. \tag{1}$$

At this time, the unloading stiffness E_C is expressed as follows:

$$E_c = \frac{\sigma}{\varepsilon - \varepsilon_c}. \tag{2}$$

The deformation modulus at the damage can be re-expressed as

$$\widetilde{E} = \frac{\varepsilon - \varepsilon_c}{\varepsilon} E_c. \tag{3}$$

Then, the damage modulus of concrete under the final cycle can be expressed as

$$D = 1 - \frac{\varepsilon - \varepsilon_C}{\varepsilon}\left(\frac{E_C}{E}\right), \tag{4}$$

where ε and ε_C are the peak strain and residual strain and E_F and E_C are the loading elastic modulus and unloading elastic modulus, respectively.

Under cyclic loading, the damage variable of concrete is a function of the cycle number, stress amplitude, and strain amplitude. When analyzing the damage change of concrete, it is necessary to consider the loading mode and the cycle number of concrete. By combining the mechanical parameters of concrete under cyclic load, the internal damage of concrete can be analyzed.

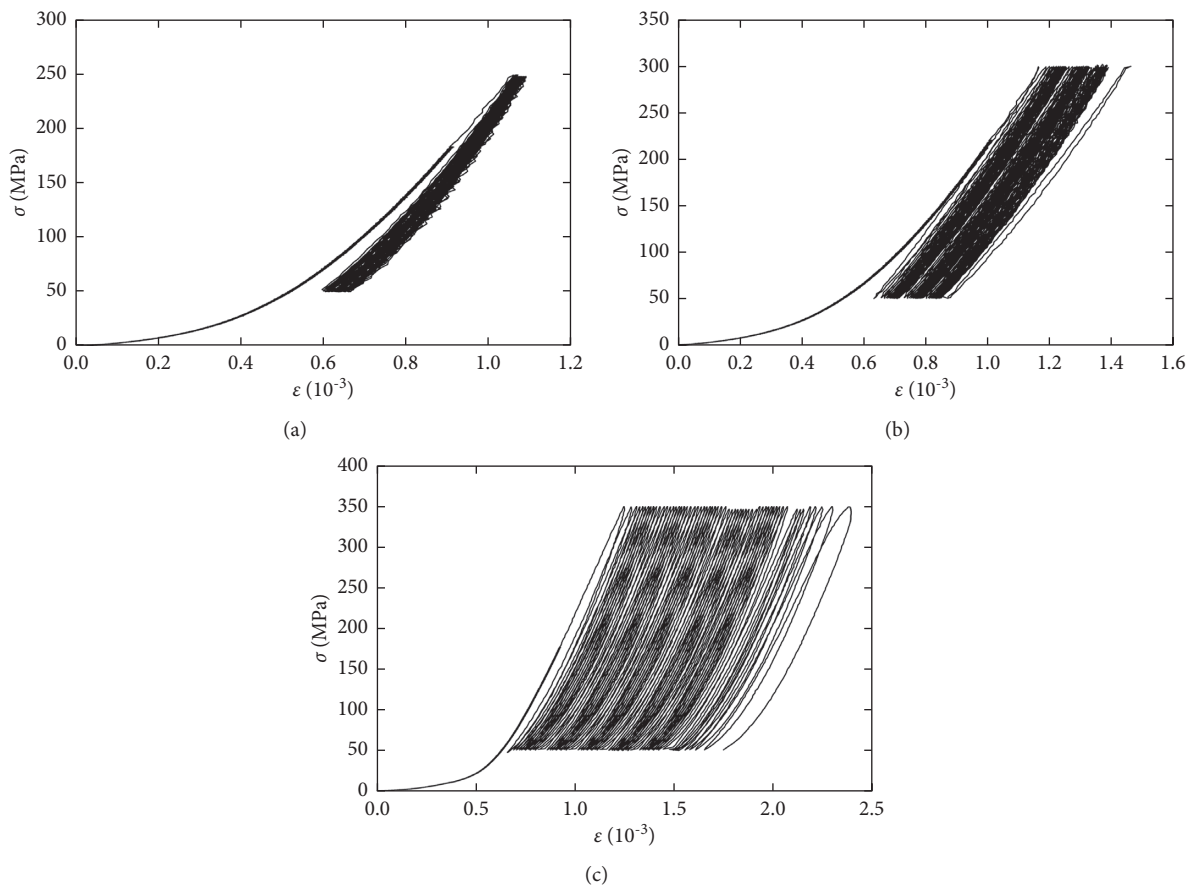

Figure 4: Stress-strain curves of concrete under cyclic loading with different stress amplitudes. (a) $\sigma_M = 25$ MPa. (b) $\sigma_M = 30$ MPa. (c) $\sigma_M = 35$ MPa.

4.2. Study on Damage of Concrete under Cyclic Loading and Unloading. Figure 6 shows the variation law of the damage variable of the concrete with the number of cycles under different stress amplitudes. As shown in Figure 6, the change law of concrete damage variables with the cycle number under four different stress amplitudes is mainly reflected in the following aspects: ① under the same stress amplitude, the damage of concrete gradually increases with the increase of the cycle number; ② with the same number of cycles, the damage variable of concrete under the large stress amplitude is generally greater than that under the small stress amplitude. After 5 cycles, the damage variable of concrete under the stress amplitude of 38 MPa is 0.37, while the damage variable of concrete under the stress amplitude of 25 MPa is 0.33.

The damage variable gradually increases with the increase of the cycle number, which indicates that the internal damage of concrete is a cumulative process. The increase of the cycle number leads to the gradual maturity of the development of internal cracks in concrete. Many cracks cannot be closed after unloading and develop to the surrounding space during the reloading. The larger the stress amplitude, the more obvious the effect.

The damage variable curve can be simply fitted linearly as follows:

$$25\,\text{MPa}: D = 0.0037C + 0.3144. R = 0.9884, \quad (5)$$

$$30\,\text{MPa}: D = 0.004C + 0.339. R = 0.959, \quad (6)$$

$$35\,\text{MPa}: D = 0.0046C + 0.3434. R = 0.9846. \quad (7)$$

When the damage variable value is set as 1, the number of cyclic loading required for the failure of concrete samples can be roughly estimated. Through calculation, 185 cycles of cyclic loading are required for the sample failure under the stress amplitude of 25 MPa, 166 cycles under 30 MPa, 142 cycles under 35 MPa, and 131 cycles under 38 MPa.

4.3. Service Life Prediction of High-Porosity Concrete under Cyclic Loading and Unloading. Due to the limitation of test conditions and the long cycle time of cyclic loading and unloading, the relationship between the cycle number and damage variables can be fitted through effective test data, and the cycle number can be obtained when the damage variable value of the sample is 1 under different stress amplitudes. When the damage variable of cyclic loading and unloading is set as 1, the cycle number under the stress amplitudes of 25 MPa and 30 MPa is obtained through calculation of equations (5)–(7). In this way, the relationship with the stress amplitude can be

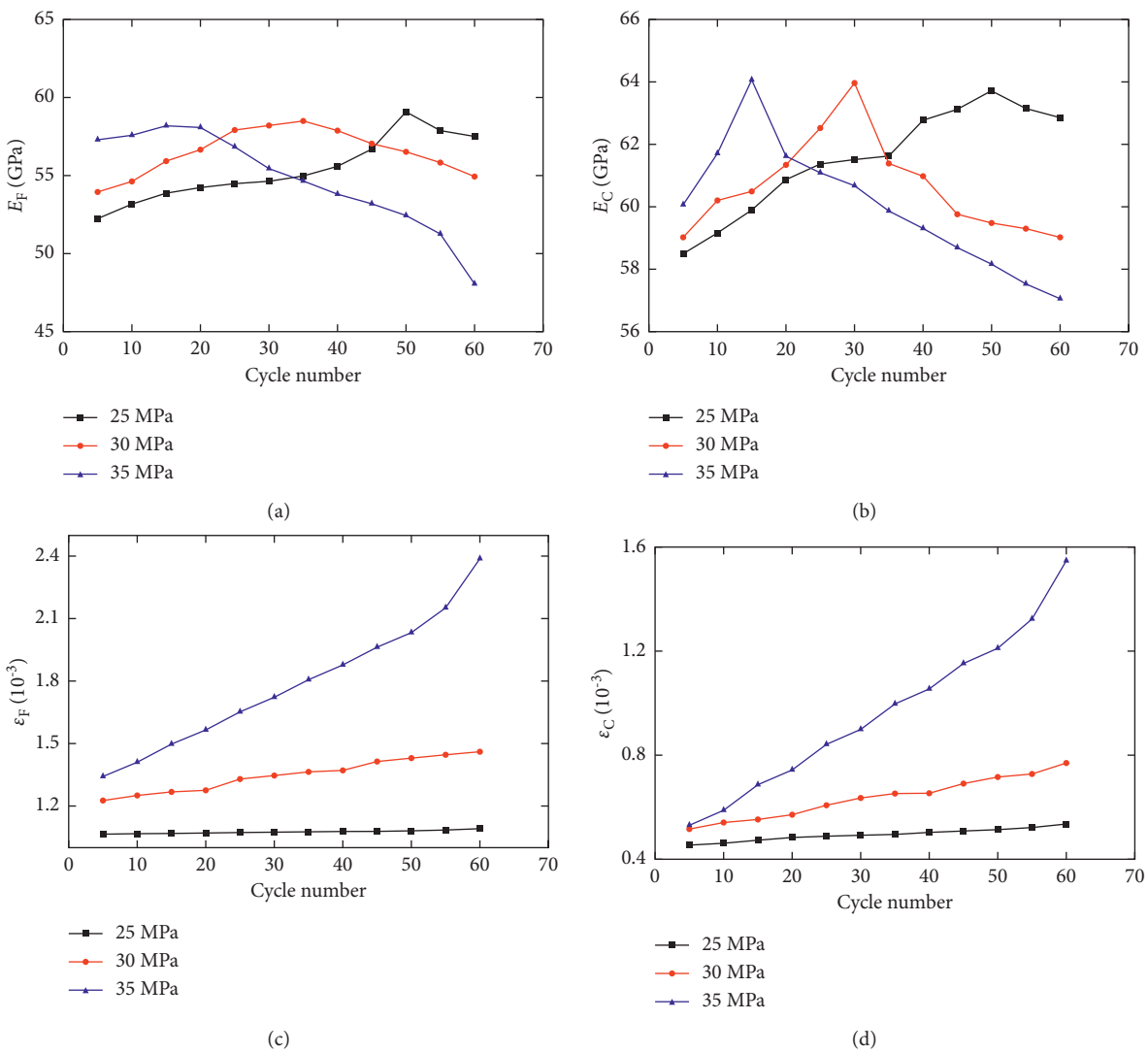

Figure 5: Variation law of mechanical properties of concrete under different stress amplitudes. (a) Variation law of loading elastic modulus E_F of concrete with the cycle number C under different stress amplitudes. (b) Variation law of unloading elastic modulus E_C of concrete with the cycle number C under different stress amplitudes. (c) Variation law of peak strain ε_F of concrete with the cycle number C under different stress amplitudes. (d) Variation law of residual plastic deformation ε_C of concrete with the cycle number C under different stress amplitudes.

established by the number of cycles when the damage variable is 1. To intuitively clarify the relationship between the damage variable of concrete and the initially applied uniaxial stress, the relationship curve between the cycle number of concrete and the stress amplitude is shown in Figure 7.

As can be seen from Figure 6, with the gradual increase of the initially applied stress, the cycle number of concrete gradually decreases. By linear fitting the initially applied stress and the cycle number, the variation law can be obtained as follows:

$$C = 2 \times 10^8 e^{-0.342\sigma_M}, \quad R^2 = 0.9489. \tag{8}$$

When the stress value of 54 MPa is substituted into equation (8), it is found that the cycle number is less than 2, which is consistent with the test results under the uniaxial compression.

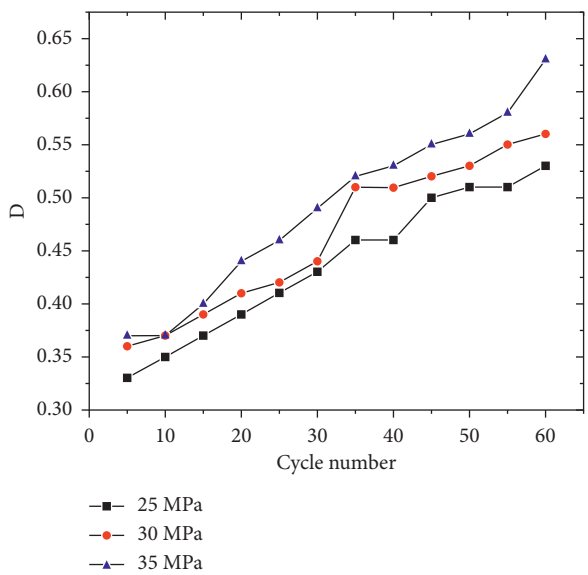

Figure 6: Variation law of damage variable D of the concrete with the cycle number C under different stress amplitudes.

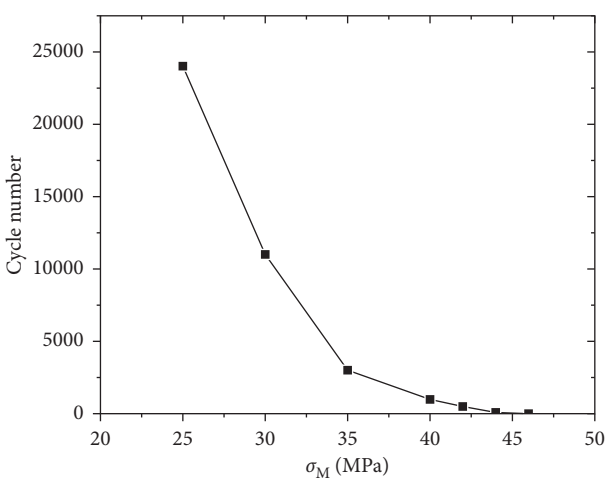

Figure 7: Relation law between cyclic number C and stress amplitude σ_M of concrete.

5. Conclusions

In this study, the universal testing machine was used to load and unload the concrete samples with the porosity of 15% under different stress amplitudes in the displacement loading mode. The effects of the changes of stress amplitude and cycle number on the mechanical properties and energy dissipation of high-porosity concrete were analyzed. The main conclusions are as follows:

(1) A total of 60 cyclic loading and unloading tests are carried out under three stress amplitudes, and the variation law of the cyclic loading and unloading stress-strain curves of concrete is obtained. The stress-strain curves of concrete under the stress amplitude of 25 MPa are changed from sparse to dense; the stress-strain curves of concrete under stress amplitudes of 30 MPa and 35 MPa are changed from sparse to dense and then sparse.

(2) The influence of stress amplitude variation on the mechanical properties of concrete is mainly reflected in the following aspects: under the three stress amplitudes, the loading and unloading elastic modulus of concrete first increases and then decreases, and the greater the stress amplitude, the faster the growth and deceleration of elastic modulus; the peak strain and residual plastic deformation increase gradually with the increase of the cycle number, and the greater the stress amplitude, the greater the peak strain and residual plastic deformation at the same cycle number; the greater the stress amplitude, the greater the dissipation energy of concrete under the same cycle number, and the variation law of concrete under the three stress amplitudes is roughly the same.

(3) The greater the stress amplitude, the higher the damage of concrete. With the increase of cyclic loading and unloading times, the damage of concrete becomes larger and larger. When the damage variable value is 1, the relationship between the cycle number and the initial stress amplitude satisfies a negative exponential function. When the stress amplitude is 54 MPa, the number of concrete cycles is 1.

Data Availability

The data used to support the findings of this study are included within the article.

Conflicts of Interest

The authors declare that they have no conflicts of interest.

Acknowledgments

This research was funded by the National Key Research and Development Program of China (2019YFC1904302) and China Energy Group Science and Technology Program (GJNY-20-111).

References

[1] J. Liu, "Review on durability of permeable concrete pavements from the perspective of sponge city," *Journal of Jiangsu College of Engineering and Technology*, vol. 16, no. 4, pp. 20–23, 2016.

[2] J. Jiang, Z. Lu, Y. Niu, J. Li, and Y. Zhang, "Study on the preparation and properties of high-porosity foamed concretes based on ordinary Portland cement," *Materials & Design*, vol. 92, pp. 949–959, 2016.

[3] K. Yu, D. Li, H. Yuan et al., ""Sponge city:" theory and practice," *City Planning Review*, vol. 39, no. 6, pp. 26–36, 2015.

[4] D. Ma, H. Duan, Q. Zhang et al., "A numerical gas fracturing model of coupled thermal, flowing and mechanical effects," *Computers, Materials & Continua*, vol. 65, no. 3, pp. 2123–2141, 2020.

[5] D. J. Cook and P. Chindaprasirt, "Influence of loading history upon the compressive properties of concrete," *Magazine of Concrete Research*, vol. 32, no. 111, pp. 89–100, 1980.
[6] D. J. Cook and P. Chindaprasirt, "Influence of loading history upon the tensile properties of concrete," *Magazine of Concrete Research*, vol. 33, no. 116, pp. 154–160, 1981.
[7] S. Akutagawa, F. L. Jeang, N. M. Hawkins, B. M. Liaw, J. Du, and A. S. Kobayashi, "Effects of loading history on fracture properties of concrete," *ACI Materials Journal*, vol. 88, no. 2, pp. 170–180, 1991.
[8] S. Xing, L. Wan, T. Deng et al., "Uniaxial compressive properties of concrete under the cyclic load," *Chinese Journal of Underground Space and Engineering*, vol. 4, no. 2, pp. 281–284, 2008.
[9] D. Ma, J. Wang, X. Cai et al., "Effects of height/diameter ratio on failure and damage properties of granite under coupled bending and splitting deformation," *Engineering Fracture Mechanics*, vol. 220, Article ID 106640, 2019.
[10] H. Hu, G. Peng, J. Xie et al., "Experimental study on dynamic compressive behaviors of concrete due to circular loading history," *Concrete*, vol. 1, pp. 51–54, 2013.
[11] Z. Wang, L. Gao, and J. Lu, "Constitutive model of concrete with uniaxial rate," *Journal of Dalian University of Technolgy*, no. 5, pp. 597–601, 2000.
[12] H. Liang, G. Peng, S. Zou et al., "Study on stress-strain curve of concrete under cyclic loading," *Journal of Civil Engineering and Management*, vol. 31, no. 4, pp. 55–59, 2014.
[13] Z. Song, T. Frtihwirt, and K. Heinz, "Inhomogeneous mechanical behaviour of concrete subjected to monotonic and cyclic loading," *International Journal of Fatigue*, vol. 132, 2020.
[14] D. Ma, H. Duan, J. Liu, X. Li, and Z. Zhou, "The role of gangue on the mitigation of mining-induced hazards and environmental pollution: an experimental investigation," *The Science of the Total Environment*, vol. 664, pp. 436–448, 2019.
[15] Z. Song, H. Konietzky, and T. Frühwirt, "Hysteresis energy-based failure indicators for concrete and brittle rocks under the condition of fatigue loading," *International Journal of Fatigue*, vol. 114, pp. 298–310, 2018.
[16] D. Ma, J. Zhang, H. Duan et al., "Reutilization of gangue wastes in underground backfilling mining: overburden aquifer protection," *Chemosphere*, vol. 264, no. 1, Article ID 128400, 2021.
[17] D. Jiang, W. Liu, J. Chen et al., "Fatigue behavior of concrete under graded discontinuous cyclic loading," *Journal of Southeast University (Natural Science Edition)*, vol. 49, no. 04, pp. 631–637, 2019.
[18] J.-Q. Xiao, D. X. Ding, G. Xu, and F. L. Jiang, "Inverted S-shaped model for nonlinear fatigue damage of rock," *International Journal of Rock Mechanics and Mining Sciences*, vol. 46, no. 3, pp. 643–648, 2009.
[19] K. Rakesh and B. Bhattacharjee, "Porosity, pore size distributionand in situ strength of concrete[J]," *Cement and Concrete Research*, vol. 33, no. 1, pp. 155–164, 2003.
[20] I. O. Yaman, N. Hearn, and H. M. Aktan, "Active and non-active porosity in concrete Part I: experimental evidence," *Materials and Structures*, vol. 35, no. 2, pp. 102–109, 2002.
[21] M. Amianti and V. R. Botaro, "Recycling of EPS: a new methodology for production of concrete impregnated with polystyrene (CIP)," *Cement and Concrete Composites*, vol. 30, no. 1, pp. 23–28, 2008.
[22] M. Balshin, "Relation of mechanical properties of powder metals and their porosity and the ultimate properties of porous meal - ceramic materials," *Doklady Akademii Nauk SSSR*, vol. 67, no. 5, pp. 831–834, 1951.
[23] D. P. H. Hasselman and R. M. Fulrath, "Effect of small fraction of spherical porosity on elastic moduli of glass," *Journal of the American Ceramic Society*, vol. 47, no. 1, pp. 52-53, 1953.
[24] F. P. knudsen, "Dependence of mechanical strength of brittle polycrystalline specimens on porosity and grain size," *Journal of the American Ceramic Society*, vol. 42, no. 8, pp. 376–387, 1949.
[25] D. Ma, H. Duan, X. Li, Z. Li, Z. Zhou, and T. Li, "Effects of seepage-induced erosion on nonlinear hydraulic properties of broken red sandstones," *Tunnelling and Underground Space Technology*, vol. 91, Article ID 102993, 2019.
[26] D. Ma, S. Kong, Z. Li, Q. Zhang, Z. Wang, and Z. Zhou, "Effect of wetting-drying cycle on hydraulic and mechanical properties of cemented paste backfill of the recycled solid wastes," *Chemosphere*, vol. 282, Article ID 131163, 2021.
[27] C. Deng and Z. Li, "Experimental study on mechanical properties of concrete with porosity," *Concrete*, no. 7, pp. 41–44, 2016.
[28] C. Xia, H. Xie, and J. Yang, "SHPB test on porous rock," *Chinese Journal of Rock Mechanics and Engineering*, vol. 5, pp. 896–900, 2006.
[29] D. Ma, H. Duan, W. Liu, X. Ma, and M. Tao, "Water-sediment two-phase flow inrush hazard in rock fractures of overburden strata during coal mining," *Mine Water and the Environment*, vol. 39, no. 2, pp. 308–319, 2020.
[30] Y. Lian, "Design of mix proportion of porous modified concrete and determination of porosity," *Transport Standardization*, vol. 35, no. 4, pp. 43–46, 2010.
[31] P. Li, Y. F. Wu, Y. Zhou, and F. Xing, "Stress-strain model for FRP-confined concrete subject to arbitrary load path," *Composites Part B: Engineering*, vol. 163, pp. 9–25, 2019.

Hindawi
Advances in Civil Engineering
Volume 2021, Article ID 5618575, 14 pages
https://doi.org/10.1155/2021/5618575

Research Article

Detection and Prediction of Internal-Caused Fire in Tunnel Cable by an Equivalent Transient Thermal Circuit Model

Yanwen Wang,[1] **Xuran Zhang**,[1] **Le Wang**,[2] **and Yinsheng Wang**[3]

[1]*School of Mechanical Electronic and Information Engineering, China University of Mining and Technology (Beijing), Beijing 100083, China*
[2]*North China Electric Power Test and Research Institute, China Datang Corporation Science and Technology Research Institute Co., Ltd., Beijing 100040, China*
[3]*Zhong Neng Power-Tech Development Co., Ltd., Beijing 100034, China*

Correspondence should be addressed to Xuran Zhang; 810801559@qq.com

Received 7 October 2021; Accepted 30 October 2021; Published 11 November 2021

Academic Editor: Mingfeng Lei

Internal-caused cable fires are one of the most common cable fires, and anomalous temperature increase of the cable core is one of the first signs. However, when a cable is operating with electricity, the temperature of the core conductor cannot be monitored directly; therefore, this characteristic cannot be used in detection and prediction of internal-caused fire in electric cable effectively. An analogous transient thermal circuit model is created, simplified, and optimized to properly compute the temperature of the cable core. Afterward, by using the cable internal-caused fire experimental platform and adjusting current carrying capacity of the tested cable, an experiment is conducted for stimulating the very early stage of three-core cable internal-caused fire. The maximum relative errors of the transient thermal circuit model and the trisection transient thermal circuit model are less than 10% when comparing the experimental data with the calculation results, and the average relative error of the calculated value of trisection transient thermal circuit model is 1.08% after layered optimization. The algorithm model can satisfy the requirement for early detection and prediction in the very early stage of cable internal-caused fire.

1. Introduction

Cable tunnel engineering has advanced significantly in recent years, for example, 220 kV Jiulong-Nanzhan cable tunnel project, 220 kV Ninghai-Mochou cable tunnel project, and 220 kV Qiuteng-Shanjiang cable tunnel project [1]. The electromagnetic environment in the cable tunnel is complicated, the air includes a considerable volume of flammable gas, and the humidity is high [2]. Power cables are usually laid crowded on cable tray in tunnel; thus, the probability of fire accidents would rise accordingly. Once a cable fire occurs, it becomes easy to spread and would cause serious losses [3–5]. In 2016, a fire broke out in the 66 kV cable tunnel in Dalian, Liaoning Province. The accident caused a large area of power failure in Dalian for more than 6 hours. The road signal lights, waterworks, hospitals, banks, and supermarkets were influenced by power failure and could not operate normally, which seriously impacted the normal operation order of the city. In Holborn, London, UK, a cable fire broke out in a cable tunnel in 2015. It took firefighters seven hours to basically control the fire. The fire forced the evacuation of 5000 people in the city center, left over 3000 families and enterprises without power supply, and halted the urban operation [6]. Power line fires account for 36.8% of all fire incidents, and casualties account for 47.1 percent of total injuries, according to a statistical analysis of significant fires from 2008 to 2016 [7]. Thus, timely detection of cable fire especially before the fire and reduction of the probability of fire are of great significance to reduce casualties and economic losses [8–11]. Nevertheless, it is difficult to detect the fire as early as possible because cable tunnels are unattended and the fire detectors currently utilized cannot accurately detect the temperature of the cable in operation. When a fire is found, the fire has generally turned to the stage of intense combustion, and extinguishing the fire will become very difficult [6]. Figure 1 shows photos of three-core

Figure 1: (a) Picture of cable laying; (b) photo of cable fire; (c) picture of cable insulation damage; (d) picture of structural analysis of three-core cable; (e) picture of cable radial section.

cable laying, cable fire, cable insulation damage, and structural damage.

To date, various studies were carried out on cable fire but primarily paid attention to the prevention, identification, and disaster reduction of power cable fire. Wang et al. investigated the performance of both fireproof cable tray and fire penetration prevention material and proposed that the performance of fire penetration prevention material is quite better than that of fireproof cable tray [12]. Pascal et al. investigated the ability of the FLASH-CAT model to predict the HRR for such configuration and proposed a video fire analysis method [13]. Zheng et al. studied the live combustion of power cable, evaluated the development process of the current numerical model of live combustion of power cable, and highlighted the fact that the current numerical simulation model of power cable fire is primarily concerned with the dynamic process after the fire [14]. Huang et al. investigated the vertical spread of cable fire in restricted space and proposed a jet temperature prediction for vertical cable fire that can estimate the harm of vertical spread of cable fire [15]. Zhang and Zhao mastered the changing rules of temperature and smoke in the fire process and highlighted the fact that the maximum ceiling temperature and the distributions of smoke are related to fire

sealing and ventilation mode, by numerically simulating the smoke flow direction and temperature in the utility tunnel cable fire's development process [16]. There exists no detailed research on the very early detection and prediction of internal-caused cable fire.

Following the different fire sources, power cable fire is often split into internal-caused fire and external-caused fire. External-caused fire occurs when a cable is pushed to burn due to the activity of an external heat source. A cable fire caused by the high heat exceeding the ignition point of insulating material generated by the cable itself is known as the internal-caused fire [17]. Protective layers such as the insulation layer and the sheath layer surround the core conductor of power cables. The cable core temperature should be kept within the temperature range that insulating material can tolerate for an extended period of time. The high temperature of the core conductor would damage the insulating medium's stability, diminish insulation capacity, and readily form electrical trees, resulting in leakage, short circuits, and internal cable fire [18, 19]. The highest working temperature of XLPE cable core is 90°C. When the temperature is higher than 137°C, there is a risk of cable internal-caused fire. At this time, the cable is in the very early stage of internal-caused fire [20]. It could be illustrated that the abnormal temperature rise of cable core in an internal-caused fire makes it possible to detect the fire in the very early stage.

Using the existing methods, it becomes difficult to measure the temperature of cable core conductor directly when the cable is running with electricity [21–23]. Therefore, precise assessment of the cable core's transient temperature is critical for early detection and forecast of cable fires caused by internal causes. There are two types of approaches that are widely used for calculating cable core temperature: analytical and numerical methods [24–26]. To calculate the cable core temperature, some researchers utilize a finite element model based on a numerical technique. However, the finite element model has a large amount of calculation, the accuracy would be influenced by the structure division and mesh size, and the real-time performance is poor, so it is not suitable for engineering applications [27].

To attain the goal of detection and prediction of internal-caused fire in electric cable and decrease the risk of cable fire, the objectives of this work are twofold: constructing an algorithm model for calculating the core temperature from the surface temperature of the outer sheath of cable; verifying the feasibility of the algorithm model in the very early detection of cable internal-caused fire by experiment. We present a trisection transient thermal circuit model based on the radial section structure of three-core cable to reduce the complexity of the model and establish a transient thermal circuit model algorithm to calculate the core temperature from the surface temperature of the outer sheath of cable in this study. Subsequently, we optimize the algorithm model by layering method for decreasing the influence of the internal temperature gradient within the cable material and the error of the algorithm model. Finally, a cable internal-caused fire experiment is conducted to verify the feasibility of the algorithm model in the very early detection and prediction of cable internal-caused fire.

2. Theoretical Algorithm Model

2.1. Transient Thermal Circuit Model. This paper takes the three-core power cable as the research object to investigate the corresponding relationship between the core temperature and the surface of outer sheath temperature and uses a three-core XLPE power cable as an example. Figure 2 depicts the structure. Considering that the diameter of the radial section is much smaller than the length of the power cable and the cable core has good thermal conductivity, the axial heat transmission of the power cable is not considered. Because the three-core power cable's radial sections are distributed in a triangle, radial thermal transfer is varied at different angles, and temperatures of the outer sheath surface are different. Assuming that the febrile responses of the three core lines of the cable are the same, the shortest path of thermal conduction on the radial section is investigated, and the temperature at the position shown at point "a" in Figure 2 is chosen as the surface temperature of the cable's outer sheath [27–31].

Accurate estimation of the transient temperature of cable core is the key to the very early identification and prediction of internal-caused fire in a cable, so a transient thermal circuit model is constructed based on the microstructure thermal transfer theory to examine the dynamic thermal transfer process of cable. The heat conduction stage in which the cable's internal heat is carried outward but has not yet reached equilibrium is referred to as transient thermal transfer of power cable. Each cable layer is treated as the cylinder wall, and the cylinder wall is also separated into microstructure, so that the cable's transient thermal circuit model can be established. According to the Fourier thermal transfer law, the thermal passage through the unit cross section per unit time is proportional to the area of the unit cross section and the temperature gradient in the direction of the vertical cross section. Then, the thermal dQ passing through the area of dA microstructure is shown in

$$\mathrm{d}Q = -R \cdot \frac{\partial t}{\partial x} \mathrm{d}A. \tag{1}$$

According to (1), the minus sign shows the direction of thermal transfer and R represents thermal resistance. Take the three-core cable sheath per unit length as an example; its longitudinal section radius is r and c is specific thermal capacity. Assume the microstructure's thickness is dr. The volume is dV; the thermal inflow and outflow in time dτ are $\mathrm{d}Q_i$ and $\mathrm{d}Q_0$, respectively; and the $\mathrm{d}Q_p$ is thermal generated by itself. Equation (2) depicts the temperature rise Δt of the microstructure.

$$\Delta t = \frac{\mathrm{d}Q_i + \mathrm{d}Q_p - \mathrm{d}Q_0}{c \cdot \mathrm{d}V}. \tag{2}$$

In (2), $\mathrm{d}V = 2\pi r \cdot \mathrm{d}r$; the thermal outflow is shown in

$$\mathrm{d}Q_0 = R \cdot \frac{\partial t}{\partial x} \cdot \mathrm{d}A \cdot \mathrm{d}\tau. \tag{3}$$

In (3), $\mathrm{d}A = 2\pi r$. Equation (3) can be substituted into (2).

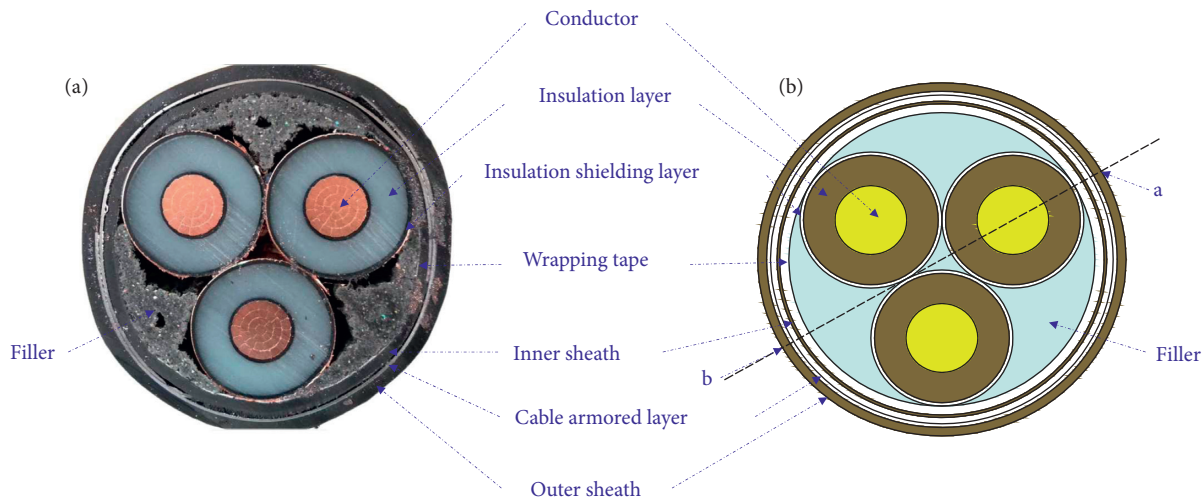

Figure 2: (a) Picture of cable radial section; (b) schematic diagram of cable radial section.

$$\frac{dQ_i}{d\tau} + \frac{dQ_p}{d\tau} = 2\pi r \cdot R\frac{\partial t}{\partial r} + \frac{2\pi rc \cdot dr \cdot \Delta t}{d\tau}. \quad (4)$$

If $P_i = (dQ_i/d\tau)$ and $P_p = (dQ_p/d\tau)$, (4) can be rewritten as

$$P_i + P_p = 2\pi r \cdot R\frac{\partial t}{\partial r} + \frac{2\pi rc \cdot dr \cdot \Delta t}{d\tau}. \quad (5)$$

Equation (5) is a cable sheath distributed parameter transient thermal circuit model. $2\pi r \cdot R(\partial t/\partial r)$ shows the heat flowing through thermal resistance P_r; $(2\pi rc \cdot dr \cdot \Delta t/d\tau)$ is the heat flowing through the heat capacity P_c. The microstructure transient thermal circuit model represented by (5) is depicted in Figure 3.

As an example, consider the cable sheath's distributed parameter thermal circuit model. The model can be applied to other layers of the power cable. Assuming the thermal capacity of each layer of the cable, the transient thermal circuit model of the power cable (YJV22-6/10 kV$^{-3} \times 50$) is established, as depicted in Figure 4. Each layer of the cable's material is considered a layer of thermal resistance, and adjacent layers with the same thermal resistivity are grouped together. The cable's three core conductors have the highest and identical temperature, and their thermal resistance and thermal loss power are in parallel; as a result, the cores of the cable are the starting point of the thermal circuit, and the three cores are grouped together as a node. The insulation shielding layer of the three core lines is classified as the second node in the thermal circuit model, the armored layer as the third node, and the surface of outer sheath of the cable as the fourth node. In order to facilitate the calculation of thermal circuit model, it uses the following assumptions:

(1) The cable's material properties are stable, and its parameters are time-independent.

(2) Each layer of the cable is tightly bonded with no contact thermal resistance.

(3) The metal material has no thermal resistance.

(4) The cable's febrile response is uniform, and the heating power of the three cores of the cable is the same.

In Figure 4, $P_c, P_d, \lambda_2 P_{ca}$, and $\lambda_2 P_c$ are the thermal loss power of core conductor, insulation layer, insulation shielding layer, and armored layer of cable, respectively; C_1', C_1'', C_2', C_4', and C_5' are the core conductor's thermal capacity, insulation layer, insulation shielding layer, armored layer, and outer sheath of the cable; C_3' is the cable filler's thermal capacity, wrapping tape, and inner sheath; θ_1, θ_2, and θ_3 show the temperature of core conductor, insulation shielding layer, and armored layer of cable; θ_0 indicates the surface temperature of outer sheath of the cable; R_1 and R_3 are the symbols of thermal resistance of cable insulation layer and cable outer sheath; and R_2 depicts the thermal resistance of cable filler, wrapping tape, and inner sheath. According to the principle that the total thermal does not vary, the parallel branch is equivalent to the series branch, and the cable's transient thermal circuit model is also simplified. The total heat flux on the left side of the thermal resistance of the insulation layer is $3P_c + 3P_d$, the total heat flux on the right side of the thermal resistance of the insulation layer is $3\lambda_1 P_c$, and the thermal resistance of the insulation layer is $R_1/3$. Then, the thermal circuit model is simplified, as illustrated in Figure 5.

In Figure 5, $C_1 = 3C_1' + 3C_1''$, $P_1 = 3P_c + 3P_d$, $P_2 = 3\lambda_1 P_c$, $C_2 = 3C_2' + C_3'$, $P_3 = 3\lambda_2 P_c$, $C_3 = C_4' + C_5'$. The transient thermal circuit model is identical to the structure of the circuit. Each portion of the cable has a heat loss power that is comparable to the power supply; the heat flux, temperature difference, thermal resistance, and thermal capacity are regarded as current, voltage difference, resistors, and capacitance, respectively, and each part's thermal capacity is comparable to its capacitance. The equations of the simplified transient thermal circuit model are illustrated below.

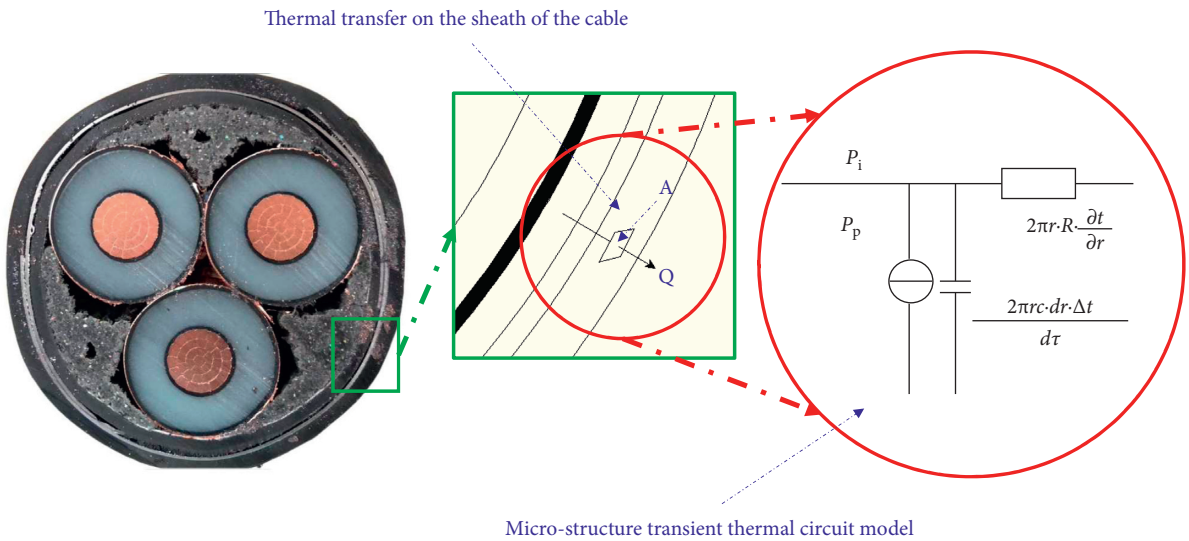

Figure 3: Transient thermal circuit model of cable sheath with microelement distributed parameters.

$$\begin{cases} C_1 \dfrac{d\theta_1}{dt} + \dfrac{3\theta_1}{R_1} - \dfrac{3\theta_2}{R_1} = P_1, \\ -\dfrac{3\theta_1}{R_1} + C_2 \dfrac{d\theta_2}{dt} + \left(\dfrac{3}{R_1} + \dfrac{1}{R_2}\right)\theta_2 - \dfrac{\theta_3}{R_2} = P_2, \\ -\dfrac{\theta_2}{R_2} + C_3 \dfrac{d\theta_3}{dt} + \left(\dfrac{1}{R_2} + \dfrac{1}{R_3}\right)\theta_3 - \dfrac{\theta_0}{R_3} = P_3. \end{cases} \tag{6}$$

In (6), t indicates time. Equation (6) is organized into matrix form, as shown in the following equation:

$$\dot{\boldsymbol{\theta}} = \mathbf{A}\boldsymbol{\theta} + \mathbf{BP}. \tag{7}$$

If $\theta(t_0) = \beta$, then (7)'s solution is

$$\boldsymbol{\theta}(t) = e^{\mathbf{A}(t-t_0)}\beta + \int_{t_0}^{t} e^{\mathbf{A}(t-t_0)}\mathbf{BP}\partial\tau. \tag{8}$$

According to (8),

$$\begin{aligned} e^{At} &= \mathbf{E} + \mathbf{A}t + \frac{1}{2!}\mathbf{A}^2t^2 + \frac{1}{3!}\mathbf{A}^3t^3 + \cdots = \sum_{k=0}^{\infty}\frac{1}{k!}\mathbf{A}^k t^k, \\ \dot{\boldsymbol{\theta}} &= \left[\frac{d\theta_1}{dt}\ \frac{d\theta_2}{dt}\ \frac{d\theta_3}{dt}\right]^T, \\ \boldsymbol{\theta} &= [\theta_1\ \theta_2\ \theta_3]^T, \\ \mathbf{A} &= \begin{bmatrix} a_{1,1} & a_{1,2} & 0 \\ a_{2,1} & a_{2,2} & a_{2,3} \\ 0 & a_{3,2} & a_{3,3} \end{bmatrix}. \end{aligned} \tag{9}$$

In matrix $\mathbf{A}$, $a_{1,1} = -3(C_1R_1)^{-1}$, $a_{1,2} = 3(C_1R_1)^{-1}$, $a_{2,1} = 3(C_2R_1)^{-1}$, $a_{2,2} = -C^{-1}(3R^{-1} + R^{-1})$, $a_{2,3} = (C_2R_2)^{-1}$, $a_{3,2} = (C_3R_2)^{-1}$, $a_{3,3} = -C_3^{-1}(R_2^{-1} + R_3^{-1})$.

$$\mathbf{B} = \begin{bmatrix} C_1^{-1} & 0 & 0 \\ 0 & C_2^{-1} & 0 \\ 0 & 0 & C_3^{-1} \end{bmatrix}. \tag{10}$$

$$\mathbf{P} = [P_1\ P_2\ P_X]^T. \tag{11}$$

In (11), $P_X = \theta_0 R_3^{-1} + P_3$. According to the surface temperature of the cable's outer sheath, the temperature of the cable core is calculated.

2.2. Trisection Transient Thermal Circuit Model. The transient thermal circuit model is complex because the impacts of mutual thermal transfer and respective external thermal transfer of three cable cores must be considered. In order to make the model less complicated, the radial section of cable is separated into three equal parts, and each part is equivalent to a single-core cable, as illustrated in Figure 6. Thermal is transported from core to point "a" on the surface of the outer sheath through insulation layer, insulation shielding layer, wrapping tape, inner sheath, armored layer, and outer sheath. Because the filler is not on the quickest thermal transfer path, only the thermal capacity of the filler is calculated instead of its thermal resistance. As shown in Figure 7, a trisection transient thermal circuit model from core conductor to point "a" on the surface of the outer sheath is created.

In Figure 7, P_1', P_1'', P_2', and P_4' mean the thermal loss power of core conductor, insulation layer, insulation shielding layer, and armored layer of cable; θ_1', θ_3', and θ_4' are temperatures of core conductor, insulation shielding layer, and armored layer of cable; θ_2' is the temperature of the cable insulation layer's outer skin; θ_5' shows the surface temperature of the outer sheath of the cable; R_1' and R_4' indicate the thermal resistance of the cable insulation layer and outer sheath; and the thermal resistance of the cable wrapping tape and inner sheath is denoted by R_2'.

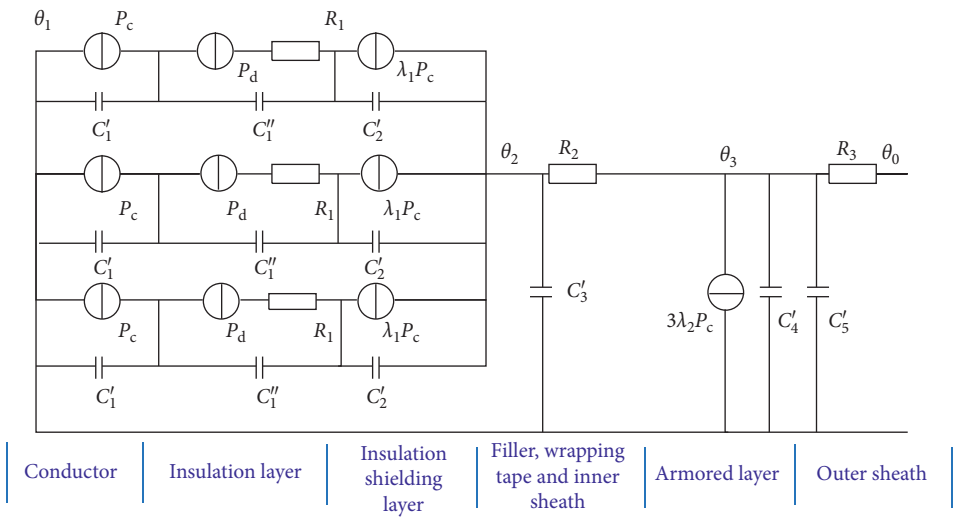

Figure 4: Transient thermal circuit model of power cable.

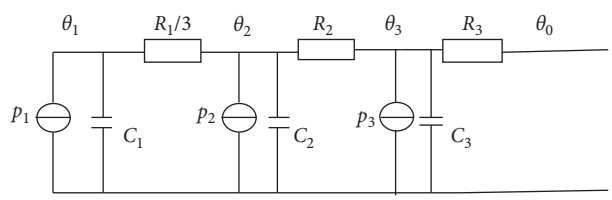

Figure 5: Modeling of a power cable's transient thermal circuit simplified.

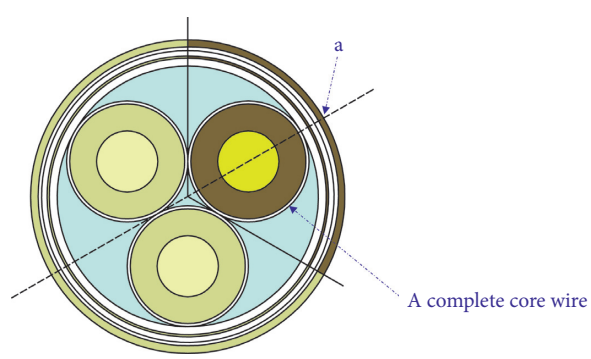

Figure 6: Schematic diagram of trisection of cable radial section.

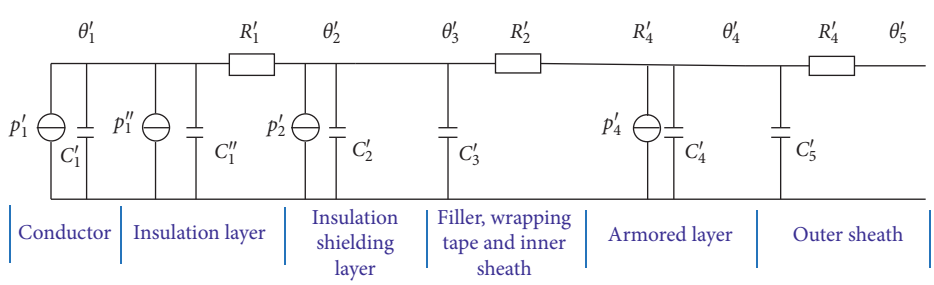

Figure 7: Thermal circuit model of power cable temperature field.

2.3. Thermal Circuit Model Layered Optimization. The thermophysical properties of the cable body material are important factors that have a significant impact on the calculation accuracy of the thermal circuit model algorithm. The thermal diffusivity, for example, in a material is a measure of the thermal transfer rate inside the material, indicative of the thermal change inside the material.

$$a = \frac{\lambda}{\rho c}. \tag{12}$$

The parameters a, ρ, λ, and c in (12) represent thermal diffusivity, density, thermal conduction coefficient, and specific thermal capacity of the material. The thermal diffusivity is mostly determined by the parameter characteristics of the material, which is directly proportional to the thermal conduction coefficient and inversely proportional to the product of density and specific thermal capacity. Materials having high thermal conduction coefficient have better thermal conductivity. As a result, the temperature difference inside the material is minimal. The insulation layer, inner sheath, and outer sheath all have a low thermal conduction coefficient, resulting in large internal temperature gradients. The insulation layer, inner sheath, and outer sheath all have a low thermal conduction coefficient, resulting in large internal temperature gradients. If the temperature of the innermost layer of material is used to represent the temperature of the entire layer of material in the calculation, it will undoubtedly result in a significant calculation error of the algorithm model, and the calculation error is positively associated with the temperature gradient. Therefore, a layered trisection transient thermal circuit model of power cable in which insulation layer, inner sheath, and outer sheath are layered is constructed, to reduce the influence of the internal temperature gradient within the cable material. The insulation layer, inner sheath, and outer sheath of the cable are separated into L layers, M layers, and N layers, respectively, and L, M, and N are positive integers. The layered trisection transient thermal circuit model is depicted in Figure 8.

In Figure 8, $C_{11}' \sim C_{1L}'$ show the thermal capacity of each layer of the cable insulation layer; the thermal loss power of each layer of the cable insulation layer is indicated by $P_{11}' \sim P_{1L}'$; $R_{11}' \sim R_{1L}'$ denote the thermal resistance of each layer of the cable insulation layer; R_3' indicates the thermal resistance of the cable wrapping tape; $C_{41}' \sim C_{4M}'$ denote the thermal capacity of each layer of the cable inner sheath; $P_{41}' \sim P_{4M}'$ are the symbols of thermal loss power of each layer of the cable inner sheath; $R_{41}' \sim R_{4M}'$ are the representations of thermal resistance of each layer of the cable inner sheath; the symbol P_5' indicates the thermal loss power of the cable armored layer; $C_{61}' \sim C_{6M}'$ represent the thermal capacity of each layer of the outer sheath of the cable; $P_{61}' \sim P_{6M}'$ depict the power loss of each layer of the outer sheath of the cable; $R_{61}' \sim R_{6M}'$ represent the thermal resistance of each layer of the outer sheath of the cable; and $\overset{0}{\theta}$ is the surface temperature of the outer sheath of the cable. As indicated in Figure 9, the multilayer thermal circuit model is integrated and simplified.

The node equations of the thermal circuit model are listed, and the following equations are obtained, based on similar properties of the thermal circuit model and the circuit.

$$\begin{cases}
C_1\dfrac{d\theta_1}{dt} + \dfrac{\theta_1}{R_1} - \dfrac{\theta_{22}}{R_1} = P_1, \\[2ex]
-\dfrac{\theta_1}{R_1} + C_{22}\dfrac{d\theta_{22}}{dt} + \left(\dfrac{1}{R_1} + \dfrac{1}{R_{22}}\right)\theta_{22} - \dfrac{\theta_{23}}{R_{22}} = P_{22}, \\[2ex]
-\dfrac{\theta_{22}}{R_{22}} + C_{23}\dfrac{d\theta_{23}}{dt} + \left(\dfrac{1}{R_{22}} + \dfrac{1}{R_{23}}\right)\theta_{23} - \dfrac{\theta_{24}}{R_{23}} = P_{23}, \\[2ex]
\vdots \\[2ex]
-\dfrac{\theta_{2L-1}}{R_{2L-1}} + C_{2L}\dfrac{d\theta_{2L}}{dt} + \left(\dfrac{1}{R_{2L-1}} + \dfrac{1}{R_{2L}}\right)\theta_{2L} - \dfrac{\theta_3}{R_{2L}} = P_{2L}, \\[2ex]
-\dfrac{\theta_{2L}}{R_{2L}} + C_3\dfrac{d\theta_3}{dt} + \left(\dfrac{1}{R_{2L}} + \dfrac{1}{R_3}\right)\theta_3 - \dfrac{\theta_{41}}{R_3} = P_3, \\[2ex]
-\dfrac{\theta_3}{R_3} + C_{41}\dfrac{d\theta_{41}}{dt} + \left(\dfrac{1}{R_3} + \dfrac{1}{R_{41}}\right)\theta_{41} - \dfrac{\theta_{42}}{R_{41}} = P_{41}, \\[2ex]
\vdots \\[2ex]
-\dfrac{\theta_{4M-1}}{R_{4M-1}} + C_{4M}\dfrac{d\theta_{4M}}{dt} + \left(\dfrac{1}{R_{4M-1}} + \dfrac{1}{R_{4M}}\right)\theta_{4M} - \dfrac{\theta_5}{R_{4M}} = P_{4M}, \\[2ex]
-\dfrac{\theta_{4M}}{R_{4M}} + C_5\dfrac{d\theta_5}{dt} + \left(\dfrac{1}{R_{4M}} + \dfrac{1}{R_5}\right)\theta_5 - \dfrac{\theta_{62}}{R_5} = P_5, \\[2ex]
-\dfrac{\theta_5}{R_5} + C_{62}\dfrac{d\theta_{62}}{dt} + \left(\dfrac{1}{R_5} + \dfrac{1}{R_{62}}\right)\theta_{62} - \dfrac{\theta_{63}}{R_{62}} = P_{62}, \\[2ex]
\vdots \\[2ex]
-\dfrac{\theta_{6N-1}}{R_{6N-1}} + C_{6N}\dfrac{d\theta_{6N}}{dt} + \left(\dfrac{1}{R_{6N-1}} + \dfrac{1}{R_{6N}}\right)\theta_{6N} - \dfrac{\theta_0}{R_{6N}} = P_{6N}.
\end{cases} \tag{13}$$

In (13), t indicates time; the other variables are shown in Figure 9. The equation is converted into matrix, and the cable core temperature is calculated using the same method as in (7).

3. Experimental Test

3.1. Experimental Apparatus and Tested Cable. The cable internal-caused fire experimental platform which includes a current increasing module and a temperature monitoring module is powered by 380 V AC. The current raising module supports low-voltage and high current output through the use of an automatic voltage regulator and current raising

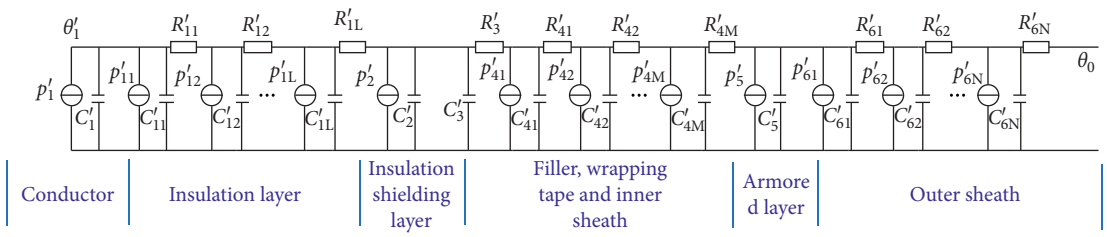

Figure 8: Layered trisection transient thermal circuit model of power cable.

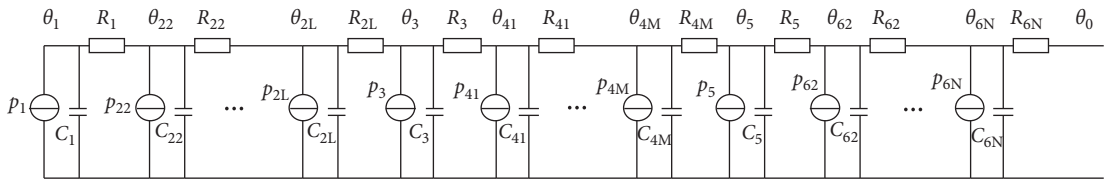

$C_1 = C'_1 + C'_{11}$, $P_1 = P'_1 + P'_{11}$, $\theta_1 = \theta'_1$, $R_1 = R'_{11}$, $P_{22}{\sim}P_{2L} = P'_{12}{\sim}P'_{1L}$, $C_{22}{\sim}C_{2L} = C'_{12}{\sim}C'_{1L}$, $R_{22}{\sim}R_{2L} = R'_{12}{\sim}R'_{1L}$, $P_3 = P'_2$, $C_3 = C'_2 + C'_3$, $R_3 = R'_3$, $P_{41}{\sim}P_{4M} = P'_{41}{\sim}P'_{4M}$, $C_{41}{\sim}C_{4M} = C'_{41}{\sim}C'_{4M}$, $R_{41}{\sim}R_{4M} = R'_{41}{\sim}R'_{4M}$, $R_5 = R'_{61}$, $P_5 = P'_5 + P'_{61}$, $C_5 = C'_5 + C'_{61}$, $P_{62}{\sim}P_{6N} = P'_{62}{\sim}P'_{6N}$, $C_{62}{\sim}C_{6N} = C'_{62}{\sim}C'_{6N}$, $R_{62}{\sim}R_{6N} = R'_{62}{\sim}R'_{6N}$

Figure 9: Simplification of layered trisection transient thermal circuit model of power cable.

device. The temperature measurement module contains real-time collection of 16 channels of temperature data. By connecting external thermocouple sensors, temperature data from each point of the tested cable can be collected and recorded [32]. Picture and system diagram of experimental platform are shown in Figure 10. The following are the main technical parameters: output current range, 0–1000 A; temperature measurement range, −80~+500°C; temperature measurement error range, ±0.1°C.

In this experiment, the XLPE power cable (YJV22-6/$10\,\mathrm{kV}^{-3} \times 50$) is selected as the tested cable. On the radial part of the cable, the three core lines are symmetrically arranged in a triangle. The structure of the cable includes core conductor, insulation layer, insulation shielding layer, filler, wrapping tape, inner sheath, cable armored layer, and outer sheath. Table 1 lists the cable parameters.

3.2. Experimental Processes

3.2.1. Experiment Preparation. Three hours before the test, the air conditioner was adjusted to 20°C to guarantee that the experimental environment and the starting temperature of the cable under test were both 20°C. The tested cable was connected with the cable internal-caused fire test platform. One end of cable is connected to large current output port of test platform, and the other end is short-circuited.

3.2.2. Thermocouple Installation. To monitor the temperature of the tested cable, thermocouple sensors are placed on the surface of the outer sheath and core conductor. Three holes in the cable are drilled to expose the core conductor, and thermocouple sensors are installed in these holes to measure temperature of core conductor of cable. Thermocouple sensors are pasted within 5 cm from drilling position on the surface of cable outer sheath to measure surface temperature of cable outer sheath. Figure 11 depicts a picture and structural schematic of a thermocouple installation.

3.2.3. Loading Experimental Current. In this experiment, continuous currents of 180 A and 380 A are used, and three-phase current is balanced. A 180 A experimental current is utilized to mimic the normal functioning condition of the cable, and then 380 A step currents are used to model the fault currents of the cable. At first, experimental current is set to 180 A to simulate normal working state of cable under test. After temperatures of core conductor and surface of outer sheath tend to be stable, output current of cable internal-caused fire experimental platform is adjusted to 380 A for stimulating the fault state of cable. When the fault simulation current is applied on the cable, the temperature of cable core rises and slowly exceeds the maximum allowable temperature of 90°C. The experiment is terminated if the observed temperature of the cable core exceeds 137°C. Figure 12 depicts the experimental current.

4. Results and Discussion

4.1. Cable Core Temperature and Outer Sheath Surface Temperature. Under normal and fault circumstances, the experiment replicates the change in cable core temperature and outer sheath surface temperature. Both the core temperature and the surface temperature of the outer sheath of the cable begin to rise, and the core temperature is greater than the surface temperature of the outer sheath of the cable, but the rate of temperature rise for both is very slow. When the load current is continuously loaded for about 2.8 hours, the temperature of the core and the surface of the outer sheath tend to remain steady. When a current of 380 A is applied, the core temperature and the surface temperature of the outer sheath of the cable begin to rise again and the

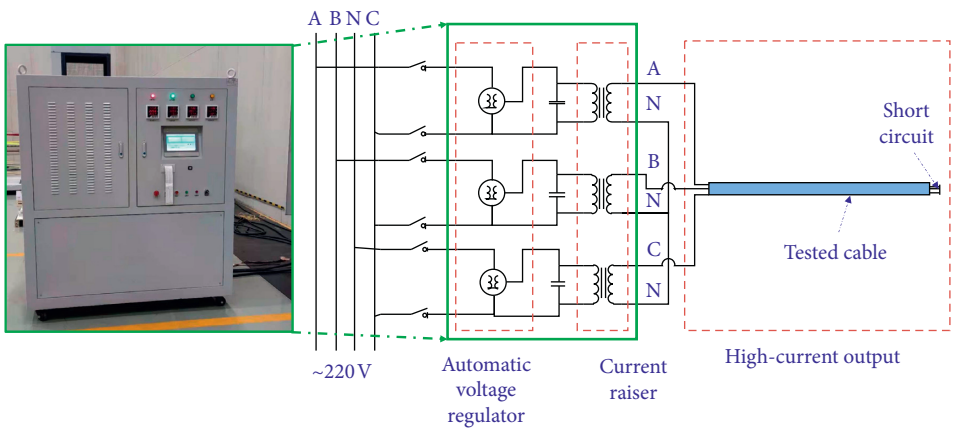

Figure 10: Picture and system diagram of experimental platform.

Table 1: Parameters of layers of YJV22 6/10 kV cable.

Structure	Inner diameter (mm)	Outer diameter (mm)	Thermal conductivity $(W(km)^{-1})$	Volumetric heat capacity $(10^4(JK^{-1}m^{-3}))$
Conductor		8.6	400	434.14
Insulation layer	8.6	17.6	0.32	303.12
Insulation shielding layer	17.6	19.2	400	434.14
Wrapping tape	44.4	45.4	0.2	196.00
Inner sheath	45.4	49.2	0.2	124.2
Cable armored layer	49.2	50.2	48	372.88
Outer sheath	50.2	55.6	0.2	124.2

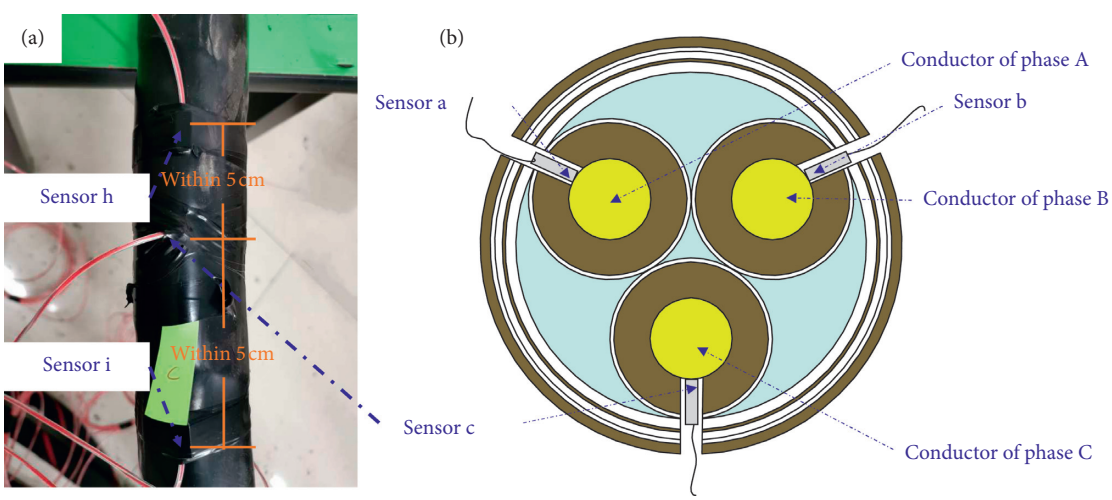

Figure 11: (a) Picture of thermocouple installation; (b) schematic diagram of thermocouple installation.

temperature rise of the outer sheath surface of the cable is lagging relative to the cable core; the temperature rise rate of outer sheath surface is less than that of the cable core. Figure 13 depicts the temperature change of the cable core and the surface temperature of the outer sheath.

4.2. Verification of the Proposed Model by Experimental Data. The current values and the surface temperatures of the outer sheath measured in the experiment are substituted into the transient thermal circuit model, and the core temperature of the cable is calculated. When the calculated value of cable core temperature is compared to the experimental observed value, it is discovered that the estimated value of cable core temperature is lower. The error analysis of the experimental and calculated values of the cable core temperature is shown in Table 2. Calculation error of the transient thermal circuit model rises as the load current, yet the typical relative and absolute errors are less than 10%, and the average absolute errors are less than 10°C.

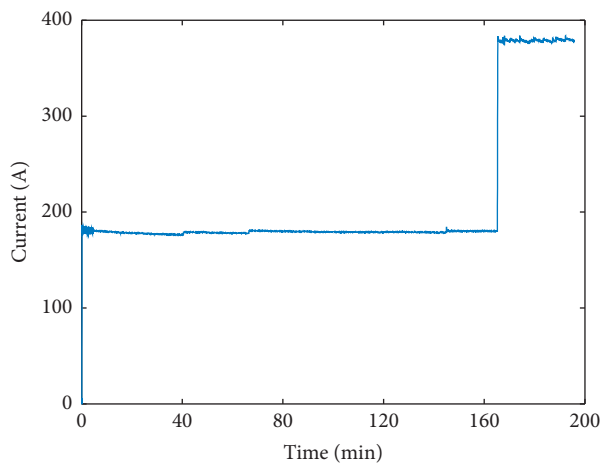

Figure 12: Cable current curve.

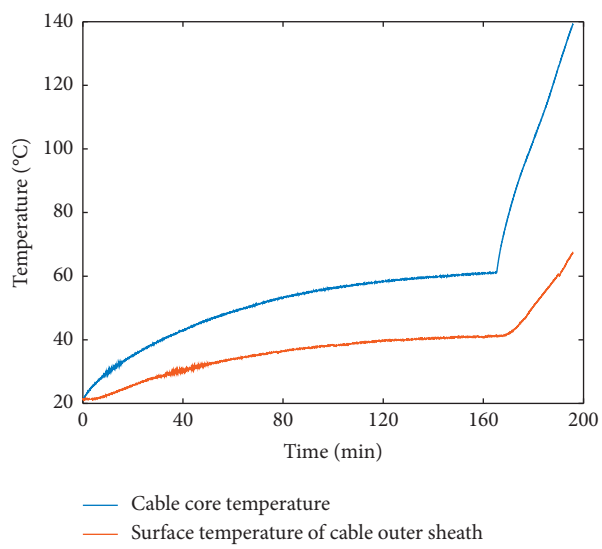

Figure 13: Change curve of cable core temperature and outer sheath surface temperature.

Table 2: Calculation error of transient thermal circuit model under various load currents.

Simulative current (A)	Average error	
	Relative error (%)	Absolute error (°C)
180	−2.49	−5.12
380	−7.98	−7.82

Similar to this, we plug the data in the experiment into trisection transient thermal circuit model and analyze the error between the calculated value and the experimental value. Table 3 shows the error analysis of experimental and estimated cable core temperature data. Calculation error of the trisection transient thermal circuit model is bigger as compared to the transient thermal circuit model and increases with the increase of the load current; the average absolute errors are less than 10°C, while the average relative errors are still less than 10%.

Table 3: Calculation error of trisection transient thermal circuit model under various load currents.

Simulative current (A)	Average error	
	Relative error (%)	Absolute error (°C)
180	−3.74	−7.73
380	−9.92	−9.55

The systematic measurement error, the contact thermal resistance, and the temperature gradient inside the material are the major causes of mistakes, with the temperature gradient being the most important component. Take insulation layer of cable as an example; it is assumed that the innermost temperature of the cable insulation layer is θ_x, the outermost temperature is θ_y, the inner diameter of the cable insulation layer is d_1, and the outer diameter is d_2, so its corresponding radius is $r_1 = (d_1/2)$ and $r_2 = (d_2/2)$. Equation (14) should be filled up using the above parameters.

$$\frac{\mathrm{d}}{\mathrm{d}r}\left(r\frac{\mathrm{d}\theta}{\mathrm{d}r}\right) = 0. \tag{14}$$

The following equation can be obtained by solving (14).

$$\theta = \theta_x + \frac{\theta_y - \theta_x}{\ln\left(r_2/r_1\right)}\ln\frac{r}{r_1}. \tag{15}$$

Take the derivative on both sides of (15).

$$\frac{\mathrm{d}\theta}{\mathrm{d}r} = \frac{1}{r}\cdot\frac{\theta_y - \theta_x}{\ln\left(r_2/r_1\right)}. \tag{16}$$

From (16), temperature gradient is inversely proportional to the radius, the closer the thermal source, the greater the temperature gradient, and the greater the influence of layering on the calculation accuracy of the transient thermal circuit model. As a consequence, layered optimization of the thermal circuit model can decrease the impact of temperature gradient on calculation results while also increasing the model's calculation accuracy. Using the controlled variable method, the insulation layer, inner sheath, and outer sheath of the cable are calculated successively from 1 to 100 layers and compared with the measured core temperature of the experiment. Figure 14 shows the variation of computation error with the number of layers. It could be seen that the layered optimization of the algorithm model can effectively decrease the calculation error and the layered insulation layer holds a greater impact on the calculation accuracy of the algorithm model as compared to the other two layers.

Increasing the number of layers can reduce the calculation error of the model; however, if the number of layers is sufficient, the temperature gradient in each layer becomes extremely tiny. When this occurs, increasing the number of layers has minimal effect on computation accuracy and would increase the calculation amount of the model. Hence, the appropriate number of layers must be selected in the layering optimization of algorithm model. Because the thermocouple sensor's measurement precision is 0.1°C in

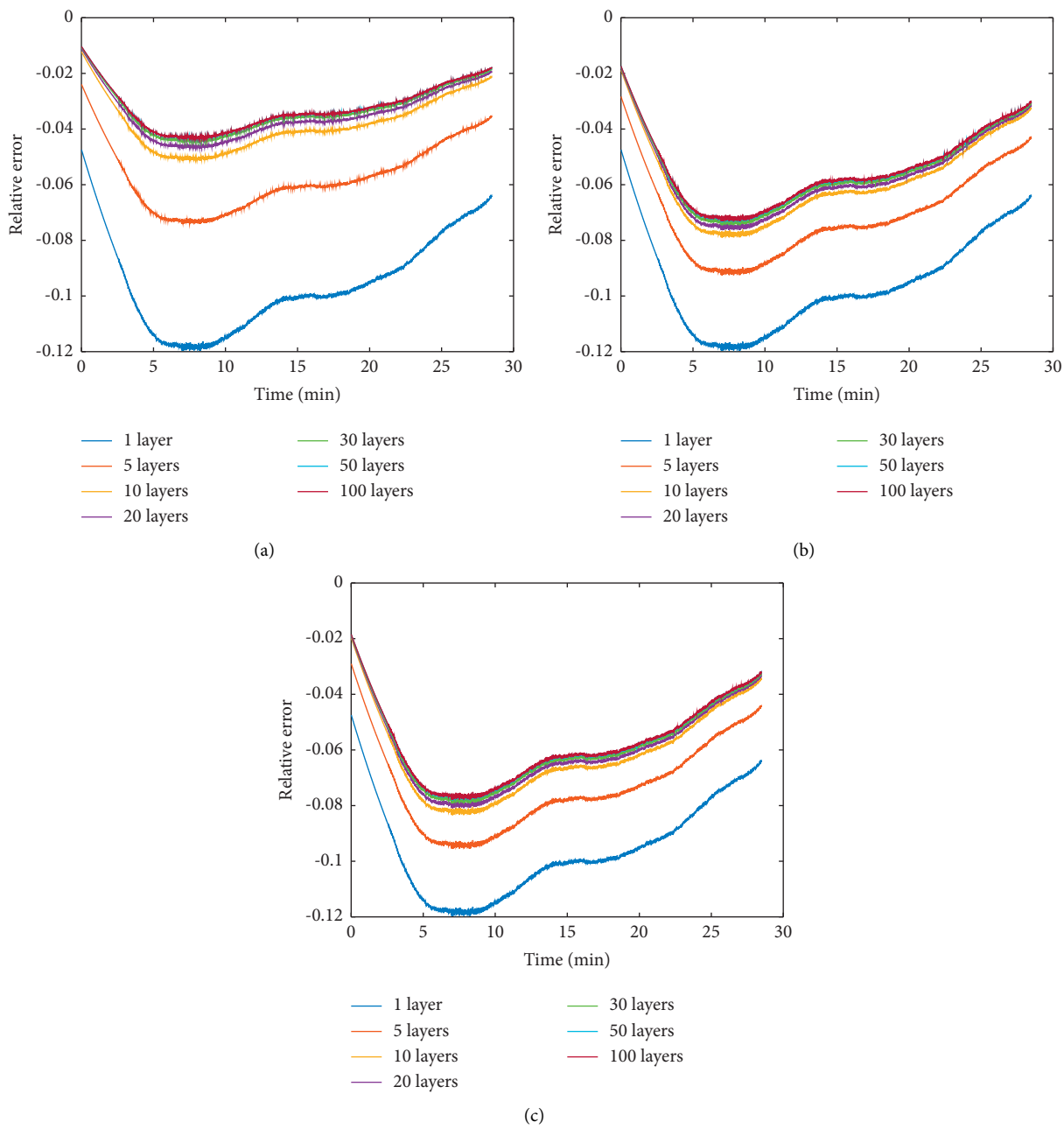

Figure 14: (a) Variation curve of relative error with the number of layers of insulation layer; (b) variation curve of relative error with the number of layers of inner sheath layer; (c) variation curve of relative error with the number of layers of outer sheath layer.

this experiment, the maximum value of the improved calculation accuracy value relative to the front stage layering is chosen to determine the appropriateness of the number of layers. When the maximum value approaches 0.1°C, we believe that the number of layers at this level is the appropriate number of layers. As illustrated in Table 4, when the numbers of layers are 50, the maximum value approaches 0.1°C. Thus, the numbers of layers of insulation, inner sheath, and outer sheath are all 50 in this study.

As a consequence, stacking the cable sheath can effectively minimize the trisection transient thermal circuit model's calculation circuit. When L=50, M=50, and N=50, the relative error of the thermal circuit model algorithm is analyzed. The estimated core temperature has a maximum relative error of less than 2 percent with an average relative error of 1.08 percent, meeting the calculation requirements of extremely early detection and prediction of cable internal-caused fire.

4.3. Response Time of the Model. It can be seen from the above analysis that the calculated value of the cable core temperature is less than the experimental measurement value. When the temperature is 137°C, the time difference between the calculated value and the measured value is

Table 4: The maximum value of the increased calculation accuracy value relative to the front level layering.

Number of layers	Maximum value (°C)		
	Insulation layer	Inner sheath	Outer sheath
5	5.23	3.1	2.7
10	1.81	1.36	1.15
20	0.7	0.54	0.51
30	0.2	0.16	0.16
50	0.1	0.11	0.1
100	0.01	0.021	0.021

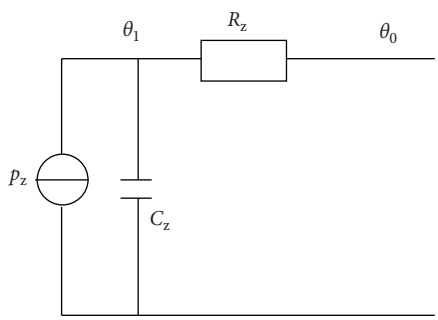

Figure 15: Equivalent first-order thermal circuit model of cable.

called the response time of detection and prediction. The response time of cable internal-caused fire early detection and prediction is an indicator to measure the rapidity of the model's response. The layered trisection transient thermal circuit model is equivalently combined into a first-order thermal circuit model of a single heat source, as shown in Figure 15.

According to the heat balance theory in heat transfer, the heat balance equation is established.

$$P_z = C_z \frac{\mathrm{d}\theta_1}{\mathrm{d}t} + \frac{\theta_1 - \theta_0}{R_z}. \tag{17}$$

Assuming that the initial temperature of the cable core when the fault current is loaded is θ_1^0, the general solution of (17) is

$$\begin{aligned} \theta_1 &= P_z R_z + \theta_0 + \left(\theta_1^0 - \theta_0 - P_z R_z\right) e^{-\left(t/R_z C_z\right)}, \\ t &= R_z C_z \left(\ln\left(\theta_1^0 - \theta_0 - P_z R_z\right) - \ln\left(\theta_1 - \theta_0 - P_z R_z\right)\right). \end{aligned} \tag{18}$$

The expression of t is a function of time as

$$t(\tau) = R_z C_z \left(\ln\left(\theta_1^0(\tau) - \theta_0(\tau) - P_z R_z\right) - \ln\left(\theta_1 - \theta_0(\tau) - P_z R_z\right)\right), \tag{19}$$

where t_1 and t_2, respectively, indicate the time when the measured value and the calculated value reach 137°C. Response time of cable internal-caused fire early detection and prediction is

$$t_Y = t_2 - t_1. \tag{20}$$

In the formula, $\theta_0(\tau)$ is the surface temperature of the outer sheath of the cable at different times; $\theta_1^0(\tau)$ is the temperature of the cable core at different times; and θ_1 is 137°C. The response time of cable internal-caused fire early detection and prediction of the model is 148 s when the experimental current is 380 A. The response time is less than 3 min, which meets the needs of cable internal-caused fire early detection and prediction.

5. Conclusion

Early detection and prediction technology of cable internal-caused fire may significantly minimize cable fire probability in tunnels and ensure cable tunnel safety. An algorithm model for estimating the core temperature from the surface temperature of cable outer sheath was developed in this work, and it was shown to be viable in the early detection of cable internal-caused fire by experiment. The main conclusions are as follows:

(1) Error analyses illustrate that the calculated value of cable core temperature is less as compared to the measured value. The reason is that the temperature of inner surface of the material has been chosen to calculate the thermal capacity of the material, leading to the calculated thermal capacity of each layer of material being greater than the actual thermal capacity.

(2) To solve the problem that the temperature of the cable core cannot be directly measured, a transient thermal circuit model has been suggested, so that the abnormal temperature rise characteristics of the cable core could be utilized for the very early detection and prediction of the cable internal-caused fire. The trisection transient thermal circuit model decreases the transient thermal circuit model's complexity while simultaneously increasing calculation error. It is noteworthy that the calculation errors of the two models are less than 10%, which could cater to the needs of very early detection and prediction of internal-caused fire of cable.

(3) Layered optimization can lower the calculation error, but once the number of layers of cable material exceeds a certain order of magnitude, increasing the number of layers has a limited impact on the calculation accuracy of the model. The highest relative error of the estimated value of the model is less than 2 percent, and the average relative error is 1.08 percent in this article when the number of layers of cable insulation layer, inner sheath, and outer sheath is 50 layers.

(4) The response time of cable internal-caused fire early detection and prediction of the layered trisection transient thermal circuit model is less than 3 min, which meets the needs of early detection and prediction of the cable internal-caused fire.

Data Availability

The data used to support the findings of this study are available from the corresponding author upon request.

Conflicts of Interest

The authors declare that there are no conflicts of interest.

References

[1] Y. Liu and X. Zhao, "Research on harmful mechanism of approaching construction to urban cable tunnels and protective suggestion," *Electric Power Survey and Design*, vol. 8, pp. 22–28, 2021.

[2] B. Wu and P. A. N. G. Zhe, "Development status of intelligent inspection robots in power tunnel environment," *Industrial Control Computer*, vol. 34, no. 7, pp. 20–22, 2021.

[3] K. Liang, X. Hao, W. An, Y. Tang, and Y. Cong, "Study on cable fire spread and smoke temperature distribution in T-shaped utility tunnel," *Case Studies in Thermal Engineering*, vol. 14, Article ID 100433, 2019.

[4] L. I. U. Yang, J. Chen, L. I. Chenying, C. H. E. N. Hong, K. Liu, and X. I. E. Qiyuan, "Experimental study on the influence of intumescent fire-resistant coating on ignition characteristics of high-voltage power cables," *Fire Safety Science*, vol. 29, no. 4, pp. 214–221, 2020.

[5] Z. H. A. O. Jing, T. U. Haoxi, and Y. Chen, "220 KV and above voltage level city cable tunnel fire protection system design," in *Proceedings of the International Conference On New Energy Science And Research (ICESR)*, pp. 463–468, Destech Publicat Inc, Changsha, China, 2015.

[6] H. Fang, *Study on Fire Risk Assessment of Urban Electric Power Cable Tunnel*, University of Science and Technology of China, Hebei, China, 2019.

[7] H. Zhang, L. V. Zonghui, L. I. Ang, and Z. H. O. U. Mei, "Statistical analysis of serious fires in China based on factor Analysis," *Journal of the Armed Police Academy*, vol. 35, no. 2, pp. 53–57, 2019.

[8] D.-E. Kim, N.-H. Kim, S.-H. Lim, and K. Gyung-Suk, "Condition monitoring technique for heating cables by detecting discharge signal," *Journal of the Korean Institute of Electrical and Electronic Material Engineers*, vol. 34, no. 2, pp. 136–141, 2021.

[9] S.-C. Yang, H.-Y. Kim, and O.-S. Kweon, "Experimental study of flame spread characteristics of a electric cable tray," *Journal of The Korean Society of Hazard Mitigation*, vol. 16, no. 4, pp. 31–35, 2016.

[10] T. Wang, X. Zhou, B. A. I. Gang, L. I. Chengyu, and Y. A. N. G. Xiaobin, "Hazard prediction of gas explosion induced by coal mine fire," *Journal of China Coal Society*, vol. 45, no. 12, pp. 4104–4110, 2020.

[11] W. Huang, C. Zhou, and X. Q. Wang, "Fire statistic and prevention measures for cables in power plant," *Advanced Materials Research*, vol. 614-615, pp. 1949–1952, 2013.

[12] X. Wang, L. I. A. O. Guangxuan, X. U. Tianrui, and C. A. I. Xin, "Real scale tests on cable tray fires to simulate actual end user's condition,"vol. 6, pp. 765–769, in *Proceedings of the 5th International Symposium on Safety Science and Technology*, vol. 6, pp. 765–769, SCIENCE PRESS USA INC, Changsha, China, August 2006.

[13] Z. Pascal, R. Hanouzet, and T. Beji, "Improved assessment of fire spread over horizontal cable trays supported by video fire analysis," *Fire Technology*, vol. 55, no. 1, pp. 233–255, 2019.

[14] J. Zheng, S. Liu, P. U. Lu, X. Su, X. Zhao, and X. U. Yang, "State of the art of combustion behavior of live power cables," *Smart Power*, vol. 48, no. 10, pp. 105–112, 2020.

[15] P. Huang, Q. I. N. Liang, Y. U. Longxing, S. Chen, L. I. N. Yuyao, and L. Huang, "Temperature field distribution of cable tray fire in utility tunnel," *Journal of Fuzhou University (Natural Science Edition)*, vol. 49, no. 4, pp. 544–550, 2021.

[16] H. Zhang and Y. Zhao, "Study on underground utility tunnel fire characteristics under sealing and ventilation conditions," *Advances in Civil Engineering*, vol. 2020, Article ID 9128704, 11 pages, 2020.

[17] V. Babrauskas, "How do electrical wiring faults lead to structure ignitions?" in *Proceedings of the Fire and Materials Conference 2001*, pp. 39–51, London, UK, September 2001.

[18] J. J. Shea, "Identifying causes for certain types of electrically initiated fires in residential circuits," *Fire and Materials*, vol. 35, no. 1, pp. 19–42, 2011.

[19] V. Babrauskas, "Mechanisms and modes for ignition of low-voltage, PVC-insulated electrotechnical products," *Fire and Materials*, vol. 30, no. 2, pp. 151–174, 2006.

[20] X. Gao, J. I. A. N. G. Yun, L. U. O. Junhua, and C. Yuan, "The principle of earlier period damage of XLPE power cable dueto temperature rise by overload," *High Voltage Engineering*, vol. 23, no. 2, pp. 62–64, 1997.

[21] D. U. Lin, Y. U. Huizong, and Y. A. N. Han, "A non-invasive temperature measurement method for high-voltage cable core based on temperature field construction and analysis," *Transactions of China Electrotechnical Society*, vol. 36, no. 7, pp. 1338–1346, 2021.

[22] R. S. Singh, J. Cobben, and V. Ćuk, "PMU-based cable temperature monitoring and thermal assessment for dynamic line rating," *IEEE Transactions on Power Delivery*, vol. 36, no. 3, pp. 1859–1868, 2021.

[23] D. Miyagi, N. Takata, and N. Takahashi, "Thermal analysis of co-axial multi-layered BSCCO HTS power cable," *IEEE Transactions on Applied Superconductivity*, vol. 21, no. 3, pp. 991–995, 2011.

[24] T. X. Sun, X. F. Zeng, Y. X. Lu, and H. J. Li, "Research on energy harvesting and its application in thermal condition monitoring of three-core power cables," in *Proceedings of the 21st International Symposium on High Voltage Engineering (ISH)*, Budapest, Hungary, 28 November 2019.

[25] Y. H. Li, S. C. Ding, G. Liu, and C. Lei, "Study on relationship between thermal conductivity and core temperature of power cable," in *Proceedings of the Asia-Pacific Power and Energy Engineering Conference (APPEEC)*, March 2011.

[26] T. A. O. Wenquan, *Numerical Heat Transfer*, Xi'an Jiaotong University Press, Xi'an, China, 2001.

[27] M. Lei, G. Liu, Y. Lai, J.-z. Li, W. Li, and Y. Liu, "Study on thermal model of dynamic temperature calculation of single-core cable based on laplace calculation method," in *Proceedings of the International Symposium On Electrical Insulation (ISEI)*, June 2010.

[28] Q. Hu, G. Liu, X. Ye, and L. Yan, "Three core cable hot field distribution and coaxial heat road model feasibility study," in *Proceedings of the General Meeting of the IEEE-Power-and-Energy-Society (PES)*, July 2013.

[29] Y. Wang and X. Zhang, "Research on spontaneous cable fire early warning based on thermal circuit model with distribution parameters," *Dynamic Systems and Applications*, vol. 29, no. 8, pp. 2557–2570, 2020.

[30] M. E. N. G. Xiao-Kai, Z.-Q. Wang, and L. I. Guo-Feng, "Dynamic analysis of core temperature of low-voltage power cable based on thermal conductivity," *Canadian Journal of Electrical and Computer Engineering*, vol. 39, no. 1, pp. 59–65, 2016.

[31] M. Rerak and P. Ocłoń, "Thermal analysis of underground power cable system," *Journal of Thermal Science*, vol. 26, no. 5, pp. 465–471, 2017.

[32] L. I. Bo, X. Zhang, and B. O. Chunbo, "Experimental study on early characteristics of internal cause of fire in power cable," *Fire Science and Technology*, vol. 38, no. 12, pp. 1772–1776, 2019.